

École Doctorale Mathématiques, Sciences de
l'Information et de l'Ingénieur

UdS – INSA – ENGEES



THESIS

presented in order to obtain the grade of

Doctor of University of Strasbourg

Discipline: Mechanics

Specialty: Biomechanics

by

Simon Chatelin

**Improvement of Traumatic Brain Injury understanding in
case of Head Trauma:**

Heterogeneity and anisotropy inclusion using medical imaging

(Temporary version)

Members of jury

<i>Tutor :</i>	M. Rémy WILLINGER, Professor, UdS
<i>Co-Tutor :</i>	M. André CONSTANTINESCO, Professor, UdS
<i>External opponent :</i>	M. Narayan YOGANANDAN, Professor, Medical College of Wisconsin
<i>External opponent :</i>	M. Ralph SINKUS, Research Director, Hôpital Beaujon CNRS
<i>Guest :</i>	Mme. Caroline DECK, Research Engineer, UdS

Table of contents

Introduction	7
CHAPTER 1 <i>Bibliographical synthesis</i>	11
1 <i>Introduction</i>	12
2 <i>In vitro mechanical testing</i>	13
2.1 Creep and relaxation tests	14
2.1.1 Creep tests in tensile/compression	14
2.1.2 Relaxation tests in tensile/compression	14
2.1.3 Relaxation tests in shear	15
2.2 Constant strain rate tensile/compression tests	18
2.3 Dynamic frequency sweep tests	20
2.3.1 Dynamic mechanical analysis in tensile/compression	23
2.3.2 Dynamic mechanical analysis in shear	23
2.4 Non linearity investigation	25
3 <i>In vivo mechanical testing</i>	26
3.1 Indentation tests	26
3.2 Brain tissue Magnetic Resonance Elastography in vivo testing	27
3.2.1 Magnetic resonance elastography methods	28
3.2.2 MRE applied to brain investigation	29
4 <i>Discussion</i>	33
4.1 From in vitro to in vivo approach	33
4.2 Heterogeneity	34
4.3 Anisotropy	34
4.4 Inter-species variations	35
4.5 Age-dependence	35
4.6 Post-mortem time	35
4.7 Experimental parameters	36
5 <i>Conclusions</i>	36

CHAPTER 2	<i>Axons deformation in case of head trauma</i>	37
1	<i>Introduction</i>	38
2	<i>Materials and method</i>	40
2.1	Human head FE model and related criteria	40
2.2	Brain Diffusion Tensor Imaging atlas	43
3	<i>Theory and calculation</i>	43
3.1	Inclusion of axonal direction into the brain FEM	43
3.2	Computation of axonal elongation under impact	48
4	<i>Results</i>	50
4.1	Introduction	50
4.2	Diffusion parameters calculation for the FEM	50
4.3	Implementation of axonal directions into the brainstem FEM	57
4.4	Axonal deformation under impact	58
5	<i>Discussion</i>	63
6	<i>FA influence on post-computing</i>	66
7	<i>Conclusion</i>	68
CHAPTER 3	<i>Isotropic heterogeneous modeling of brain tissue</i>	71
1	<i>Introduction</i>	72
2	<i>Heterogeneity inclusion in brain FEM</i>	73
2.1	Introduction	73
2.2	Experimental brain MRE data	73
2.3	Heterogeneous viscoelastic law	73
2.3.1	Introduction	73
2.3.2	Scaling of the MEF on the MRE data	74
2.3.3	Viscoelastic parameters calculation	76
2.3.4	Heterogeneous linear viscoelastic model	77
2.3.5	Conclusion	78

2.4	Conclusion.....	78
3	<i>Application to accident simulation.....</i>	79
3.1	Introduction	79
3.2	Brain Finite Element Models	79
3.3	Human brain heterogeneous models	80
3.3.1	Introduction	80
3.3.2	Influence of heterogeneity with low stiff models.....	81
3.3.3	Influence of heterogeneity with high stiff models.....	82
3.3.4	Maximal values for the four models.....	83
3.3.5	Axonal deformation of a brain heterogeneous model.....	83
3.4	Conclusion.....	86
4	<i>Conclusion</i>	86
 CHAPTER 4 <i>Non-linear visco-hyperelastic anisotropic constitutive model for brain</i>		
tissue	89	
1	<i>Introduction</i>	90
2	<i>Evaluation of existing brain tissue FE constitutive models</i>	91
2.1	Introduction	91
2.2	Description of the model	91
2.2.1	Introduction	91
2.2.2	Geometry and meshing.....	92
2.2.3	Mechanical properties	92
2.2.4	Boundary conditions and loadings.....	95
2.2.5	Conclusion.....	97
2.3	FE simulation of rheometric tests	97
2.3.1	Introduction	97
2.3.2	Shear simulations	98
2.3.3	Tensile simulations	100
2.3.4	Compression simulations	101
2.3.5	Strain rate influence in compression	102
2.3.6	Conclusion.....	108
2.4	Conclusion.....	109

3	<i>Brain anisotropic model</i>	110
3.1	Introduction	110
3.2	Anisotropic visco-hyperelastic law	110
3.2.1	Introduction	110
3.2.2	Theoretical description	110
3.2.3	Identification of the parameters.....	113
3.2.4	Implementation under LS-DYNA® software	114
3.2.5	Evaluation of the anisotropic visco-hyperelastic law	116
3.2.6	Conclusion.....	119
4	<i>Anisotropic brain Finite Element Model</i>	119
4.1	Introduction	119
4.2	Presentation of the model	119
4.3	Illustration on a real accident case	120
4.3.1	Conclusion.....	122
4.4	Conclusion.....	123
5	<i>Conclusion</i>	123
	<i>Conclusions and future developments</i>	125
	<i>References</i>	131
Appendix A	<i>Bibliographical study</i>	145

Introduction

The aim of this PhD Thesis is to improve understanding of brain injuries mechanisms in case of head impact, and also build an improved human brain mechanical model using medical imaging. This work is performed as part of biological soft tissue characterization for impact biomechanics within the Biomechanics department located at the Fluid and Solid Mechanics Institute in Strasbourg.

Traumatic Brain Injury (TBI) is one of the most common causes of death and disability and it remains an important public health problem. Motor vehicle traffic is the second cause of TBI, just after injuries due to falling (Faul *et al.*, 2010). According to the World Health Organization (WHO), 1.2 million people died of motor vehicle traffic injuries in 2002 all over the world. Annual incidence of TBI is estimated at 235/100,000 inhabitant in Europe, 98/100,000 inhabitant in the US and 160/100,000 inhabitant in India by Tazarourte *et al.* (2008). In France, death rate caused by TBI is 22% (Tiret *et al.*, 1990). Diffusion Axon Injuries (DAI) appear in almost half (48.2%) of TBI and is the second reason of death by TBI, according to Bain and Meaney (2000).

Impact Biomechanics aims at linking brain loading to resulting brain injuries in case of head trauma. Dynamic brain response to an impact is characterized in terms of intracranial pressure, stress and strain fields. In this way, loading, mechanical response and brain mechanical properties can be linked to each other. Consequently, brain tissue mechanical properties have to be modeled in order to develop brain model that can simulate brain mechanical response and injuries in case of head trauma. Since 1970', Finite Element human Head Models (FEHM) have been developed as predicting tools for head injury risk and eventually TBI location, notably concerning DAI. This technique enables to simulate injuries with the opportunity of evaluating many mechanical parameters and developing injury protection tool with reduced cost and time. In particular, finite element head modeling have been proposed within the Biomechanics department based on works of Kang *et al.* (1997) with the development of the *Strasbourg University Element Head Model* (SUFHEM). DAI criteria has been proposed from this model and a large number of detailed head impact injuries simulations in terms of Von Mises stress, maximal principal strain and Von Mises stress by Willinger and Baumgartner (2003), Marjoux *et al.* (2008) and Deck *et al.* (2008). However, in the same line as most of the head finite element models from the literature (Kang *et al.*, 1997; King *et al.*, 2003; Takhounts *et al.*, 2003; Belingardi *et al.*, 2005; Iwamoto *et al.*, 2007; Takhounts *et al.*, 2008), SUFHEM brain is considered as linear viscoelastic, homogeneous and isotropic with properties identified by *in vitro* experimental data.

Work of this PhD thesis will concern this last observation. We will aim at including for the first time heterogeneity and anisotropy extracted from medical imaging based techniques within a brain finite element model.

In the first chapter different anatomical and mechanical properties of brain tissue will be explained within the framework of a detailed bibliographic study for human brain numerical modeling. Firstly axonal fibers distribution will be studied. Then, literature review on brain tissue mechanical properties will be proposed by focusing on the comparison of results between classical *in vitro* and recent *in vivo* experimental techniques. Different models from the literature for brain tissue will be then proposed.

The first aim of this thesis is to take brain anisotropy into account for the first time for real-world injuries reconstruction. From last ten years, a new imaging technique, call Diffusion Tensor Imaging (DTI), is used to observe the water molecules Brownian movement constrained by axonal fibers into the brain (Basser *et al.* 1994; LeBihan *et al.*, 2001; Kraus *et al.*, 2007). By imaging these displacements (diffusion) using Magnetic Resonance Imaging (MRI), a tridimensional map of main axonal fibers orientation can be obtained. The purpose of this work in chapter 2 is to develop a new method for DAI prediction and location based on the assumption of axons elongations by post-treating classical isotropic accident simulation. Information on axons fibers orientation and density will be taken into account in the post-treatment of the simulations. Influence of taking anisotropy into account will then be illustrated on two well documented motorcyclist accident cases.

Further, heterogeneity will be implemented into the brain from a three dimensional map of viscoelasticity obtained *in vivo* by Magnetic Resonance Elastography (MRE). For less than ten years, *in vivo* mechanical properties of the brain have been proposed using MRE by analyzing displacements induced by shear wave propagation into the brain. The study proposed in chapter 3 will concern the implementation of these *in vivo* MRE based heterogeneous data into the brain finite element model. Influence of heterogeneity inclusion on brain response will be then evaluated by reconstructing two well documented motorcyclist accident cases.

Conclusions and observations from the three first chapters will be then for the first time synthesized for the development of an anisotropic, heterogeneous visco-hyperelastic law for brain finite element model behavior. The last chapter will begin by evaluating on numerical samples the different brain models from the literature. These laws will be tested on numerical simulation of classical rheological tests (tensile, compression and shear). Conclusion from these comparisons and from the chapters 1, 2 and 3 will then be used to propose a new anisotropic visco-hyperelastic law for brain tissue, identified by *in vivo* data from MRE and DTI. Then, this law will be implemented into the SUFEHM geometry. For the first time, a brain finite element model will be presented with all of the following properties:

- Anisotropy due to local orientations of axonal fibers;

- Heterogeneity;
- Dissociation of mechanical behavior between cerebral matrix and axons fibers;
- *In vivo* mechanical parameters identified using MRE and DTI;
- Viscosity;
- Inclusion of non-linearities, involving rigidifying of brain tissue at high strain.

Then, this new model will be used to reconstruct a well documented motorcyclist accident case. We will aim at estimating its capability to reproduce brain injury mechanisms, especially concerning DAI.

CHAPTER 1

Bibliographical synthesis

1 Introduction

Aim of this chapter is to develop notions necessary to the development and understanding of the thesis. Following aspects have been developed in the French version of this manuscript:

- Anatomy of the central nervous system. This part is an introduction to the main notions for brain traumatism understanding. The emphasis is put on the anatomical description of main axons fibers fasciculi of the brain white matter. For more details, readers can refer to the Gray's Anatomy (Standring, 2005);
- A second part is dedicated to the description of medical imaging techniques. The following techniques are successively described: Nuclear Magnetic Resonance (NMR), Magnetic Resonance Imaging (MRI), Diffusion Tensor Imaging (DTI) and Magnetic Resonance Elastography (MRE). More details about DTI and MRE can be respectively found in LeBihan *et al.* (2001) and Muthupillai *et al.* (1995);
- Synthesis of literature brain tissue testing. The aim is to extract main mechanical properties of brain tissue. This part have been integrally translated in the English version of the manuscript and is proposed hereunder;
- Main models applied in the literature for brain tissue. Linear viscoelastic (Generalized Maxwell) as well as hyperelastic (Ogden, Mooney-Rivlin, and Eight Chains) or micro/macro (axon fiber, composite) models are detailed.

Insofar as main conclusions of this chapter for the development of the thesis are extracted from the literature review on brain tissue experimental characterization, only this part is translated for the English version.

In order to understand how an external mechanical load can create injuries in the case of brain trauma it is essential to characterize the mechanical behavior of brain. The detailed mechanical parameters of brain tissue are needed to deduce brain material constitutive laws that can then be implemented in finite elements models of the head. Investigations of brain mechanics can also be applied in other domains such as neuropathology or neurosurgery leading to better diagnosis and therapies in the future. Beginning at the end of the 1960's,

most of the experimentation has been performed using *vitro* tests on excised samples that may be the source of alterations in brain properties. In spite of more than fifty years of research and a huge number of different studies on brain biomechanics, it remains difficult to accurately characterize and model brain tissue. These difficulties are illustrated by the large disparity in protocols and results reported in the literature. The present paper also suffers from this problem in that we have summarized and allowed comparisons to be made between studies on brain biomechanics. However, only the experimental aspects of studies will be presented without considering their approach to modeling. Recently, new techniques and protocols have been proposed in the literature to carry out *in vivo* investigations on healthy animal and human subjects in order to obtain more realistic results. In this context this study presents a review of *in vivo*-based techniques and compares their results with each other as well as with previously obtained *in vitro* work.

An early literature review on brain mechanical properties was proposed by Ommaya et al. (1968). Thibault and Gennarelli (1985) proposed a review that concerned the whole central nervous system. Donnelly (1998) as well as Cheng et al. (2008) published literature reviews that concentrated on comparing brain and spinal cord properties. Also recently, Hrapko et al. (2008) proposed a literature review focusing on *in vitro* experimental protocols. In 2010, Di Ieva et al. presented a review that focused on imaging applications for the mechanical characterization of brain tissue. The present paper complements existing literature reviews on brain tissue mechanics by presenting more recent results and focusing on the comparison between results from *in vitro* and *in vivo* tests, greatly developed since 2005. The emphasis will therefore be put on comparisons between *in vitro* and *in vivo* results, especially those concerning Magnetic Resonance Elastography (MRE). After detailing the *in vitro* creep, relaxation and dynamic frequency sweep tests as well as the *in vivo* magnetic resonance elastography tests, the emphasis will be put on pointing out the results of both *in vitro* and *in vivo* experimental protocols.

2 In vitro mechanical testing

Most of the *in vitro* tests proposed in the literature were based on compression creep tests and on relaxation tests in compression and shear, or on dynamic frequency or strain sweep experiments. Both quasi-static and dynamic brain matter analysis will be dealt with in this article as they provide complementary information.

2.1 Creep and relaxation tests

2.1.1 Creep tests in tensile/compression

The first in vitro brain tissue investigations were concerned with compression creep tests and performed on animal brain samples. Dodgson (1962) carried out creep tests on 2-mm diameter samples of mouse brain with the Hencky-von Mises energy hypothesis. From microscopic observations it was concluded there is a lack of free fluid in brain tissue, and a quasi-linear relation between logarithmic scaled time and compression strain was found.

This last result was confirmed four years later by Koenman (1966) who performed compression creep tests on porcine, calf and rabbit defrosted brain samples for 0.2 to 200 s, at different temperatures. In addition to inter-species variations, compression results pointed to the effect of temperature on the proportionality coefficient between logarithmic scaled time and strain.

2.1.2 Relaxation tests in tensile/compression

Compression stress relaxation tests were first described by Galford and McElhaney (1970) on monkey and human brain samples at 37°C. The resulting curves showed a quick relaxation for less than 100 s, with an initial relaxation modulus of 6.65 kPa for human and 10.3 kPa for monkey brain, and creep tests showed linearity between logarithmic scaled time and compliance. From the results, the brain tissue was considered as linear viscoelastic from 0 to $30 \pm 10\%$ strain.

These tests are completed in the work of McElhaney et al. (1973) by investigating the bulk modulus anisotropy and heterogeneity between white and gray matter. The next static compression tests were done 24 years later by Lin et al. (1997) by means of ultrasound tests on a lamb brain. The ultrasonic wave speed was obtained for the cortico-basal, antero-posterior and medio-lateral directions, and was found much higher in the first than in the two other directions. In accord with previously mentioned tests of McElhaney et al. (1973), it was shown that bulk modulus has values of 2.41 and 2.28 GPa for white and gray matter, respectively. Most recently, relaxation tests were done in compression by Prange and Margulies (2002), Cheng and Bilston (2007) and Prevost et al. (2010) and confirm the decrease in the stress relaxation modulus.

2.1.3 Relaxation tests in shear

Shearing relaxation tests were performed by Arbogast et al. (1995) in relaxation at 2.5%, 5% and 7.5% strain levels on brain stem samples cut from 2 to 3 years old pigs. The samples were placed in an experimental device made of a fixed lower plate and a mobile upper plate measuring the displacement and the resulting force. The main investigation of this study concerned the anisotropy by selecting the samples cut parallel and perpendicular to the direction of fiber orientation. Relaxation times were observed to be independent of the direction and the stress. However, the relaxation modulus was observed to be two times higher for samples cut parallel to the direction of fiber orientation.

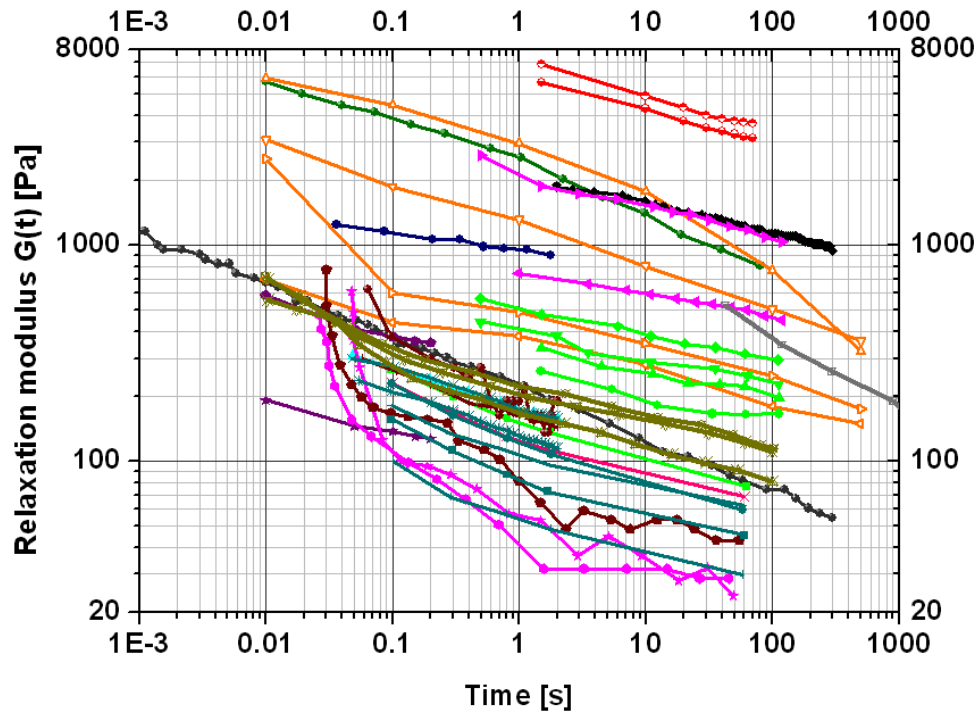
Bilston et al. (1997) used relaxation shear tests to estimate the limit of a linear viscoelastic response of brain tissue. Tests were performed on bovine white matter with a 3000 s relaxation time at 0.01% to 7% strain levels. A significant increase of the relaxation modulus was found at > 0.1% strain level. This result was correlated with harmonic analysis from 1 to 20 Hz showing a strain dependence of the complex shear modulus, G , defined by Eq. (1 - 1):

$$G = \sqrt{G'^2 + G''^2} \quad (1 - 1)$$

where G' and G'' are the storage and loss moduli, from 0.1% strain level. In the following, the term “complex shear modulus” will be used to represent the complex modulus, following linear viscoelasticity theory, as well as its magnitude to make the link with the elastic Hookean theory.

Long time ($t > 100$ s) relaxation modulus was also noted to be less than 100 Pa. Bilston et al. (2001) described an investigation based on relaxation tests of bovine brain tissue under high shear strain levels to complete the previously mentioned tests. The relaxation modulus was obtained was higher than most of other author's values.

As illustrated in Figure 1- 1, relaxation was found to be slower at higher strains, confirming the strain-time dependence of brain tissue. Such a decrease of relaxation modulus with increasing strain is observed by most of the authors. Only Takhoumts et al. (2003) observed an opposite trend.



Compression relaxation tests

- Galford et McElhaney 1970 (Human, 35% strain)
- Galford et McElhaney 1970 (Monkey, 35% strain)
- Prange et Margulies 2002 (Human, 2,5-50% strain)
- Cheng et Bilston 2007 (Calf, 5% strain)
- Prevost et al. 2010 (Porcine, 50% strain)

Shear relaxation tests

- Arbogast et al. 1995 (Porcine, 7,5% strain)
- Bilston et al. 1997 (Bovine, 7% strain)
- Peters et al. 1997 (Bovine, 1% strain)
- Prange et al. 2000 (Human, cortical gray matter, 50% strain)
- Prange et al. 2000 (Porcine, corona radiata white matter, parallel to fibers, 50% strain)
- Prange et al. 2000 (Porcine, corona radiata white matter, orthogonal to fibers, 50% strain)
- Prange et al. 2000 (Porcine, corpus callosum white matter, parallel to fibers, 50% strain)
- Prange et al. 2000 (Porcine, corpus callosum white matter, orthogonal to fibers, 50% strain)
- Brands et al. 2000 (Porcine, 5% strain)
- Brands et al. 2000 (Porcine, 10% strain)
- Brands et al. 2000 (Porcine, deformation 20% strain)
- Bilston et al. 2001 (Bovine, 0,08% strain)
- Bilston et al. 2001 (Bovine, 1,25% strain)
- Bilston et al. 2001 (Bovine, 5,54% strain)
- Bilston et al. 2001 (Bovine, 10,6% strain)
- Prange et Margulies 2002 (Human, 2,5-50% strain)
- Takhounst et al. 2003 (Bovine / Human, 12,5-50% strain)
- Nicolle et al. 2004 (Porcine, 0,1 à 1% strain)
- Nicolle et al. 2004 (Porcine, 5% strain)
- Nicolle et al. 2004 (Porcine, 10% strain)
- Nicolle et al. 2004 (Porcine, 20% strain)
- Nicolle et al. 2004 (Porcine, 30% strain)
- Nicolle et al. 2004 (Porcine, 50% strain)
- Hrapko et al. 2006 (Porcine, 1% strain)
- Hrapko et al. 2006 (Porcine, 0,05-0,1-0,15-0,2% strain)
- Ning et al. 2006 (Porcine, Brain stem, Parallel Parallel direction, 50% strain)
- Ning et al. 2006 (Porcine, Brain stem, Parallel Transverse direction, 50% strain)
- Ning et al. 2006 (Porcine, Brain stem, Transverse Transverse directio, 50% strain)
- Shen et al. 2006 (Porcine, 20% strain)
- Shen et al. 2006 (Porcine, 10% strain)
- Shen et al. 2006 (Porcine, 5% strain)
- Shen et al. 2006 (Porcine, 0,5% strain)

Figure 1- 1. In vitro relaxation modulus versus time from the literature. Curves are obtained from either compression or shear quasi-static experiments.

After isotherm shear tests in torsion, Peters et al. (1997) using calf brain, applied the time-temperature superposition principle to extend the range of shear rates over which complex shear and the relaxation moduli can be measured.

More shear relaxation tests were performed by Brands et al. (2000) on brain samples of 6 months old pigs with 100s relaxation time for 5%, 10% and 20% strain levels. Normalized relaxation modulus was found to be from 0.367 ± 0.130 kPa at 0.1s to 0.173 ± 0.047 kPa at 10s, which seems to be in accord with previously mentioned results.

Using relaxation shear tests, the isotropy of cortical gray matter as well as the anisotropy of white matter were shown in 2000 by Prange et al. and in 2006 by Ning et al.. An increase in the relaxation modulus with decreasing strain was also observed in most of the recent studies, such as Bilston et al. 2001, Prange and Margulies 2002, Nicolle et al. 2004, Hrapko et al. 2006 and Shen et al. 2006.

Figure 1- 1 presents a superposition of relaxation moduli versus time from the literature under relaxation shear and compressive tests, assuming tissue incompressibility. The relaxation modulus obtained in compression load is compared with the shear relaxation modulus using Eq. (1 - 2) under the incompressibility hypothesis:

$$G^* = E^*/3$$

$$G' + jG'' = E'/3 + jE''/3 \quad (1 - 2)$$

where G^* , G' and G'' and E^* , E' and E'' represent the complex, storage and loss shear and elastic moduli, respectively.

According to the incompressibility hypothesis, compression relaxation results yield very different values from those of shear relaxation results. The main observation concerns the great influence of strain level.

2.2 Constant strain rate tensile/compression tests

The strain rate influence on in vitro uniaxial compression was investigated by Miller and Chinzei (1997) on porcine brain samples. Non linear stress-strain relations were observed at 0.64, 0.64×10^{-2} and $0.64 \times 10^{-5} \text{ s}^{-1}$ strain rates as it were seen that stress increases with strain rate. These results were very close and reported the same conclusions as those of Estes and McElhaney (1970) at a compression strain rate of 0.08, 0.8, 8 and 40 s^{-1} and expressed as Young's modulus real and imaginary parts of 4.7 kPa and 0.28 to 2.8 kPa respectively. Compression tests of Miller and Chinzei were completed with uniaxial traction tests at 0.64 and $0.64 \times 10^{-2} \text{ s}^{-1}$ strain rates. Again a significant rigidifying of brain tissue with strain rate increase was observed. Uniaxial, quasi static and cyclic loading under tensile-compression were performed on 86 human brain samples at 5 mm/min by Franceschini et al. (2006). In addition to a non linear mechanical behavior, hysteresis and dependence of the stress-strain response on pre-load were observed. Influence of preload is characterized by a reduction in stress after the initial extension, characteristic of filled elastomers. The existence of permanent deformations called "bio-plasticity" and a viscous component of the solid phase deformation were also shown.

Most of the recent in vitro work on brain tissue describes constant strain rate tests, essentially in traction or compression, and hyperelastic materials and models are involved, which are usually used for elastomers. This is also observed in tensile studies of Velardi et al. (2006) or compression studies of Shen et al. (2006), Vappou (2007), Cheng et Bilston (2007) and Prevost et al. (2010). Sensitivity to, and increase of brain stiffness with strain rate is confirmed in 2009 by Pervin and Chen at very high strain rates ($1000, 2000$ and 3000 s^{-1}).

Results reported in the literature on in vitro compression and tensile studies are shown in Figure 1- 2 and Figure 1- 3, respectively, and appear to be relatively consistent. In particular the effect of strain rate can be seen. This indicates that brain has an important viscous component, which is confirmed through Dynamic Frequency Sweep tests.

More recently, such in vitro results completed with Dynamic Frequency Sweep experiments made it possible to observe brain properties such as non linear behavior, anisotropy and strain rate dependence. These properties were compared to other well-described and non biological materials such as polymers by Franceschini et al. or composites by Arbogast and Margulies (1998).

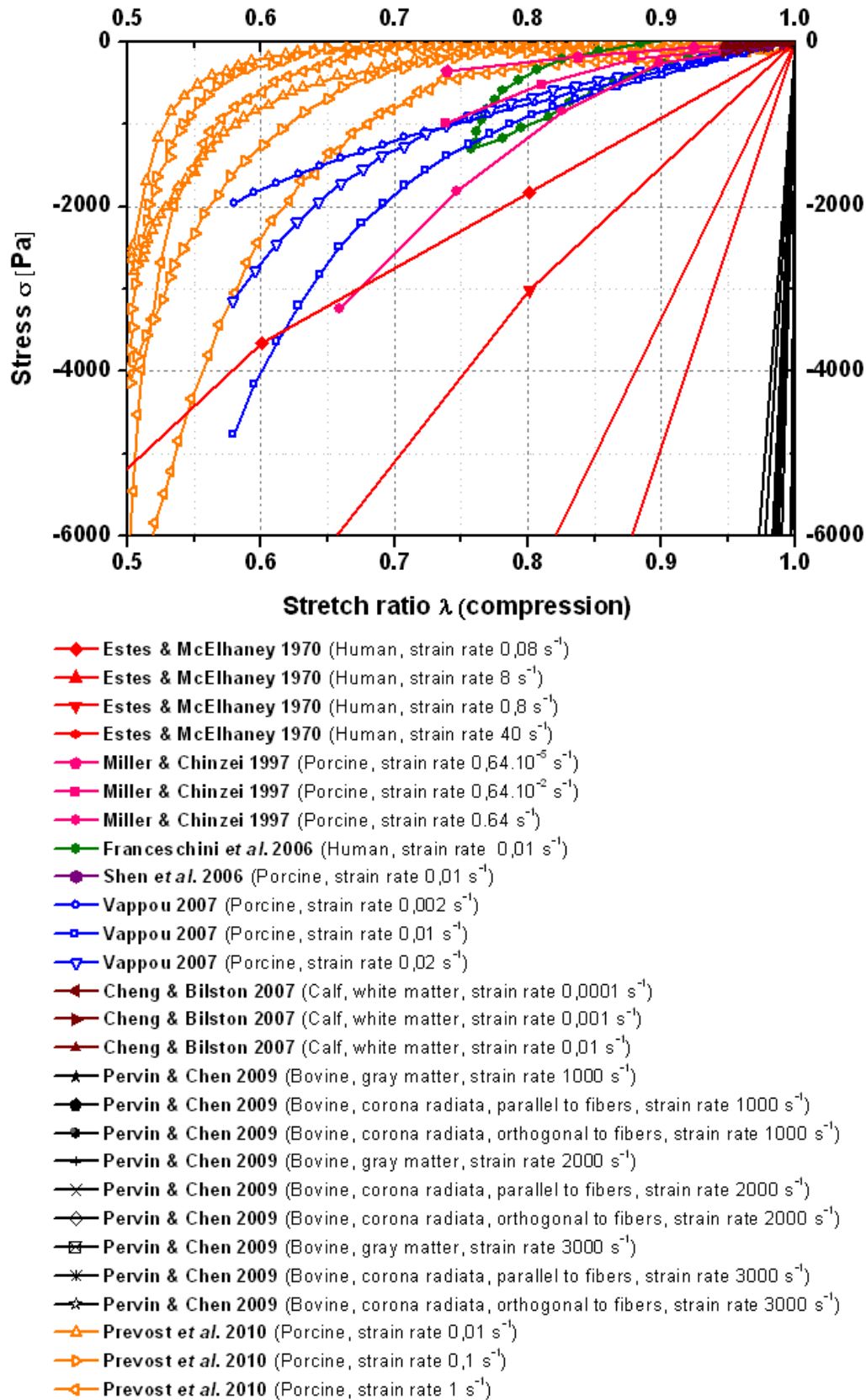


Figure 1- 2. Literature review on quasi static in vitro compression strain sweep tests. Curves show a significant influence of strain rate.

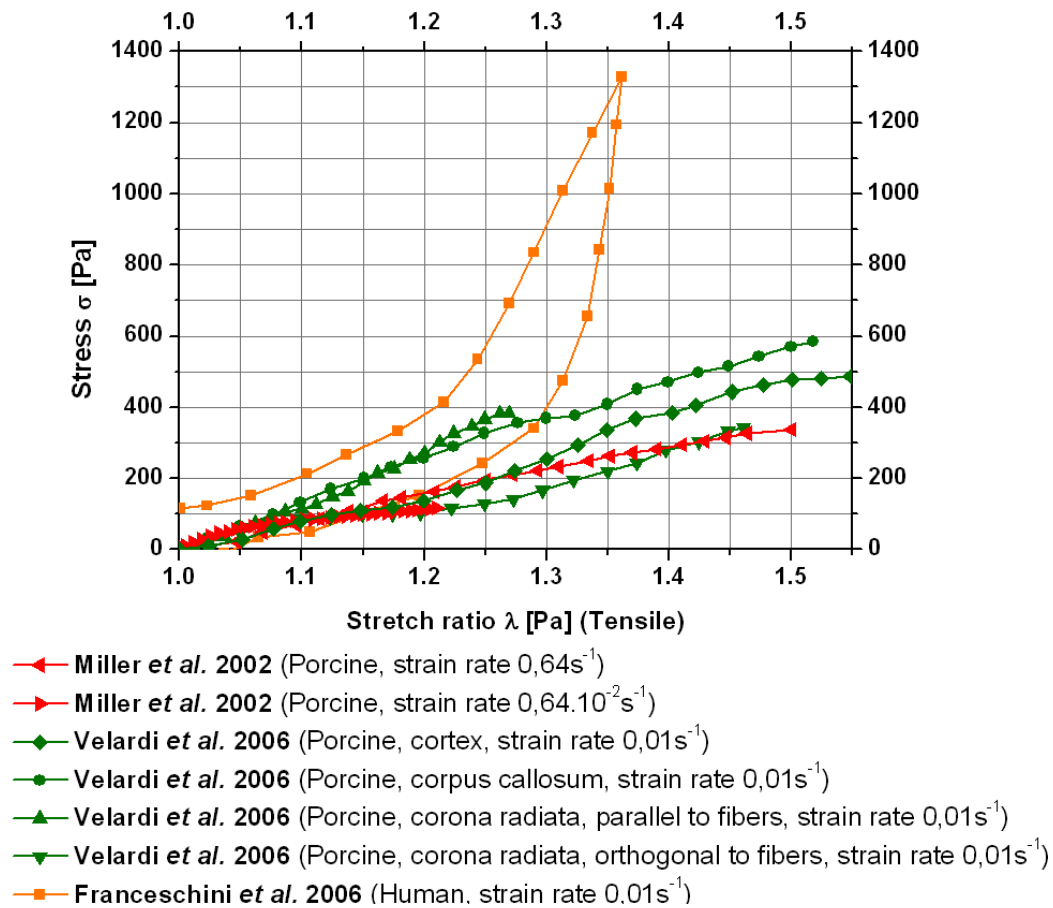


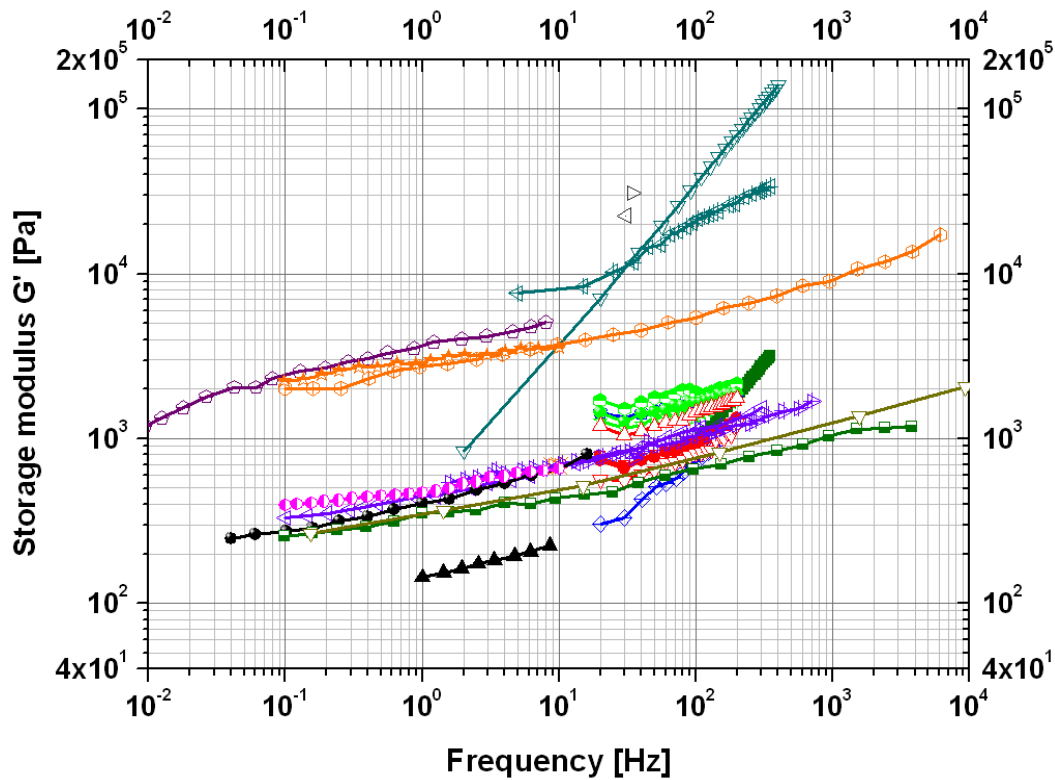
Figure 1- 3. Literature review on quasi static in vitro tensile strain sweep tests. Curves show a significant influence of strain rate.

2.3 Dynamic frequency sweep tests

To characterize viscoelastic brain behavior at small strain, most of the in vitro experiments have been performed dynamically, commonly using a dynamic frequency sweep. Thus, most of the dynamic frequency sweep protocols have investigated tissues in the linear strain domain.

Although most of the dynamic frequency sweep tests have been carried out in shear, some dynamic frequency sweep experiments have been done in tensile/compression mode.

The results are shown plotted as storage and loss moduli against frequency in Figure 1- 4 and Figure 1- 5, respectively.



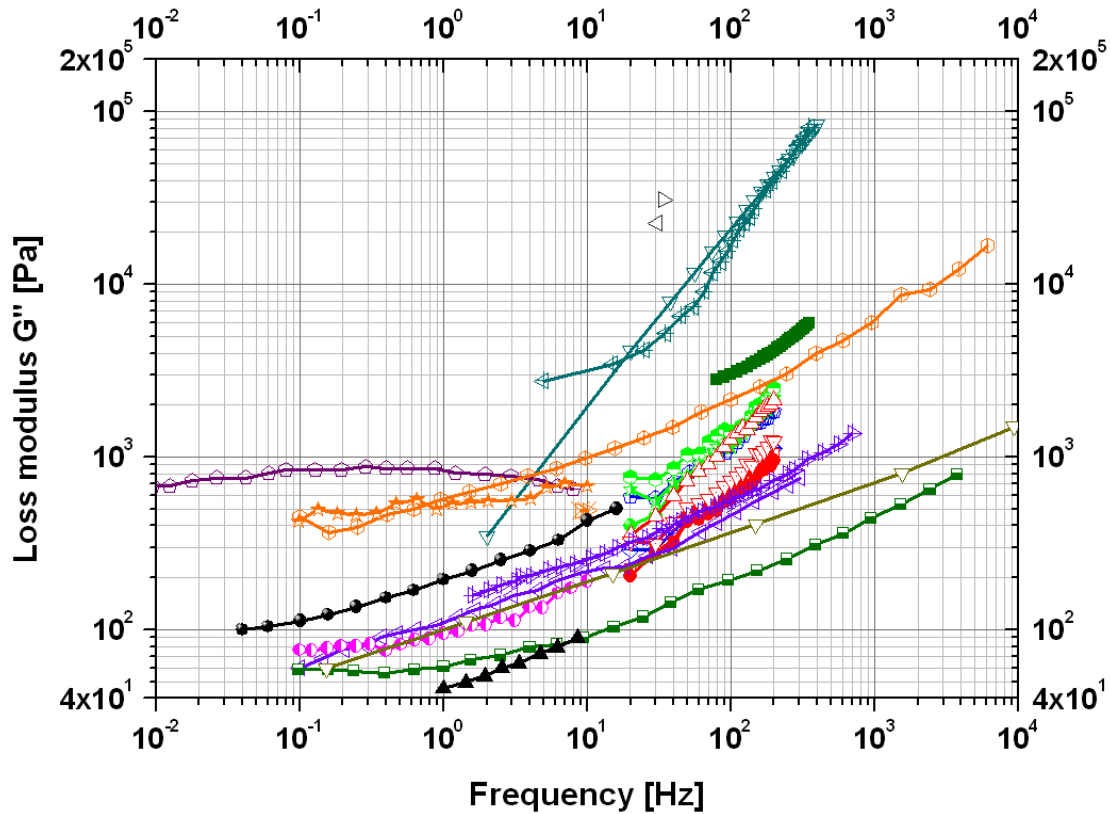
Compression in DMA

- Koeneman 1966 (Rabbit, Rat, Porcine, 25% strain)
- △— Galford et McElhaney 1970 (Monkey, 20% strain)
- ▽— Galford et McElhaney 1970 (Human, 20% strain)

Shear in DMA

- △— Fallenstein et Hulce 1969 (Human, 7 à 24,5% strain)
- ▽— Shuck et Advani 1970 (Human, 2,6% strain)
- △— Shuck et Advani 1972 (Human, 1,23% strain)
- ×— McElhaney et al. 1973 (Human et Monkey)
- ▽— Peters et al. 1997 (Porcine, 1% strain)
- ◇— Arbogast et al. 1997 (Porcine, brain, 2,5% strain)
- ◇— Arbogast et al. 1997 (Porcine, brain stem, 2,5% strain)
- ◇— Arbogast et Margulies 1998 (Porcine, brain stem, Parallel Transverse direction, 2,5% strain)
- ◇— Arbogast et Margulies 1998 (Porcine, brain stem, Transverse Transverse direction, 2,5% strain)
- ◇— Arbogast et Margulies 1998 (Porcine, brain stem, Parallel Parallel direction, 2,5% strain)
- ◇— Thibault et Margulies 1998 (Young porcine, 2,5% strain)
- ◇— Thibault et Margulies 1998 (Young porcine, 5% strain)
- ◇— Thibault et Margulies 1998 (Old porcine, 2,5% strain)
- ◇— Thibault et Margulies 1998 (Old porcine, 5% strain)
- ◇— Brands et al. 1999 (Porcine, 1% strain)
- ◇— Brands et al. 2000 (Porcine, 1% strain)
- ◇— Darvish et Crandall 2001 (Bovine, 1% strain)
- ◇— Bilston et al. 2001 (Bovine, 0,1% strain)
- ◇— Nicolle et al. 2004 (Human, Porcine, 0,001% strain)
- ◇— Nicolle et al. 2004 (Human, Porcine, 0,1% strain)
- ◇— Hrapko et al. 2006 (Porcine, 1% strain)
- ◇— Shen et al. 2006 (Porcine, 1% strain)
- ◇— Vappou et al. 2007 (Porcine, 0,5% strain)
- ◇— Garo et al. 2007 (Porcine, 1% strain)

Figure 1- 4. Storage modulus of brain tissue provided from the literature of in vitro dynamic frequency sweep tests in shear.



Compression in DMA

- Koeneman 1966 (Rabbit, Rat, Porcine, 25% strain)
- ◁ Galford et McElhaney 1970 (Monkey, 20% strain)
- ▷ Galford et McElhaney 1970 (Human, 20% strain)

Shear in DMA

- △ Fallenstein et Hulce 1969 (Human, 7 à 24,5% strain)
- ▽ Shuck et Advani 1970 (Human, 2,6% strain)
- ◁ Shuck et Advani 1972 (Human, 1,23% strain)
- ✕ McElhaney et al. 1973 (Human et Monkey)
- ▽ Peters et al. 1997 (Porcine, 1% strain)
- ◇ Arbogast et al. 1997 (Porcine, brain, 2,5% strain)
- ◇ Arbogast et al. 1997 (Porcine, brain stem, 2,5% strain)
- ◇ Arbogast et Margulies 1998 (Porcine, brain stem, Parallel Transverse direction, 2,5% strain)
- ◇ Arbogast et Margulies 1998 (Porcine, brain stem, Transverse Transverse direction, 2,5% strain)
- ◇ Arbogast et Margulies 1998 (Porcine, brain stem, Parallel Parallel direction, 2,5% strain)
- ◻ Thibault et Margulies 1998 (Young porcine, 2,5% strain)
- Thibault et Margulies 1998 (Young porcine, 5% strain)
- △ Thibault et Margulies 1998 (Old porcine, 2,5% strain)
- ▽ Thibault et Margulies 1998 (Old porcine, 5% strain)
- ◇ Brands et al. 1999 (Porcine, 1% strain)
- ◇ Brands et al. 2000 (Porcine, 1% strain)
- ✕ Darvish et Crandall 2001 (Bovine, 1% strain)
- ◇ Bilston et al. 2001 (Bovine, 0,1% strain)
- ◇ Nicolle et al. 2004 (Human, Porcine, 0,001% strain)
- ◇ Nicolle et al. 2004 (Human, Porcine, 0,1% strain)
- Hrapko et al. 2006 (Porcine, 1% strain)
- ◇ Shen et al. 2006 (Porcine, 1% strain)
- ◇ Vappou et al. 2007 (Porcine, 0,5% strain)
- Garo et al. 2007 (Porcine, 1% strain)

Figure 1- 5. Loss modulus of brain tissue provided from the literature of in vitro dynamic frequency sweep tests in shear.

2.3.1 Dynamic mechanical analysis in tensile/compression

While many in vitro dynamic tests have been performed in shear, a few dynamic oscillatory strain experiments with compression load can be found in the literature. Such tests were conducted by Koenman (1966) on cylindrical samples. Sinusoidal stress was applied on rabbit, calf and porcine defrosted brain samples. Assuming tissue incompressibility, the complex shear modulus G^* can be obtained from the complex dynamic elastic modulus E^* and decomposed in storage and loss moduli following Eq. (1 - 1).

The respective storage and loss moduli values at frequencies from 80 to 350 Hz were found to be from 2.7 to 5 kPa and from 0.5 to 3.2 kPa. The complex shear modulus was seen as relatively constant with frequency, varying only from 2.7 to 5 kPa. This observation was also true of the dynamic viscosity that increased with compression strain only with forces in the sample radial direction. For instance the dynamic viscosity was found to be 4.35 Pa s at 25% strain.

2.3.2 Dynamic mechanical analysis in shear

In vitro shear dynamic tests were first performed in shear by Fallenstein and Hulse (1969) on 8 adult human brains with 10 to 62 hours post-mortem time. Thirteen moisturized white matter plan-parallel samples were used at 37°C. Shear strain levels from 7% to 24.5% were applied but no effect was observed on dynamic shear moduli. Frequency ranged from 9 to 10 Hz, and storage and loss moduli varied with frequency from 0.6 to 1.1 kPa and 0.35 to 0.6 kPa, respectively. The dynamic viscosity, defined by loss modulus divided by frequency, was evaluated between 5.6 and 9.6 Pa.s corresponding to approximately twice the value found by Koenman. This difference could be explained by the difference in experimental setups. These values have been confirmed by McElhaney et al. (1973). By comparing brain matter viscosities with the mechanical properties of other organs, Fallenstein et al. (1969) estimated that the rigidity of in vitro human brain tissue is a little less than that of in vivo human muscular tissue. The first in vitro studies of shear under dynamic torsion of tissue were carried out by Shuck and Advani (1970) on human brain samples from the callous corpus at frequencies from 5 to 350 Hz and different strain values and at a strain rate of 77 s⁻¹. Storage and loss moduli varied from 7.6 to 33.9 kPa and 2.76 to 81.4 kPa for brain tissue considering it as isotropic and incompressible. These tests made it possible to evaluate a viscoelastic linearity limit at 2.6% strain. Shuck and Advani (1972) completed these tests and refined this linearity limit. It was also evaluated at 3.5% strain at frequencies less than 10 Hz. It was observed that, for a constant strain less than 1.3%, the viscoelastic properties were highly frequency dependant. Shuck and Advani observed that the tissue was ruined at frequencies higher than 60 Hz and at strains larger than 1.3%. The results of Arbogast and Margulies

(1997) were confirmed and completed over the same frequency range (20 to 200 Hz) by Thibault and Margulies (1998) and by Arbogast and Margulies (1998) who investigated brain tissue anisotropy and age mechanical dependence, respectively.

An important aspect of dynamical mechanical testing is higher frequency range. According to Brands et al., this range should be increased to 1000 Hz. By applying the time-temperature principle from 4 to 38°C with 1% strain, Brands et al. obtained dynamic shear moduli from 1.25 to 2 kPa over a frequency range of 260 to 1000 Hz. Also, Hrapko et al. (2008) and Nicolle et al. (2004) attested the so-called slipping effect, inducing a decrease of storage and loss moduli and an increase of viscosity when testing thinner samples. The problem could be solved by gluing each specimen to the plates with cyanoacrylate adhesive without creating a new coupling. After investigating the effects of post-mortem time degeneration and direction of measurement Nicolle et al. (2005) measured shear moduli on 18 human brain glued samples over a frequency range from 0.1 to 6310 Hz. They found values of storage and loss moduli of 2.1 ± 0.9 to 16.8 ± 2.0 kPa and 0.4 ± 0.2 to 18.7 ± 2.3 kPa, respectively, corresponding to a complex shear modulus from 16.9 ± 2.2 kPa to 18.7 ± 2.3 kPa. The results were of the same order of magnitude as those reported by Bilston et al. (2001) or Brands et al. (2000) with, respectively, 20% and 45% variation of the shear mechanical properties. Results of Hrapko et al. (2006) from oscillatory shear tests with 1% strain and over a frequency range from 0.04 to 16 Hz on corona radiata white matter samples gave storage and loss moduli around 0.248 to 0.801 kPa and 0.100 to 0.503 kPa respectively. These values correspond to a complex shear modulus that varied from 0.267 to 0.946 kPa. Assuming the time-temperature superposition principle, tests at 1% strain on calf brain white matter samples between 7 and 37°C were tested from 0.16 - 16 Hz to 10 and 20 - 100 Hz. The complex shear modulus at 10 Hz and from 20 to 100 Hz was found to be respectively 0.5 to 0.6 kPa and 0.6 to 0.9 kPa by Peters et al. These results were similar to those proposed by Fallenstein and Hulce (1969). However, Arbogast and Margulies (1997) showed limitations in applying such a time-temperature principle on low frequency and isothermal oscillatory tests. Arbogast and Margulies (1995) proposed similar results to those of Peters et al. (1997).

The dependence of the dynamic shear modulus on strain level is a crucial point. Translational shear experiments were performed by Arbogast and Margulies (1997) on porcine samples from 20 to 200 Hz with 10-Hz steps and at 2.5% and 5% strain level. These strain values were higher than previously proposed linearity limits. The surroundings were kept highly moist at 25°C and in complex shear the brain storage and loss moduli were found to be 1.3 to 2.7 kPa, 1.25 to 1.65 kPa and 0.4 to 2.15 kPa respectively for 2.5% strain and

0.5 to 1.25 kPa, 0.3 to 1.25 kPa and 0.4 to 1.25 kPa for 5% strain. The complex shear modulus at 5% strain was 42% less than the shear modulus at 25% showing brain softening. Darvish and Crandall (2001) performed oscillatory dynamic shear experiments in adding Gaussian white noise in samples provided from corona radiata bovine brain and made up of white matter, with 12 days post mortem time. Over a 1 to 100 Hz frequency range the shear modulus decreased as the strain increased from 3 to 21%. The same trend with increasing strain had already been observed for the relaxation modulus by Bilston et al. (2001) in accord with most of the literature results.

A comparison can be made between most of the results on storage and loss moduli for in vitro dynamic frequency sweep tests as presented in Figure 1- 4 and Figure 1- 5. Thanks to the previously mentioned mechanical similarities between human and porcine brain tissue this comparison is possible in spite of the fact that tests were performed on different species. The first observation concerns the significant disparity of the results at all strain levels. Nevertheless, the same trend for shear moduli increasing with increasing frequency is always noted, as well as higher storage than loss moduli. Concerning the comparison between shear storage and loss moduli, an inflection point around 150 Hz characterizing an inversion of the elastic and viscous components was proposed by Shuck and Advani (1972) and Thibault and Margulies (1998) and at more than 1000 Hz by Nicolle et al. (2004). In general two main results trends seems to come out of the plots of modulus vs. frequency: while Arbogast and Margulies (1997), Thibault and Margulies or Brands et al. (2000) proposed values between 100 and 1000 Pa, Shuck and Advani (1972) and Nicolle et al. (2005) obtained about 10 times higher shear moduli. In order to compare these results with other investigation techniques, a maximal resulting curve from Shuck et al., a mean curve from Nicolle et al. (2004) and a minimal curve from Brands et al. (2000) will be used in the following. Because DMA tests allow characterization of brain tissue only at low strains, very little recently published work was done in DMA, such as Shen et al. in 2006, Vappou et al. or Garo et al. in 2007.

2.4 Non linearity investigation

Knowing the limit of the linear response is critical for brain tissue characterization. Free dynamic drop experiments in compression were proposed by Galford and McElhaney (1970). These aimed at completing their previously mentioned relaxation results with more information for short times. The emphasis was put on comparing human and monkey brain tissue samples. Particularly human samples were cylindrical, of 1.27 cm diameter and 0.64 mm height, and consisted of 95% white matter. 20% strain was applied at 34Hz. For human samples the complex elastic modulus and its real and imaginary parts were found to be 72.8,

67.8 and 26.6 kPa, respectively. Assuming brain tissue incompressibility it corresponded to a complex shear modulus of 24.2 kPa, which was higher than the values found in the same frequency range by Koenman (1966) or most recent authors. However it was close to values obtained in dynamic shear by Shuck and Advani (1972). Peters et al. showed that brain tissue had linear behavior under 1% strain and non linear behavior over this value, and today this is the most commonly adopted value. This result was further confirmed by Brands et al. (2000) and Nicolle et al. (2004). Most of the recent work has investigated large deformation mechanical investigation based on creep and relaxation tests of brain tissue with methods based on a linear hypothesis.

3 In vivo mechanical testing

3.1 Indentation tests

First invasive in vivo tests were performed by Wang and Wineman (1972), in the continuation of work by Fallenstein and Hulce (1969). A hole was cut in the skull of an anesthetized monkey, close to the midline, over the frontal lobe. After removing the dura mater, a small dynamic probe with 0.1 cm^2 areas was positioned vertically over the hole, harmonic vibrations of 80 Hz frequency were induced and force, displacement and phase angle between force and displacement were measured. Tests performed on 8 rhesus monkeys with blood pressure monitoring gave mean values of 19.6 kPa for the real and 11.2 kPa for the complex part of the elastic modulus. These tests were extended by Miller et al. (2000) to indentation experiments on an anesthetized pig with an embedded head. In the frontal region part of scalp, skull and dura mater were removed. A 10mm diameter cylindrical indenter was used for uniaxial compression into the brain at 1 mm s^{-1} speed and 3.9 mm penetration depth to avoid irreversible damages. A signal processing was used to remove the effects of heart beats and animal breath. Even if only one animal was tested, results presented a force-displacement curve and, assuming brain tissue linearity, Young's modulus and Poisson's ratio respectively were obtained as 3.240 kPa and 0.499. This result supported the assumption of in vivo brain tissue incompressibility. These indentation tests at 0.13 Hz showed results that were 2.3 times lower than those of Fallenstein and Hulce (1969) at 80 Hz. In 2010, van Dommelen et al. carried out indentation tests on porcine brain at 20 Hz and 0.1 s^{-1} and measured a shear modulus of 955 Pa. This value is very close to that obtained by Brands et al. (2000). The same year, indentation tests were made by Christ et al. at 1 Hz. Assuming the incompressibility of brain tissue, we can evaluate the shear modulus for white and gray matter at 74 and 114 Pa respectively. These values are much lower than all the previously presented results and show that gray matter is stiffer than white matter.

We performed a comparison between the main dynamic strain sweeps results that point to similarities with the values obtained from the indentation tests. Figure 1- 6 shows that the indentation results exhibit the same trend as the dynamic strain sweep results. Thus, the results of Gefen et al. (2003) were comparable to values reported by Brands et al. (2000) between 100 and 1000 Pa, and Wang and Wineman (1972) confirmed the results of Shuck and Advani (1972) with values over 10 kPa.

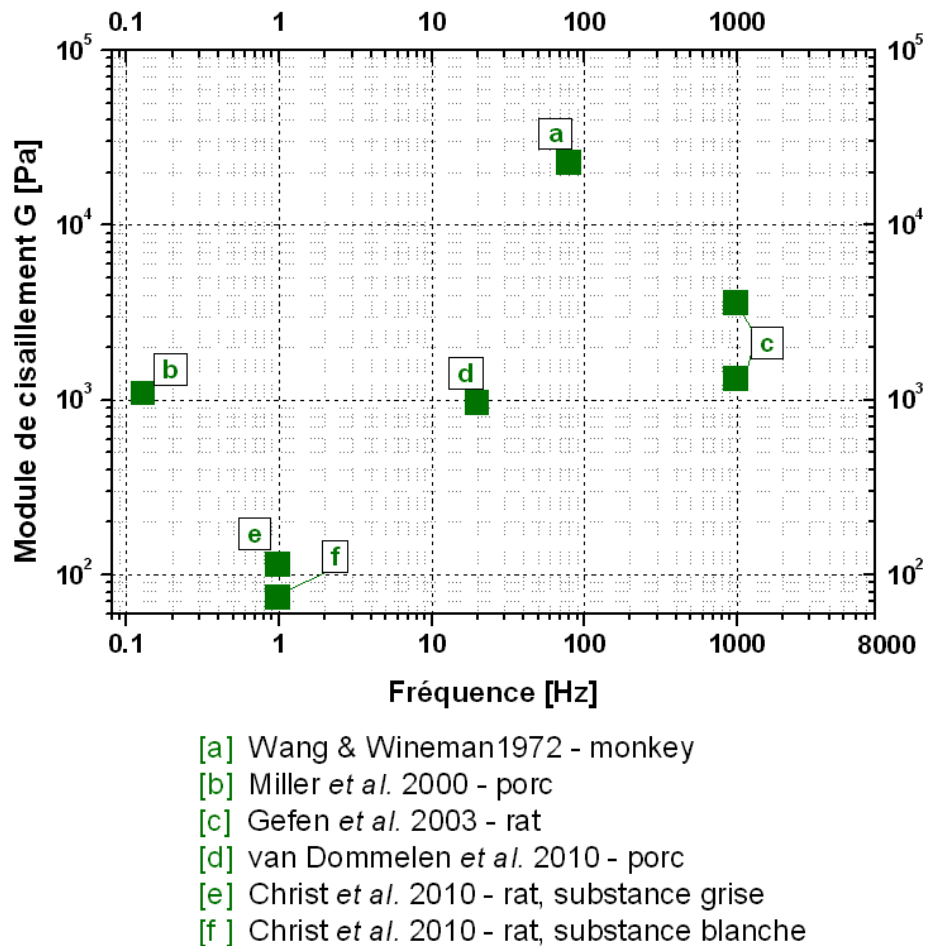


Figure 1- 6. Shear modulus versus frequency for dynamic in vitro and in vivo indentation testing from the literature.

3.2 Brain tissue Magnetic Resonance Elastography in vivo testing

The limitations of the in vitro classical protocols have been pointed out above. New in vivo non invasive techniques based on magnetic resonance elastography (MRE) have now been developed to investigate biological soft tissue. These new protocols have made it possible to work under biologically realistic experimental conditions.

3.2.1 Magnetic resonance elastography methods

Magnetic resonance elastography is a recently developed method aimed at measuring in vivo dynamic properties of biological soft tissues. Biomechanical parameters can be measured in a noninvasive way by coupling a mechanical excitation, which propagates waves in the soft medium, to a magnetic resonance imaging (MRI) device for visualizing the wave propagation, as illustrated in Figure 1- 7. The principle that differences in nuclear magnetic resonance (NMR) spectral frequencies are induced by harmonic wave propagation in a soft medium was first proposed in theory by Lewa et al. (1991). Muthupillai et al (1995) then applied this principle to calculate tissue stiffness by showing how MR wave propagation images can be processed with an inversion algorithm to generate the dynamic MR Elastography images.

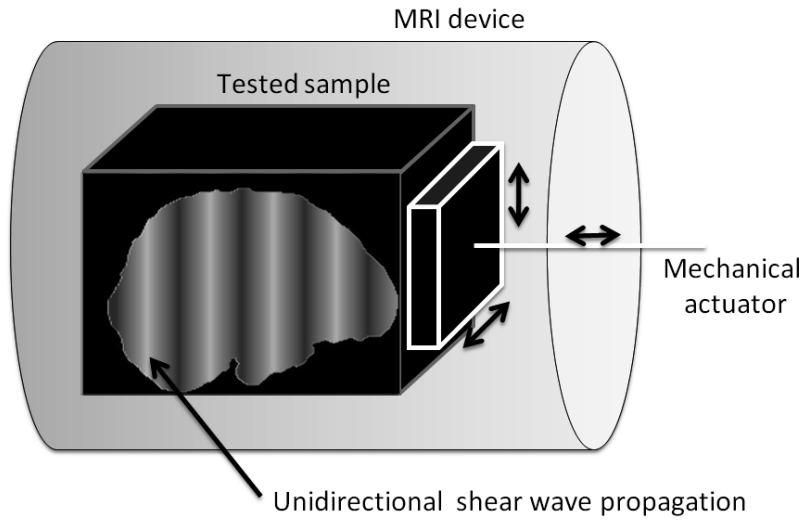


Figure 1- 7. Simplified schematic representation of a magnetic resonance elastography device with different possible directions for shear wave generation.

It has been shown that the generated harmonic motion can be encoded by motion-sensitizing gradients according to a principle proposed by Stejskal and Tanner (1965) that developed spin diffusion measurements. Displacements can be encoded by considering the following extension of Larmor's relation in Eq. (1 - 3):

$$\omega(x, y, z, t) = \gamma(B_0 + \overrightarrow{G_m}(t) \cdot \vec{r}(t)) \quad (1 - 3)$$

where ω is the proton precession resonance pulsation, γ the gyromagnetic ratio of hydrogen, x , y and z the spatial coordinates, t the time and $\overrightarrow{G_m}$ the modified magnetic field gradient, and $\vec{r} = \vec{r}_0 + \vec{\xi}$ where \vec{r} , \vec{r}_0 and $\vec{\xi}$ are the position, at rest and during displacement of a spin. As a consequence it is possible to integrate over a period T to express this result in terms of a phase shift Φ as given by Eq. (1 - 4).

$$\Phi = \gamma \int_T \overrightarrow{G_m}(t) \cdot \vec{\xi}(t) dt \quad (1 - 4)$$

$\vec{\xi}$ can be expressed from the measurement of the phase shift Φ and the application of an appropriate time dependence of the motion sensitizing gradient $\overrightarrow{G_m}(t)$. In the presence of cyclic motion encoding gradients at the same frequency as cyclic motion, phase shift NMR recorded induced displacement phase shift that can be given by Eq. (1 - 5):

$$\Phi = \frac{2\gamma NT(\overrightarrow{G_0} \cdot \vec{\xi}_0)}{\pi} \cos(\vec{k} \cdot \vec{r} + \theta) \quad (1 - 5)$$

where N is the number of cycles, T the period of the gradient waveform, θ the phase difference induced between motion and motion encoding gradient and \vec{k} the shear wave number. First application of this technique was shown by Muthupillai et al. (1995). It was also proposed to measure the global shear modulus G of a soft medium from the shear wave propagation following Eq. (1 - 6):

$$G = \rho V_s^2 = \rho(f\lambda)^2 = \rho(\omega k^{-1})^2 \quad (1 - 6)$$

where V_s is the shear wave speed, ρ the medium density, f the wave frequency and λ the wave length. In most studies, brain tissue density was assumed to be 1000 kg/m³. Extension to viscoelastic rheological properties of considered soft tissue was made possible with the development of inverse approach proposed few years later by Romano et al. (1998), Oliphant et al. (2001) and Manduca et al. (2001). Among others, application of this technique for in vivo human tissue has been done by for breast by Sinkus et al. (2005) and more recently for brain tissue by Sack et al. (2007) and Vappou et al. (2008). The most recent advances in MRE studies of brain tissue include a three-dimensional analysis of shear wave propagation by Green et al. (2008).

3.2.2 MRE applied to brain investigation

Although in vivo MRE devices for brain were already studied in 2001 by Braun et al., the first brain tissue values from in vivo MRE studies were described by McCracken et al. (2005) based on their use of both transient and harmonic excitation. This wave was electromechanically induced on a living human subject through a bite bar, rotating the head in a left-to-right motion with the axis of rotation in the back of the head with 80-Hz sinusoidal motion or transient tests using a 6.25-ms rectangular impulse. A displacement magnitude of

about 120 μm was applied. After comparing harmonic and transient excitation on gels, tests were performed with both techniques on six healthy volunteers. By selecting regions of interest (ROI) on MR images, the shear modulus in harmonic and transient tests was found to be 5.3 ± 1.3 and 7.5 ± 1.6 kPa, respectively, for gray matter and 10.7 ± 4.4 and 11.6 ± 2.4 kPa for white matter.. According to the authors, the results showed the feasibility of measuring brain stiffness using a transient mechanical excitation. The authors pointed out that the two techniques complemented each other. Transient magnetic resonance elastography seemed to be better at depicting the deeper structures of the brain. Similar tests using the same MRI device were proposed by Kruse et al. (2007). Two different harmonic motion generators were used at 100 Hz: the first one created vibration in the anterior-posterior direction via a cradle block and the second one in the right-left direction by a bite block. In both cases, the subject lay supine with the head on a cradle and blocks were attached to an electromechanical actuator. Tests were performed on 25 healthy adult volunteers aged from 23 to 79 years. The shear modulus was obtained separately on white and gray matter by selecting the ROI. White and gray matter had shear moduli of 13.6 ± 1.3 and 5.22 ± 0.46 kPa, respectively. Uffmann et al. (2004) carried out similar tests. Mechanical waves were induced through a bite bar attached to a piezoelectric oscillator in the left-right direction. The derivative of spatial phase resulting from a sinusoidal fit gave information on wave vector and the shear modulus was also calculated using Eq. (1 - 6) above. Tests performed on seven healthy young volunteers yielded shear moduli of 15.2 ± 1.4 and 12.9 ± 0.9 Pa for white and gray matter respectively.

Hamhaber et al. (2007) obtained in the vivo brain shear modulus based on a three-dimensional analysis of shear wave propagation. Shear waves at 83.33 Hz were generated by a remote motion generator based on a commercial loudspeaker. A carbon fiber rod transmitted vibrations from the loudspeaker membrane to a pin joint on top of a head rocker. The displacement magnitude was estimated to be 0.3 – 0.5 mm. In order to provide more information about wave propagation directions, 3-D MRE experiments were performed. An algorithm identifying minimal wave velocities along rays from the surface into the brain made it possible to determine the direction of wave propagation. Mechanical wave propagation at 83.33 Hz into the brain of a healthy volunteer yielded a shear modulus about 3.5 kPa. This study was completed and published the same year by Sack et al. who carried out tests at 25 Hz and 50Hz with the same MRE device. Tests were performed on six healthy volunteers that underwent a high number of MRE studies. Resulting data were expressed in assigning a shear modulus, μ , to the dynamic modulus and shear viscosity, η , to the loss modulus. A complex wave inversion was performed to obtain the complex modulus: $G = G' + jG'' = \mu + j\eta\omega$. As described by Klatt et al. (2006), these moduli were obtained

from the complex wave number. At 25 Hz in a selected ROI along the lower edge of the corpus callosum, authors measured interindividual shear moduli and shear viscosities at 1.17 ± 0.03 and 3.1 ± 0.4 Pa s, corresponding to a loss modulus of 0.487 ± 0.06 kPa at 50 Hz. Values were found to be 1.56 ± 0.07 and 3.4 ± 0.2 Pa s, respectively, that corresponded to a loss modulus of 0.534 ± 0.03 kPa. The main advantage of this technique was to provide not only elastic but also viscoelastic parameters for brain tissue in vivo. The authors completed this work one year later by investigating the impact of aging and gender on brain viscoelasticity with the same in vivo technique. A comparable algorithm was developed by Vappou et al. (2008) after performing experiments on seven anesthetized rats. Here, the technique was novel in the use of a dedicated low field MRI device (0.1T). This low field made it possible to move the excitation part closer to the MRI device and also to optimize the mechanical wave propagation to the animal head. By inverting the Helmholtz wave propagation equation, estimated storage and loss moduli were obtained from the complex wave number from Eq. (1 - 7):

$$k = \sqrt{\frac{-\nabla^2(FT(u))}{FT(u)}} \quad \text{where: } \nabla^2 = \left(\frac{\partial^2}{\partial x^2} + \frac{\partial^2}{\partial y^2} \right) \quad (1 - 7)$$

$$\text{and} \quad G^* = G' + jG'' = \rho \frac{\omega^2}{k^{*2}} = \rho \frac{\omega^2}{(k' + jk'')^2}$$

Here, k is the wave number, i.e. k^* with k' and k'' for real and imaginary parts when considered as a complex number under the viscoelasticity hypothesis; Ω is the pulsation, u the displacement in the xy-plane and $FT(u)$ its Fourier transform.

Storage and loss values obtained were found to be 6.330 and 4.770 kPa, 8.450 kPa and 7.140, and 8.650 and 8.150 kPa, at 150, 180 and 210 Hz respectively. The results indicated a measurement uncertainty of about 5% and 10% for the shear storage and loss moduli, respectively. Other investigations in an anesthetized mouse of brain mechanical properties by MRE were proposed the same year by Atay et al. (2008) who studied brain anisotropy. This study reported tests at a higher frequency (1200 Hz) measuring displacements in three different frontal planes using Eq. (1 - 6) where the imaginary parts of k^* and G^* are neglected. With such an algorithm, the shear modulus, obtained in the three planes, was 18.7, 15.3 and 16.5 kPa, respectively. Other MRE tests were performed by Green et al. (2008). Vibrations were transmitted at 90 Hz through a bite bar to the head. A full three dimensional approach was used by removing contributions of the dilatational wave by applying a curl operator. As a consequence, the same equations from the Helmholtz equation wave propagation inversion were proposed. Results were obtained from five healthy volunteers. These in vivo results

were the first that separated gray and white matter and were also expressed in terms of viscoelastic properties. For gray matter storage and loss moduli had been found to be 3.1 ± 0.1 and 2.5 ± 0.2 kPa, while for white matter these moduli, characteristic for elasticity and viscosity, were 2.7 ± 0.1 and 2.5 ± 0.2 kPa. Thus, gray matter appeared to be significantly stiffer than white matter, while loss moduli were not different in gray and white matters.

Superposition of in vivo MRE tests from the literature is presented in Figure 1- 8. In spite of the many species tested, algorithm differences and a relative disparity, results appear to confirm the higher in vitro results. Brain tissue seems to present a shear modulus value of about 10 kPa at about 100 Hz.

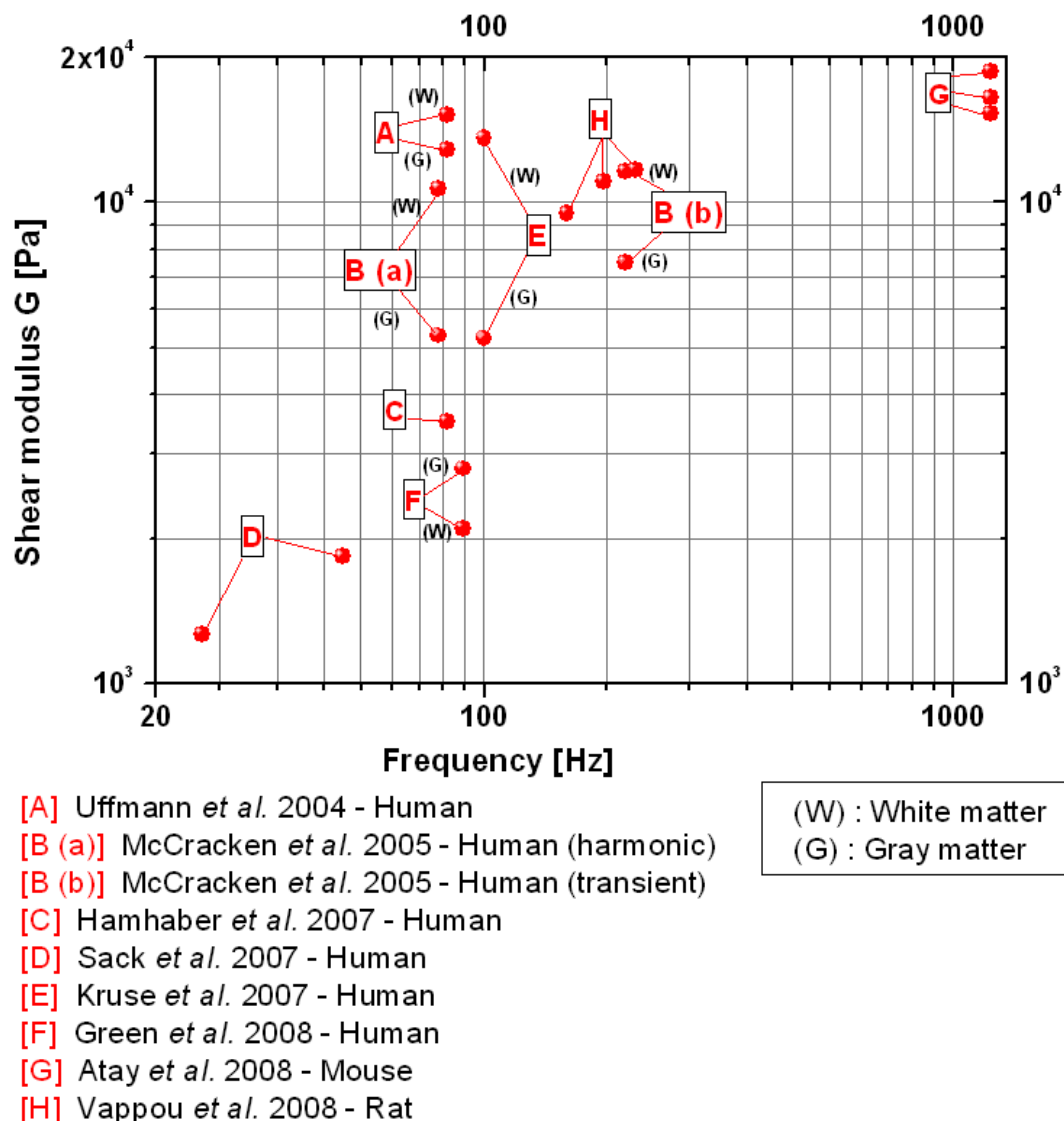


Figure 1- 8. Superposition of storage and loss moduli obtained in vivo by magnetic resonance elastography presented in the literature. In spite of many protocol and algorithm disparities between all the authors, a relative consistency in the results can be observed.

4 Discussion

4.1 From in vitro to in vivo approach

The comparison between in the vivo and in vitro mechanical behavior of brain tissue was already explored by Gefen and Margulies. However this study was published in 2004 and it appears interesting to compare their conclusions with more recent MRE results. Gefen and Margulies showed that in vitro protocols contribute to create a preconditioning and indeed an initial and long-term shear modulus underestimation of 30% and 50%, respectively. These observations were already found by Miller et al. (1999) showing an in vivo indentation shear modulus about 31% higher than the vitro modulus. From a comparison between the in vitro and in vivo shear modulus results shown in Figure 1- 9 it is evident that the MRE values appear to agree with the intermediate in vitro values. In particular this is true of the “mean results” of Bilston et al. (1997), Nicolle et al. (2004) or Shuck and Advani (1972). These mean results would also be confirmed by the indentation module from Wang and Wineman (1972) and the MRE values from Kruse et al.

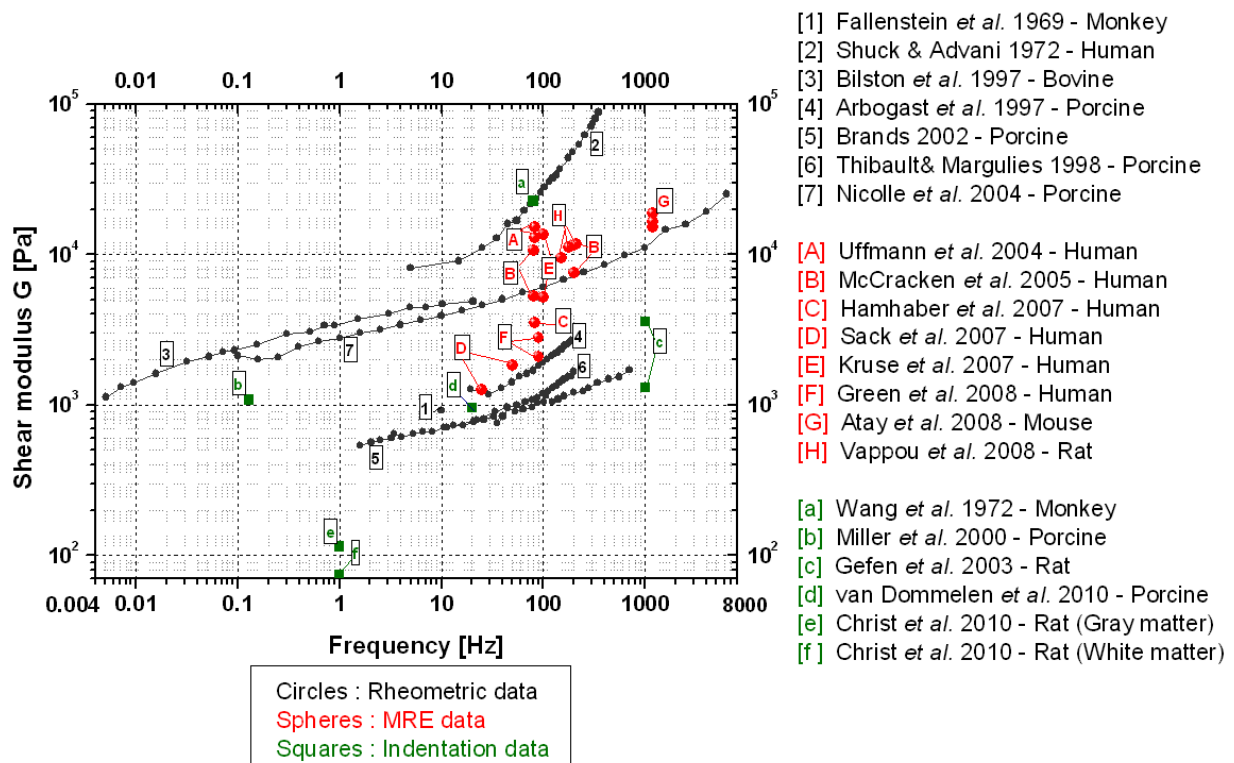


Figure 1- 9. Comparison of shear modulus obtained in vitro by dynamical mechanical analysis, or in vivo by indentation and magnetic resonance elastography

After having detailed both in vitro and in vivo tests from the literature, comparison of rheometric, indentation and MRE dynamic results seems to be relevant in terms of shear

modulus as presented in Figure 1- 9. The same disparity appears for all the protocols and it is difficult to bring referent values to light. Nevertheless a “mean curve” can be highlighted by associating results from Nicolle et al.. These curves are correlated with MRE results of McCracken et al. Globally MRE results contribute to confirm the intermediate in vitro results, of which results from Nicolle et al. (2004) seem to be the closest. For MRE most commonly used frequency range, i.e. between 70 and 120 Hz, the assumption of about 10 kPa for shear modulus seems to be confirmed. With in vitro protocols, alterations in mechanical properties may exist, because of the absence of vascular network pressurization and autolytic processes. In vivo MRE seems to be the best solution to avoid these difficulties and approximations for more biorealistic experimental conditions. Many difficulties inherent to brain tissue anatomy and neuroarchitecture are pointed out in the literature and are discussed below.

4.2 Heterogeneity

The local differences in brain mechanical behavior are directly linked to the composition of individual components of the organ. Using dynamic translational shear tests, Arbogast et al. (1997) showed that the brain stem is from 20% to 100% stiffer than the cortex. In dynamic and relaxation shear tests Prange and Margulies (2002) observed that the corona radiata is significantly stiffer than the corpus callosum, but Velardi et al. (2006) observed opposite results from tensile/compression tests. However, investigations of tissue heterogeneity are mainly concerned with comparisons between the mechanical properties white and gray matter. This difference can be explained from a neuroarchitectural point of view. According to Prange et al. (2000), Prange and Margulies (2002) or Nicolle et al. (2004), white matter was also shown to be 1.3 times stiffer than grey matter at large strains. Most of the MRE results tend to validate this observation with white matter shear modulus 1.2 to 2.6 times higher than of gray matter. Moreover, MRE can embark on new perspectives; for instance, this method is able to express the complex shear modulus as a function of location, as shown by Atay et al. (2008).

4.3 Anisotropy

Brain anisotropy was first observed by Shuck et al. Brain stem anisotropy and isotropy transversally to the axons' main orientation were highlighted by Arbogast and Margulies (1998). According to Prange and Margulies (2002), white matter showed more anisotropy than gray matter. To the best of our knowledge, to date, no data is available on brain anisotropy using MRE. Indeed, anisotropic MRE by taking wave propagation in different

directions into account could presumably be one of the next improvements for brain tissue investigations.

4.4 Inter-species variations

Owing to the difficulty of obtaining human brain tissue for testing, experiments are usually performed either on human or animal brain samples (monkey, porcine, bovine, rabbit, calf, rat or mouse). Galford and McElhaney showed that shear, storage and loss moduli are 1.5, 1.4 and 2 times higher for monkeys than for humans. Differences between human and porcine brain properties were pointed out by Prange et al. (2000) who demonstrated that human brain tissue stiffness was 1.3 times higher than that of porcine brain. However Nicolle et al. observed no significant difference between the mechanical properties of human and porcine brain matter. These inter species differences of rigidity are difficult to characterize as only few MRE tests have been carried out on animals: those reported by Atay et al. (2008) on mouse and by Vappou et al. (2008) on rats showing no significant differences. In addition, the literature reports differences such as 2 times higher shear moduli. It should be mentioned that general dispersion of results can be as high as 10 to 20 times. However, the non invasive nature of MRE confines its use essentially to human subjects. Pervin and Chen found no difference between the in vitro dynamic mechanical responses of brain matter to compression at high strain rate in four bovine species.

4.5 Age-dependence

Very few studies deal with the influence of age on brain mechanical properties. The first one was described in 1998 on developing porcine subjects by Thibault and Margulies who showed that storage, loss and complex shear moduli seem to increase with age. It was concluded that shear modulus of young brain tissue is independent of strain level whereas shear modulus of adult brain tissue decreases when strain increases. To the best of our knowledge no in vivo investigation is available that compares young and adult brain mechanical properties. Sack et al. (2009) showed by MRE that brain tissue undergoes steady parenchymal “liquefaction” between the ages of 18 and 88.

4.6 Post-mortem time

Metz and Weber (1970) inflated a balloon inserted into the brain tissue and monitored its volume increase as a function of its pressure. Compared to the elastic modulus of the living brain they found about a 35% change 5 minutes after death and a 70% change 45 minutes after death. At far longer post-mortem time, Darvish and Crandall (2001) found no link

between storage times from 3 to 16 days and variations in mechanical parameters. Vappou et al. made a first attempt to measure changes in shear storage and loss moduli of rat brain tissue before and after death using the same MRE protocol. The result showed no significant difference in shear loss modulus in vivo and just after death, but a 50% decrease at 24 hr post mortem. In contrast, the shear storage modulus increased a 100% just after death but at 24 hr post mortem this increase had disappeared. In earlier work, Fallenstein and Hulse (1969) reported that freezing Rhesus monkey brain resulted in gross changes in shear moduli: lowering the storage modulus by an order of magnitude and the loss modulus by a factor of 3.

4.7 Experimental parameters

One can notice that some other parameters, such as temperature, sliding or preload, linked with experimental protocols and devices can be observed and may exercise influence of results obtained. In addition, the temperature of the samples being tested tests or the sample shape, preconditioning and attachment methods between samples and lastly the experimental device itself can be mentioned as parameters to be considered in the vitro tests.

5 Conclusions

In this paper the problems associated with in vitro studies that came to light through in vivo experimental protocols have been pointed out. In addition, it is especially noticeable that brain incompressibility and anisotropy are brain region specific. White matter exhibits higher anisotropy due to its different neuroarchitecture. It can be seen that, no matter what experimental protocol is used, inter-species differences are important whereas age only has an effect between infants or children and adults. These points have necessarily to be taken into account for bio-realistic brain tissue modeling. In this way, more recently developed non invasive protocols seem to be really efficient. Indeed these protocols are able to minimize some alterations in mechanical parameters due to in vitro testing, such as brain samples cutting, post mortem time, testing temperature or moisturizing. However, taking together the fifty years brain tissue investigation, the main observation concerns the huge disparities in the results, essentially linked with variations in the protocols. Thus, when selecting one of the existing experimental protocols and its results, it has to be oriented towards the objectives in brain tissue modeling, such as brain injury reconstruction or simulation of a surgical operation. All these results have to be taken into account for the development of this thesis.

CHAPTER 2

Axons deformation in case of head trauma

1 Introduction

Traumatic Brain injury (TBI) is one of the most common causes of death or disability and it remains an important public health problem. In the United States, The Centers of Disease Control and Prevention (CDC) (2010) estimate that TBI involves annually about 1,365,000 emergency department visits, 275,000 hospitalizations and 52,000 deaths. According to Faul *et al.* (2010), 1.7 million people would sustain a TBI annually in the US. It contributes to about a third (31.8 %) of all injury related deaths in the US. According to the authors, motor vehicle traffic is the leading cause of TBI death and represents 17.3 % of all the related TBI between 2002 and 2006 in the US, just after falls injuries (35.2 %). Direct medical and indirect costs of TBI were estimated to \$60 billion in the US in 2000, according to Finkelstein *et al.* (2006).

One of the most frequent types of closed head injury is Diffuse Axonal Injury (DAI). DAI occurs in almost half (48.2 %) of primary intra-axial lesions of brain, according to Gentry *et al.* (1988), and is the second cause of death by TBI, according to Bain and Meaney (2000). DAI results from rapid tensile elongation of the axons, with eventually axon fibers rupture called "first axotomy" (Thibault *et al.*, 1990; Aldrich *et al.*, 1992). The axons rupture leads to retraction of the cutted axon to its cellular nucleus, giving birth to retraction balls with about 30 μm diameters, as described by Arfanakis *et al.* (2002). This process is followed by axon degeneracy. According to Smith and Meaney (2000), rapid axon elongations resulting to head injury involve a decrease of brain tissue elasticity. Even if no DAI has been diagnosed, local axonal ruptures could appear until seventy-two hours after TBI, according to some authors (Gennarelli, 1997; Pettus and Povlishock, 1996; Kelley *et al.* 2006). In the most severe TBI cases, DAI is the main cause of prolong coma, without presenting obvious marks, pressure increase or blood flow decrease. The only observable marks are many associated microscopic hemorrhages in cerebral white matter. According to various epidemiological studies (Gennarelli *et al.*, 1982; Gentry *et al.*, 1988; Ng *et al.*, 1994; Graham and Gennarelli, 1997; Arfanakis *et al.*, 2002), axonal injuries are mainly concentrated in the white matter or gray/white matter interface (corticomedullary junction). Unlike cerebral contusions and hematomas, DAI diagnosis and location remain difficult and sometimes not visible with usual medical imaging techniques. One of the main ways proposed in the literature in terms of injury is to identify the adequate intra-cerebral mechanical parameters which could act as a DAI prediction metric.

Various experimental studies evaluate the limit for DAI in terms of maximal principal strain (Gennarelli *et al.*, 1982, Thibault *et al.*, 1990, Bain *et al.*, 1996) either around 0.10 (Thibault

et al. 1993) or between 0.18 and 0.21 (Bain and Meaney, 2000). These values are reported in Table 2 - 1.

Authors and proposed criteria		DAI
Limites de tolérance expérimentales	Thibault (1993) (<i>in vivo</i> giant squid nerves)	
	Maximum Principal Strain [%]	10
	Bain & Meaney (2000) (<i>in vivo</i> guinea pig optic nerve)	
	Maximum Principal Strain [%]	18
	Morrison <i>et al.</i> (2003) (cell culture)	
	Maximum Principal Strain [%]	21

Table 2 - 1. Experimental strain values limits for axons rupture and DAI appearance.

Since seventieth, Finite Element Human Head Models (FEHM) have been developed as tools to assess head injury risk and eventually injury location, notably concerning DAI. In last decades, about twenty FEHM have been reported in the literature (Shugar, 1977; Ward *et al.*, 1980; Hosey *et al.*, 1980; Ruan *et al.*, 1991; Di Masi *et al.*, 1991; Mendis *et al.*, 1992; Bandak *et al.*, 1994; Zhou *et al.*, 1995; Al-Bsharat *et al.*, 1999; Kang *et al.*, 1997; Zhang *et al.*, 2001; Kleiven *et al.*, 2002; Brands *et al.*, 2002; Takhounts *et al.*, 2003; King *et al.*, 2003; Horgan *et al.*, 2005; Kleiven, 2007; Iwamoto *et al.*, 2007; Takhounts *et al.*, 2008). Based on these models and well documented head trauma simulations, brain shear stress and strain rate have been shown as pertinent parameters for DAI prediction (King *et al.*, 2003, Kleiven, 2007, Deck *et al.*, 2008). These criteria are reported in Table 2 - 2.

For about ten years, a new imaging technique, called Diffusion Tensor Imaging (DTI), has been developed (Basser *et al.* 1994; LeBihan *et al.*, 2001; Kraus *et al.*, 2007). By imaging the tridimensional Brownian movement of water molecules using Magnetic Resonance Imaging (MRI), a tridimensional map of main axonal fibers orientation can be obtained. In the present study it is proposed to couple structural information from DTI with a classical FEHM mechanical analysis in order to compute tensile elongation of axons during TBI, which is thought to be the most realistic mechanism of DAI according to most of the authors (Thibault and Gennarelli (1990), Bain and Meaney (2000), Meythaler *et al.* (2001), Morrison *et al.*(2003), Takhounts *et al.* (2003), Takhounts *et al.*(2008), Deck *et al.*(2008)). Based on the assumption of a correlation between axonal structural anisotropy and mechanical response, according to Tamura *et al.* (2007) the purpose of this work is to develop a new method for DAI prediction and location based on the assumption of axons elongations.

Authors and proposed criteria		Mild DAI	Severe DAI
Numerical criteria	Anderson et al. (1999)		
	VonMises's stress [kPa]	27	43
	Kleiven et al. (2007)		
	Maximum Principal Strain [%]	-	10
	CSDM [%]	-	47
	WSU criteria (King et al., 2003)		
	Strain rate [s^{-1}]	-	60
	Strain * Strain rate [s^{-1}]	-	19
	SIMon DAI criteria (Takhounts et al., 2003)		
	Maximum Principal Strain [%]	-	15
	CSDM [%]	-	55
	SIMon DAI criteria (Takhounst et al., 2008)		
	Maximum Principal Strain [%]	-	25
	CSDM [%]	-	54
	SUFEHM DAI criteria (Deck et al., 2008)		
	Brain Von Mises stress [kPa]	28	53
	Brain Von Mises strain [%]	30	57
	Brain First principal strain [%]	33	67

Table 2 - 2. Numerical DAI criteria from the literature

After a presentation of the brain finite element model and DTI data used for this study, the method of coupling these two modalities as well as the axonal elongation calculation is presented. The novel axon elongation computation technique is then applied to real world head trauma cases as a first attempt to investigate axon elongation based DAI mechanism. The methodology as well as the obtained results is finally discussed before concluding.

2 Materials and method

2.1 Human head FE model and related criteria

The finite element head model used in this study was developed at the University of Strasbourg under Radioss software by Kang *et al.* (1997). As shown in Figure 2- 1, the Strasbourg University Finite Element Head Model (SUFEHM) includes the scalp, the brain, the brainstem and the cerebrospinal fluid (CSF) modeled with brick elements as well as the skull, the face and two membranes (the falx and the tentorium) modeled with shell elements.

The geometry is a feature of an adult human head with a 4.7 kg mass. To insure anatomical accuracy, the geometry of inner and outer surfaces of the skull was digitized from a healthy human adult male skull. At least, the SUFEHM presents a continuous mesh that is made up with 13208 elements, 5320 of which are dedicated to the brain.

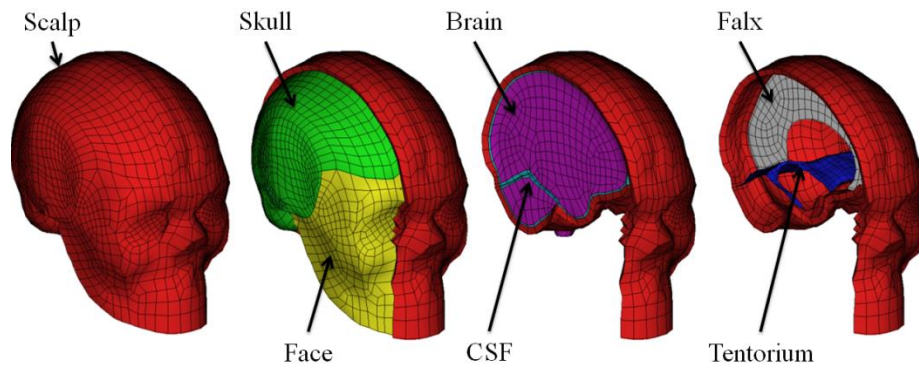


Figure 2- 1. Details Strasbourg University Finite Element Head Model developed by Kang *et al.* (1997).

Mechanical models applied to each of the SUFEHM parts are supposed to be isotropic, homogeneous and elastic, except the brain that is assumed to be visco-elastic and the skull modeled by a rigid body. These parameters were proposed and implemented under Radioss software by Willinger *et al.* (1995) and LS-DYNA software by Deck and Willinger (2008). Mechanical properties and element characteristics used for the SUFEHM are summarized in Table 2 - 3. The skull was modeled by a rigid body. The skull was modeled by a rigid body. This modeling was chosen because only simulation inputs were implemented as accelerations.

	Density [kg/m ³]	Young's modulus [Pa]	Poisson ratio	Element type	Shell thickness [m]
Face	2,500	5.10 ⁹	0.23	Shell	1.10 ⁻²
Scalp	1,000	1.67.10 ⁷	0.42	Brick	-
Brain	1,040	<i>Viscoelastic</i>		Brick	-
Brain stem	1,040	<i>Viscoelastic</i>		Brick	-
CSF	1,040	1.2.10 ⁴	0.49	Brick	-
Falx	1,140	3.15.10 ⁷	0.45	Shell	1.10 ⁻³
Tentorium	1,140	3.15.10 ⁷	0.45	Shell	2.10 ⁻³

Table 2 - 3. Mechanical properties implemented into the Strasbourg University Finite Element Head Model. These parameters were first proposed under Radioss software (Willinger *et al.*, 1995) and used in this study under LS-DYNA® software (Deck *et al.*, 2008).

A linear visco-elastic and isotropic law is affected to the whole brain. This law was described by Herrmann and Peterson (1968) in terms of relaxation shear modulus, in accordance with expression (2 - 1).

$$G(t) = G_{\infty} + (G_0 - G_{\infty})e^{-\beta t} \quad (2 - 1)$$

where G_0 , G_{∞} and β represent the short-time modulus, the long-time modulus and the decay constant respectively. Parameters were identified from experimental data on human brain tissue, i.e. *in vitro* results proposed by Shuck and Advani (1972) as well as *in vivo* based values from Magnetic Resonance Elastography (MRE) published by Kruse *et al.* (2007), with following values: $G_0 = 49.10^3$ Pa, $G_{\infty} = 1.62.10^4$ Pa, $\beta = 145$ s⁻¹.

Validation of this FEHM was proposed by Kang *et al.* (1997), Willinger *et al.* (2003), Deck *et al.* (2004) under Radioss code and by Deck and Willinger (2008) under LS-Dyna code. Validation consisted by reproducing experimental cadaver impact tests coming from the literature. This validation includes skull deformation and rupture according to Yoganandan tests (1994) as well as intra-cranial pressure in conformity with Nahum (1977) and Trosseille (1992) data and brain deformation by considering experimental data reported by Hardy *et al.* (2001). In order to prove finite element head model performance, Deck and Willinger (2009) proposed a rational approach in order to evaluate the ability of head model to provide predicted brain pressures and brain displacements by using statistical approach. The main conclusion of this study is that finite element modelling is a good method for assessing head injury risk. All models can reproduce experimental results with good agreement and could be used to predict some lesions.

Tolerance limits to specific injury mechanisms derived from extensive real world head trauma simulations by Deck and Willinger (2008). These criteria for Diffuse Axonal Injuries (DAI) reported in Table 2 - 4 results from a methodology proposed by Deck *et al.* (2008). Values corresponding to a 50 % risk of injuries were obtained by simulating 11 motorcycle, 20 American football and 28 pedestrian real world accident cases.

<i>SUFEHM DAI criteria (Deck et al., 2008)</i>	Mild DAI	Severe DAI
Brain Von Mises stress [kPa]	28	53
Brain Von Mises strain [%]	30	57
Brain First principal strain [%]	33	67

Table 2 - 4. DAI criteria proposed in 2008 by Deck *et al.* using the Strasbourg University Finite Element Head Model.

2.2 Brain Diffusion Tensor Imaging atlas

Concerning Diffusion Tensor Imaging (DTI), all Magnetic Resonance acquisitions were performed on a 1.5-T scanner (Magnetom Vision; Siemens Medical Systems, Erlangen, Germany) using a 60 gradients sequence with two b_0 images for 12 controls. Acquisition parameters were a repetition time (TR) of 6.8 s, a time to echo of 100 ms, a b-value of 1000 s.mm⁻² and resolution of 1.7 by 1.7 by 3.5 mm for an image size of 182 by 182 by 218 mm. Imaging was performed on 12 healthy volunteers with the approval of the local ethics committee. From the diffusion data, diffusion tensors are estimated with a standard least square algorithm. A scalar measurement describing the diffusion anisotropy, called Fractional Anisotropy (FA) (Pierpaoli and Basser, 1996), is computed for each patient. The affine transformations are calculated between each FA map and the International Consortium or Brain Mapping (ICBM)-DTI template (Mori *et al.*, 2008) and then performed using the Mutual Information criterion (Horsfield, 1999). Each component of the diffusion tensor is registered in the template space using a sinus cardinal interpolation strategy, according to Nikou *et al.* (2003). The orientation and shape information of tensor imaging are preserved using the Preservation of Principal Direction (PPD) reorientation strategy defined by Alexander *et al.* (2001). At least the Euclidian mean values for the diffusion tensor are calculated for all the directions at the same spatial location. At least voxels and pictures size are 1 by 1 by 1 mm and 181 by 181 by 217 mm respectively.

3 Theory and calculation

3.1 Inclusion of axonal direction into the brain FEM

Aim of this part is to obtain, from 3D DTI picture and FE model meshing, a 3D map of axons fibers directions and diffusion anisotropy at FE model scale and resolution. This protocol is described by the Figure 2- 2. As further explained later, this map will never been implemented in the brain material of the FE model but will only be used in post-treatment of classical isotropic FE simulations.

Correspondence between DTI data and the brain FEM involves a fitting between imaging and numerical extern geometries. This was performed using rigid transformations, i.e. only rotation and translation, with a linear scaling of all the nodes from the Strasbourg University Finite Element Head Model (SUFEHM). It permitted to fit the finite elements outlines to the twelve patients-based DTI mask. The correspondence between DTI voxels and the FEM has been performed using the Matlab 7.4 software (The Mathworks, Inc., Natick, MA, USA).

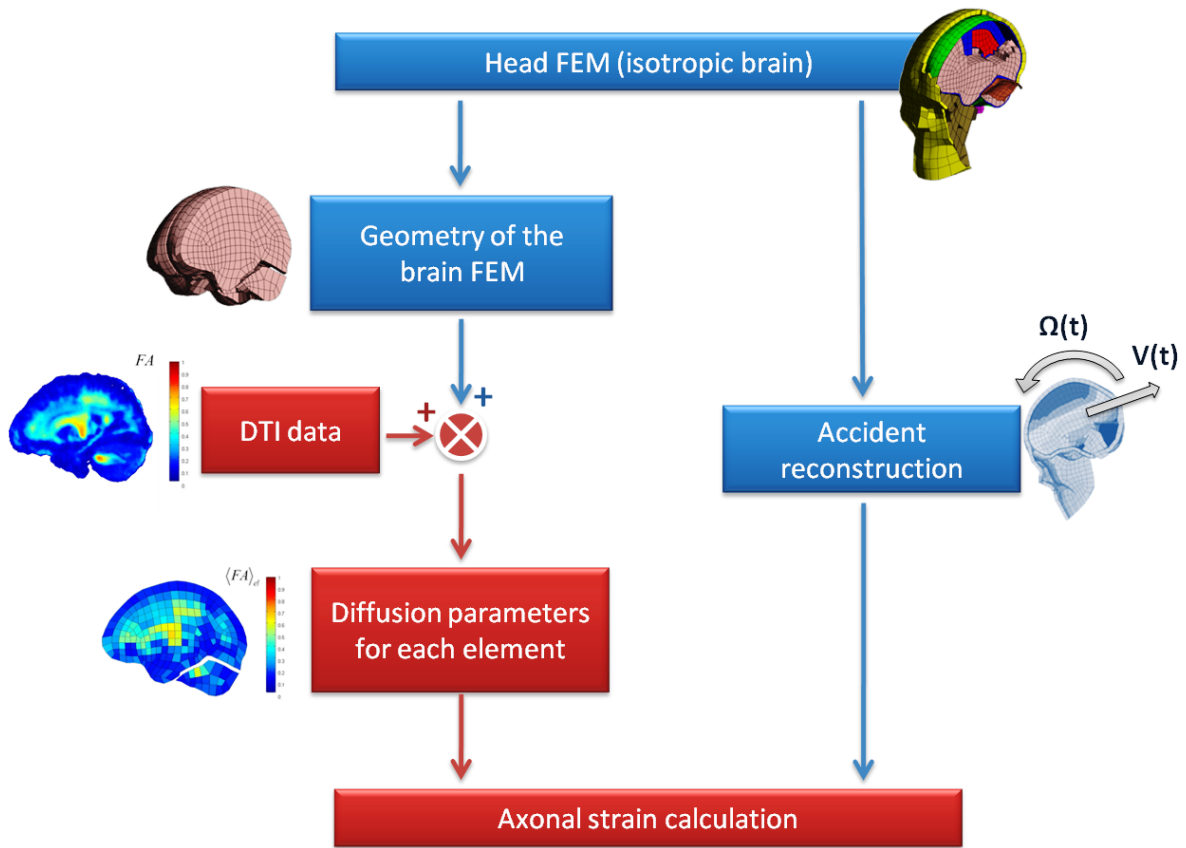


Figure 2- 2. Description of the global protocol for diffusion information mapping at FE model resolution.

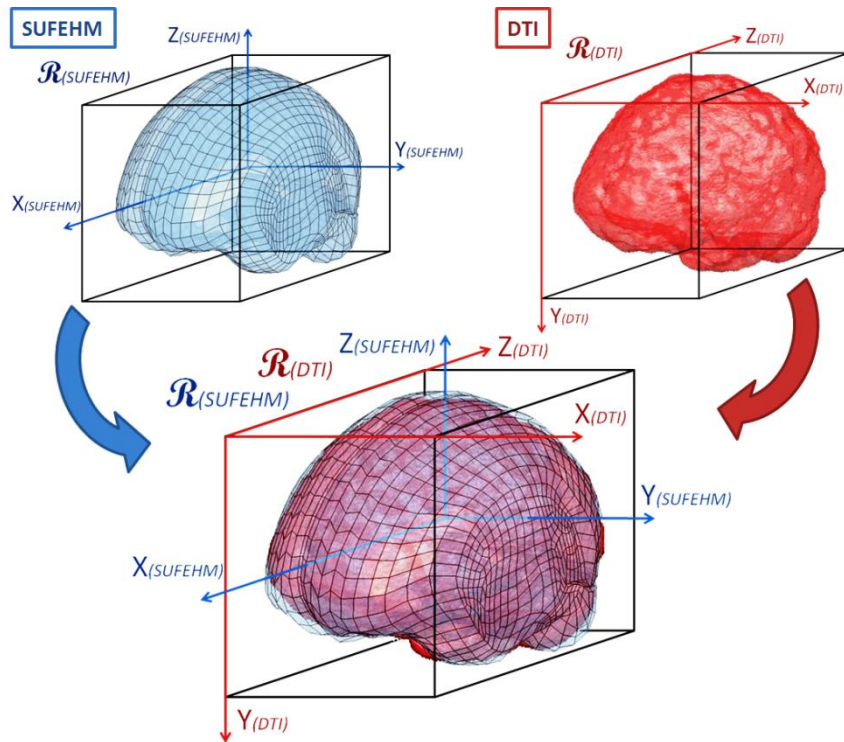


Figure 2- 3. Rigid transformation application to ensure correspondence between external geometries (mask) of diffusion data (in red) and brain FEM (in blue), with associated frames.

$$\underbrace{\begin{pmatrix} X_{\mathcal{R}(DTI)} \\ Y_{\mathcal{R}(DTI)} \\ Z_{\mathcal{R}(DTI)} \end{pmatrix}}_{\text{Coordinates in DTI frame}} = \underbrace{\begin{pmatrix} 1.02 & 0 & 0 \\ 0 & 1.08 & 0 \\ 0 & 0 & 1.05 \end{pmatrix}}_{\text{Scale factor}} \times \underbrace{\begin{pmatrix} 0 & 1 & 0 \\ 0 & 0 & -1 \\ -1 & 0 & 0 \end{pmatrix}}_{\text{Rotation}} \times \underbrace{\begin{pmatrix} X_{\mathcal{R}(SUFEHM)} \\ Y_{\mathcal{R}(SUFEHM)} \\ Z_{\mathcal{R}(SUFEHM)} \end{pmatrix}}_{\text{Coordinates in FEM frame}} + \underbrace{\begin{pmatrix} 91.02 \\ 120.53 \\ 101.52 \end{pmatrix}}_{\text{Translation}} \quad (2-2)$$

To implement information from the tridimensional diffusion image into the FEM, the next step consists in selecting voxels from DTI for each element. While DTI brain are brought into line with a regular plan-parallel meshing characterized by 1 by 1 by 1 mm voxel size, elements have different local orientation with a characteristic element size from 1.14 to 7.73 mm. To compensate this difference in resolution, the voxels included into the smallest parallelepiped lined with the regular DTI meshing and incorporating the considered finite element are selected for each element, as illustrated in Figure 2- 4.

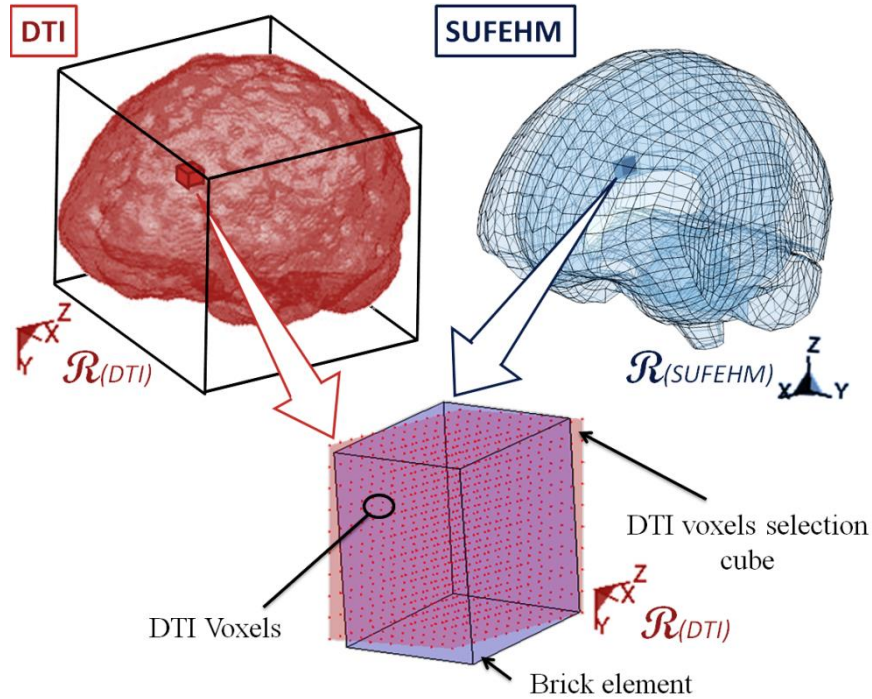


Figure 2- 4. Illustration of the correspondence between the SUFEHM and the DTI 3D picture on a single element. Selected voxels (red points) are all included into the smallest cube (orange) including the finite element (blue parallelepiped).

For each element, four different volume have been tested in order to select DTI voxels:

- The smallest cube including the element, with the same center than the element and with edges lined with DTI frame (Figure 2- 5 – A);
- The sphere with the same center than the element and diameter chosen to be half the diagonal of the element (Figure 2- 5 – B);

- The sphere with the same center than the element and diameter chosen to be 2/3 of the diagonal of the element (Figure 2- 5 – C);
- The highest ellipsoid included into and with the same center than the element (Figure 2- 5 – D);

Choice of one of these methods has been performed using mean diffusion parameters calculation for each element.

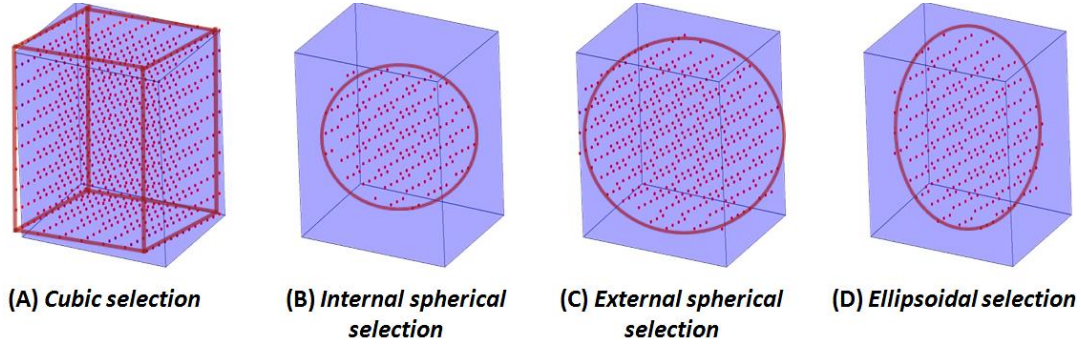


Figure 2- 5. Illustration on a finite element of the 4 DTI voxels selections: cubic (A), Internal spherical (B), external spherical (C) or ellipsoidal (D).

For each finite element, two parameters are investigated for each of the selected DTI voxels. Firstly the three component of the and the Fractional Anisotropy (FA) coefficient, obtained from the eigenvalues λ_1 , λ_2 et λ_3 of the diffusion tensor and expressed in Equation (2 - 3) (Pierpaoli and Bassar, 1996). While a FA value of zero means that the corresponded voxel is perfectly isotropic, a FA value of 1 corresponds to a totally anisotropic voxel, with all the axons included in the voxel oriented along one direction. Second parameter is the anisotropy vector \vec{l} , indicating the main axons orientation for the voxel volume, and corresponds to the eigenvector associated with the diffusion tensor maximal Eigen value. By definition, the norm of the vector \vec{l} is FA .

$$FA = \left(\sqrt{3 \left[(\lambda_1 - \langle \lambda \rangle)^2 + (\lambda_2 - \langle \lambda \rangle)^2 + (\lambda_3 - \langle \lambda \rangle)^2 \right]} \right) / \left(\sqrt{2(\lambda_1^2 + \lambda_2^2 + \lambda_3^2)} \right) \quad (2 - 3)$$

where:

$$\langle \lambda \rangle = (\lambda_1 + \lambda_2 + \lambda_3) / 3$$

The resulting diffusion parameters are calculated for each finite element as the mean values of all the selected voxels. In order to reinforce the diffusion parameters influence close to the center of the element, these are weighted by the distance D (center of the element to center of the voxel). The half length of the element diagonal is noted L_e . This

weighting is illustrated in Figure 2- 6 and the weighting function is given in equation (2 - 4). This weighting method corresponds to the exponentially weighted moving average proposed in 1959 by Roberts for economics statistics.

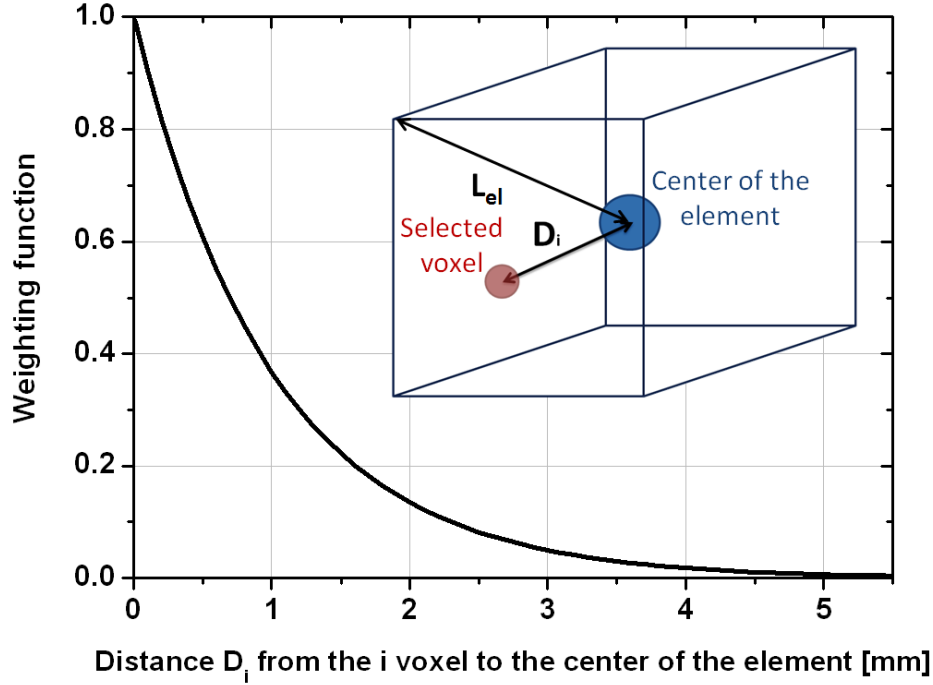


Figure 2- 6. Exponential weighting function depending on the distance from the selected voxels to the element center. The more the voxel is far from the center of the element, the lower its weight for mean parameters calculation is.

$$f(D_i) = e^{-D_i/L_e} \quad (2 - 4)$$

Anisotropy coefficients are expressed in terms of mean weighted anisotropy vector $\langle \vec{l} \rangle_{el}$ and Fractional Anisotropy $\langle FA \rangle_{el}$ as exposed in Equations (2 - 5) and (2 - 6).

$$\langle \vec{l} \rangle_{el} = \left(\sum_{i=1}^N \vec{l}_i e^{-D_i/L_e} \right) / \left(\sum_{i=1}^N e^{-D_i/L_e} \right) \quad (2 - 5)$$

$$\langle FA \rangle_{el} = \left(\sum_{i=1}^N FA_i e^{-D_i/L_e} \right) / \left(\sum_{i=1}^N e^{-D_i/L_e} \right) \quad (2 - 6)$$

In Equations (3) and (4), N refers to the number of selected voxels for the considered finite element and FA_i , \vec{l}_i , D_i respectively to the FA value, the anisotropy vector and the distance to the center of the element for each selected voxel.

3.2 Computation of axonal elongation under impact

For the computation of the axonal elongation in case of head impact, the impact is firstly simulated with the SUFEHM in a classical way and with an isotropic brain constitutive law. Results are expressed for each element in terms of strain tensor from which maximal principal strain and Von Mises strain are calculated, according to Equation (2 - 7) where $\underline{\underline{\varepsilon}}^d$, $\underline{\underline{\varepsilon}}$ and I_3 are the deviatoric, the Left Green-Lagrange strain and the unit tensor respectively. The diffusion anisotropy for each element is never integrated in the brain FE material but is used as a tridimensional map of axons adapted to finite elements dimensions.

$$\varepsilon_{VM} = \sqrt{\frac{3}{2} \underline{\underline{\varepsilon}}^d : \underline{\underline{\varepsilon}}^d} \quad (2 - 7)$$

where:

$$\underline{\underline{\varepsilon}}^d = \underline{\underline{\varepsilon}} - (1/3)(\underline{\underline{\varepsilon}} : I_3)I_3$$

Maximal principal strain and Von Mises strain will be noted ε_I and ε_{VM} respectively. Computation of the strain along axonal direction occurs in a second step, by calculating strain along the main anisotropy direction of the element implemented in the previous section. This axonal strain value, noted ε_{axon} , is oriented along anisotropy direction $\langle \vec{l} \rangle_{el}$ according to Equation (2 - 8) and includes information about axons elongation and fractional anisotropy of the element.

$$\varepsilon_{axon} = \left(\underline{\underline{\varepsilon}} \times \langle \vec{l} \rangle_{el} \right) \cdot \frac{\langle \vec{l} \rangle_{el}}{\langle FA \rangle_{el}} \quad (2 - 8)$$

According to van Dommelen *et al.* (2010), there are significant differences in stiffness between white and gray matter. This parameter induces by FA value higher strains in white matter regions. It integrates brain heterogeneity in post-treatment, while simulations were performed with mechanically homogeneous brain.

As an illustration of this axon elongation computation method, two well documented motorcyclist accidents were simulated. The cases were extracted from the database described by Chinn *et al.* (1999) and reconstructed in collaboration with Transport Research Laboratory (TRL) and the Glasgow Southern Hospital within the framework of the COST 327 project. Accident scenarios were analyzed by accidentologists and the helmets collected on

the scene. Information related to the two male victims is summarized in table 3 by exposing the medical reports in terms of Diffuse Axonal Injury (DAI), Subdural Hematoma (SDH), contusions and skull fracture. 6D head acceleration (three linear and three rotational accelerations) was obtained experimentally using helmeted Hybrid III dummy head dropped from various heights to anvils at required velocity, as described by Willinger *et al.* (2000). The aim was to replicate head impact sustained during the real world accidents while measuring the dynamics of the head. From experimental values, the Head Injury Criterion (HIC), criteria proposed in 1972 by the National Highway Traffic Safety Administration (NHTSA) and based on the work of Gadd (1966), is calculated using Equations (2 - 9) where a stands for linear acceleration at time t , t_1 the initial and t_2 the end time of the contact. The results for HIC criteria are exposed in Table 2 - 5.

	Age [years]	Impact location	DAI	SDH	Contusion	Fracture	Death	HIC value
Case 1	34	Lateral	0	0	0	0	0	578
Case 2	23	Lateral	severe	1	0	0	1	2934

Table 2 - 5. Detailed information from medical report for the two motorcyclist cases used in this study. While case 1 has no severe injury, case 2 presents severe Diffuse Axonal Injury (DAI) as well as Subdural Hematoma (SDH).

$$HIC = (t_2 - t_1) \cdot \left[\left(1 / (t_2 - t_1) \right) \int_{t_1}^{t_2} a \cdot dt \right]^{2.5} \quad (2 - 9)$$

From the experimental 6D acceleration time histories provided, the velocity was calculated as a function of time at three points on the skull FE model. This was used as input to the FE accident simulation. Intra-cranial response was then computed with the LS-Dyna FE code in terms of strain tensor as a function of time. It is finally these data which will constitute the input information of the developed methodology designed for the computation of the axonal elongation.

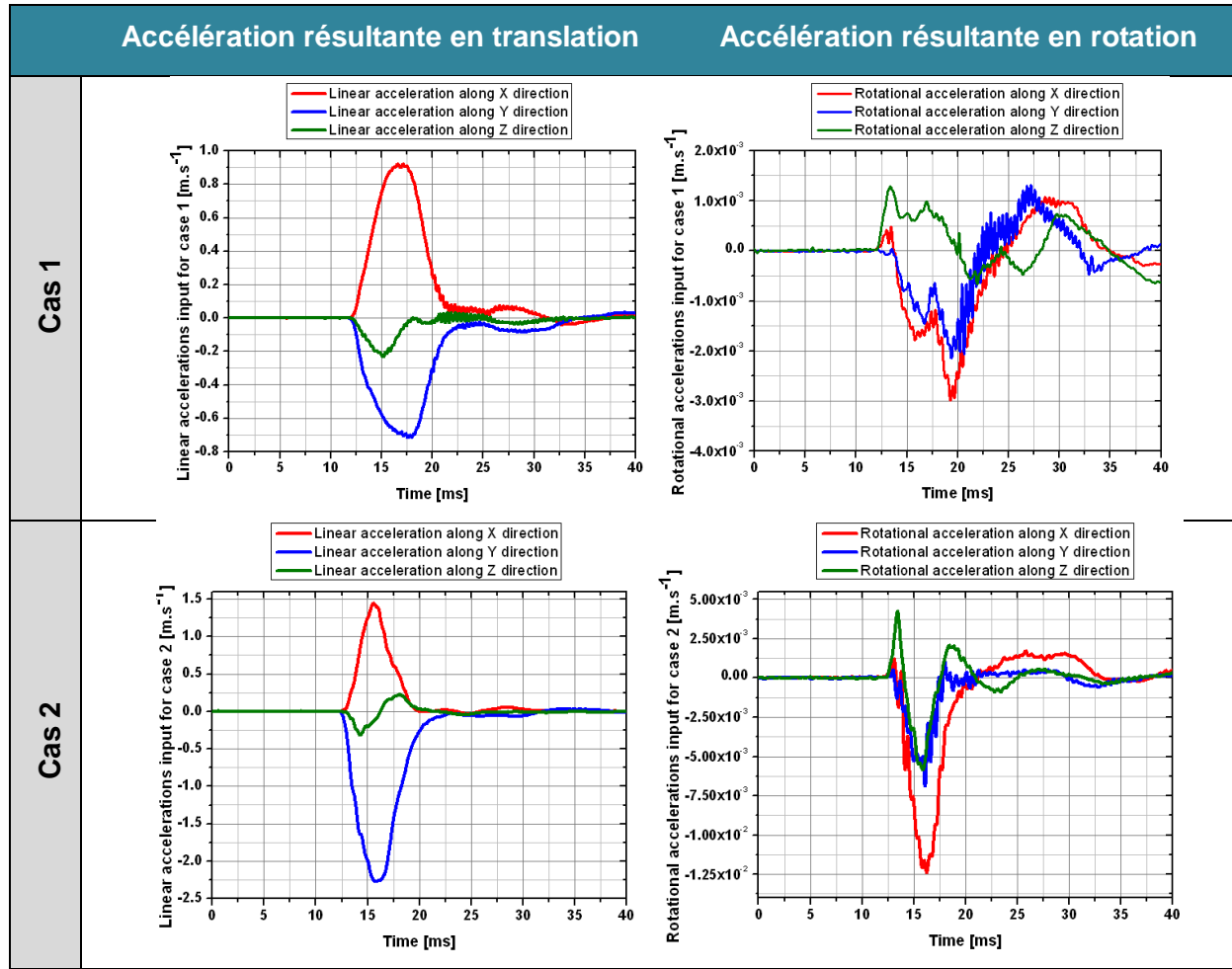


Figure 2- 7. Courbes d'accélération en translation et en rotation implémentées en entrée pour les deux simulations d'accidents considérées.

4 Results

4.1 Introduction

The aim of this part is to present the results from the calculation of a mean FA parameter and a mean anisotropy vector for each of 5320 FEM element. Results are then proposed for the use of this information in accident simulation post-computing, with the previously presented method.

4.2 Diffusion parameters calculation for the FEM

First part concerns choice of one of the four methods presented in Figure 2- 5 for voxels selection. Therefore, the mean number of selected voxels N and standard deviation $\langle ES \rangle_{el}$ (equation (2 - 10)) on $\langle FA \rangle_{el}$ calculation are presented in Table 2 - 6. Considering these

results, cubic selection has been chosen and will be systematically the only one used for the rest of this study.

$$\langle ES \rangle_{el} = \sqrt{\frac{1}{N} \cdot \frac{1}{(N-1)} \sum_{i=1}^N (FA_i - \langle FA \rangle_{el})^2} \quad (2-10)$$

Method of voxels selection	(A) Cubic	(B) Internal sphere	(C) External sphere	(D) Ellipsoid
Number of selected voxels N	899	183,9	432,94	178,1
Standard deviation ES	0,004	0,006	0,005	0,006

Table 2 - 6. Number of selected voxels and standard deviation on FA calculation by the four voxels selection methods (cubic, internal sphere, external sphere, ellipsoid).

The previously exposed method of correspondence between finite elements and DTI voxels leads to consider from 70 to 4096 voxels for each of the 5320 brain finite elements with a mean number of voxel selected by finite element of 899 ± 449 . At least 0.5 % of the finite elements include less than 150 voxels. At the opposite 0.8 % of the elements are linked with more than 2500 voxels as shown in Figure 2- 8.

The DTI voxels selection for each brain element has to be firstly observed on a single finite element for illustration purpose. This particular element has been arbitrarily chosen in the middle of a cerebral hemisphere, into the *corona radiata* white matter. With the previously proposed technique of voxel selection, this element is related with 910 DTI voxels. Figure 2- 9 illustrates the three Eigen values for each of the selected DTI voxels. A systematic predominance of the first Eigen value can be noted, characteristic for a relatively constant anisotropy degree of the selected voxels. It emphasizes the consistence of the selected voxels anisotropy properties. Figure 2- 9 is proposed as illustration for a characteristic element. It illustrates in the same time:

- The relative homogeneity of all the voxels diffusion properties that are selected for this element;
- The difference between first eigenvalue and others eigenvalues is characteristic for voxel anisotropy. The systematic predominance of the first eigenvalue can be observed in this picture that leads to conclude to homogeneity of diffusion degree of all the selected voxels in this element.

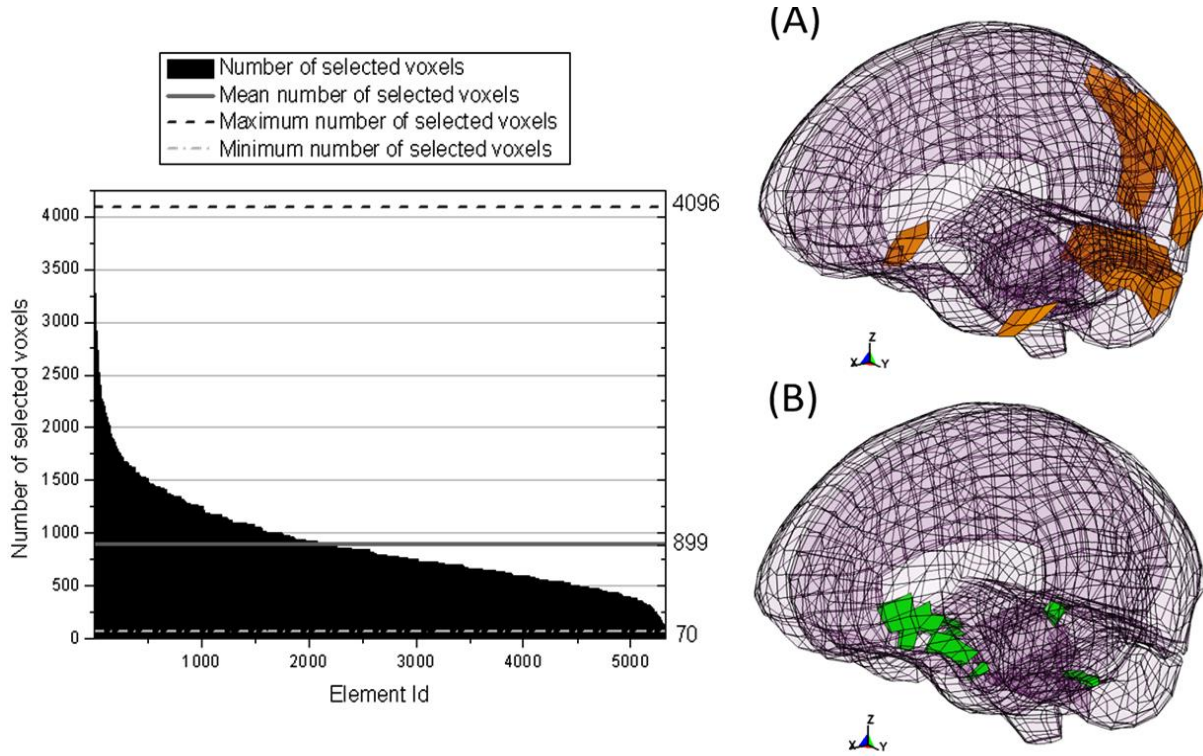


Figure 2- 8. Number of DTI voxels selected for each of the 5320 elements of the SUFEHM. Each element is characterized by considering from 70 to 4096 voxels. Extreme configuration elements are represented: those selecting either more 2500 voxels (A) or less than 150 voxels (B).

It contributes to illustrate the pertinence of our voxel selection method for all the finite elements. For this element as well as for all the others, one other critical aspect concerns the anisotropy mean parameters. Concerning $\langle FA \rangle_{el}$ calculation, while classical algebraic mean value (0.53) and weighted mean value (0.56) are not significantly different, the weighting of voxel parameters by the distance to the center of the element decreases the standard deviation (0.26 and 0.03 with and without weighting respectively). This aspect is reported in figure 6 that shows mean weighted Fractional Anisotropy values obtained for the 5320 brain elements. Figure 2- 10 shows FA value with standard deviation obtained for all of the finite elements, associated with the illustration maximum and minimum FA values location. It leads first to observe the low values for standard deviation that contribute to validate our method for mean diffusion parameters calculation. On top of that, representation of maximum and minimum FA value elements seems to correspond to white and grey matter repartition into the brain.

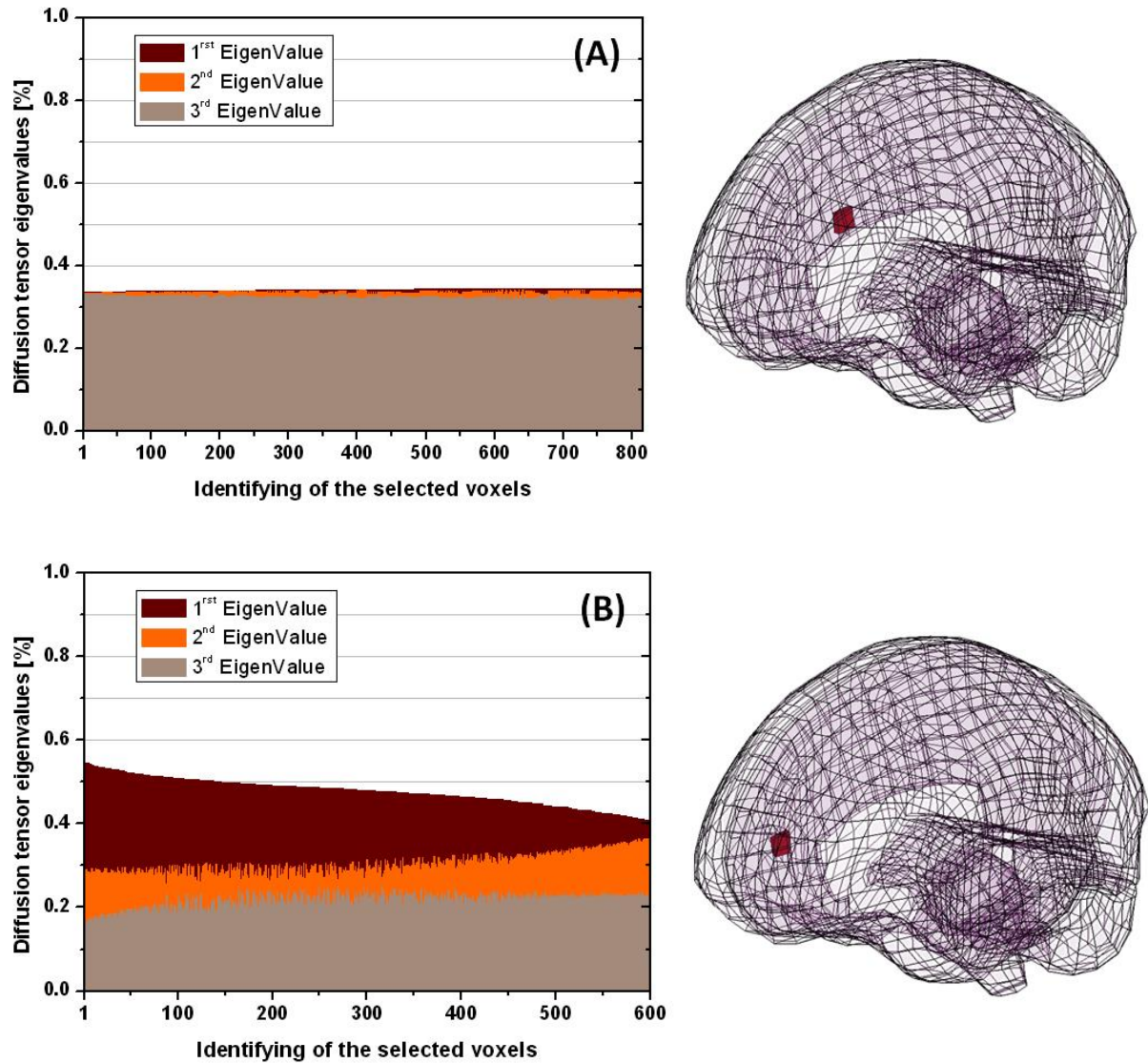


Figure 2- 9. Eigenvalues of diffusion tensor for 2 elements. While 816 voxels with similar eigenvalues are selected for the element 1200 (A) (located close to the extern part of the brain), the 600 voxels selected for the element 2600 (B) (located in the middle of the brain) show a higher first eigenvalue. Consequently, FA value will be higher for the element 2600 (B) than for the element 1200 (A).

Figure 2- 11 proposes a comparison of fractional anisotropy values between DTI data and the SUFEHM on a hemisphere sagittal cut of the right cerebral hemisphere. Highest FA values point out the main axonal fibers within the brain:

- the *corpus callosum* and *cingulum* in the middle of the hemisphere;
- the superior longitudinal fascia between the occipital and frontal lobes;
- white matter fibers in the middle of the *cerebellum*;

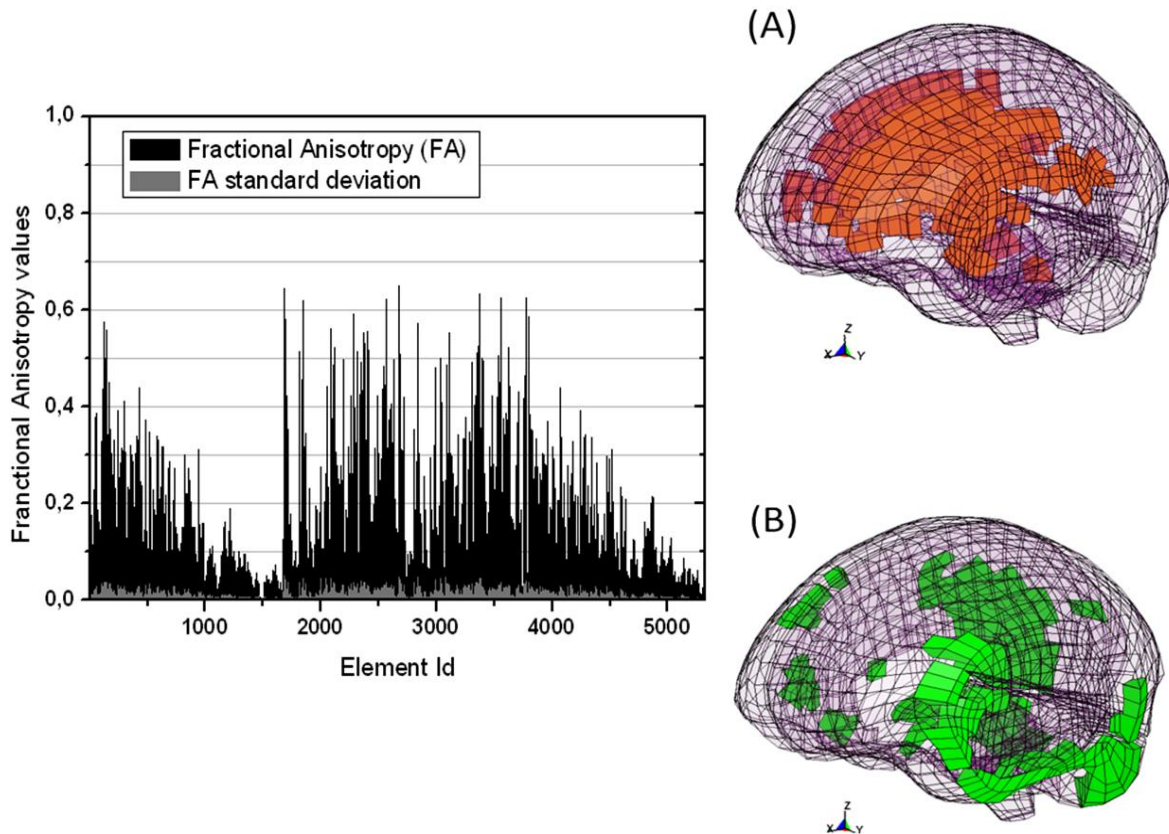


Figure 2- 10. Mean weighted Fractional Anisotropy (FA) values obtained for each of the 5320 brain elements of the SUFEHM. Values vary as a function of element location in the brain. While maximum FA over 0.32 (4.5 % of the elements) are essentially located in the middle of white matter, in the corona radiata and corpus callosum (A), minimum FA under 0.002 (4.1 % of the elements) are at the periphery of the brain and cerebellum, in the cerebral and cerebellum cortex (B).

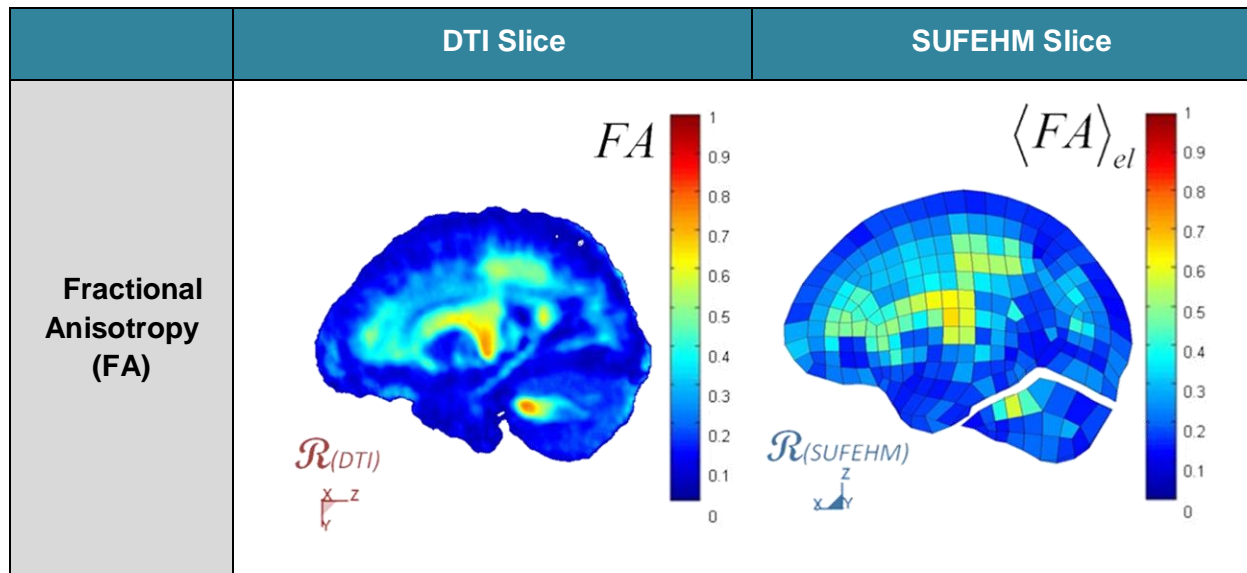


Figure 2- 11. Fractional Anisotropy (FA) values of DTI data and in the finite element brain model illustrated in a sagittal slice. The diffusion anisotropy for each element is not integrated in the brain FE material but is used as a tridimensional map of axons adapted to finite elements dimensions. Highest anisotropy is observed in brain stem and corpus callosum.

The mean square error is evaluated between initial DTI and FEM calculated FA values. Visualization of this error is proposed in a sagittal slice in Figure 2- 12.

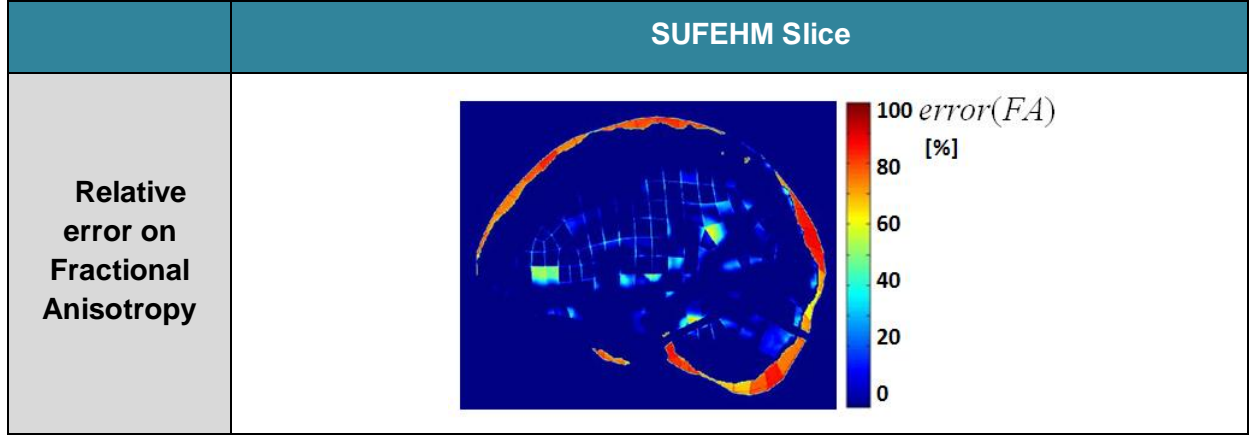


Figure 2- 12. Erreur relative sur une coupe sagittale entre les valeurs de FA du DTI et calculées pour le SUFEBM. Les valeurs les plus élevées se situent sur l'extérieur du cerveau ainsi qu'au niveau des zones de forte variation spatiale du FA.

The tridimensional correlation coefficient is calculated using the equation (2 - 11) where the tridimensional picture, the mean FA values and the associated standard deviations for DTI and Fem diffusion data are noted FA_{DTI} , FA_{SUFEBM} . $\overline{FA_{DTI}}$, $\overline{FA_{SUFEBM}}$, $std(FA_{DTI})$ and $std(FA_{SUFEBM})$ respectively. This correlation coefficient is evaluated at 0.9 for the whole brain. It indicates a good correlation between initial DTI and FEM calculated diffusion data.

$$corr(FA_{DTI}, FA_{SUFEBM}) = \frac{\sum_{x=1}^{181} \sum_{y=1}^{181} \sum_{z=1}^{217} (FA_{DTI}(x, y, z) - \overline{FA_{DTI}}) (FA_{SUFEBM}(x, y, z) - \overline{FA_{SUFEBM}})}{181 \times 181 \times 217 \cdot std(FA_{DTI}) \cdot std(FA_{SUFEBM})} \quad (2 - 11)$$

For DTI as for the SUFEBM, highest FA values correspond to anatomical white matter location. Dissociation can be made using FA values for the SUFEBM insofar as white matter is much more anisotropic as grey matter, according to Pierpaoli and Basser (1996).

In order to evaluate the correspondence between DTI data and SUFEBM axonal directions, anisotropy vectors \vec{l} and $\langle \vec{l} \rangle_{el}$ have to be considered for DTI pictures and SUFEBM respectively. Figure 2- 13 presents projection l_x and $\langle l_x \rangle_{el}$, along transverse direction, l_y and $\langle l_y \rangle_{el}$, along antero-posterior direction, l_z and $\langle l_z \rangle_{el}$, along vertical direction of DTI voxels and SUFEBM elements anisotropy vector respectively. To homogenize and simplify the visualization, vectors are normalized for these illustrations only. Visualization is proposed in Figure 2- 13 on a hemispherical sagittal cut of the right cerebral hemisphere. In the whole study, letters x,y and z will be used to design lateral, antero-posterior and vertical directions

of the brain respectively. These directions are encoded in the present figures as usually by the red, green and blue colors respectively.

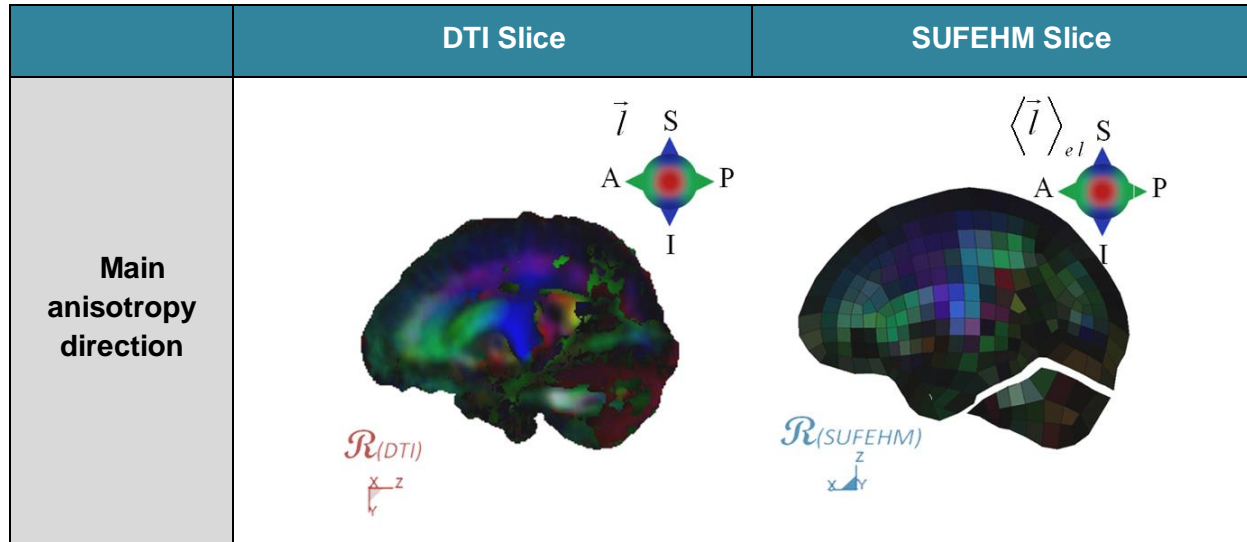


Figure 2- 13. Anisotropy vectors encoded in colors along transverse (red), antero-posterior (green) and vertical (blue) directions for the finite element brain model illustrated in a sagittal slice.

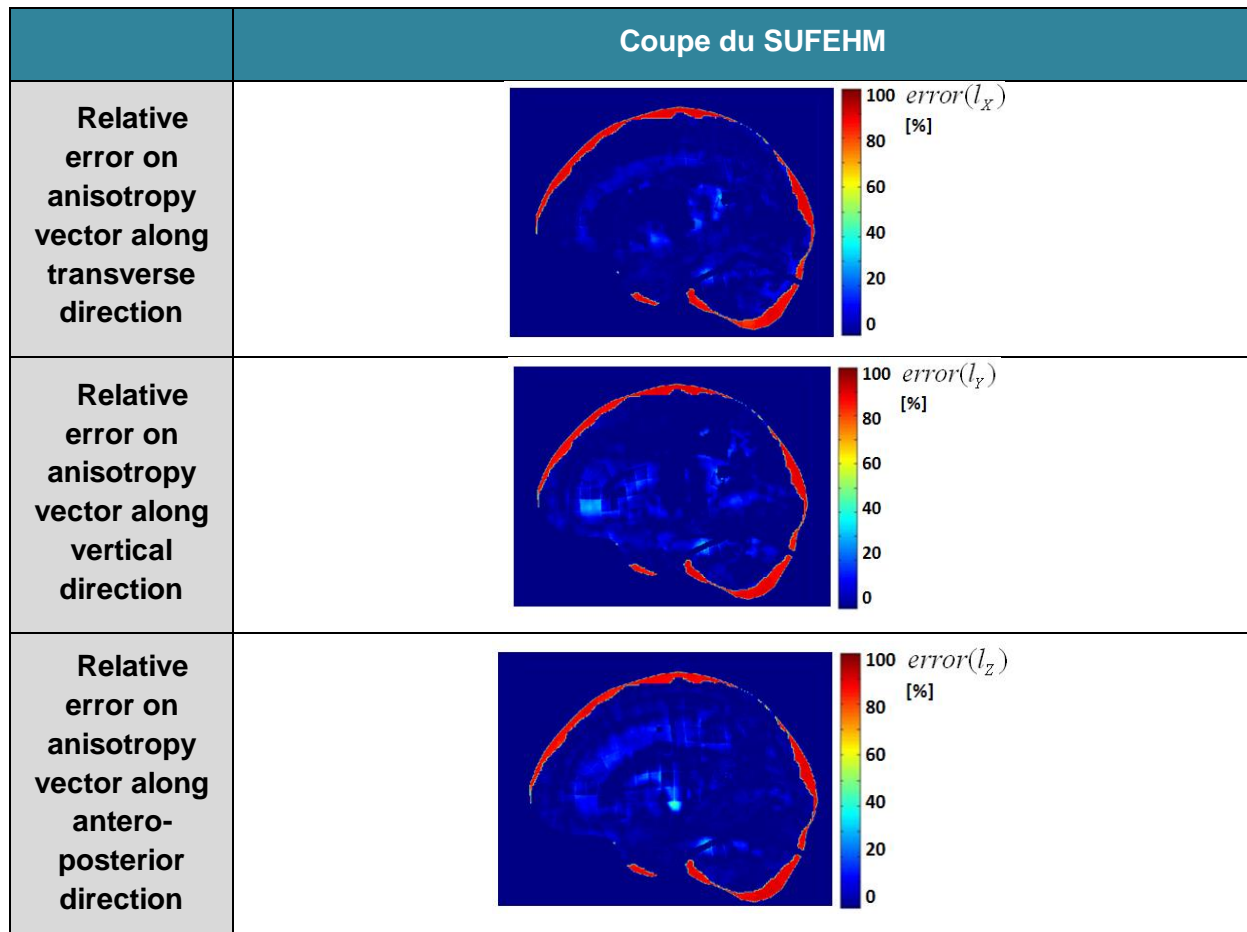


Figure 2- 14. Erreur relative sur une coupe sagittale entre les composantes du vecteur d'anisotropie du DTI et calculées pour le SUFEHM selon les axes transverse (X), vertical (Y) et antéropostérieur (Z). Les valeurs les plus élevées se situent quasiment exclusivement sur l'extérieur du cerveau.

Even if it is not visible in Figure 2- 11 and Figure 2- 13, a very good correspondence between DTI anisotropy information and brainstem elements is obtained, in agreement with anatomical organization of axonal fibers. Anisotropy is higher in brainstem than in brain hemispheres and brainstem fibers are almost exclusively oriented along vertical direction, except for the cerebella peduncles.

4.3 Implementation of axonal directions into the brainstem FEM

A similar procedure is applied for the brain stem Finite Element Model. Figure 2- 15 shows the FA values calculated for each of the 188 brain stem elements.

Highest FA elements for brain stem are presented in Figure 2- 15 (A). They are essentially located into the internal part of the brain stem pons. These locations are validated on FA map sagittal cuts in Figure 2- 16. An illustration of fibers orientation in Figure 2- 17 shows that medulla is essentially oriented along the vertical direction. Pons fibers are oriented all around the brain stem medulla with a horseshoe shape. This comments are conform to the anatomy.

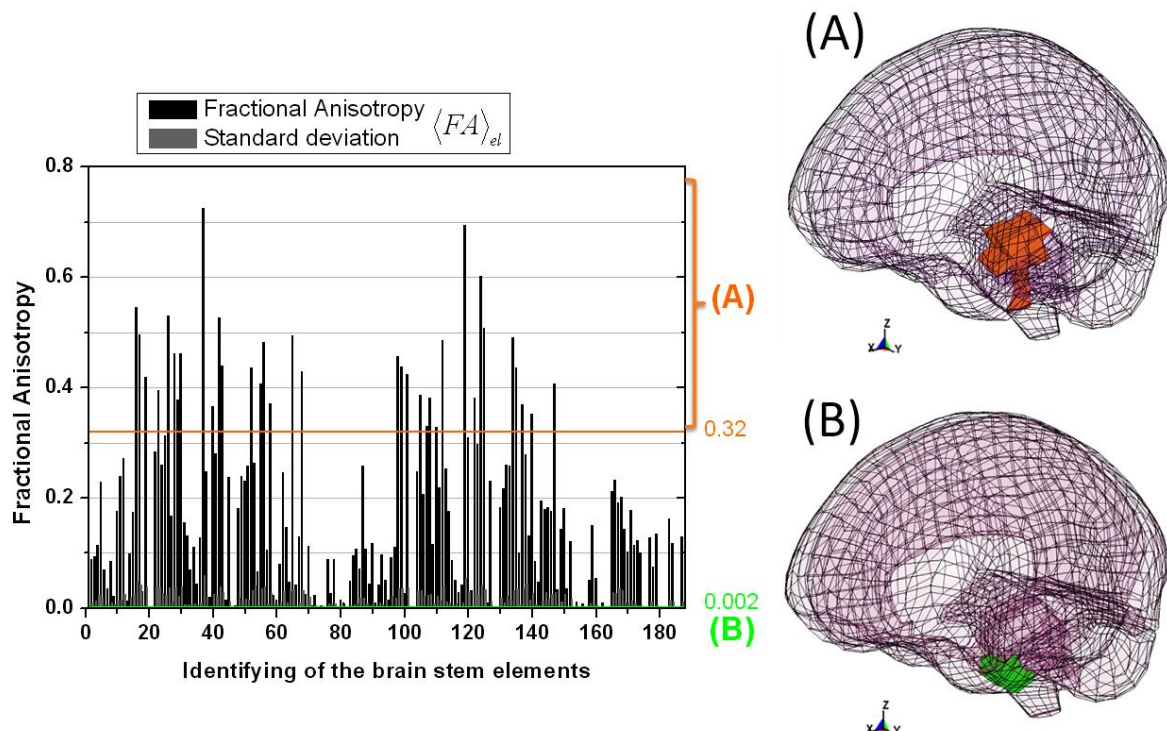


Figure 2- 15. Mean weighted Fractional Anisotropy (FA) values obtained for each of the 188 brain stem elements of the SUFEHM. Values vary as a function of element location in the brain. While maximum FA over 0.32 (18.6 % of the elements) are essentially located along the medulla (A), minimum FA under 0.002 (9.0 % of the elements) are at the periphery of the pons (B).

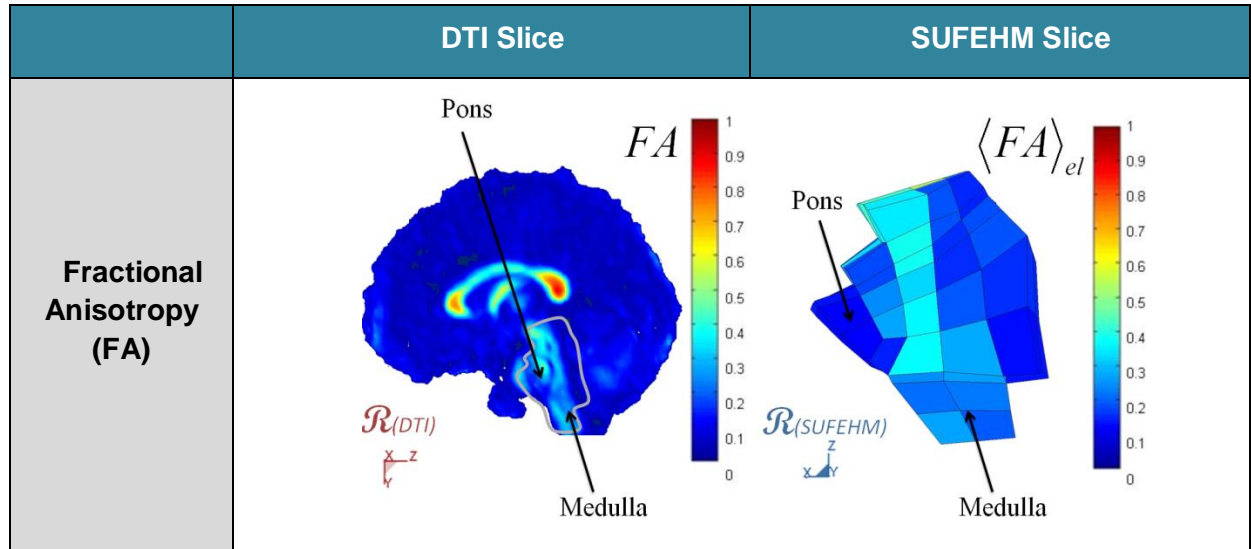


Figure 2- 16. Fractional Anisotropy (FA) values of DTI data and in the brain stem finite element brain model illustrated in a sagittal slice. The diffusion anisotropy for each element is not integrated in the brain stem FE material but is used as a tridimensional map of axons adapted to finite elements dimensions. Highest anisotropy is observed along the medulla.

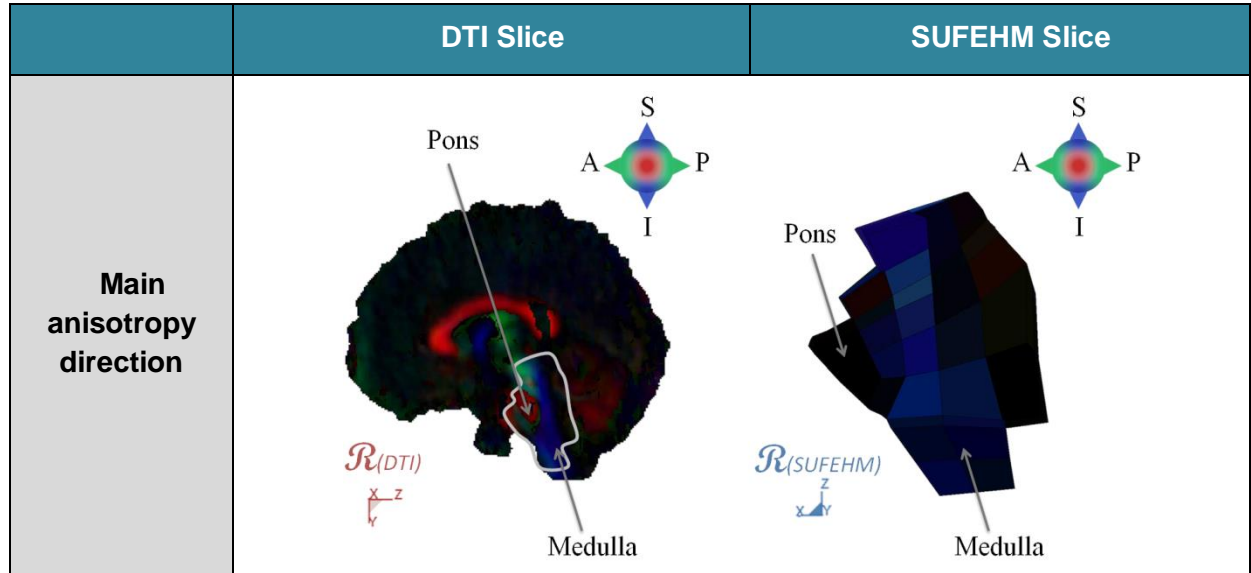


Figure 2- 17. Anisotropy vectors encoded in colors along transverse (red), antero-posterior (green) and vertical (blue) directions for the finite element brain stem model illustrated in a sagittal slice.

4.4 Axonal deformation under impact

According to the above presented methodology, the two real world head impacts are simulated in a classical way with the SUFEHM and results are expressed in terms of axonal elongation. Maximal principal strain ε_I , Von Mises ε_{VM} and axonal ε_{axon} strain values are calculated according the equations (2 - 7) and (2 - 8) for each element and at each time step of the classical numerical simulation performed with homogeneous and isotropic brain material. Only the maximal values for all the time steps are stored and will be noted ε_I , ε_{VM} and ε_{axon} . Finally, for a given simulation, only one maximal principal ε_I , one Von Mises ε_{VM}

and one axonal ε_{axon} maximum strain values are calculated for each of the 5320 brain elements. Results are represented in histograms in Figure 2- 18. For maximal principal, Von Mises and axonal strain, values are significantly higher for case 2, in accordance with its medical report. However, if maximum values are randomly spread out for ε_I and ε_{VM} , they are more located on specific elements when ε_{axon} is concentrated. Variations in time of strains have also to be taken into account to insure that maximum value shown in figure 9 is not only due to an artifact in the modeling process.

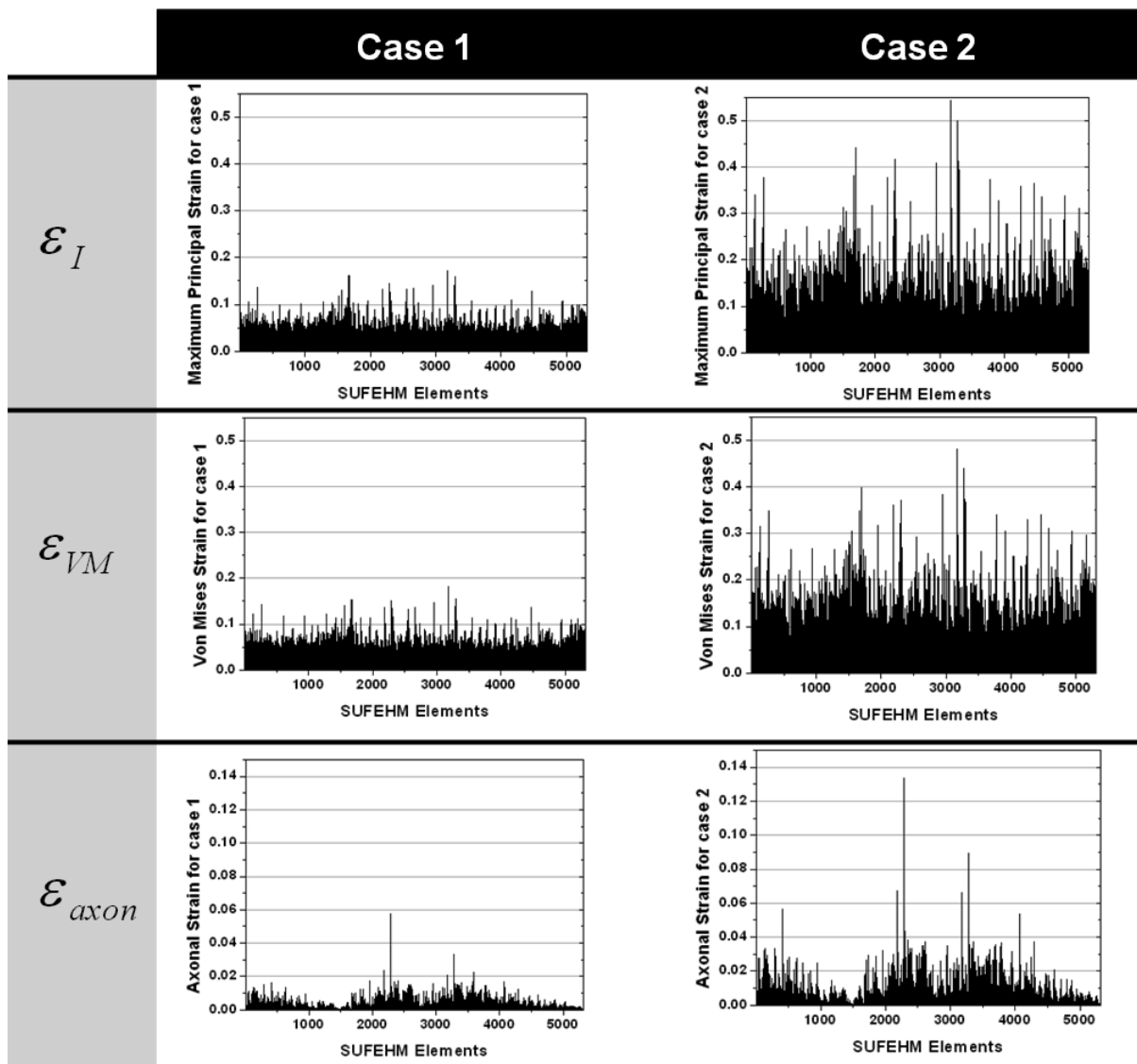


Figure 2- 18. Maximum first principal ε_I , Von Mises ε_{VM} and Axonal ε_{Axon} strain values obtained during the simulation and for each brain element for the two considered head impact cases.

Figure 10 proposes a representation of results focusing on ε_{axon} by representing six sagittal cuts of the cerebral hemisphere. Maximum axonal strain values are mainly located in the *corona radiata*, in the *corpus callosum* and all around the brain stem. In terms of maximum values, a same trend between cases 1 and 2 can be underlined concerning the maximum strain values for all the elements as shown in table 4. If it is obvious that case 2 presents higher values than case 1, it should be mentioned that maximum axonal elongations are significantly lower than maximum first principal and Von Mises strains.

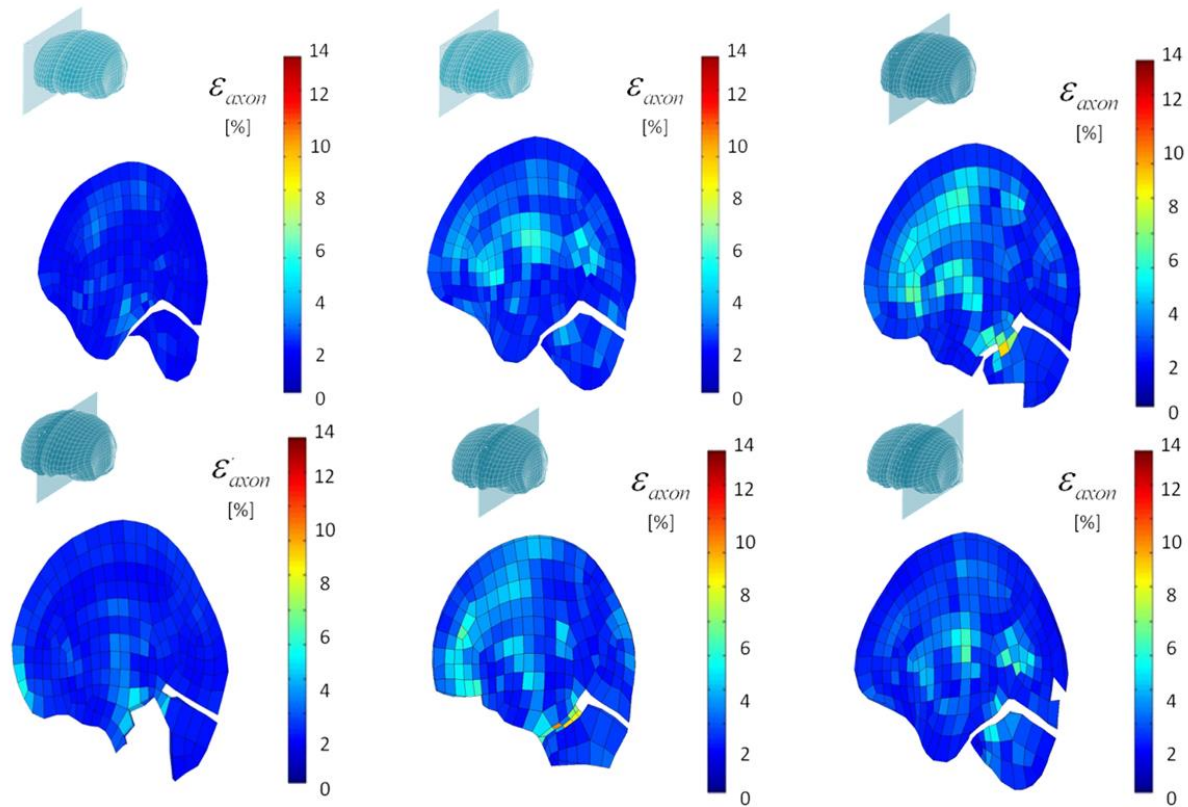


Figure 2- 19. Axonal strain values obtained into the brain for impact case 2. Results are presented through six sagittal cuts from an external to a median cut (from Up-Left to Down-Right). Highest values are located in the corona radiata, in the corpus callosum and all around the brain stem.

	$\max(\varepsilon_1)$ [%]	$\max(\varepsilon_{VM})$ [%]	$\max(\varepsilon_{Axon})$ [%]
Case 1	17.17	18.14	5.77
Case 2	54.42	48.05	13.32

Table 2 - 7. Maximal first principal, Von Mises and Axonal strain values obtained during all the simulation and for the brain elements for the two considered head trauma cases reconstructed using homogeneous and isotropic brain material.

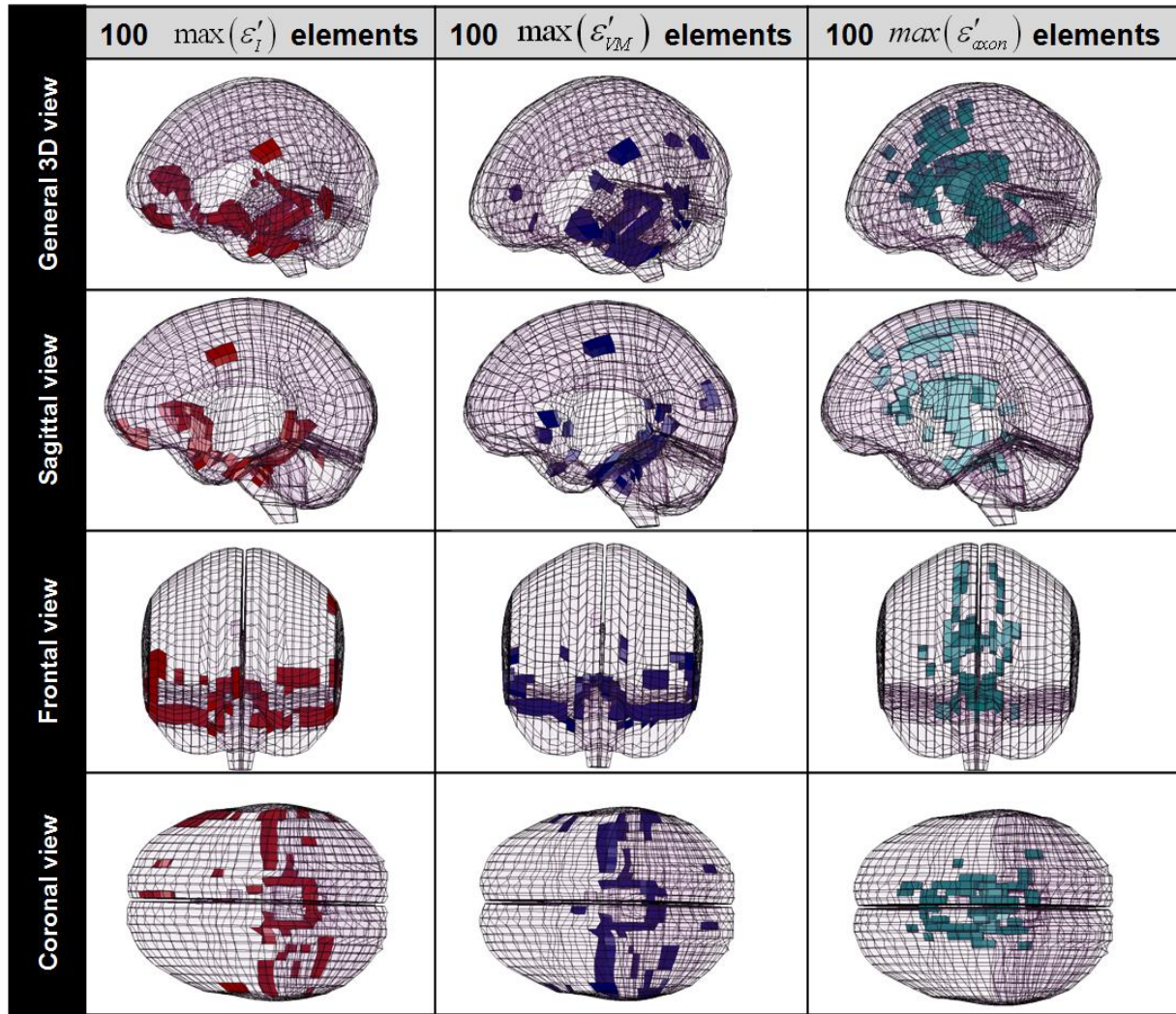


Figure 2- 20. Comparison of the 100 elements presenting maximal first principal ε_I , Von Mises ε_{VM} and axonal ε_{Axon} strain values obtained from the simulation of case 1 (severe DAI). Results are presented in a global view and in three different views: sagittal, frontal and Coronal.

Figure 2- 21 shows arbitrarily 1.9 % of the brain elements (100 elements) presenting the maximum first principal strain (ε_I , left column), Von Mises strain (ε_{VM} , middle column) and axonal strain (ε_{axon} , right column) values for case 2. Results are presented in a 3D view as well as in a sagittal, frontal and coronal plane. It permits to visualize elements sustaining the highest DAI risk. All these 100 elements have an axonal strain value over 2.8 %. While highest first principal and Von Mises strain values, that do not take axonal direction into account, concern exclusively elements located in brain periphery, axonal strain values bring elements to light, which are located in commonly injured area, in accordance with previously related epidemiological studies. These elements are essentially located in the middle of the white matter and along the main axonal fibers of the brain, i.e. in the *corpus callosum*, the *cingulum*, the superior longitudinal fascia between the occipital and frontal lobes and on the

brain stem. Same observations concerning maxima location can be done for case 1 with lower strain values.

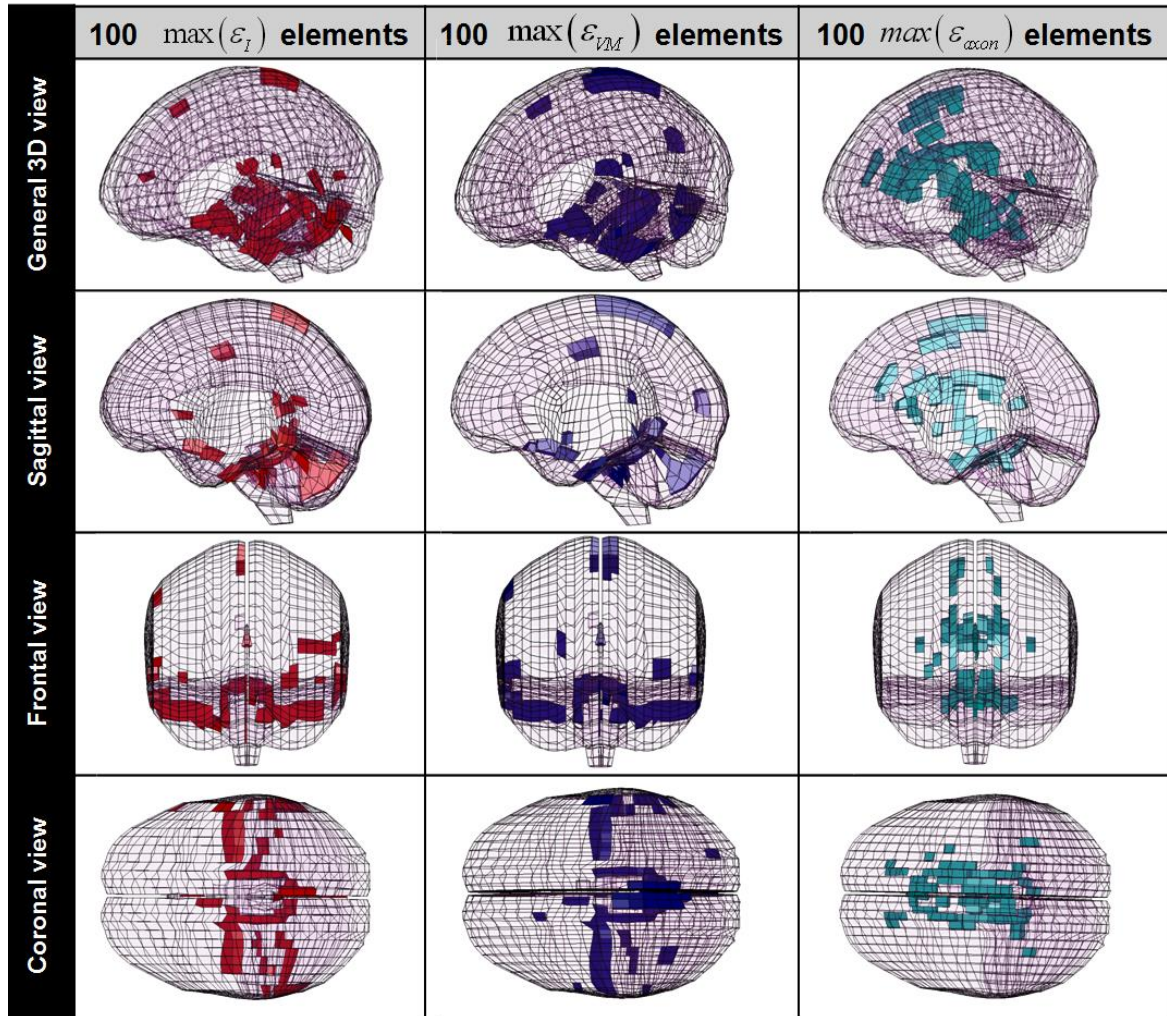


Figure 2- 21. Comparison of the 100 elements presenting maximal first principal ε_I , Von Mises ε_{VM} and axonal ε_{Axon} strain values obtained from the simulation of case 2 (severe DAI). Results are presented in a global view and in three different views: sagittal, frontal and Coronal.

All along the simulations, stability of the model was investigated. For each of the numerical simulations, hourglass, internal and kinetic energies were registered. Hourglass energy was survey to be always less than five percent of the total energy of the model. Elements with most skew in warpage were identified during each of the simulations. Results show that none of these elements correspond to the most strained elements.

By considering the 100 elements selected in Figure 2- 21, their mean values in terms of ε_I , ε_{VM} and ε_{axon} respectively are 0.105 ± 0.017 , 0.105 ± 0.017 , 0.105 ± 0.017 for case 1 and 0.105 ± 0.017 , 0.105 ± 0.017 , 0.105 ± 0.017 for case 2. First observation can be made on standard deviation. While mean on the 100 maximal values varies for ε_I and ε_{VM} from 16%

to 22%, it is about 33% to 40% for ε_{axon} . It leads to conclude to a larger disparity of results with axonal strain. Then this aspect is reinforced by comparison between maximum (in table 4) and mean on the 100 maximal ε_I , ε_{VM} and ε_{axon} values. While maximum values are 1.6 to 1.9 times than mean values on the 100 maximal values for ε_I and ε_{VM} , this difference increase to 3.8 times for ε_{axon} . It contributes to reinforce the assumption that axonal strain increases significantly the disparities between highly and few deformed elements. Last observation concerns magnitude of maximal values. Maximum strain values are 3 to 4 times lower and mean strain values on the 100 maxima are 7 to 8 times lower for ε_{axon} than for ε_I and ε_{VM} . This observation can be explained by two parameters: projection of strain along a direction and FA value between 0 and 1 decreases automatically axonal strain value.

5 Discussion

Discussion of the present paper involves different levels such as the implementation of axonal direction into the FEM which is the bases of axonal elongation computation; then the interest and limitation of considering axonal elongation as a candidate parameter for DAI prediction; or the bases of the preserved head trauma simulation.

Investigating the number of selected DTI voxels for each of the finite elements shows that on average 899 and 70 to 4096 voxels are selected by element, according to Figure 2- 8.

The main problematic appears with finite elements selecting no or not enough DTI voxels of the brain to be considered as significant. These point results directly from the rigid transformation that could involve errors in scaling the FEM on the DTI brain shape data. At least, results show that only 6 elements (i.e. 0.11 % of the elements) select individually less than 100 DTI voxels. They are essentially located close to the membranes and are relatively thin elements. This aspect contributes to validate the morphological rigid adaptation between DTI and FEM geometry without need to take non-rigid transformation into account. On the other hand, the high numbers of selected voxels per element led to the necessity of weighting diffusion parameters of the selected voxels as a function of its distance to the center of the element. The influence of diffusion parameters related to the voxels close to the edges of the element is decreased. From this protocol, two main observations can be made. The first one constitutes a limit case. If an element presents in its center diffusion parameters locally different than in all the rest of the area, the diffusion parameters influence of these concentrated voxels will be significantly and maybe excessively increased. Since DAI appears in the most anisotropic parts of the brain, it would yet not affect the efficiency of the

method proposed in this study for DAI prediction. The second aspect involved by such a voxel mean diffusion parameters calculation is a smoothing of diffusion parameters values between elements. This is particularly notable in FA map comparison between DTI and FEM in Figure 2- 11. Weighting to the center of the element attenuates this smoothing. It appears that essentially main contrasts zone are therefore conserved, for instance at the interface between white and grey matter or at the *claustrum*, sections with the higher DAI risk according to the epidemiological literature.

Another critical aspect consists in the scaling from DTI voxels (1 by 1 by 1 mm of resolution) to the finite element brain model (element characteristic size from 1.14 to 7.73 mm). Indeed a scaling leads systematically to a loose of information. This observation is valid all the more so DTI constitutes itself a scaling from axons (characteristic size about 10 μm) to voxels size. Local thinner meshing of FEM geometry would be possible to get closer to DTI dimensions for the most heterogeneous parts of the brain. However it would not be possible with the existing DTI data to access to a small enough meshing at the axon size for the whole brain. Nevertheless only the mean diffusion parameters seem to be satisfying to obtain a realistic orientation and an anatomical anisotropy degree for each of the finite elements. This aspect is confirmed by the comparison between DTI pictures and SUFEM values in terms of FA values and normalized anisotropy vector projections along main brain axes, as shown in Figure 2- 11 and Figure 2- 13. Even if model used in this study was already validated, changes in meshing size could influence strain calculation. Further developments of this work could consist in investigating meshing influence on diffusion parameters calculation.

Changes in the FE model meshing could also affect its robustness. As for most of the existing and validated head FE models, the effect of different mesh densities on strain results was not evaluated. Even if it seems that all models can reproduce experimental results even if meshing density was totally different, according to Deck and Willinger (2009), this step would be fundamental for further development of this study.

By computing axonal elongation after the FE simulation of head impact, it was possible, with the developed method, to evaluate the influence of structural anisotropy in DAI prediction. Comparison between maximal principal and Von Mises strain, actually currently used as injury criteria, and new proposed axonal strain, characteristic for axon elongation and axonal fiber density, put in light the efficiency of axonal strain for DAI prediction. Anisotropy was not implemented for anisotropic FEM simulation due to the today difficulty to obtain from in vivo experimental protocols enough accurate mechanical parameters for brain material both, in terms of heterogeneity (white vs. gray matter) and in terms of anisotropy

(longitudinal and transverse behavior). According to further development in this domain, it could constitute one of the next developments of the method proposed in this study as long as new relevant mechanical parameters are identified. As shown in Figure 2- 20 and Figure 2- 21 for the severely injured case, axonal strain is first of all efficient for DAI location. Elements notified by first principal as well as Von Mises strains are essentially located in the cerebral cortex, which does not represent common location of DAI, according to the epidemiological studies. Location of the elements with the highest axonal strain values correspond to the most important axonal fibers of white matter and agreed with the epidemiological studies. These locations are in good agreement with results of a clinical study proposed by Gentry *et al.* (1988) and with DAI locations listed from various epidemiological studies in the introduction of this study. Figure 2- 22 illustrates main DAI locations listed in various epidemiological studies (Gennarelli *et al.*, 1982; Gentry *et al.*, 1988; Ng *et al.*, 1994; Graham and Gennarelli, 1997; Arfanakis *et al.*, 2002) compared with axonal strain locations. Axonal injuries are represented on the brain slices by stars.

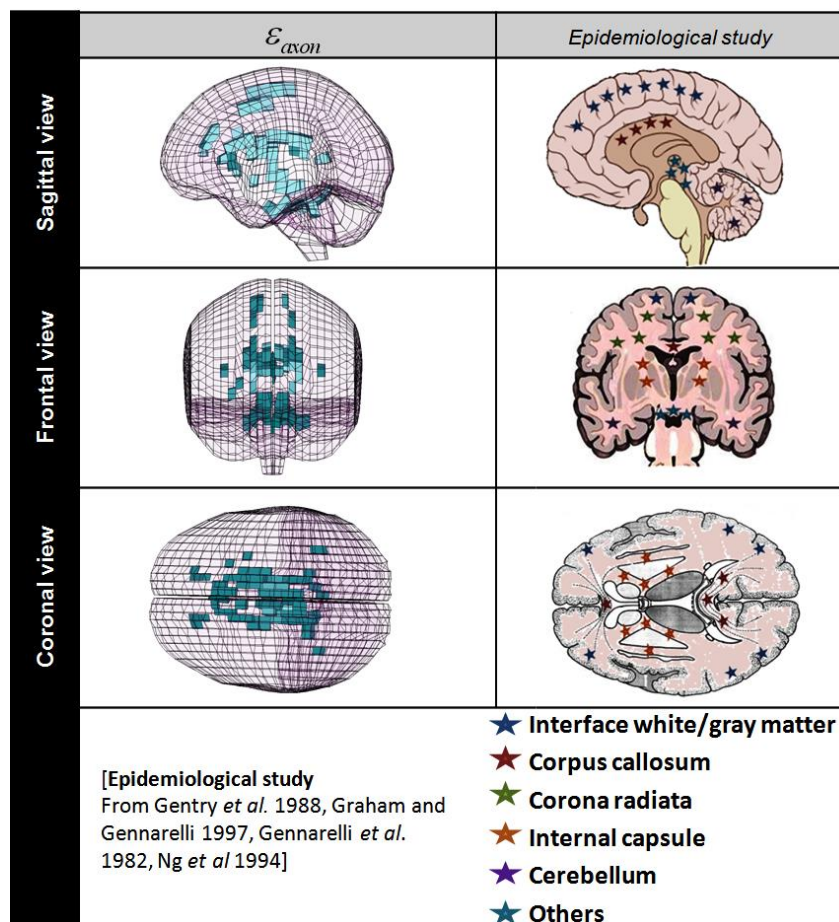


Figure 2- 22. Comparison in terms of location between the 100 elements (2 %) with the highest axonal strain values and the most common DAI regions.

In the here presented results, some elements, all around the upper part of the brainstem, are common to the maximum first principal, Von Mises and axonal strain selection. For these

reasons, concerning locations and at the opposite of maximum first principal and Von Mises strain elements, maximum axonal strain elements are in good agreement for DAI location prediction. On top of that, the fact that not all the parts of brain with high values results in high axonal deformation lead to consider that this parameter is able to take the axons elongation as much as the fiber density into account. Axonal strain seems to be consistent with DAI mechanism, in contrast to previously proposed DAI metrics. Indeed maximal principal strain and Von Mises give relatively few different results one from the other without seeming to correlate DAI physics during accident numerical reconstruction.

Moreover, axonal strain seems not only to be efficient to determine DAI location, but also as DAI predictor. The two cases are presented only as illustration. Even if this study contributes to consider axons tensile elongation as a possible brain injury metric for DAI prediction, it does not allow proposing threshold values as DAI criterion at this stage. To evaluate the capability of axonal strain to become a DAI predictor criterion, a statistical study should be extended to a significant number of head trauma simulations including a detailed description of DAI location. However, this work proposes a new tool to compute anatomical parameters with a head FEM as special dedicated post-processor permits to take into account the structural anisotropy into the FEM. It makes it possible to couple classical finite element simulation with axonal structure anisotropy in order to address axonal elongation under head impact. Next perspective for this study could consist in integrating the diffusion anisotropy map in the brain material. Uniaxial composite laws that take fiber ratio into account could be investigated for each finite element. Structural anisotropy would also be directly integrated in the FE model as mechanical anisotropy.

6 FA influence on post-computing

Axonal strain ε_{axon} previously presented takes in the same time the anisotropy direction and the fractional anisotropy (FA) coefficient into account. The objective of this part is to evaluate the influence of FA coefficient in axonal deformation calculation. Aim is to ensure that results showed in Figure 2- 22 are not only a FA map illustration.

A new axonal strain, noted ε'_{axon} , is calculated in this part. This new value is defined in equation (2 - 12) and does not take FA value into account. It is only a projection of strain along anisotropy direction.

$$\varepsilon'_{axon} = \left(\varepsilon \times \frac{\langle \vec{l} \rangle_{el}}{\langle FA \rangle_{el}} \right) \cdot \frac{\langle \vec{l} \rangle_{el}}{\langle FA \rangle_{el}} \quad (2 - 12)$$

Results on the two accident reconstructions are presented in terms of maximum ϵ'_{axon} values in Table 2 - 8.

$\max(\epsilon_{VM}/FA) [\%]$	
Cas 1	13.9
Cas 2	31.5

Table 2 - 8. Valeurs maximales d'élongation axonale obtenues pour l'ensemble du cerveau sur les deux cas d'accidents motocyclistes reconstruits avec le SUFEHM. Le modèle possède un cerveau isotrope et l'anisotropie de diffusion n'est intégrée qu'en post-traitement des résultats de simulation

Same trend is significant for both simulations: ϵ'_{axon} values correspond to ϵ_{axon} values multiplied by a factor between 36 and 4 for each of the 5320 brain finite element. It confirms that results in terms of ϵ_{axon} are not only due to FA distribution but is first due to strain projection along main anisotropy direction.

Maximal values in Table 2 - 8 shows significantly different values between cases 1 and 2. ϵ'_{axon} are 3 times higher than ϵ_{axon} , in accordance with previous observations. Otherwise maximum ϵ'_{axon} values of 16.5% and 51.84% for cases 1 and 2 respectively are very close to maximum principal strain values presented in Table 2 - 7 (17.17% and 54.52% for cases 1 and 2 respectively). These similarities show that maximal strains are oriented along a direction which is very close to anisotropy direction.

Locations of the 100 elements with highest ϵ_{axon} and ϵ'_{axon} are presented in Figure 2- 23 for the accident case 2. Comparison is made with most common DAI locations in accordance with the epidemiological study. Following observations can be done:

- In sagittal view, elements from the claustrum and located at the interface between brain and brain stem are highlighted. While maximum ϵ_{axon} elements are located in the superior longitudinal fasciculus and the internal capsule, maximum ϵ'_{axon} elements highlight not only the cerebellum but also about 20 element in the cortical gray matter;
- In frontal view, maximum ϵ_{axon} are located in the corpus callosum, at the interface brain and brain stem and all along the internal capsule. ϵ'_{axon} are located at the interface between brain, brain stem and cerebellum;
- In coronal view, both strains highlight corpus callosum.

These locations reinforce the assumption of structural anisotropy influence on brain tissue mechanical anisotropy and DAI appearance. However ϵ'_{axon} (that takes not FA value into account) does not allow to remove a part of the elements with low FA value when subjected to high strains. FA inclusion in axonal strain ϵ_{axon} makes it possible to conserve locations from

ε'_{axon} by removing low anisotropy parts. Indeed ε_{axon} distribution highlight common DAI location parts of the brain by coupling in the same time fibers density and orientation.

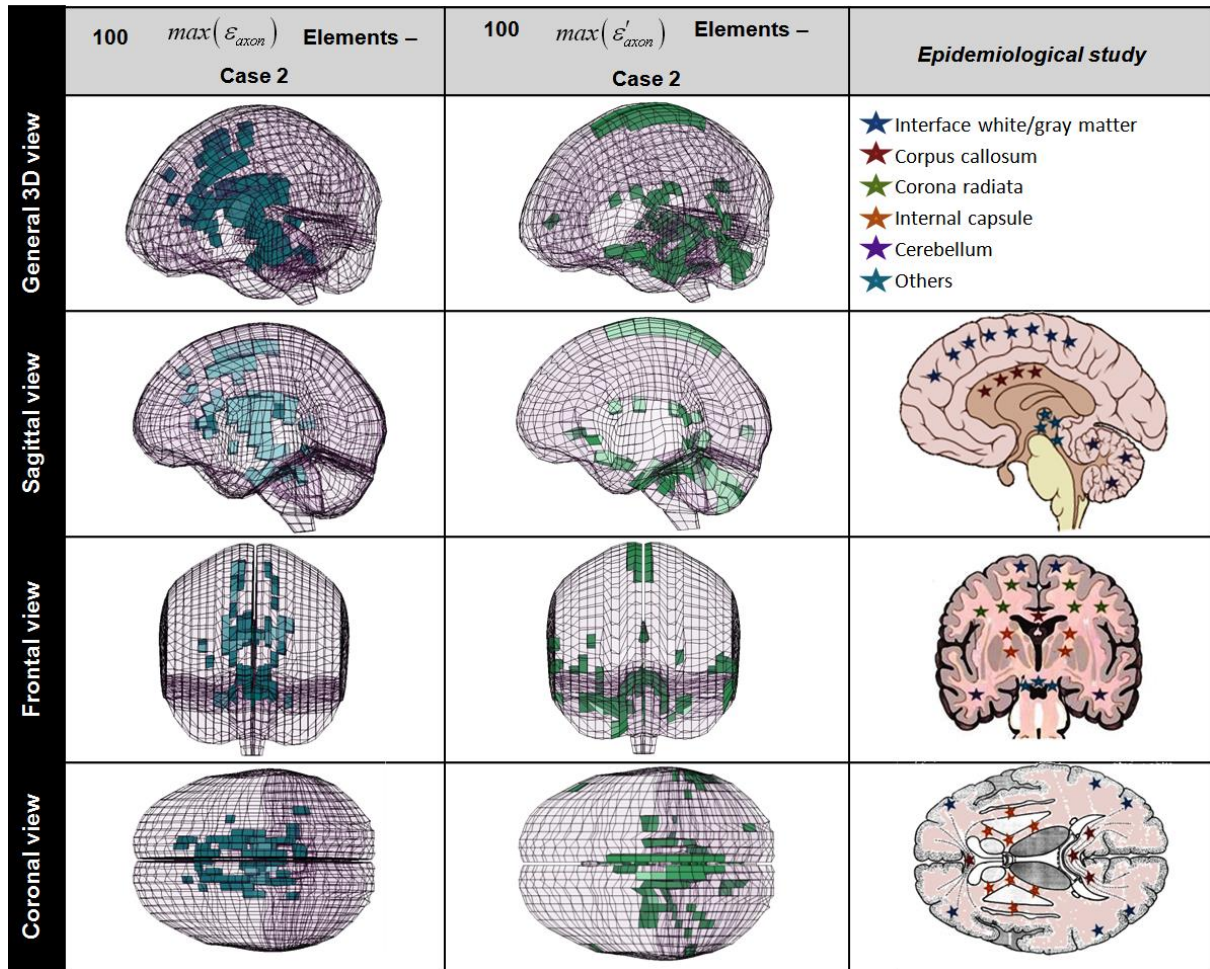


Figure 2- 23. Comparison of the 100 elements (2 %) presenting the highest axonal elongation values for the case 1 (left column) and the case 2 (central column). Results are presented in a global view and in three different views: sagittal, frontal and Coronal. They are compared with common DAI locations coming from epidemiological study (Right column).

7 Conclusion

In this paper a methodology is presented which permits it to compute axonal elongation in case of head impact based on head FE simulation and axons direction determined by medical imaging technique. A twelve healthy patients-based DTI database was integrated into the finite element brain meshing. The brain response in terms of stress and strain tensor with a classical isotropic finite element approach was then calculated and used for the elongation computation along the above defined “axonal direction” in each element.

The approach based on the computation of this novel injury metric has finally been applied to the simulation of two real world head trauma for a demonstrative purpose. Results in terms of location and maximum axonal elongation contribute to validate the assumption of axons

elongation as main cause of DAI as elements sustaining maximum axonal strain are located where this injury is typically observed. This study has demonstrated the feasibility of implementing in a realistic way anisotropic brain structure into an existing brain finite element model. It constitutes an easily implemented post-processing tool for existing isotropic head FEM. In a next step a number of well documented real world head trauma simulations will permit the development of a threshold for this new metric of DAI.

Further development of this study could concern also anisotropic and heterogeneous brain constitutive laws implementation for the brain FEM as soon as relevant parameters can be established in the future. Indeed this study initiates innovative and promising possibilities to improve biofidelity of finite element simulations and thus to extract more realistic injury criteria for DAI.

CHAPTER 3

Isotropic heterogeneous modeling of brain tissue

1 Introduction

Most of the brain Finite Element Models (FEM) proposed in the literature have homogeneous mechanical laws identified from *in vitro* brain tissue experiments. However bibliographic study on brain tissue experiments in the first chapter has highlighted significant heterogeneities. For instance white matter is 2.6 times stiffer than gray matter (Kruse *et al.*, 2007) and white matter from corona radiata 30% stiffer than corpus callosum (Prange *et al.*, 2000). These disparities are not taken into account into the existing brain FEM. At the very most, white matter is dissociated from gray matter. The assumption of homogeneity in the model does not allow predicting injuries location within the brain with classical parameters (Von Mises stress, strain, maximal principal strain and pressure).

This chapter aims at including heterogeneity into the brain FEM. The here developed methodology is exposed in Figure 3 - 1. Only the protocol, main results and conclusions are presented in this version. The reader can refer to the French version for more details about this work.

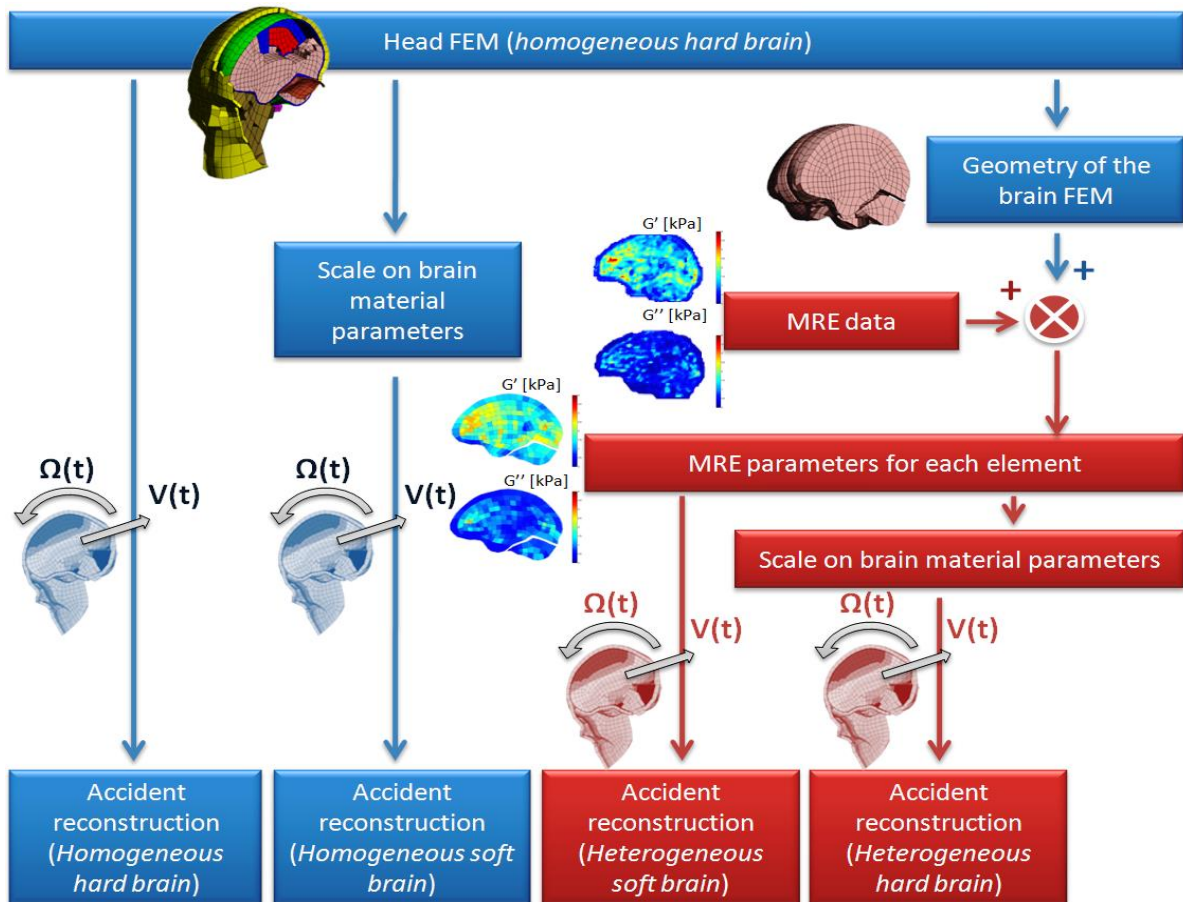


Figure 3 - 1. Illustration of the protocol developed in this chapter. Heterogeneity and stiffness are evaluated using four different brain models. While parts with a homogeneous model are shown in blue, parts including heterogeneity are illustrated in red.

In a first time a heterogeneous brain tissue law will be developed from a three dimensional *in vivo* map of viscoelasticity and included into the SUFEHM brain geometry. Next step will consist in studying brain tissue heterogeneity influence on accident reconstructions in function of brain stiffness. Simulations on four different brains FEM will be analyzed:

- A stiff homogeneous brain FEM (SUFEHM in its actual version);
- A soft heterogeneous brain FEM (corresponding to the MRE 3D map);
- A soft homogeneous brain FEM;
- A stiff homogeneous brain FEM (obtained by rigidifying the MRE 3D map).

Results are analyzed in terms of stress, pressure and strain to evaluate the heterogeneity influence in the brain FEM.

2 Heterogeneity inclusion in brain FEM

2.1 Introduction

Brain FEM used in this study is the SUFEHM presented in chapter 2. This model has a homogeneous isotropic viscoelastic law identified on *in vitro* experiments (Shuck and Advani, 1972). Objective of this chapter is not only to identify parameters based on *in vivo* experiments but also to include the anisotropy into the brain FEM. As presented in the chapter 1, Magnetic Resonance Elastography (MRE) is the only one experimental modality which can correspond to both characteristics. In the framework of collaboration with the INSERM Paris, tridimensional viscoelastic MRE data have been obtained and used in order to identify a viscoelastic law proper to each of the 5320 elements of the brain FEM.

2.2 Experimental brain MRE data

MRE data have been provided by the INSERM Paris from a single healthy volunteer (39 years old). Values are obtained at 50Hz. At least two three dimensional (96 x 96 x 43) maps (one for the storage modulus G' , one for the loss modulus G'') have been used with 3 x 3 x 3mm resolution.

2.3 Heterogeneous viscoelastic law

2.3.1 Introduction

The aim of this part is to integrate the MRE data into the geometry of the brain FEM (SUFEHM). First step consists in determining only one storage and one loss modulus from

MRE data for each of the 5320 brain elements. Then a viscoelastic model proper to each of the elements is proposed and integrated into the FEM.

2.3.2 Scaling of the MEF on the MRE data

Correspondence between DTI data and the brain FEM involves a fitting between imaging (MRE) and numerical (SUFEHM) extern geometries. This was performed using rigid transformations (matrix in (2 - 2), i.e. only rotation and translation, with a linear scaling of all the nodes from the SUFEHM. It permitted to fit the finite elements outlines to the twelve patients-based DTI mask. The correspondence between DTI voxels and the FEM has been performed using the Matlab 7.4 software (The Mathworks, Inc., Natick, MA, USA). This step is illustrated in Figure 3 - 2.

$$\underbrace{\begin{pmatrix} X_{\mathfrak{R}(ERM)} \\ Y_{\mathfrak{R}(ERM)} \\ Z_{\mathfrak{R}(ERM)} \end{pmatrix}}_{\text{Coordinates in MRE frame}} = \underbrace{\begin{pmatrix} 0,38 & 0 & 0 \\ 0 & 0,36 & 0 \\ 0 & 0 & 0,29 \end{pmatrix}}_{\text{Scale factor}} \times \underbrace{\begin{pmatrix} 1 & 0 & 0 \\ 0 & 1 & 0 \\ 0 & 0 & 1 \end{pmatrix}}_{\text{Rotation}} \times \underbrace{\begin{pmatrix} X_{\mathfrak{R}(SUFEHM)} \\ Y_{\mathfrak{R}(SUFEHM)} \\ Z_{\mathfrak{R}(SUFEHM)} \end{pmatrix}}_{\text{Coordinates in FEM frame}} + \underbrace{\begin{pmatrix} 32,49 \\ 25,49 \\ 17,28 \end{pmatrix}}_{\text{Translation}} \quad (3 - 1)$$

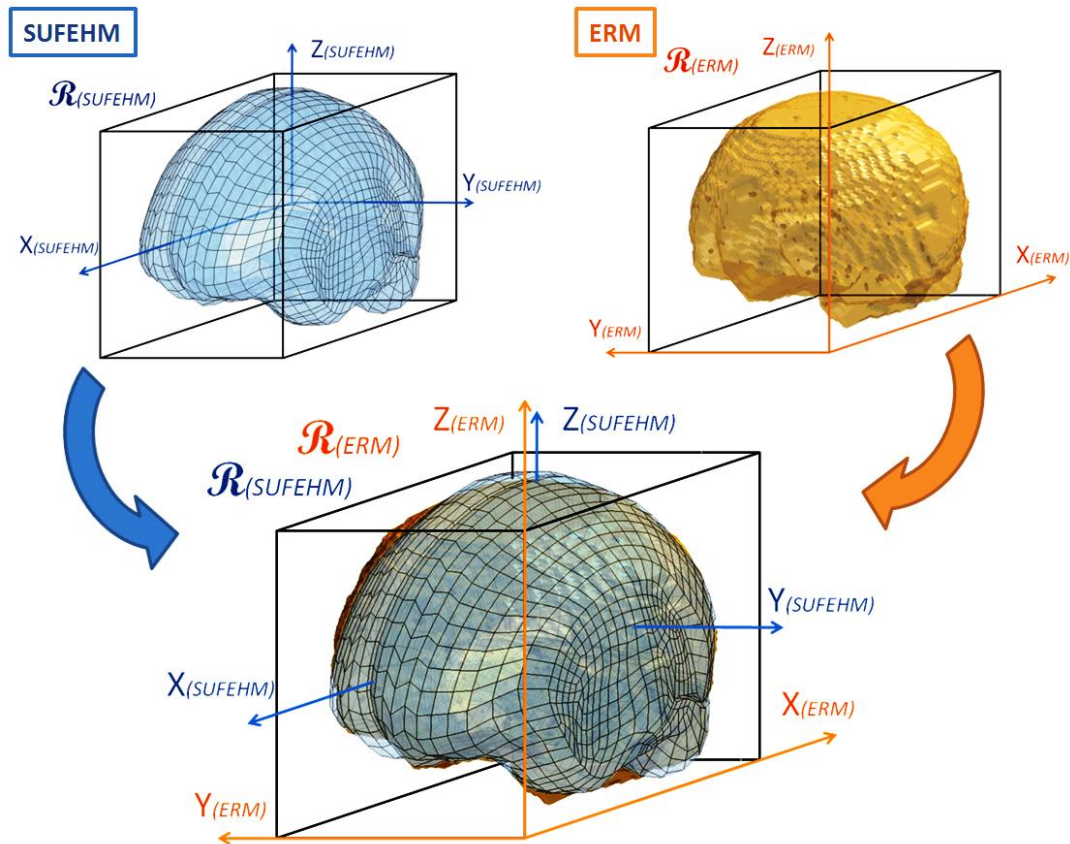


Figure 3 - 2. Rigid transformation application to ensure correspondence between extern geometries (mask) of MRE data (in orange) and brain FEM (in blue), with associated frames.

To implement information from the tridimensional diffusion image into the FEM, the next step consists in selecting voxels from DTI for each element. While DTI brain are brought into line with a regular plan-parallel meshing characterized by 1 by 1 by 1 mm voxel size, elements have different local orientation with a characteristic element size from 1.14 to 7.73 mm. To compensate this difference in resolution, the voxels included into the smallest parallelepiped lined with the regular DTI meshing and incorporating the considered finite element are selected for each element, as illustrated in Figure 3 - 3.

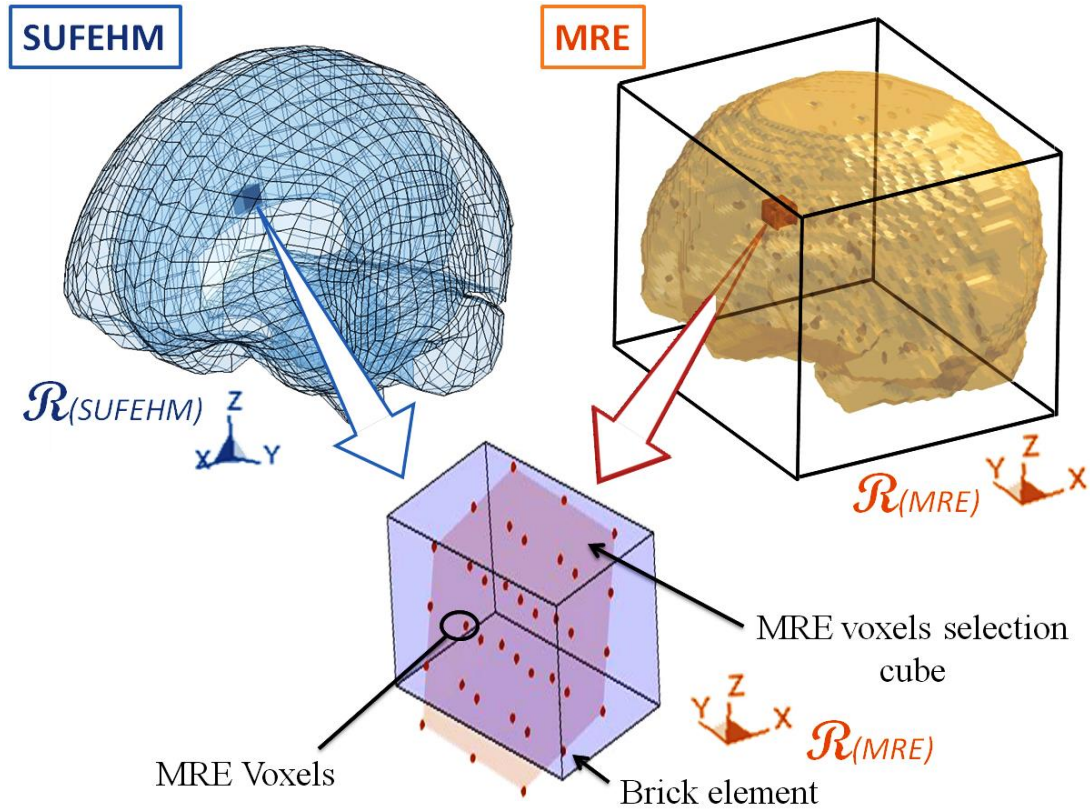


Figure 3 - 3. Illustration of the correspondence between the SUFEHM and the MRE 3D picture on a single element. Selected voxels (red points) are all included into the smallest cube (red) including the finite element (blue parallelepiped).

The method of correspondence between finite elements and MRE voxels leads to consider from 2 to 168 voxels for each of the 5320 brain finite elements with a mean number of voxel selected for each finite element of 31 ± 17 . At least 1.1 % of the finite elements include less than 4 voxels. At the opposite 0.7 % of the elements are linked with more than 100 voxels as shown in Figure 3 - 4.

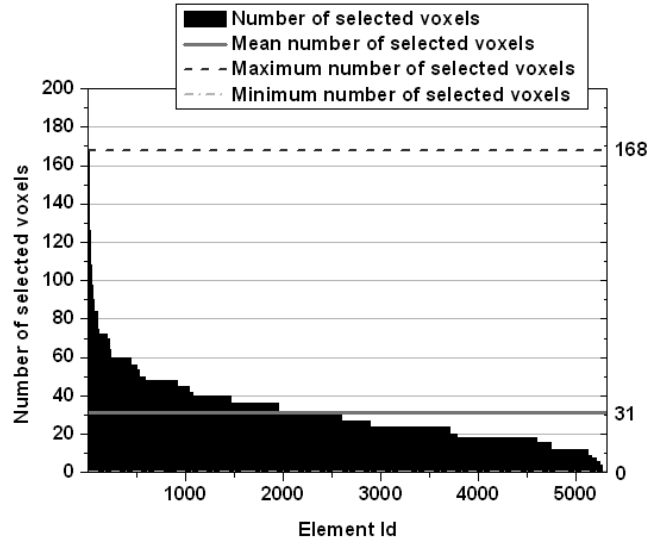


Figure 3 - 4. Number of MRE voxels selected for each of the 5320 elements of the SUFEHM. Each element is characterized by considering from 2 to 168 voxels.

2.3.3 Viscoelastic parameters calculation

For each element, one storage and one loss modulus are calculated as the mean values of all the selected voxels. In order to reinforce the diffusion parameters influence close to the center of the element, these are weighted by the distance D (center of the element to center of the voxel). The half length of the element diagonal is noted L_e .

$$\langle G' \rangle_{el} = \frac{\sum_{i=1}^N G'_i e^{-D_i/L_{el}}}{\sum_{i=1}^N e^{-D_i/L_{el}}} \quad (3 - 2)$$

$$\langle G'' \rangle_{el} = \frac{\sum_{i=1}^N G''_i e^{-D_i/L_{el}}}{\sum_{i=1}^N e^{-D_i/L_{el}}} \quad (3 - 3)$$

N is the number of selected voxels, G'_i , G''_i and D_i the storage modulus, the loss modulus and the distance from the center of the element to the voxel respectively for each selected voxel.

Shear, storage and loss moduli values obtained for each of the 5320 brain finite elements are presented in Figure 3 - 5. The mean values for these three parameters are $1,47 \pm 0,62$ kPa, $1,35 \pm 0,56$ kPa et $0,54 \pm 0,32$ kPa respectively. These mean values are close to values proposed *in vitro* using DMA by Thibault and Margulies (1998) or *in vivo* using ERM by Sack *et al.* (2007).

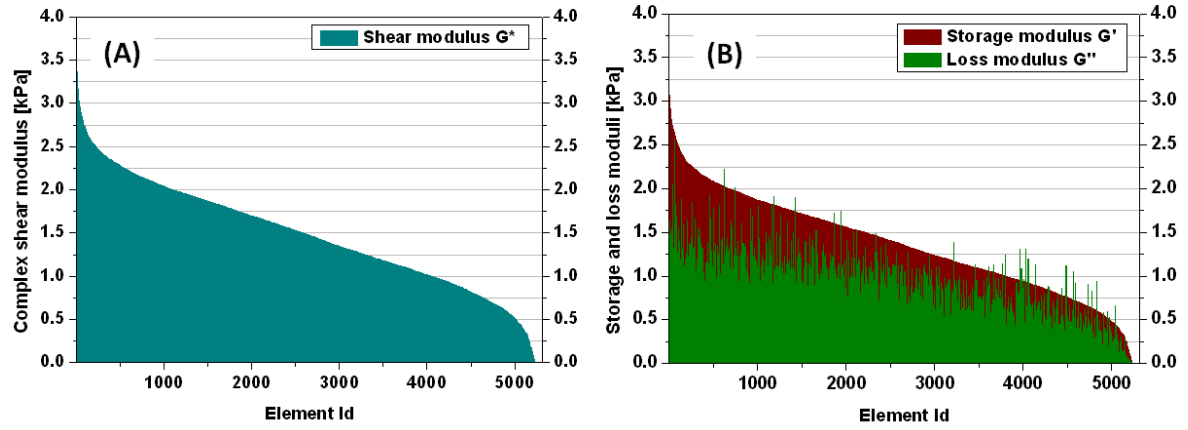


Figure 3 - 5. Shear, storage and loss moduli calculated for each of the 5320 elements of the brain FEM.

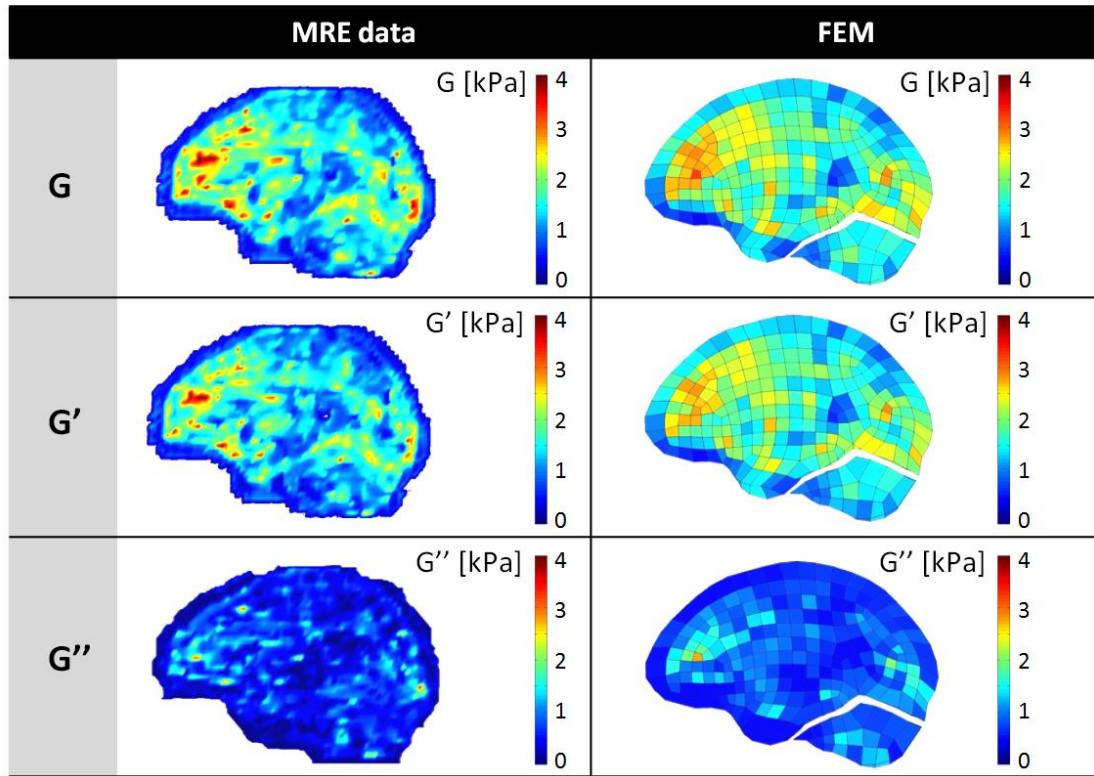


Figure 3 - 6. Comparison on a sagittal slice between MRE (left) and SUFEHM (right) data for G^* , G' , G'' .

Calculation and location of relative error and 3D correlation coefficient between MRE data and calculated moduli for the SUFEHM has been performed. Error values contribute to validate our method.

2.3.4 Heterogeneous linear viscoelastic model

For each element un first order Generalized Maxwell model is calculated from the G' and G'' using equations (3 - 4) et (3 - 5) where G_0 , G_∞ and β are the model parameters and $\omega = 2\pi f$ the pulsation for a frequency f of 50 Hz. Obtained values are shown on a sagittal slice in Figure 3 - 7, element with maximal values are shown in Figure 3 - 8. Because MRE data are available at only one frequency, β values are the same for the whole brain model.

$$G_0 = G'(\omega) + \beta \frac{G''(\omega)}{\omega} \quad (3 - 4)$$

$$G_\infty = G'(\omega) - \omega \frac{G''(\omega)}{\beta} \quad (3 - 5)$$

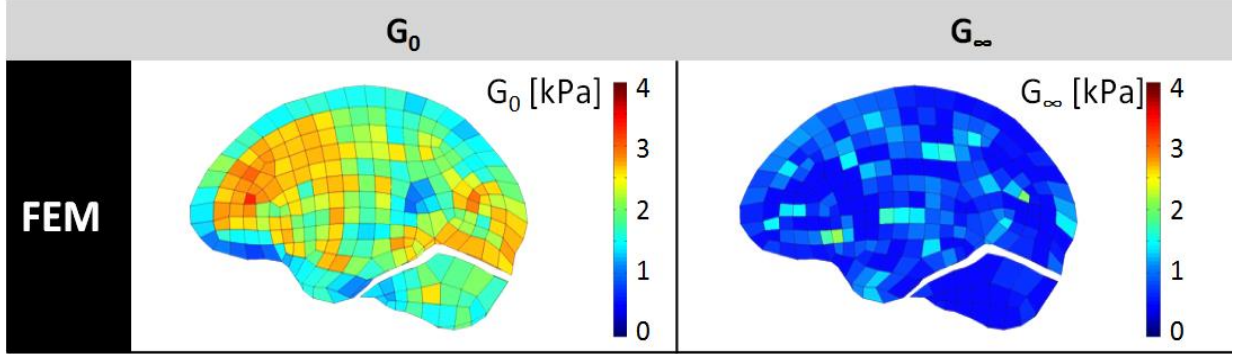


Figure 3 - 7. Comparison on a sagittal slice between MRE (left) and SUFEHM (right) data for G_0 and G_∞ .

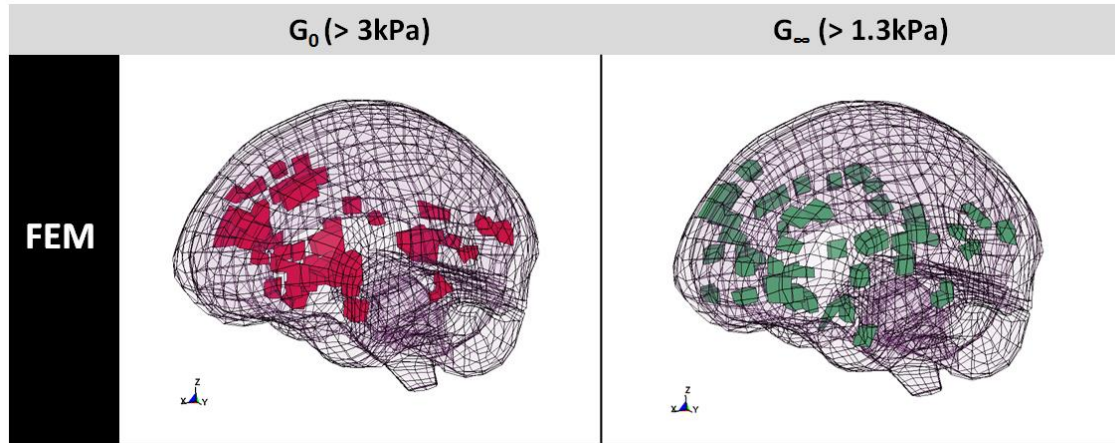


Figure 3 - 8. Maximal G_0 (> 3 kPa, 1.6 % of the elements) and G_∞ (>1.3 kPa, 1.4 % of the elements).

These values are implemented into the brain FEM using LS-DYNA® software.

2.3.5 Conclusion

Each element of the brain has now a particular value of G_0 , G_∞ and β .

2.4 Conclusion

We have developed in this part a complete heterogeneous model with a mean shear modulus of 1.47kPa. This model will be named “MRE FE model” in the next parts.

3 Application to accident simulation

3.1 Introduction

We propose in this part to illustrate the modifying induced by heterogeneity of the brain FEM on two accident cases. Comparison is done between homogeneous and heterogeneous models with the same mean rigidity values. This comparison is done with stiff and soft models.

3.2 Brain Finite Element Models

The following models have been used for this study:

- **Model 1:** This model is homogeneous with high stiffness. This model is the SUFEHM in its actual version. The parameters are presented in Table 3 - 1. This model have been validated under LS-DYNA® by Deck *et al.* (2008) and will be named “Stiff Homogeneous” in the following parts of this chapter.

	ρ [kg.dm ⁻³]	K [MPa]	G ₀ [kPa]	G _∞ [kPa]	β [s ⁻¹]
Model 1	1,040	1125	49	16,2	145

Table 3 - 1. Parameters implemented in the Model1.

- **Modèle 2:** This model is homogeneous with low stiffness. The parameters correspond to the MRE data mean values and are presented in Table 3 - 1. This model will be named “Soft Homogeneous” in the following parts of this chapter.

	ρ [kg.dm ⁻³]	K [MPa]	G ₀ [kPa]	G _∞ [kPa]	β [s ⁻¹]
Model 2	1,040	1125	1,87	0,80	300

Table 3 - 2. Table 3 - 3. Parameters implemented in the Model1.

- **Model 3:** This model is heterogeneous with low stiffness and corresponds to the MRE FE model. This model will be named “Soft Heterogeneous” in the following parts of this chapter.
- **Model 4:** This model is heterogeneous with high stiffness and corresponds to the MRE FE model scaled to have a mean rigidity value similar to the SUFEHM. This model will be named “Stiff Heterogeneous” in the following parts of this chapter.

3.3 Human brain heterogeneous models

3.3.1 Introduction

The aim of this part is to simulate accident cases with the four models previously presented. We will investigate heterogeneity influence in case of stiff or soft brain model. The four models are used to simulate the two real world accident cases presented in chapter 2. Locations and maximal values are proposed for the following parameters:

- Intra-cranial pressure P ;
- Von Mises stress σ_{VM} defined, with the incompressibility assumption, by the equation (3 - 6), where σ_{ii} et τ_{ij} are the coefficients of stress tensor;

$$\sigma_{VM} = \frac{1}{\sqrt{2}} \sqrt{(\sigma_{xx} - \sigma_{yy})^2 + (\sigma_{yy} - \sigma_{zz})^2 + (\sigma_{zz} - \sigma_{xx})^2 + 6(\tau_{xy}^2 + \tau_{yz}^2 + \tau_{xz}^2)} \quad (3 - 6)$$

- Maximal principal strain ϵ_I ;
- Von mises stress ϵ'_{VM} defined, with the incompressibility assumption, by the equation (3 - 7), where $\underline{\underline{\epsilon}}$ is the Green Lagrange strain tensor.

$$\epsilon_{VM} = \sqrt{\frac{3}{2} \underline{\underline{\epsilon}} : \underline{\underline{\epsilon}}} \quad (3 - 7)$$

Firstly, the 100 elements with maximal values are presented in terms of pressure, Von Mises stress, maximal principal strain and Von Mises strain.

Following comparisons are successively done:

- Influence of heterogeneity on models with low stiffness. Comparison is made between models 2 and 3;
- Influence of heterogeneity on models with high stiffness. Comparison is made between models 1 and 4;
- General comparison on results with the 4 FEM;

In a last part, we propose to analyze the influence of the model characteristics (heterogeneity and stiffness) on the anisotropic post-processing proposed in chapter 2. The post-processing proposed in chapter 2 for axons elongation calculation is applied to the 4 models and for the two accident cases.

3.3.2 Influence of heterogeneity with low stiff models

This first comparison concerns influence of heterogeneity on models with lowest stiffness. Models 2 and 3 are tested on the two accident cases. Comparison is done on maxima locations. Figure 3 - 9 shows locations of 100 elements with highest parameters for case 1.

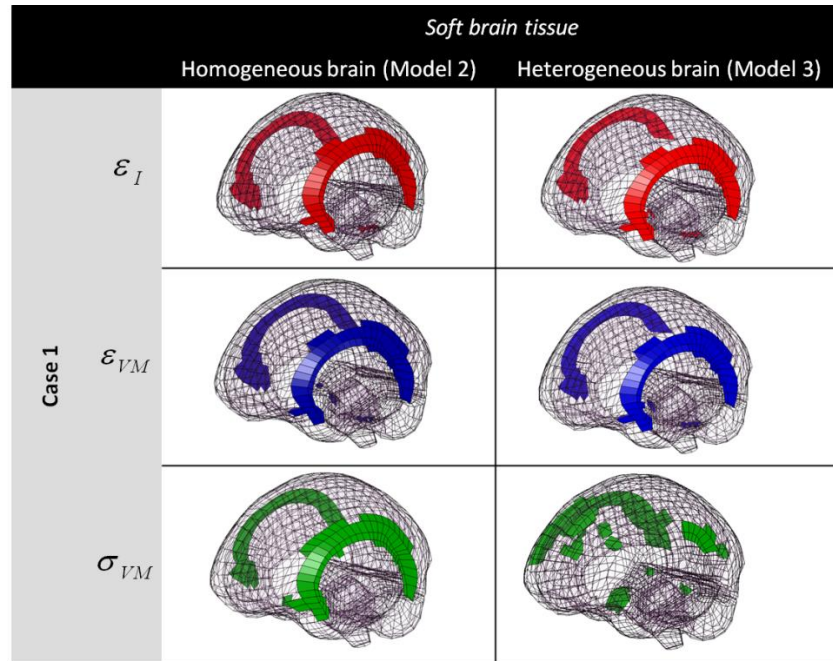


Figure 3 - 9. Location of the 100 elements with highest stress and strain values for case 1 simulation. Comparison is done on softest brain models (Models 2 and 3).

Same results are proposed in Figure 3 - 10 for the case 1.

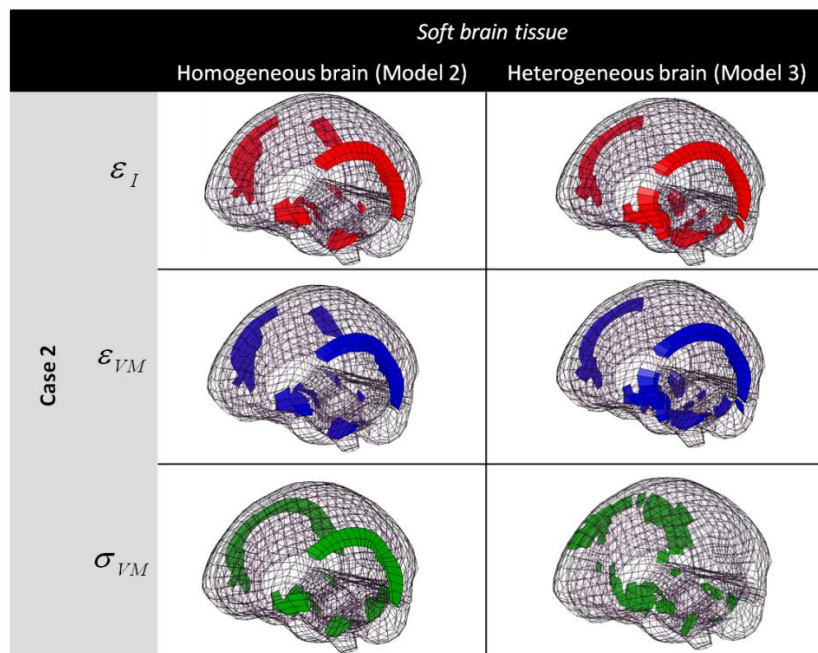


Figure 3 - 10. Location of the 100 elements with highest stress and strain values for case 2 simulation. Comparison is done on softest brain models (Models 2 and 3).

3.3.3 Influence of heterogeneity with high stiff models

This first comparison concerns influence of heterogeneity on models with highest stiffness. Models 1 and 4 are tested on the two accident cases. Comparison is done on maxima locations. Figure 3 - 11 shows locations of 100 elements with highest parameters for case 1.

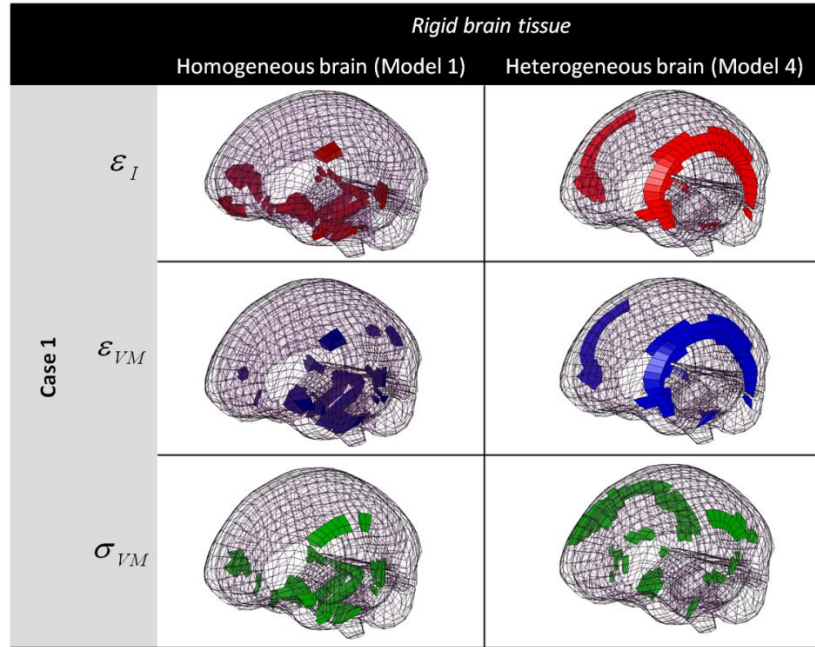


Figure 3 - 11. Location of the 100 elements with highest stress and strain values for case 1 simulation. Comparison is done on the stiffest brain models (Models 1 and 4).

Same results are proposed in Figure 3 - 12 for the case 1.

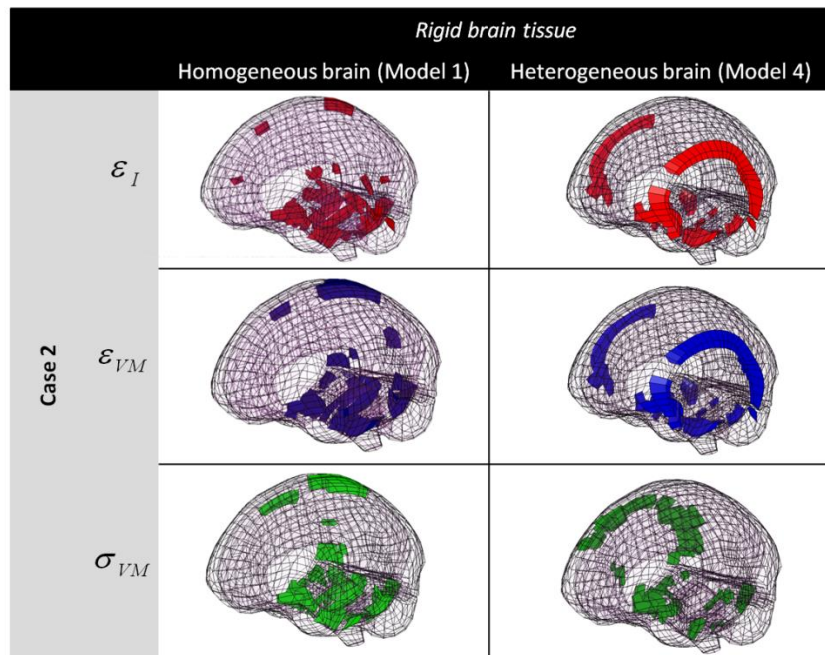


Figure 3 - 12. Location of the 100 elements with highest stress and strain values for case 2 simulation. Comparison is done on the stiffest brain models (Models 1 and 4).

3.3.4 Maximal values for the four models

Table 3 - 4 and Table 3 - 5 synthesize maximal values from simulation with the four brain models for case 1 and case 2 respectively.

		Homogeneous models		Heterogeneous models	
		Model 1	Model 2	Model 3	Model 4
Case 1	P [kPa]	129,9	133,4	133,5	131,4
	σ_{VM} [kPa]	22,74	3,75	2,62	10,01
	ε_I	0,18	1,91	2,29	0,95
	ε_{VM}	0,17	1,43	1,68	0,77

Table 3 - 4. Maximal values obtained for the simulation of case 1 with the four brain FEM.

		Homogeneous models		Heterogeneous models	
		Model 1	Model 2	Model 3	Model 4
Case 2	P [kPa]	318,2	339,3	338,7	329,3
	σ_{VM} [kPa]	57,40	4,27	4,93	23,88
	ε_I	0,54	3,22	3,91	1,52
	ε_{VM}	0,48	2,31	2,78	1,16

Table 3 - 5. Maximal values obtained for the simulation of case 1 with the four brain FEM.

Maximum of pressure is independent of the model, with maximal values of 130kPa and 330kPa for case 1 and case 2 respectively. This aspect is reinforced by considering the location of the 100 elements with maximal pressure. These elements are similar for both cases as presented in Figure 3 - 13.

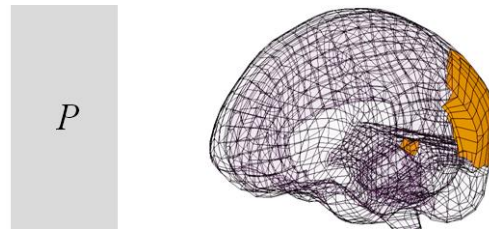


Figure 3 - 13. Location of the 100 elements with highest pressure values.

3.3.5 Axonal deformation of a brain heterogeneous model

In this section we will study the influence of heterogeneity on the inclusion of anisotropy brain in post-processing of simulation, using the methodology presented in Chapter 2. In

addition to the quantities supplied by the LS-DYNA® software, axonal deformation will be calculated from the equation (3 - 8) $\langle \vec{l} \rangle_{el}$ and $\langle FA \rangle_{el}$ are the anisotropy direction and Fractional Anisotropy respectively.

$$\varepsilon_{axon} = \left(\varepsilon \times \langle \vec{l} \rangle_{el} \right) \cdot \frac{\langle \vec{l} \rangle_{el}}{\langle FA \rangle_{el}} \quad (3 - 8)$$

Post-processing of anisotropy is applied to both simulated motorcycle accidents for each of the four proposed models. The maximum values of axonal strain are presented in Table 3 - 6 for the case 1 and in Table 3 - 7 for the case 2.

ε_{Axon} (Case 1)	Homogeneous brain	Heterogeneous brain
Low stiffness	<i>Model 2</i> 1.60	<i>Model 3</i> 1.91
High stiffness	<i>Model 1</i> 0.17	<i>Model 4</i> 0.80

Table 3 - 6. Maximal axonal strain values obtained for the simulation of case 1 with the four brain FEM.

ε_{Axon} (Case 2)	Homogeneous brain	Heterogeneous brain
Low stiffness	<i>Model 2</i> 2.68	<i>Model 3</i> 3.25
High stiffness	<i>Model 1</i> 0.52	<i>Model 4</i> 1.26

Table 3 - 7. Maximal axonal strain values obtained for the simulation of case 2 with the four brain FEM.

We propose to consider the location of maximal axonal strain values for the case 2. Figure 3 - 14, Figure 3 - 15 and Figure 3 - 16 show locations of the 100 elements with highest parameters for case 2 in coronal, frontal and sagittal views respectively.

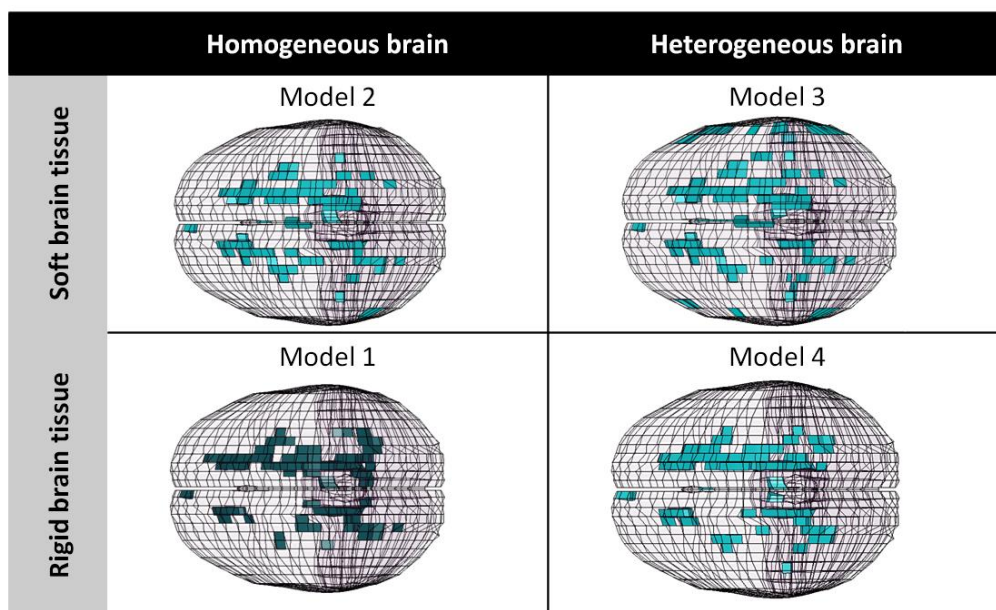


Figure 3 - 14. Location of the 100 elements with highest axonal strain values in coronal view.

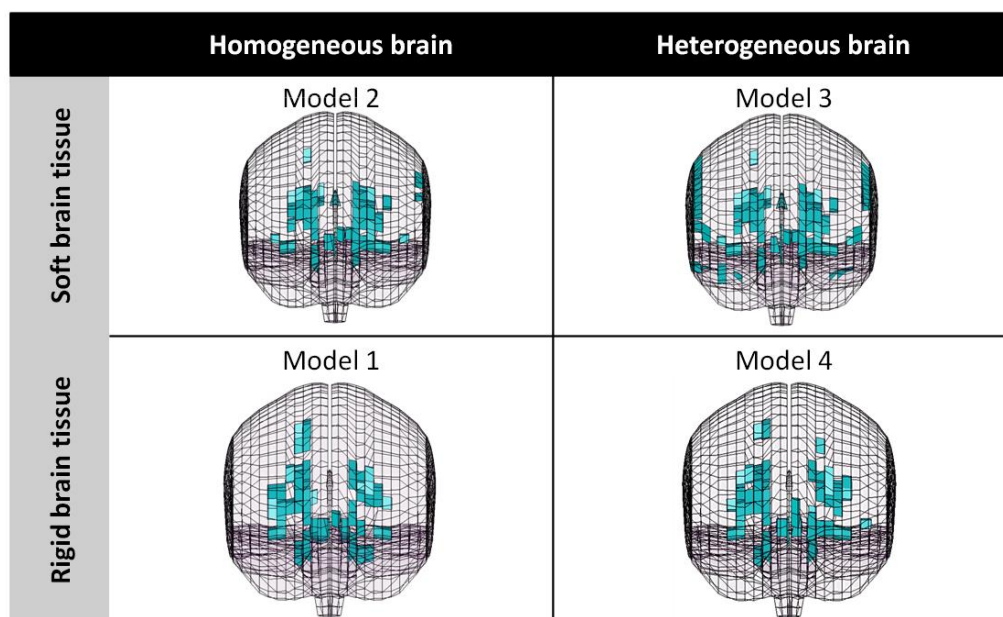


Figure 3 - 15. Location of the 100 elements with highest axonal strain values in frontal view.

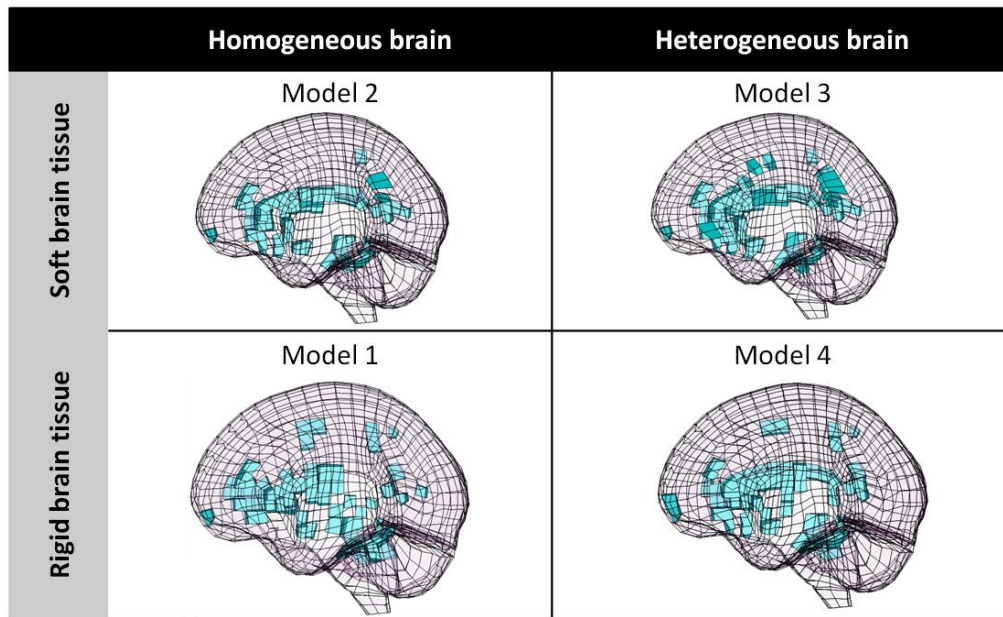


Figure 3 - 16. Location of the 100 elements with highest axonal strain values in sagittal view.

3.4 Conclusion

The study showed the influence of stiffness and heterogeneity on the constitutive brain during accident reconstruction. Intracranial pressure seems to be independent of the model used, depending only on the simulation itself. On the other hand, while heterogeneity has influence for highly stiff models only, heterogeneity changes the location of maxima for the mechanical parameters that are commonly used as brain injury criteria.

4 Conclusion

We have seen in this chapter how the *in vivo* viscoelastic information from the MRE could be implemented in numerical models of the human brain. Same accident cases were simulated with four different models of the brain to develop a parametric study on two properties of the brain: heterogeneity and rigidity. In accordance with the protocol illustrated in Figure 3 - 1, the following four models were used:

- A stiff homogeneous brain FEM (SUFEHM in its actual version);
- A soft heterogeneous brain FEM (corresponding to the MRE 3D map);
- A soft homogeneous brain FEM;
- A stiff homogeneous brain FEM (obtained by rigidifying the MRE 3D map).

These models would require validation to be used for the establishment of injury criteria and prediction of brain damage.

However results make it possible to conclude that the maxima and distribution of intracranial pressure are independent of the model used, whatever their heterogeneity or stiffness. This observation could justify that all the brain visco-elastic FEM proposed to date are validated in terms of intra-cerebral pressure in accordance with the data of Nahum et al. (1977) and Trosseille et al. (1992).

It was also concluded that the heterogeneity has influence on accident simulations for highly stiff brain models only (shear modulus of at least 10 kPa). According to conclusions on literature review in Chapter 1, brain model must have a high stiffness to better simulate *in vivo* brain tissue. Consequently it is essential to take heterogeneity into account for the numerical simulation of accidents in a realistic way.

Next conclusions concern the anisotropic post-processing of the simulations with heterogeneous brain. Locations of maximal axonal strains agreed with the most common DAI locations for the stiffest brain only. No influence of heterogeneity was observed for these locations. Only the maximal axonal strain values differ on simulations between homogeneous and heterogeneous brains.

In conclusion of this chapter, one of the most realistic way to develop a isotropic visco-elastic brain FEM for accident simulation is to implement heterogeneous data with high mean stiffness (shear modulus of at least 10 kPa). At the end of this chapter we have developed such a model based on *in vivo* MRE data. This is a first step to integration of heterogeneity by coupling with anisotropy information in a more realistic brain FEM.

CHAPTER 4

Non-linear visco-hyperelastic anisotropic constitutive model for brain tissue

1 Introduction

The previous chapters have highlighted a significant influence of axons fibers on DAI appearance in case of head impact. The possibility of taking this information from DTI in FE accident simulation in a dedicated post-processing has also been proposed. At present time, no one of the existing brain FEM integrate anisotropy information in its brain material. In the same way heterogeneity is at best only partially integrated by dissociated white and gray matter mechanical behavior. These remarks concern notably brain FEM associated with criteria for DAI prediction.

The aim of this last chapter is to use the conclusion from the previous chapter on brain mechanical properties in order to develop a new constitutive model for brain tissue including following properties:

- Anisotropy of the mechanical law by separating the behavior of axon fibers from brain matrix;
- A viscoelastic linear behavior at small strain that is based on experimental *in vivo* MRE results;
- Non linearities generating stiffness increase at high strains.

Firstly we will try to bring out the main characteristics and limits of brain materials proposed for FEM in the literature. This investigation will be performed numerically on cylindrical samples simulating classical rheological tests (in tensile, compression and shear). From these observations and using DTI information from chapter 2, a new anisotropic non linear visco-hyperelastic constitutive law will be proposed, that insure stability for implementation under LS-DYNA® FE software. Next step consists in implementing this new law in the SUFEHM geometry. The use of this new anisotropic model will be illustrated on simulation of two motorcyclist accident cases. At least comparison from this model mechanical response will be compared with the anisotropic post-processing method proposed in chapter 2 for DAI prediction and location.

The aim of this new model is simulate brain behavior in more realistic way in case of head trauma and to evaluate the influence of axon fibers on brain mechanical anisotropy in this situation.

2 Evaluation of existing brain tissue FE constitutive models

2.1 Introduction

Constitutive models for brain tissue used for FEM have been detailed in the French version of the chapter 1. 8 brain models actually used for accident simulation will be compared in this study:

- The Strasbourg University Finite Element Head Model (SUFEHM) (Kang *et al.*, 1997) ;
- The Wayne State University Brain Injury Model (WSUBIM) (King *et al.*, 2003) ;
- The Toyota model (THUMS) (Iwamoto *et al.*, 2007) ;
- The SIMulator Monitoring model, developed in 2003 by the NHTSA (SIMon 2003) (Takhounts *et al.*, 2003) ;
- The SIMulator Monitoring model, developed in 2008 by the NHTSA (SIMon 2008) (Takhounts *et al.*, 2008) ;
- The Torino University model (Belingardi *et al.*, 2005) ;
- The Stockholm University model (KTH) (Kleiven, 2007), reused by the University of Dublin (Horgan *et al.*, 2005) ;

Even if studies have already been proposed to compare the response of these integral models in case of impact, no comparison has been done on the brain constitutive models.

To overcome effects due to FEM geometry or complex kinematics, we propose in this part to compare the different laws by simulating classical rheological tests (in compression, tensile and shear) on cylindrical shape samples. By comparison of the results with the bibliographic study of chapter 1, the aim is to bring properties to light that insure numerical stability of the law in the most realistic way.

2.2 Description of the model

2.2.1 Introduction

We will first describe the model used for this comparative study: its geometry, the implemented laws as well as boundary conditions and loads of the numerical simulations in shear, tensile and compression.

2.2.2 Geometry and meshing

The model has a cylindrical shape (24mm in height, 32mm in diameter), is composed by 17472 elements divided in 24 horizontal layers. Elements are hexagonal with 1mm characteristic size. This model has been meshed under LS-DYNA® software and is shown in Figure 4 - 1. While symmetry axis of the cylinder is noted Z, axis in the transverse horizontal plane are noted X and Y. These characteristics correspond to compromise between sizes of all the samples experimentally tested (*in vitro*) in the literature. A preliminary study that is not presented in this part showed the independence of sample behavior with shape and meshing size.

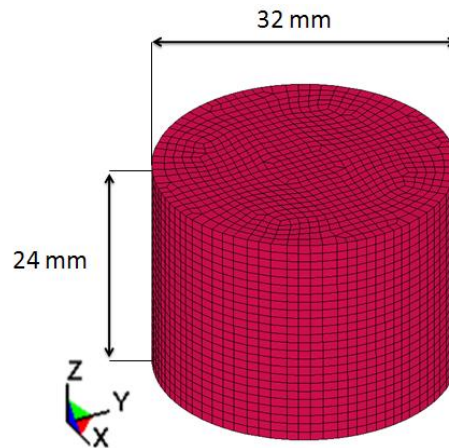


Figure 4 - 1. Illustration of the cylindrical shape sample for numerical simulation of experimental rheological tests.

2.2.3 Mechanical properties

6 linear viscoelastic laws are successively evaluated in this study. Material parameters are implemented under LS-DYNA® using the MAT_006 (*MAT_GENERAL_VISCOELASTIC) law. It corresponds to a generalized Maxwell model at first order. Parameters are detailed in Table 4 - 1 and values are given in Table 4 - 2.

Parameters	Units	Meaning
ρ	$[\text{kg.m}^{-3}]$	Density
K	$[\text{Pa}]$	Bulk modulus
G_0	$[\text{Pa}]$	Short term shear modulus
G_∞	$[\text{Pa}]$	Long term shear modulus
β	$[\text{s}^{-1}]$	Time constant

Table 4 - 1. Mechanical parameters for the LS-DYNA® MAT_006 law.

Models	Authors	ρ [kg.m ⁻³]	K [GPa]	G ₀ [kPa]	G _∞ [kPa]	β [s ⁻¹]
Turin	(Belingardi <i>et al.</i> 2005)	1140	5,625	49	16,2	145
SUFEHM	(Kang <i>et al.</i> 1997)	1040	1,125	49	16,2	145
THUMS	(Iwamoto <i>et al.</i> 2007)	1000	2,16	12,5	6,1	100
SIMon	(Takhounts <i>et al.</i> 2003)	1040	0,56	10,34	5,2	100
WSUBIM	(King <i>et al.</i> 2003)	1060	2,19	12,5	2,5	80
SIMon	(Takhounts <i>et al.</i> 2008)	1040	0,56	1,66	0,928	16,95

Table 4 - 2. Mechanical parameters implemented under LS-DYNA® for the MAT_006 law.

Only two models have a different law for brain tissue: model called “KTH and model from the University of Dublin. These models are similar and will be called « KTH » in the following parts. It consists in a non linear hyperelastic model (Ogden model) including viscosity effects. Material parameters are implemented under LS-DYNA® using the MAT_O77 (*MAT_OGDEN_RUBBER) law. Parameters are detailed in Table 4 - 3 and implemented values in Table 4 - 4.

Parameters	Units	Meaning
ρ	[kg.m ⁻³]	Density
ν	-	Poisson's ratio
α_i	-	Ogden parameters
β_i	-	
G_i	[Pa]	Long term shear moduli
β_i	[s ⁻¹]	Time constants

Table 4 - 3. Mechanical parameters for the LS-DYNA® MAT_077 law.

	ρ [kg.m ⁻³]	1040	ν	0.499999
Hyperelasticity (order n=2)	μ_1 [Pa]	26,9	α_1	10,1
	μ_2 [Pa]	-60,2	α_2	-12,9
Viscosity (order N=6)	G_1 [Pa]	160	β_1 [s ⁻¹]	10 ⁶
	G_2 [Pa]	39	β_2 [s ⁻¹]	10 ⁵
	G_3 [Pa]	3,1	β_3 [s ⁻¹]	10 ⁴
	G_4 [Pa]	4,0	β_4 [s ⁻¹]	10 ³
	G_5 [Pa]	0,05	β_5 [s ⁻¹]	10 ²
	G_6 [Pa]	1,5	β_6 [s ⁻¹]	10 ¹

Table 4 - 4. . Mechanical parameters implemented under LS-DYNA® for the MAT_006 law

Comparison of these eight theoretical models is proposed with experimental data from literature in Figure 4 - 2 in terms of relaxation modulus (for 200ms relaxation time).

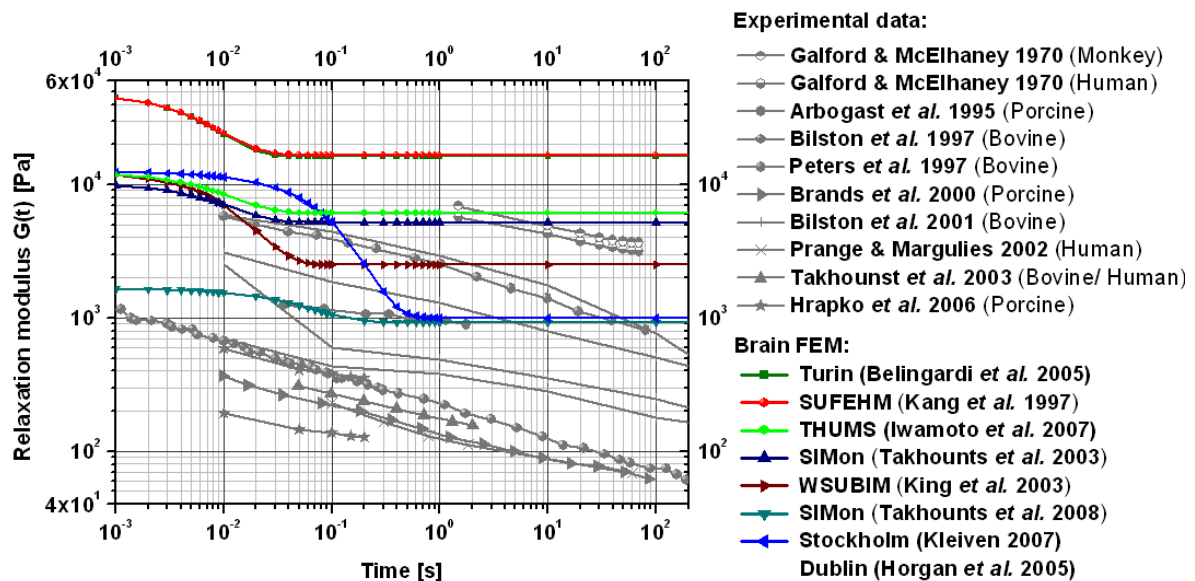


Figure 4 - 2. Theoretical comparison of the investigated models in terms of shear relaxation modulus (200ms relaxation time).

While there are only three different short term moduli, each model present a particular long term modulus.

Il apparaît clairement que les modèles ne correspondent que localement aux courbes expérimentales, essentiellement pour des temps inférieurs à 0,1s. Ceci est en partie lié aux ordres de grandeurs des tests dynamiques ou en relaxation dont sont déduites ces lois numériques.

2.2.4 Boundary conditions and loadings

Numerical simulations are performed on cylindrical shape samples with following conditions:

- In **shear**, a displacement at constant speed (1m. s^{-1}) of upper plate nodes along X axis until $\gamma_{\max} = 35\%$ shear strain as shown in Table 4 - 5. Stress relaxation is then observed during 30ms. Upper plate nodes are constrained in translation along Z direction only. Lower plates are constrained for all the degrees of freedom except rotation along Y and Z axis;
- In **tensile**, a displacement at constant speed (1m. s^{-1}) of upper plate nodes along Z axis until $\epsilon_{\max} = 50\%$ strain as shown in Table 4 - 5. Stress relaxation is then observed during 33ms. Lower plates are constrained in translation along Z direction only;
- In **compression**, displacement is not imposed to cylinder nodes but to two plates meshed with shell elements. These plates have 1000 kg.m^{-3} density, a Young modulus of 210GPa and a Poisson ratio of 0.285 to correspond to the rheometer steel plates properties (Ashby et Jones, 2008). Two interfaces are developed between each of the plates and the cylinder (AUTOMATIC_NODES_TO_SURFACE under LS-DYNA®). To reproduce contact between biological soft tissue and steel, a friction coefficient of 0.3 is implemented, in accordance with Zhang et Mak (1997) and El-Shimi (1977). Displacements are registered at the upper interface and force along Z axis at the lower interface. Displacements are imposed to the upper plate at constant speed (1m. s^{-1}) along Z axis until $\epsilon_{\max} = 50\%$ strain as shown in Table 4 - 5. Stress relaxation is then observed during 33ms.

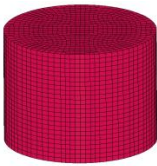
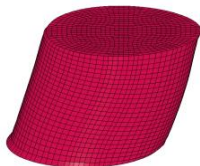
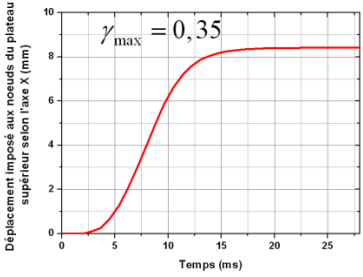


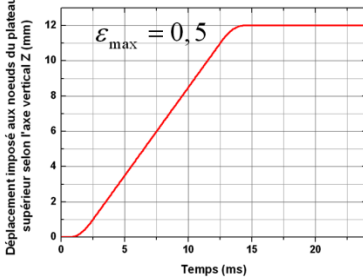
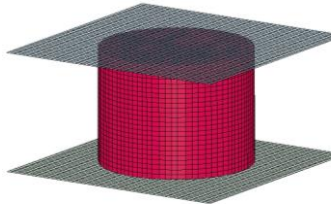
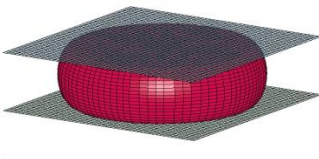
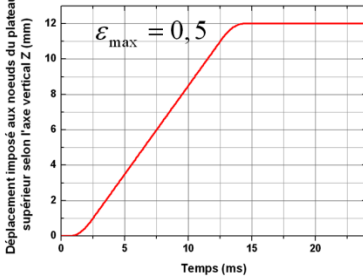
Tests	Initial state	Final state	Imposed displacement
Shear			
Tensile			
Compression			

Table 4 - 5. Illustration of the numerical simulations with the cylindrical shape sample.

Results are observed in terms of:

- Von Mises stress σ_{VM} , expressed in equation (4 - 1), and pressure P in time for the central element.

$$\sigma_{VM} = \frac{2}{3} \sqrt{\frac{3}{2} (s_{xx}^2 + s_{yy}^2 + s_{zz}^2) + \frac{3}{4} (t_{xy}^2 + t_{yz}^2 + t_{xz}^2)} \quad (4 - 1)$$

s_{ij} and t_{ij} are the deviatoric stresses defined in equation (4 - 2) from the coefficients σ_{ij} and τ_{ij} of stress tensor.

$$\begin{cases} s_{xx} = \frac{2}{3}\sigma_{xx} - \frac{1}{3}\sigma_{yy} - \frac{1}{3}\sigma_{zz} \\ s_{yy} = -\frac{1}{3}\sigma_{xx} + \frac{2}{3}\sigma_{yy} - \frac{1}{3}\sigma_{zz} \\ s_{zz} = -\frac{1}{3}\sigma_{xx} - \frac{1}{3}\sigma_{yy} + \frac{2}{3}\sigma_{zz} \\ t_{ij} = 2\tau_{ij} \end{cases} \quad (4 - 2)$$

With incompressibility assumption, equation (4 - 3) become equation (4 - 3);

$$\sigma_{VM} = \frac{1}{\sqrt{2}} \sqrt{(\sigma_{xx} - \sigma_{yy})^2 + (\sigma_{yy} - \sigma_{zz})^2 + (\sigma_{zz} - \sigma_{xx})^2 + 6(t_{xy}^2 + t_{yz}^2 + t_{xz}^2)} \quad (4 - 3)$$

- Values and location of maxima for Von Mises stress, pressure, Von Mises strain, maximum principal strain as well as strains ε_x , ε_y and ε_z along X, Y and Z axis;
- For compression tests only, force in time along Z direction F_z and displacement U_z in time are registered and allow to express relationship between stress σ and stretch ratio λ using equations (4 - 4) and (4 - 5) (L_0 and S_0 are the initial height and upper surface of the cylinder).

$$\sigma(t) = \frac{F_z(t)}{S_0} \quad (4 - 4)$$

$$\lambda(t) = \varepsilon(t) + 1 = \frac{U_z(t)}{L_0} + 1 \quad (4 - 5)$$

All the results are filtered using a law pass filter at 1000Hz, according to the SAE (*Society of Automotive Engineer*) norms.

2.2.5 Conclusion

These simulations will make it possible to compare the response of the different models from the literature on simple tests. By comparing with experimental data from the literature, we will then try to extract the most realistic properties that should be taken into account to simulate brain FEM in the most realistic way.

2.3 FE simulation of rheometric tests

2.3.1 Introduction

Results are here presented for the constant strain rate and relaxation simulations on cylindrical shape elements for the considered models (successively in shear, tensile and

compression). Loading speed influence will then be investigated by simulating compression tests different constant strain rates.

2.3.2 Shear simulations

Results in shear are presented in this part in terms of Von Mises stress in Figure 4 - 3, pressure in Figure 4 - 4 of the central element and displacements along X axis for central node in Figure 4 - 5.

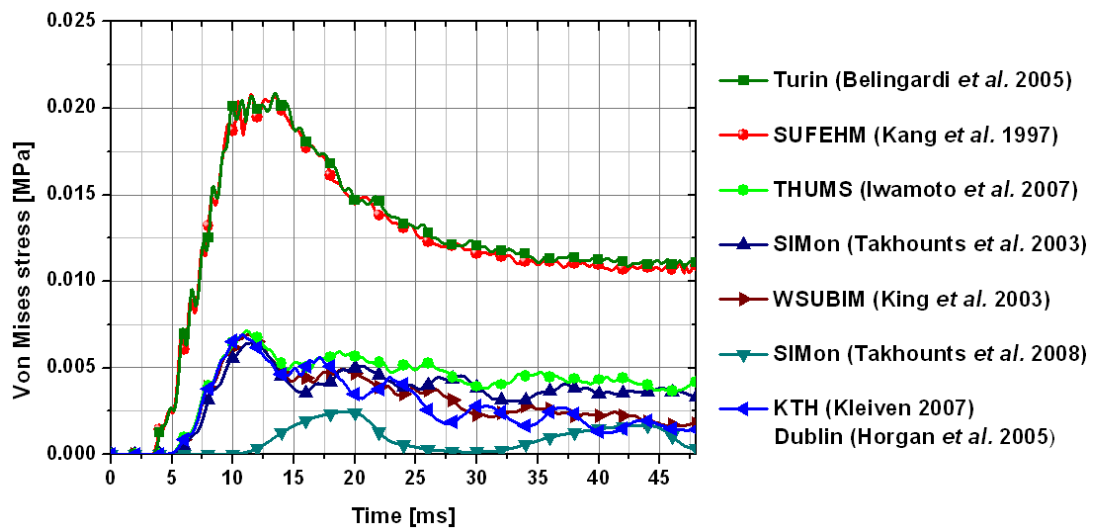


Figure 4 - 3. Comparison in shear of the models in terms of Von Mises stress at central element.

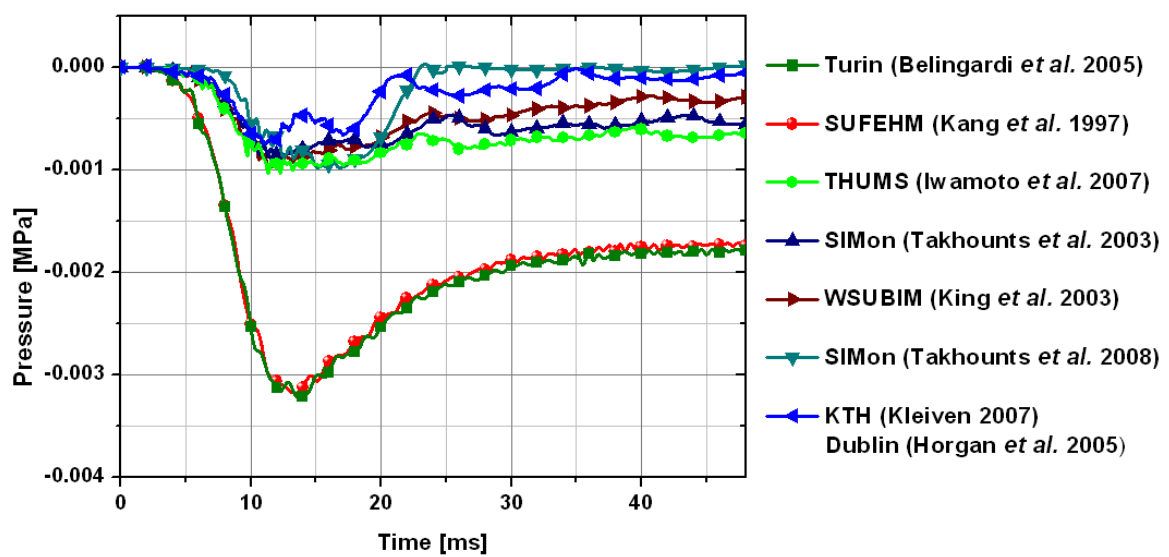


Figure 4 - 4. Comparison in shear of the models in terms of pressure at central element.

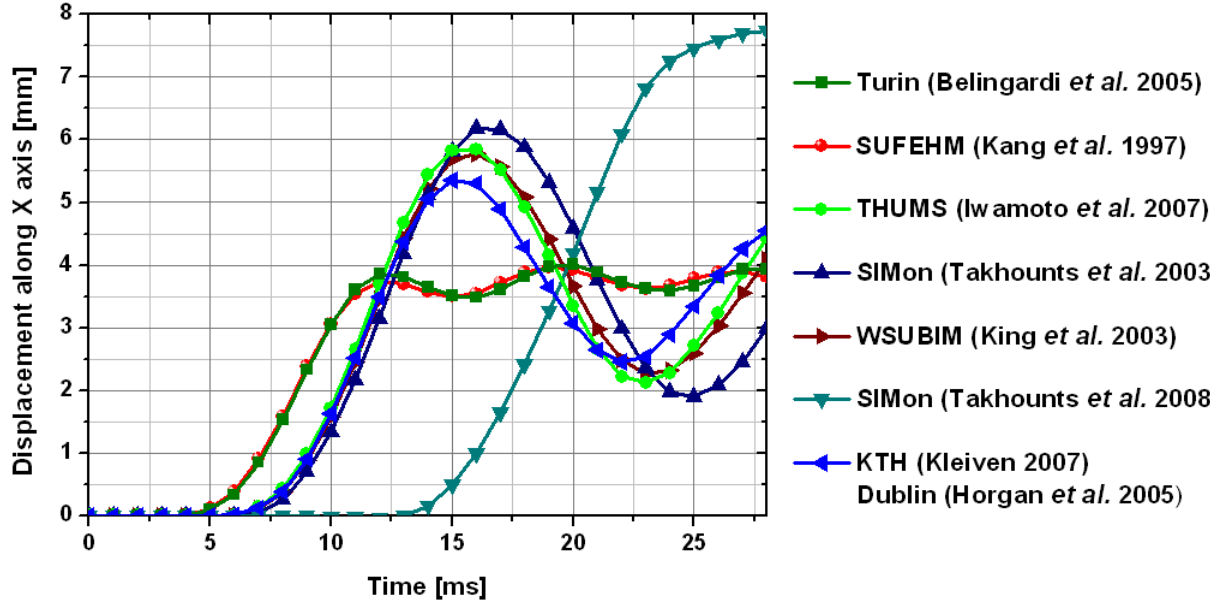


Figure 4 - 5. Comparison in shear of the models in terms of displacement along X direction at central node.

From the last figure, shear wave propagation is observed. With the assumption of purely elastic medium and incompressibility, periods T_s of waves are measured to calculate frequency f_s , wave speed c_s and wave length λ_s with equations (4 - 6) to (4 - 8). G and ρ are the equivalent shear modulus and the density of brain tissue for the considered model. Calculated values are detailed in Figure 4 - 6.

$$f_s = \frac{1}{T_s} \quad (4 - 6)$$

$$c_s = \sqrt{\frac{G}{\rho}} \quad (4 - 7)$$

$$\lambda_s = T_s \sqrt{\frac{G}{\rho}} \quad (4 - 8)$$

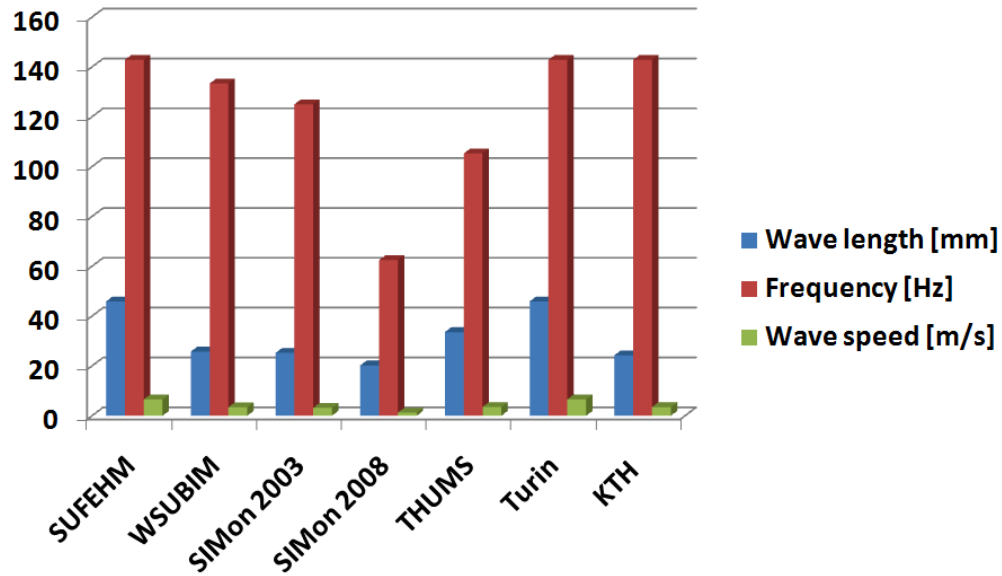


Figure 4 - 6. Wave length, frequency and wave speed values calculated for the evaluated models by considering shear wave propagation in shear simulation.

2.3.3 Tensile simulations

Results in tensile are presented in this part in terms of Von Mises stress in Figure 4 - 7 and pressure in Figure 4 - 8.

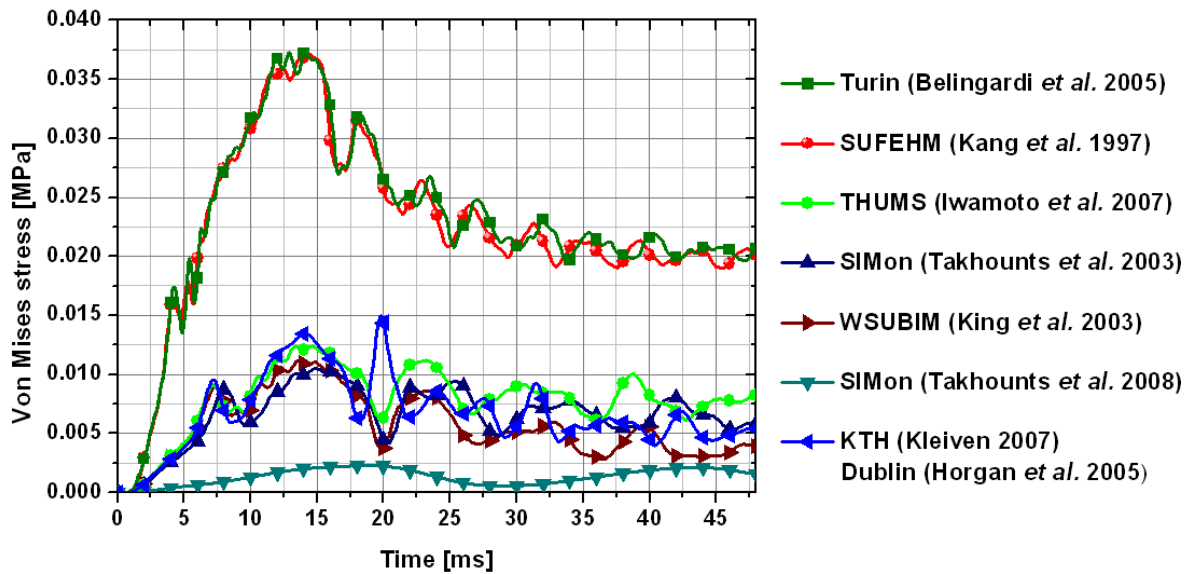


Figure 4 - 7. Comparison in Tensile of the models in terms of Von Mises stress at central element.

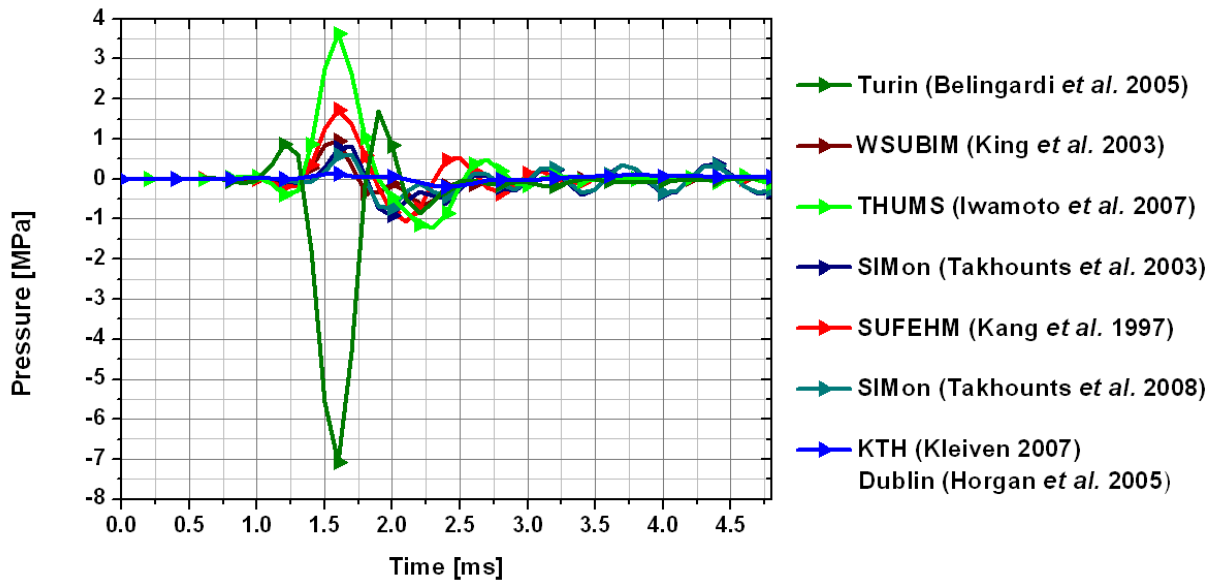


Figure 4 - 8. Comparison in tensile of the models in terms of pressure at central element.

Calculated values for shear wave propagation are detailed in Figure 4 - 9.

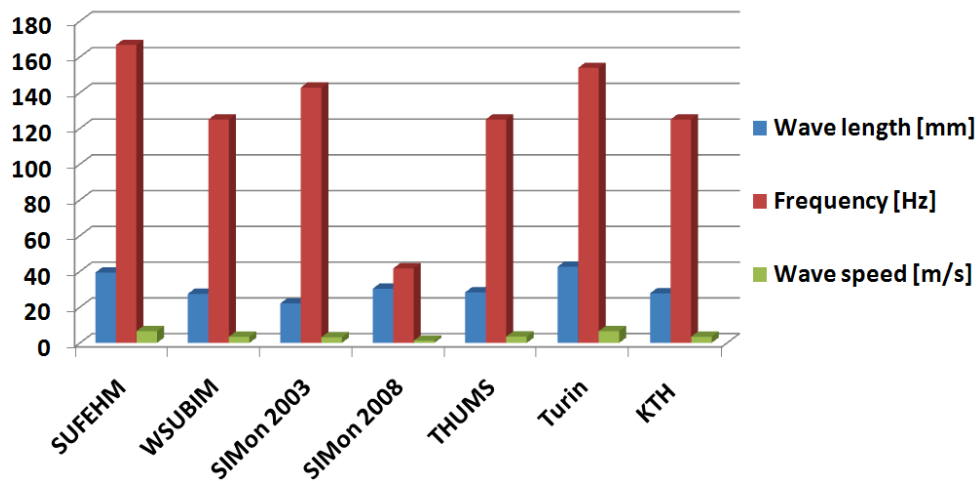


Figure 4 - 9. Wave length, frequency and wave speed values calculated for the evaluated models by considering shear wave propagation in tensile simulation.

2.3.4 Compression simulations

Results in compression are presented in this part in terms of Von Mises stress in Figure 4 - 10 and pressure in Figure 4 - 11.

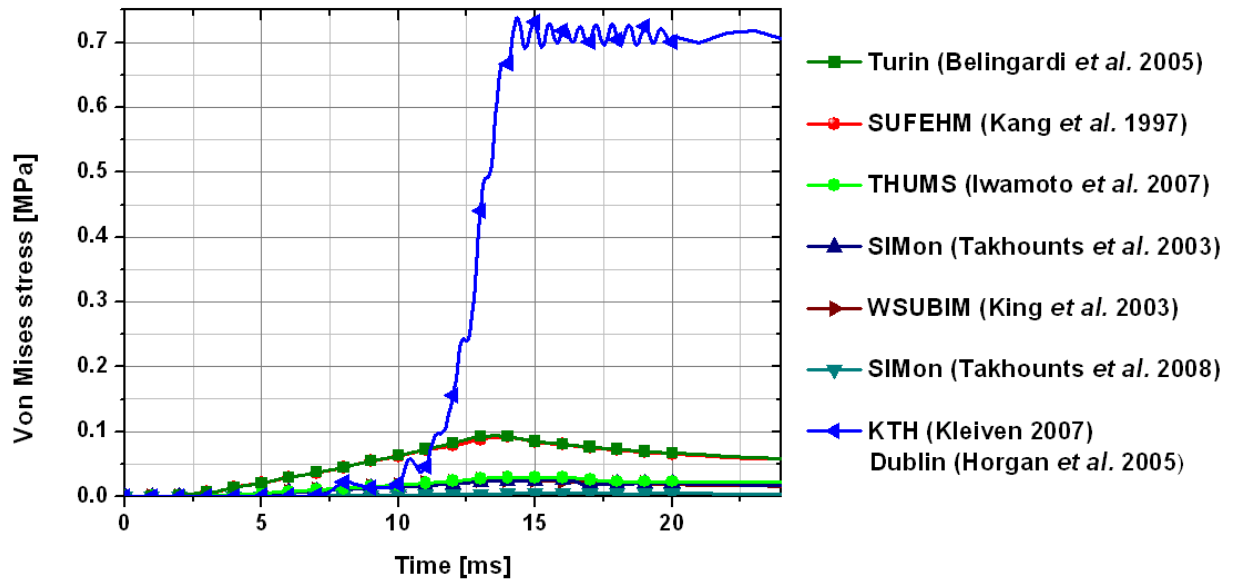


Figure 4 - 10. Comparison in compression of the models in terms of Von Mises stress at central element.

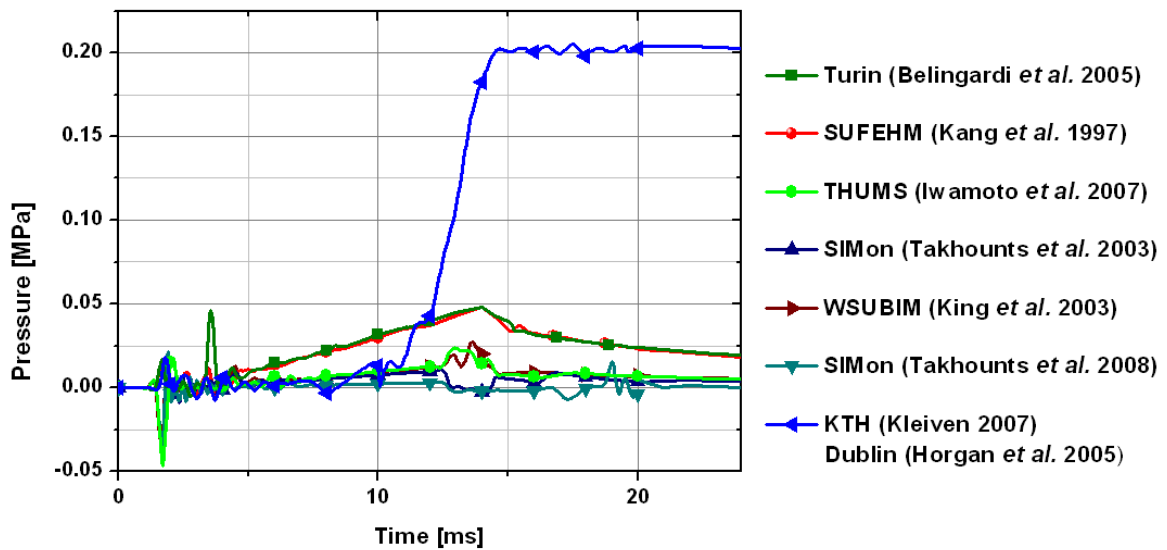


Figure 4 - 11. Comparison in compression of the models in terms of pressure at central element.

2.3.5 Strain rate influence in compression

In order to evaluate sensitivity of the models to strain rate, compression tests are proposed until 50% strain in compression with 3 different strain rates:

- 42s^{-1} (equivalent to compression speed of 1m.s^{-1}). This value correspond to the order of magnitude for accidentology;

- 1000s^{-1} (equivalent to compression speed of 24m.s^{-1}) to estimate response at high speed. This speed is similar to experimental data proposed by Pervin and Chen (2009) with Hopkinson device;
- 1s^{-1} (equivalent to compression speed of 0.024m.s^{-1}) to estimate response at low speed. This value corresponds to the order of magnitude for some *in vitro* rheological experimental tests on brain tissue from the literature.

Results are expressed with the help of force and displacement in terms relationship between stress and stretch ratio. Slope at small strain (10%, according to bibliographic study of chapter 1 – Nicolle *et al.*, 2004) correspond to Young modulus value for the considered speed.

Results at 42s^{-1} , 1000s^{-1} and 1s^{-1} are presented in Figure 4 - 12, Figure 4 - 13 and Figure 4 - 14 respectively. KTH appears only for 42s^{-1} because of the lack of stability with strain rate changes for this model.

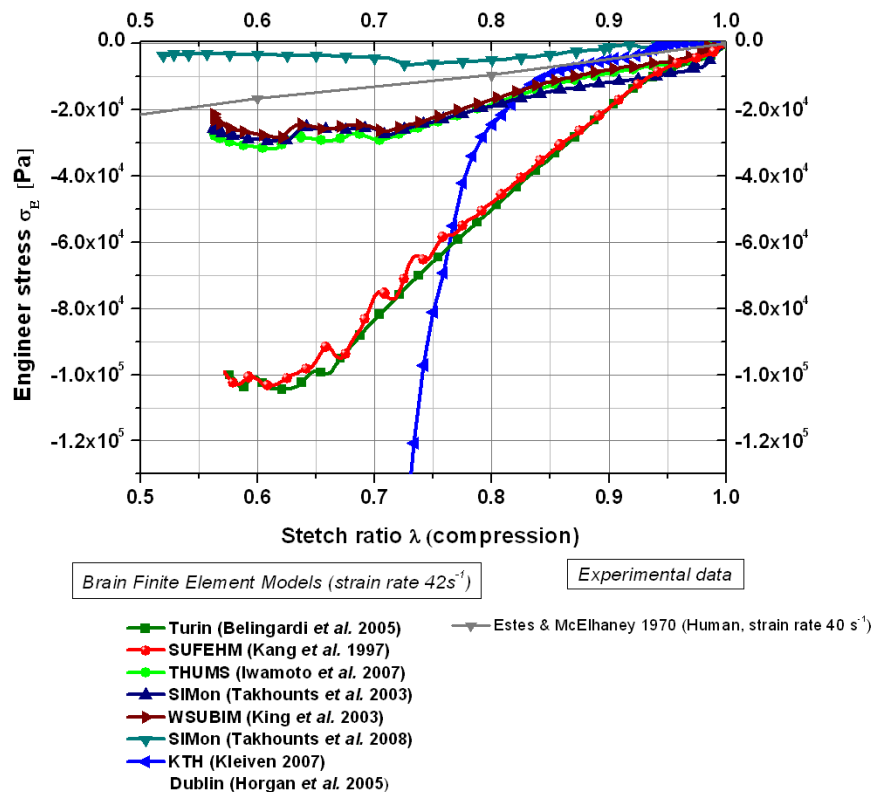


Figure 4 - 12. Comparison at 42s^{-1} constant strain rate in compression in terms of stress / stretch ratio for simulations on cylinder models. Curves are compared with data from the literature provided from experimental tests at similar strain rate.

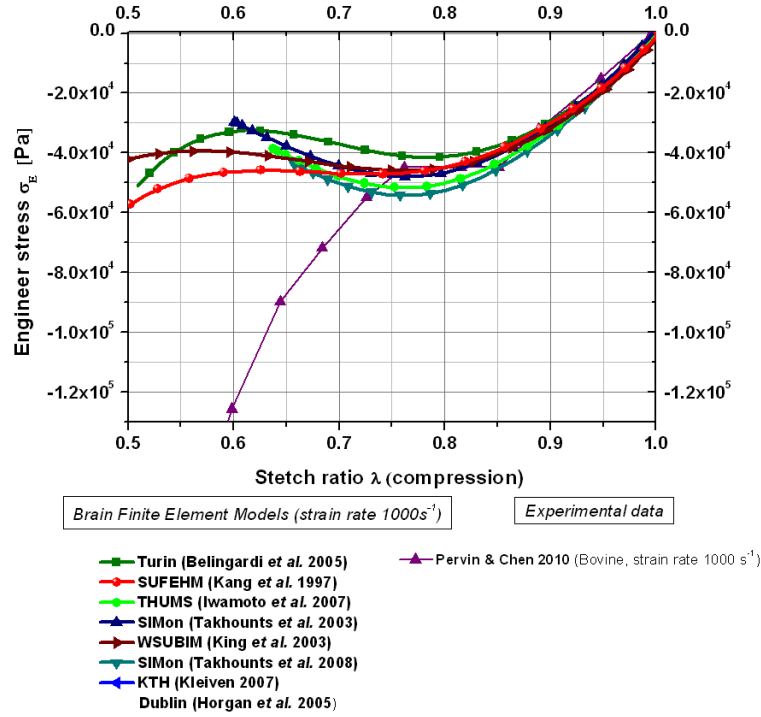


Figure 4 - 13. Comparison at 1000 s^{-1} constant strain rate in compression in terms of stress / stretch ratio for simulations on cylinder models. Curves are compared with data from the literature provided from experimental tests at similar strain rate.

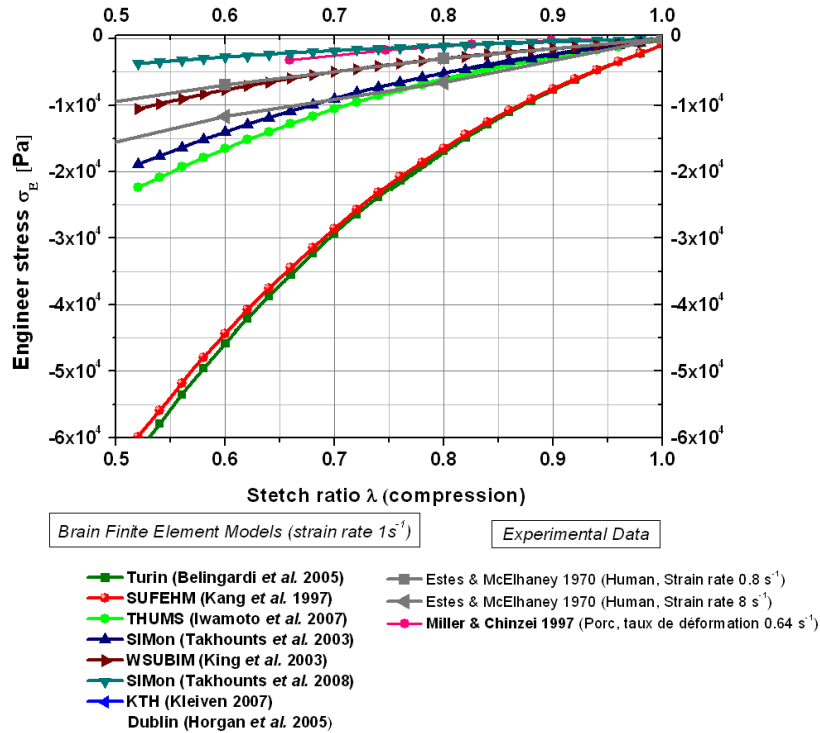


Figure 4 - 14. Comparison at 1 s^{-1} constant strain rate in compression in terms of stress / stretch ratio for simulations on cylinder models. Curves are compared with data from the literature provided from experimental tests at similar strain rate.

At 1 s^{-1} strain rate, Young moduli are calculated from the slopes at small strain. Values are reported in

	SUFEHM	Turin	THUMS	SIMon 2003	WSUBIM	SIMon 2008
Young modulus [kPa]	73	73	26	20	11	5

Table 4 - 6. Young modulus calculated as slope at small strain from the stress/stretch ratio at 1 s^{-1} strain rate for the simulated brain models.

To extend the strain rate range, the SUFEHM is evaluated at five strain rates: 0.1 s^{-1} (2.4 mm.s^{-1}), 1 s^{-1} (24 mm.s^{-1}), 10 s^{-1} (0.24 m.s^{-1}), 42 s^{-1} (1 m.s^{-1}) et 1000 s^{-1} (24 m.s^{-1}). The stress/stretch ratio curves are related in Figure 4 - 15 and compared with experimental data at same strain rates (*in vitro* data from Estes and McElhaney, 1970, Miller and Chinzei, 1997, Prévost *et al.*, 2010 and Pervin and Chen, 2010).

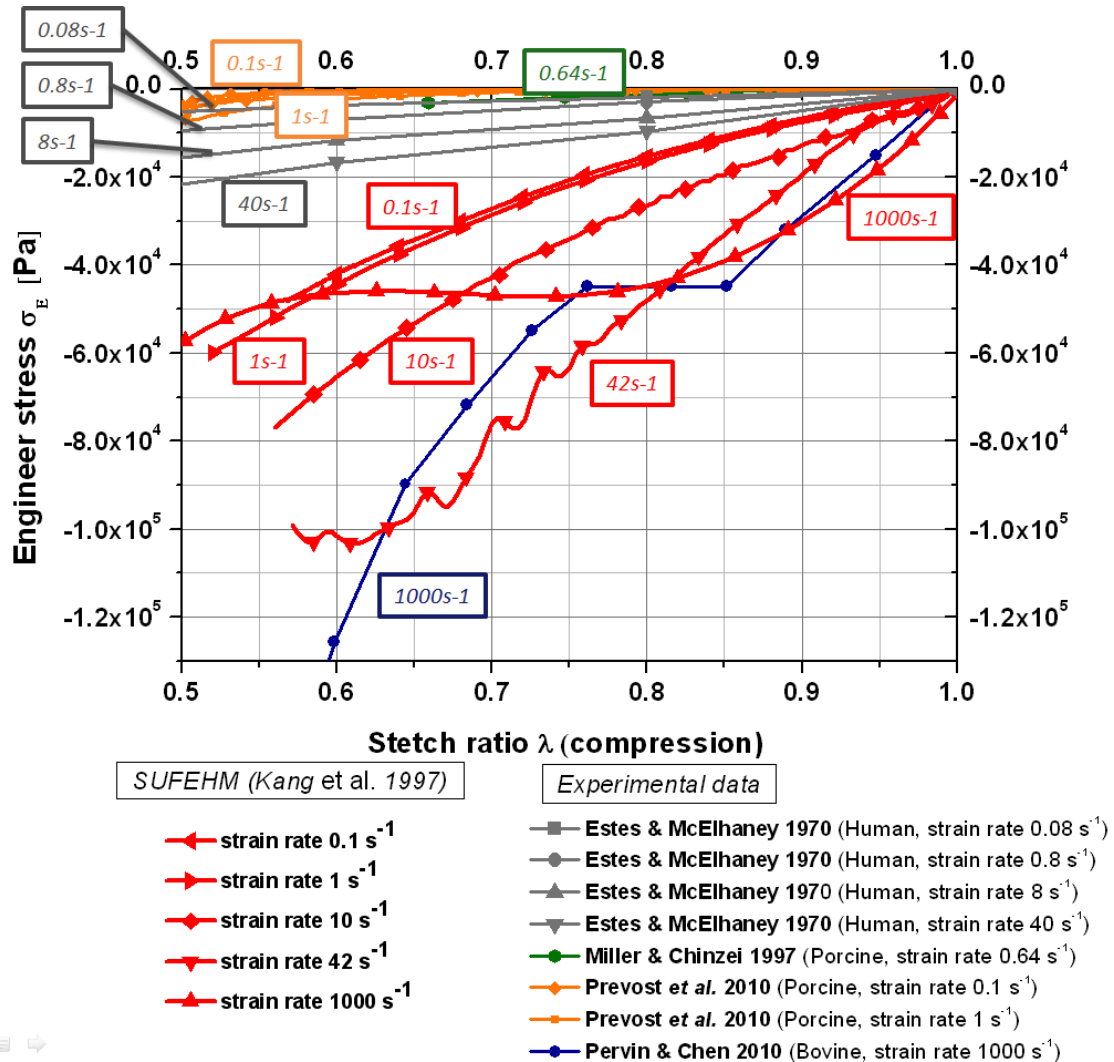


Figure 4 - 15. Comparison at 5 different constant strain rates in compression in terms of stress / stretch ratio for simulations on cylinder model for the SUFEM law. Curves are compared with data from the literature provided from experimental tests at similar strain rate.

From this figure, Young moduli are calculated from the slopes at small strains. Values are related in Figure 4 - 16.

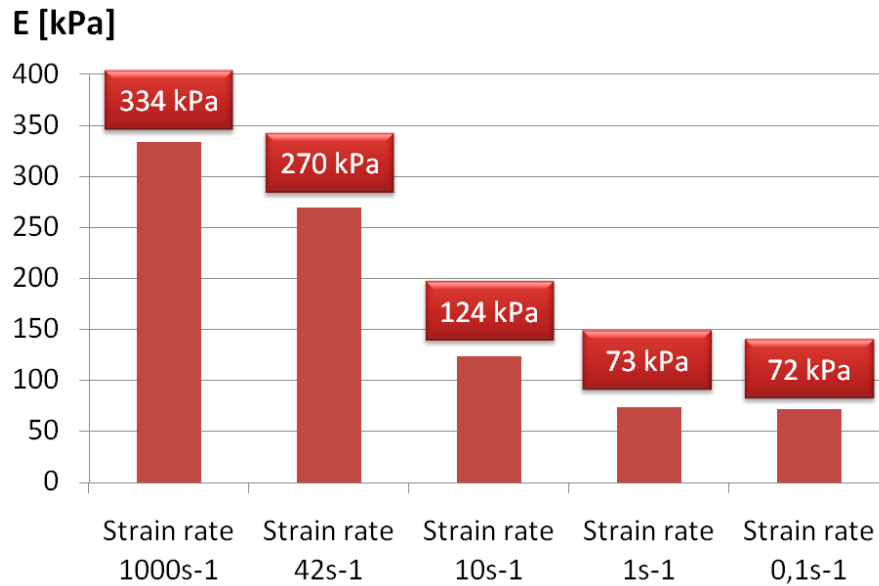


Figure 4 - 16. Young moduli calculated as slope at small strain from the stress/stretch ratio for each strain rate for the SUFEHM.

We propose to compare the results of constant strain rate compression tests for all the considered FEM with experimental data from the literature. For FEM simulations values as well as results from the literature will be expressed by Young modulus versus strain rate. Values for each of the four following modalities are compared:

- Results from FEM simulations;
- *In vitro* compression tests at constant strain rate;
- *In vivo* indentation tests;
- MRE tests.

Main difficulty is to find a same manner to express results from all the modalities. Assumptions have to be considered to calculate the strain rate imposed for each of these modalities:

- For FEM simulations, the strain rate is assumed to be constant all along the test;

- For *in vitro* constant strain rate compression tests, compression speed V_0 is generally mentioned in the publications. Strain rate $\dot{\epsilon}_0$ is deduced from compression speed by equation (1 – 38) where L_0 is the initial height of the sample;

$$\dot{\epsilon} = \frac{V_0}{L_0} \quad (4 - 9)$$

- For *indentation tests*, compression speed V_0 is generally mentioned in the publications. Strain rate $\dot{\epsilon}_0$ is then estimated using equation (1 – 38) by considering brain as a cylinder with symmetry axis lined up with indentation direction. L_0 is assumed to be to be height of this “brain equivalent” cylinder;
- For *MRE tests*, mechanical waves are assumed to be perfectly sinusoidal, with unidirectional propagation and integrally transmitted to the brain tissue. By assuming a sinusoidal global displacement, speed $\dot{\xi}(t)$ is expressed by equation (4 - 10) where ξ_0 , ϕ , ω , t are maximum displacement, phase offset, pulsation and time. Maximal strain rate is deduced by considering brain as a cylinder with symmetry axis lined up with wave propagation direction. Strain rate is expressed by equation (4 - 11) where L_0 is assumed to be to be height of this “brain equivalent” cylinder;

$$\dot{\xi}(t) = \omega \xi_0 \sin(\omega t + \phi) \quad (4 - 10)$$

$$\dot{\epsilon} = \frac{\omega \xi_0}{L_0} \quad (4 - 11)$$

In the same way, assumptions have to be taken for Young modulus determination:

- For *FEM simulations*, Young Modulus is deduced from stress/stretch ratio curves by considering the slope at small strains (<10%);
- For *in vitro* constant strain rate compression tests, Young Modulus is deduced from stress/stretch ratio or stress/strain curves by considering the slope at small strains (<10%);
- For *indentation tests*, Young Modulus value is directly mentioned in the publications;
- For *MRE tests*, Young Modulus is deduced from shear modulus proposed in the publications by assuming incompressibility of brain tissue.

Results in terms of Young modulus versus strain rate are presented in Figure 4 - 17.

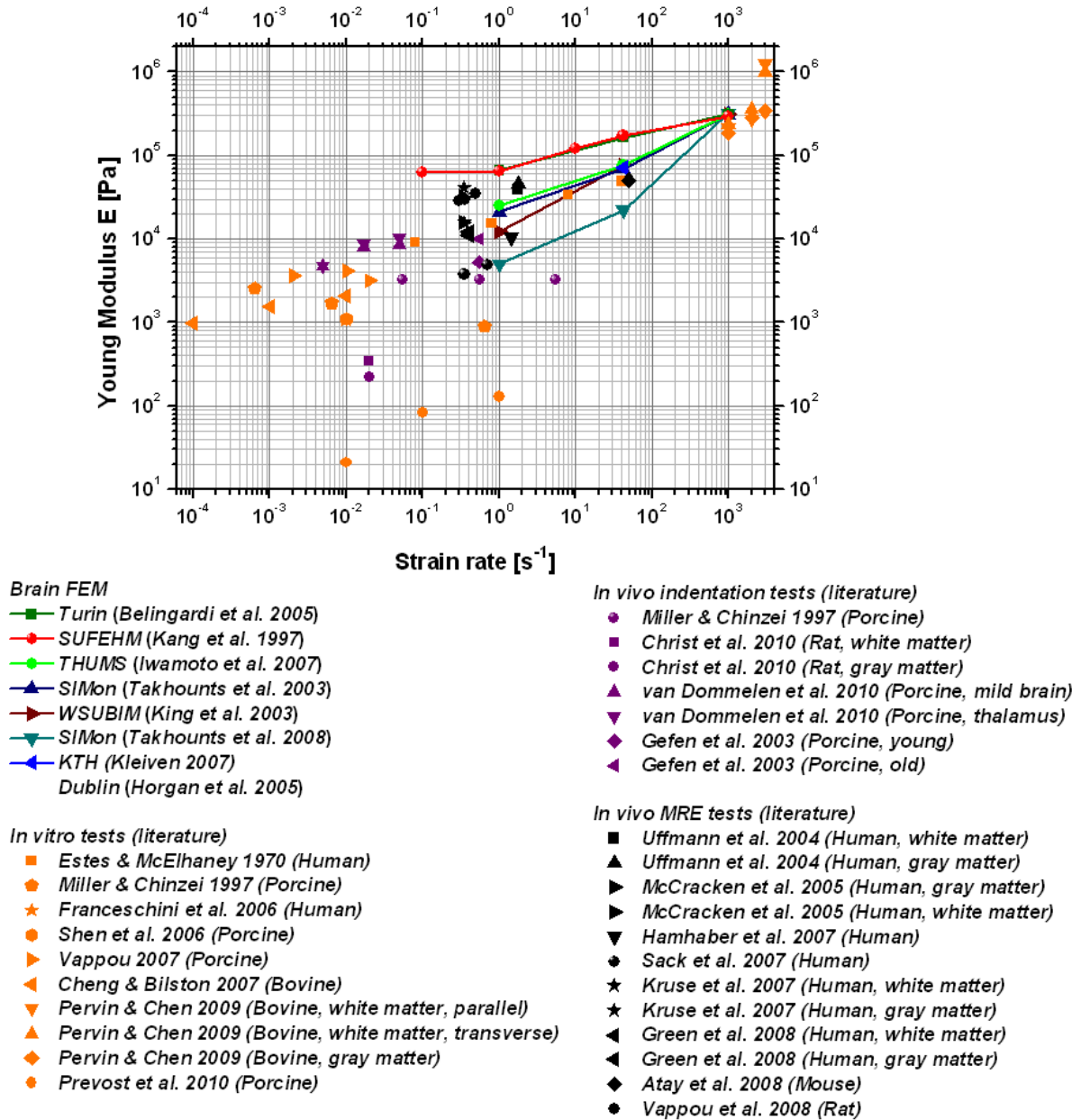


Figure 4 - 17. Comparison of Young modulus versus strain rate from our FEM simulations compared with literature experimental data (from *in vitro*, indentation and MRE tests).

2.3.6 Conclusion

In this section the behavior of each brain FEM model from the literature have been studied on numerical replication of experimental rheological tests in tensile, compression and shear. We observed that only one of these models (KTH) takes non linearities at high strain into account but is not consistent when strain rate varies.

The first conclusions of this section concern pressure. This is independent of the FEM in shear and very few dependants on the model properties in tensile and compression. In that case, pressure will depend on model compressibility as well as long term stiffness.

Whatever the test (tensile, compression or shear) at 1 m.s^{-1} speed, shear wave propagation is observed. The stiffer the FEM, the higher frequency and speed of this wave propagation.

Last observations concern high sensitivity of brain FEM with strain rate. By comparing with literature data the stiffness measured versus strain rate from each model simulation, In terms of dependence on strain rate, the stiffest models best reproduce the *in vivo* behavior of brain matter.

All these aspects have to be taken into account for a more realistic modeling of human brain tissue.

2.4 Conclusion

Numerical simulation on cylindrical numerical samples allowed comparing response of the different brain FEM from the literature. Three main categories of brain FEM are highlighted in function of their stiffness. By comparing results of these simulations with similar experimental tests from the literature, two main observations have been made about properties that have to be conserved for further brain FE modeling:

- An important viscosity, which causes strain rate influence of the model stiffness;
- High stiffness. Indeed stiffest brain FEM are the most able to reproduce *in vivo* brain behavior.

From this study, it seems to be necessary to consider other aspects that have today not been taken into account in existing brain FEM:

- Non linearities, which are cause of increase in stiffness at high strain. Main difficulty for non linear modeling is to ensure stability for a wide velocity range;
- Different mechanical properties in tensile and compression;
- Anisotropy involved by axons fibers, especially in tensile.

These conclusions will underlie a new FE brain tissue model in the continuation of this chapter.

3 Brain anisotropic model

3.1 Introduction

None of the previously presented mechanical laws for brain tissue takes axons and resulting anisotropy into account. The objective of this part is to develop a new constitutive law for brain tissue including the following properties:

- Linearity at small strain;
- Non linearities at high strain;
- Viscosity for strain rate dependence;
- Stability with strain rate;
- Anisotropy, especially in tensile.

According to the conclusions of chapter 2, we assume that mechanical anisotropy is essentially due to axons fibers orientation into the brain. DTI information presented in chapter 2 and the SUFEHM geometry will be coupled with a new anisotropic visco-hyperelastic law in order to propose a new brain FEM implemented under LS-DYNA®. Properties of this new brain FEM model will be illustrated on the simulation of a real-world motorcyclist accident simulation.

3.2 Anisotropic visco-hyperelastic law

3.2.1 Introduction

The aim of this part is to describe the anisotropic visco-hyperelastic law developed for brain tissue and the identifying of its parameters.

3.2.2 Theoretical description

The model developed in this study has been developed by Weiss *et al.* (1996) et Weiss (1998) to include collagen fibers in human tendon model. This material behavior is defined from strain energy function in three components: 2 deviatoric and 1 volumetric as expressed in equation (4 - 12) where $\bar{I}_C = III_C^{-1/3} I_C$ and $\bar{II}_C = III_C^{-2/3} II_C$ are the 2 first invariants of the deviatoric part $\bar{C} = III_C^{-1/3} C$ of right Cauchy-Green strain tensor C .

The soft tissue is considered as a composite material which consists of axon fibers embedded in a softer isotropic (brain matrix) material. The strain energy function of the soft tissue material has three terms, as expressed by equation (4 - 12).

$$W = W_{Matrix}^d(\overline{I}_C, \overline{II}_C) + W_{Fibers}^d(\overline{\lambda}) + W^v(III_C) \quad (4 - 12)$$

I_C , II_C , III_C and $\overline{\lambda}$ are the 3 invariants of the right Cauchy-Green strain tensor \mathbf{C} and the projection of \mathbf{C} along the main orientation of fiber for the considered element, as defined in equation (4 - 13). λ_i are main dilatations and l_0 fibers orientation with l_{AX} , l_{AY} et l_{AZ} coordinates.

$$\begin{cases} I_C = \lambda_1^2 + \lambda_2^2 + \lambda_3^2 \\ II_C = \lambda_1^2 \lambda_2^2 + \lambda_2^2 \lambda_3^2 + \lambda_3^2 \lambda_1^2 \\ III_C = \lambda_1^2 \lambda_2^2 \lambda_3^2 \\ \overline{\lambda} = \sqrt{l_0 \cdot \overline{C} \cdot l_0} \end{cases} \quad (4 - 13)$$

- W_{Matrix}^d The first term models the ground substance matrix as a Mooney-Rivlin material:

W_{Matrix}^d is defines in equation (4 - 14).

$$W_{Matrix}^d(\overline{I}_C, \overline{II}_C) = C_{10}(\overline{I}_C - 3) + C_{01}(\overline{II}_C - 3) \quad (4 - 14)$$

C_{01} et C_{10} , représentent elastic long term response of the material.

- W_{Fibers}^d is defined to capture the behavior of crimped collagen in tension and it works only in the fiber direction defined in the model. Its derivative (i.e., stress) has an exponential function which describes the straightening of the fibers and a linear function once they are straightened past a critical stretch level $\overline{\lambda}$ (projection of deformation along fibers orientation)

$$\overline{\lambda} \frac{\partial W_{Fibers}^d}{\partial \overline{\lambda}}(\overline{\lambda}) = \begin{cases} 0 & 0 < \overline{\lambda} < 1 \\ C_3 \left(e^{FA * C_4 (\overline{\lambda} - 1)} - 1 \right) & \overline{\lambda} \geq 1 \end{cases} \quad (4 - 15)$$

The tissu is isotropic in compression and anisotropic in tensile, due to the presence of the fibers. This result is in accordance with the observation of Miller and Chinzei (2002) and Franceschini *et al.* (2006).

- The role of the last term in the strain energy function is to ensure nearly-incompressible material behavior, as presented in equation (4 - 16) where K is the bulk modulus.

$$W^v(I_{III_c}) = \frac{1}{2} K \left(\ln(I_{III_c}^{1/2}) \right)^2 \quad (4 - 16)$$

Viscosity inclusion is done by dissociating the second Piola-Kirchoff stress tensor $\mathbf{S}(\mathbf{C}, t)$ in an hyperelastic $\mathbf{S}^e(\mathbf{C})$ and a viscous $\mathbf{S}^v(\mathbf{C}, t)$, depending on time, according to the equation (4 - 17).

$$\mathbf{S}(\mathbf{C}, t) = \mathbf{S}^e(\mathbf{C}) + \mathbf{S}^v(\mathbf{C}, t) \quad (4 - 17)$$

- $\mathbf{S}^e(\mathbf{C})$ is defined under incompressibility assumption by equation (4 - 18) where p is an hydrostatic pressure.

$$\sigma_i^e = \lambda_i \frac{\partial W_{Matrix}^d}{\partial \lambda_i} + \lambda_i \frac{\partial W_{Fibers}^d}{\partial \lambda_i} - p \quad (4 - 18)$$

For tensile ($\lambda \geq 1$) and compression ($0 < \lambda < 1$) long the fiber orientation axis ($\bar{\lambda} = \lambda$), the maximal principal hyperelastic stress σ is given by equation (4 - 19).

$$\sigma^e(\lambda) = \begin{cases} 2 \left(\lambda^2 - \frac{1}{\lambda} \right) \left(C_{10} + \frac{C_{01}}{\lambda} \right) & 0 < \lambda < 1 \\ 2 \left(\lambda^2 - \frac{1}{\lambda} \right) \left(C_{10} + \frac{C_{01}}{\lambda} \right) + C_3 \left(e^{FA * C_4 (\lambda - 1)} - 1 \right) & \lambda \geq 1 \end{cases} \quad (4 - 19)$$

Fractional Anisotropy coefficient weights principal stretch projection along fiber axis. In case of purely isotropic material (FA=0), the term for fiber will be equal to zero.

In case tensile / compression orthogonal to fiber orientation ($\bar{\lambda} = 1$), σ is given by equation (4 - 20)

$$\sigma^e(\lambda) = 2 \left(\lambda^2 - \frac{1}{\lambda} \right) \left(C_{10} + \frac{C_{01}}{\lambda} \right) \quad (4 - 20)$$

C_{10} and C_{01} , are related to hyperelastic behavior of brain matrix; C_3 and C_4 correspond to the fibers behavior, including an increase in stiffness for brain tissue.

- $\mathbf{S}^v(\mathbf{C})$ is given by equation (4 - 21). $G(t-s)$ is the reduced relaxation function, decomposed in Prony series, as expressed in equation (4 - 22).

$$S^v(C, t) = \int_0^t 2G(t-s) \frac{\partial W}{\partial C(s)} ds \quad (4 - 21)$$

$$G(t) = \sum_{i=1}^6 S_i e^{-t/T_i} \quad (4 - 22)$$

S_i and T_i parameters include viscosity in the model.

3.2.3 Identification of the parameters

Anisotropic visco-hyperelastic parameters for the new law have been identified from *in vitro* and *in vivo* experimental data on brain tissue from a purely anisotropic material (FA=1). Steps for parameters identifying are detailed in the French version of the thesis. These identifications have successively been performed on stress / stretch ratio experimental curves using following data:

- Compression curves obtained *in vitro* by constant strain rate (40s⁻¹) tests by Estes and McElhaney (1970) are applied to brain matrix;
- Parameters at small strain by *in vivo* MRE from Kruse *et al.* (2007) are applied to brain matrix stiffness at small strain;
- Non linearities at high strain in compression for brain matrix on *in vitro* tests from Prevost *et al.* (2010);
- Results of *in vitro* DMA tests from Arbogast *et al.* (1995) and Velardi *et al.* (2006) for fibers 1.8 to 2 times stiffer than brain matrix at small strain;
- Results of *in vitro* DMA tests from Ning *et al.* (2006) for fibers about 9.5 times stiffer than brain matrix at 50% strain.

Theoretical model is presented in Figure 4 - 18. Yellow curve is for global brain matter, blue curve for brain matrix and purple curve for fibers. In compression, fibers have no influence and model curve corresponds to the yellow one. In tensile, depending on fibers orientation and FA value, model curve will be intermediate between blue and yellow curve. Viscosity information completes the model by keeping time relaxation constants similar to the SUFEHM.

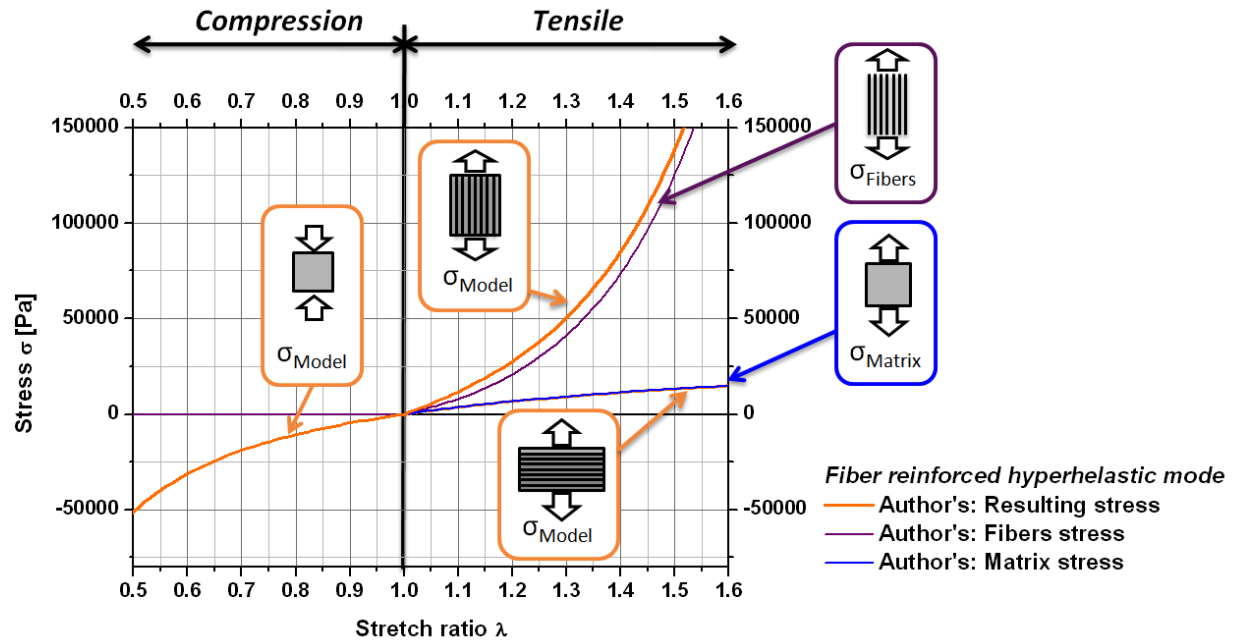


Figure 4 - 18. Courbes de contrainte / dilatation en traction / compression illustrant la loi de comportement développée (en orange). Celle-ci se décompose en traction en une loi pour la matrice cérébral et une loi pour les fibres axonales. Le comportement en traction va se situer entre les courbes caractéristiques de la matrice et des fibres selon l'orientation de ces dernières dans le plan de traction.

3.2.4 Implementation under LS-DYNA® software

Implementation of this new law has been done under LS-DYNA® software. Information about anisotropy (anisotropy vector and FA) is defined for each element from DTI map at FEM scale as presented in chapter 2. Anisotropy vector l_0 is defined for each element in a local frame defined from axis A (coordinates A_x , A_y and A_z in FEM global frame) and B (coordinates B_x , B_y and B_z in FEM global frame).

Parameters implemented for the lax *MAT_092_SOFT_TISSUE_VISCO under LS-DYNA® are summarized in Table 4 - 7. Values previously identified are presented in Table 4 - 8.

The same law but with different l_0 and FA parameters was implemented successively for each of the 5320 SUFEHM brain elements.

LS-DYNA parameters	Theoretical parameters	Units	Meaning
ρ	ρ	$[\text{kg.m}^{-3}]$	Density
K	K	$[\text{Pa}]$	Bulk modulus
C_1	C_{10}	$[\text{Pa}]$	Mooney Rivlin parameters
C_2	C_{01}	$[\text{Pa}]$	
C_3	C_3	$[\text{Pa}]$	Fibers influence parameters
C_4	C_4	-	
S_i	S_i	$[\text{Pa}]$	Long term shear moduli
T_i	T_i	$[\text{s}]$	Time constants
AX, AY, AZ BX, BY, BZ	-	-	Local frame $\mathcal{R}_{(element)}$ definition
LAX, LAY, LAZ	L_{AX}, L_{AY}, L_{AZ}	-	Main anisotropy vector l_0 defined in the local frame

Table 4 - 7 Parameters implemented for the *MAT_092_SOFT_TISSUE_VISCO law under LS-DYNA® software.

	ρ $[\text{kg.m}^{-3}]$	1040	K $[\text{MPa}]$	1125
Matrix	C_1 $[\text{kPa}]$	-1,034	C_2 $[\text{kPa}]$	7,809
Fibers	C_3 $[\text{kPa}]$	13,646	C_4	4,64
Viscosity	S_1 $[\text{kPa}]$	4,5	T_1 $[\text{s}^{-1}]$	1.10^9
	S_2 $[\text{kPa}]$	9,11	T_2 $[\text{s}^{-1}]$	6,8966

Table 4 - 8. Numerical values of parameters implemented for the *MAT_092_SOFT_TISSUE_VISCO law under LS-DYNA® software.

3.2.5 Evaluation of the anisotropic visco-hyperelastic law

This new law has been evaluated on numerical samples with protocols defined in Table 4 - 5. More details and results are available in the French version of this work.

To extend the strain rate range, the SUFEHM is evaluated at five strain rates: 1 s^{-1} (24 mm.s^{-1}), 10 s^{-1} (0.24 m.s^{-1}), 42 s^{-1} (1 m.s^{-1}) et 1000 s^{-1} (24 m.s^{-1}). The stress/stretch ratio curves are related in Figure 4 - 15 and compared with experimental data at same strain rates (*in vitro* data from Estes and McElhaney, 1970, Miller and Chinzei, 1997, Prévost *et al.*, 2010, Pervin and Chen, 2010 and Rashid *et al.*, 2010).

The objective is to investigate stability of the new law with strain rate in different fiber configurations. Results are presented in terms of stress/stretch ratio curves. The simulations are done with three different configurations:

- With fibers along Z axis (along the compression axis) in Figure 4 - 19 ;
- With fibers along X axis (orthogonal to compression axis) in Figure 4 - 20 ;
- With « oblique » fibers (fibers oriented at $(45^\circ, 45^\circ)$ in the global frame) in Figure 4 - 22.

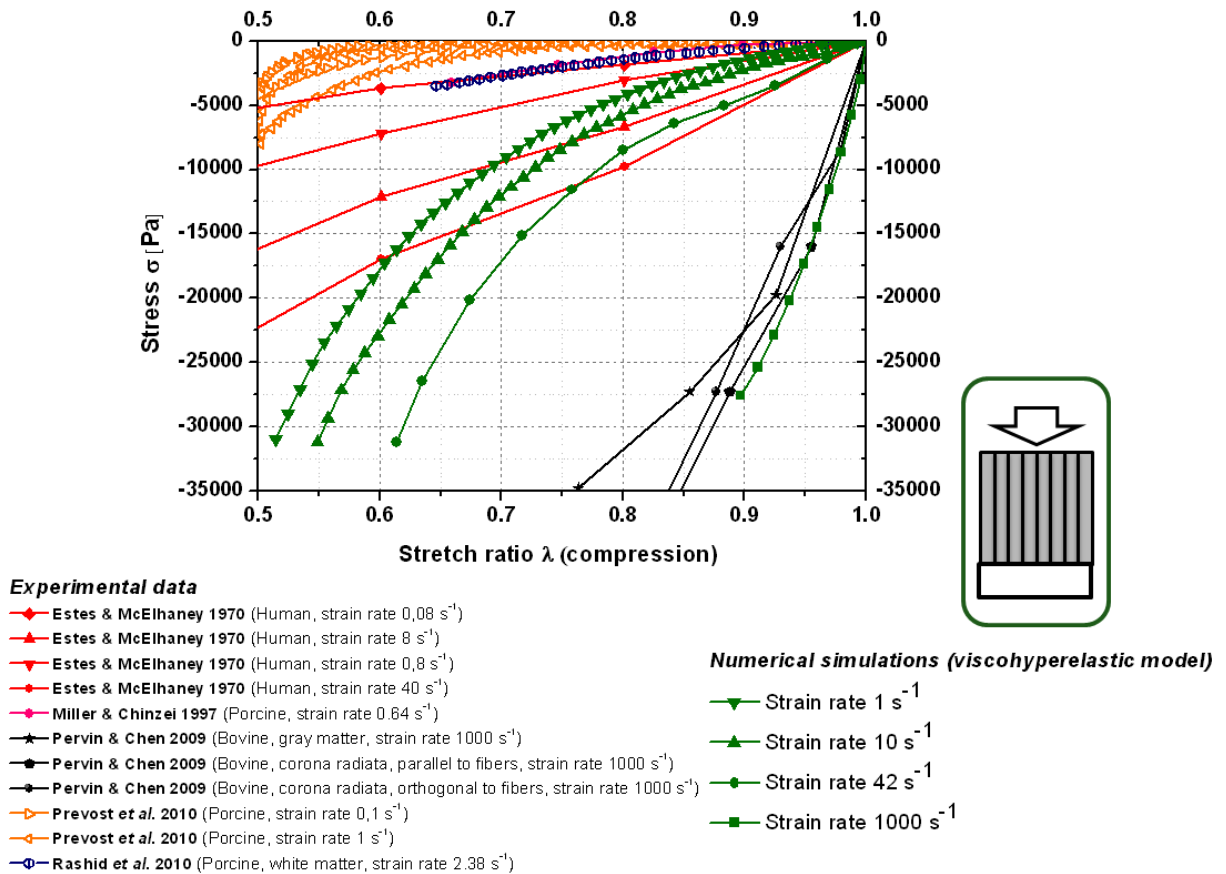


Figure 4 - 19. Comparison at 4 different constant strain rates in compression in terms of stress / stretch ratio for simulations on cylinder model for the new law. Fibers are oriented along Z direction. Curves are compared with data from the literature provided from experimental tests at similar strain rate.

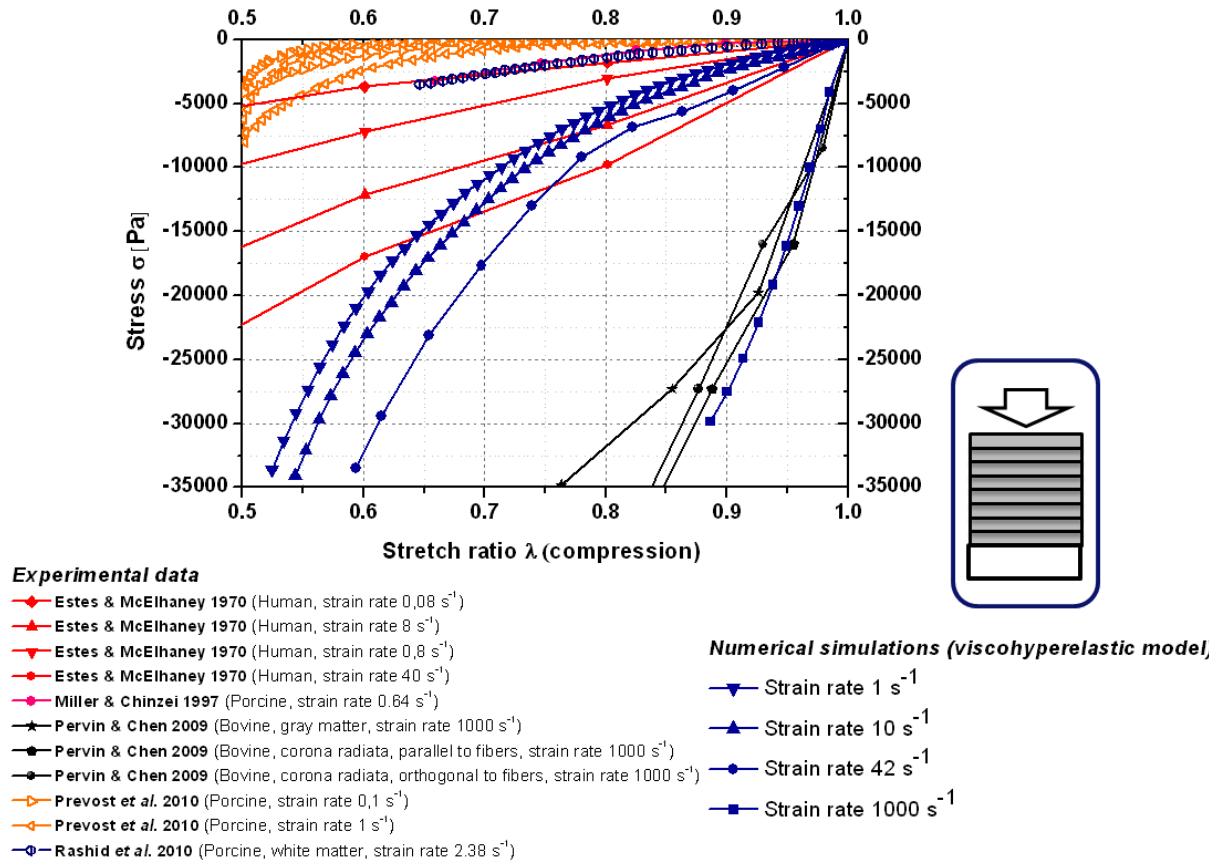


Figure 4 - 20. Comparison at 4 different constant strain rates in compression in terms of stress / stretch ratio for simulations on cylinder model for the new law. Fibers are oriented along X direction. Curves are compared with data from the literature provided from experimental tests at similar strain rate.

Figure 4 - 21 show the Von Mises stresses distribution at 50% strain with fibers oriented along X direction (orthogonal to compression direction) for the new FE model. Model fibers and nearly incompressibility results in tensile and indeed anisotropy in transverse plane (X,Y).

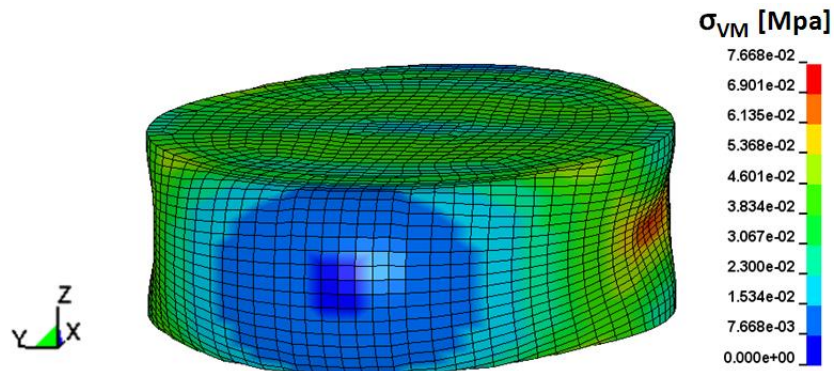


Figure 4 - 21. Illustration of Von Mises stresses distribution at 50% strain with fibers oriented along X direction (orthogonal to compression direction) for the new FE model. Model fibers and nearly incompressibility results in tensile and indeed anisotropy in transverse plane (X,Y).

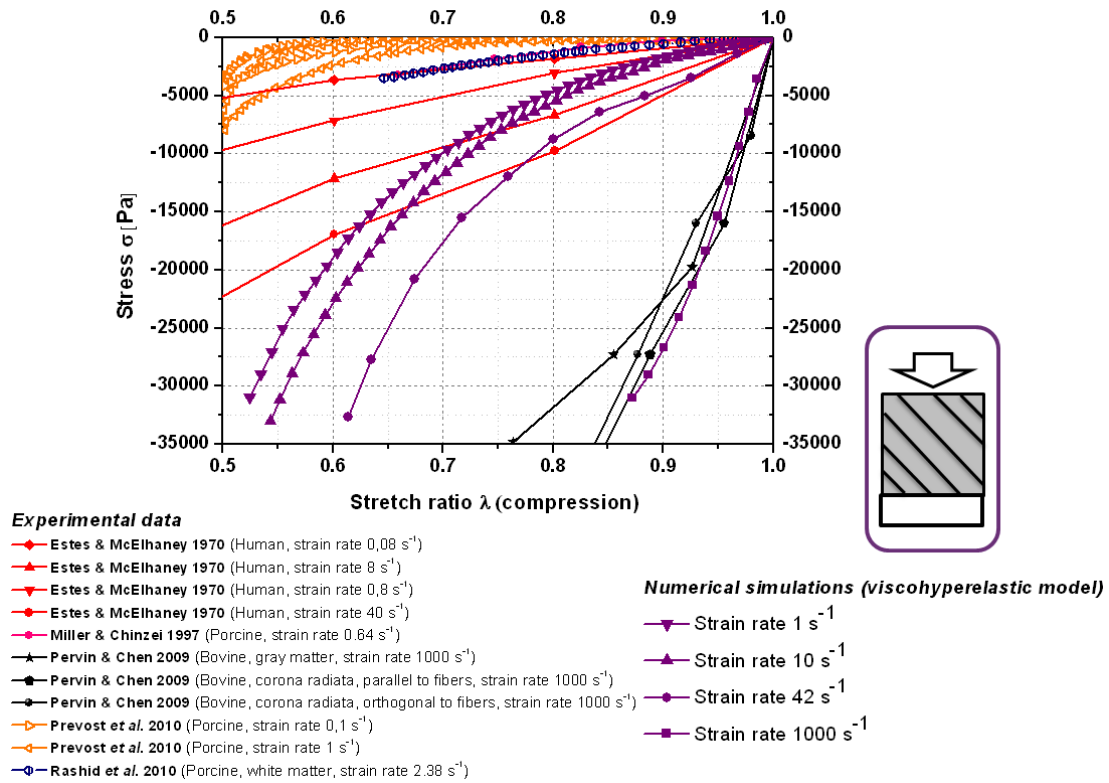


Figure 4 - 22. Comparison at 4 different constant strain rates in compression in terms of stress / stretch ratio for simulations on cylinder model for the new law. Fibers are oriented along “oblique” direction. Curves are compared with data from the literature provided from experimental tests at similar strain rate.

Young modulus is calculated by considering slopes at small strain from Figure 4 - 19, Figure 4 - 20 and Figure 4 - 22. Results are shown in Figure 4 - 23. This figure confirms that, while in tensile fibers have influence when oriented along tensile direction, in compression fibers have influence when oriented in the plane transverse to compression direction.

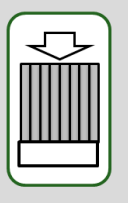
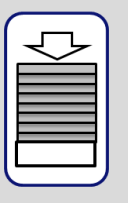
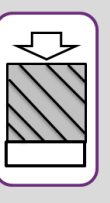
			
Strain rate 1000 s^{-1}	E = 278.5 kPa	E = 283.1 kPa	E = 277.4 kPa
Strain rate 42 s^{-1}	E = 42.6 kPa	E = 43.6 kPa	E = 42.1 kPa
Strain rate 10 s^{-1}	E = 20.1 kPa	E = 23.2 kPa	E = 19.8 kPa
Strain rate 1 s^{-1}	E = 15.7 kPa	E = 19.4 kPa	E = 16.6 kPa

Figure 4 - 23. Young moduli calculated at small strain from the slopes of previous figures, for four different strain rates and in the three fibers configurations.

3.2.6 Conclusion

In this part, a new anisotropic visco-hyperelastic law has been proposed to modeled brain tissue. This model takes fibers density and orientation into account. Following characteristics have been observed on simple simulations of this law implemented under LS-DYNA® software:

- Une grande rigidification du tissu en grandes déformations, d'autant plus grande que la déformation est alignée avec l'orientation des fibres ;
- En traction, une grande influence des fibres sur la rigidité du tissu lorsque celles sont alignées avec l'axe de traction ;
- En compression, une grande influence des fibres sur la rigidité du tissu lorsque celles sont orthogonales à l'axe de compression ;
- Une forte dépendance de la rigidité du tissu avec la vitesse de chargement ;
- Une influence des fibres sur cette dépendance d'autant plus importante que la vitesse est faible.

4 Anisotropic brain Finite Element Model

4.1 Introduction

Next step consists in implementing the new law in the SUFEHM brain geometry. The anisotropic visco-hyperelastic Finite Element Model will be then used as illustration on a motorcyclist accident simulation. Post-processing proposed in Chapter 2 will be then applied to simulation results. The aim is to compare influence of integrating anisotropy in post-processing and by direct inclusion in brain mechanical properties.

4.2 Presentation of the model

The new brain model is obtained by coupling three modalities:

- Brain meshing from the SUFEHM ;
- DTI map at FEM scale, as presented in Chapter 2;
- The anisotropic visco-hyperelastic law previously developed in this chapter.

Coupling between these modalities is illustrated in Figure 4 - 24. In sagittal, coronal and frontal views, the brain SUFEHM meshing and the anisotropy vectors are represented.

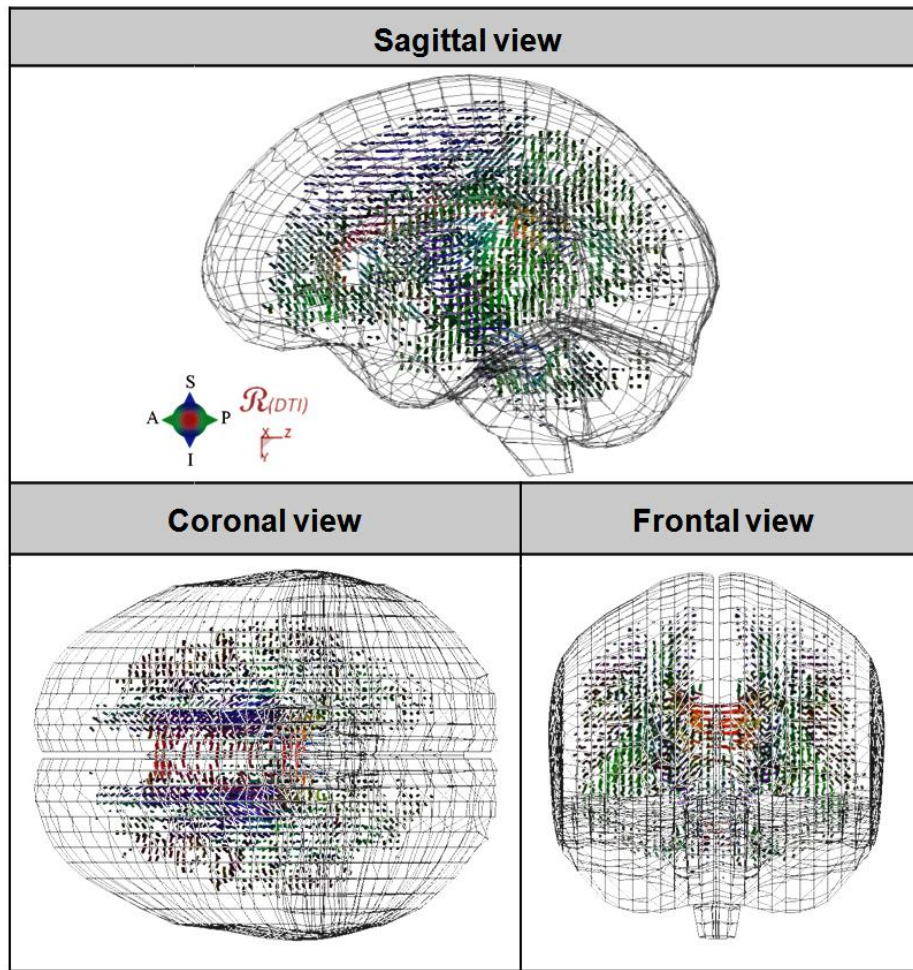


Figure 4 - 24. Illustration of the coupling between anisotropy information and brain FEM meshing. Anisotropy vectors are shown (Red: transverse direction; Green: antero-posterior direction; Blue: vertical direction).

For each element a particular law is implemented, with the parameters exposed in Table 4 - 8 as well as a fractional anisotropy and an anisotropy direction from DTI information.

4.3 Illustration on a real accident case

The developed model was applied to two cases of accidents reported in Chapter 2. The results are analyzed in terms of stress, pressure and strain. The objective is to evaluate the model response in terms of Von Mises stress, pressure, maximum principal strain, von Mises strain, and axonal elongation.

The objective is to successively compare these different values from the simulation of the accident for three models of brain:

- An isotropic homogeneous model (SUFEHM in its actual version). Anisotropy is included in post-processing only for this model (as proposed in chapter 2) to calculate axonale strain ϵ_{axon} ;

- An isotropic heterogeneous model, corresponding to the MRE map with increase of stiffness, as presented in chapter 3. Anisotropy is included in post-processing only for this model to calculate axonale strain ϵ_{axon} ;
- The new anisotropic visco-hyperelastic model developed in this chapter. Axons deformation is also evaluated with this model. However, since FA value is already included in the law, axonal strain will be calculated as strain projection only (ϵ'_{axon} value as defined in chapter 2).

To concentrate investigations on heterogeneity and anisotropy, these three models have similar stiffness (between 13.5 and 49kPa).

These models are used to simulate the case 2 of motorcyclist accident (presented in chapter 2). Maximal values obtained are presented in Table 4 - 9 for the three models in terms of classical stress, pressure and strains as well as axonal strain.

	$\max(\sigma_{VM})$ [kPa]	$\max(P)$ [kPa]	$\max(\epsilon_i)$ [%]	$\max(\epsilon_{VM})$ [%]	$\max(\epsilon_{axon})$ [%]	$\max(\epsilon'_{axon})$ [%]
Isotropic Homogeneous brain (SUFEHM)	57,40	318,2	54	48	52	-
Isotropic Heterogeneous brain (MRE)	23,88	329,3	152	116	126	-
Anisotropic brain	47,64	333,0	85	70	-	64

Table 4 - 9. Maximal values obtained in terms of Von Mises stress, pressure, maximal principal strain, Von Mises strain, and axonal strains.

Results are detailed for classical parameters in the French version, especially in terms of resulting parameters distribution.

Figure 4 - 25 show results from simulations for the new parameters developed in this thesis. It compares locations for the 100 elements sustaining maximal:

- Axonal strain ϵ_{axon} including FA value for the SUFEHM (isotropic);
- Axonal strain ϵ'_{axon} as strain projection only for the new anisotropic brain FEM;

Comparison is made with the epidemiological study on common DAI locations from first chapter.

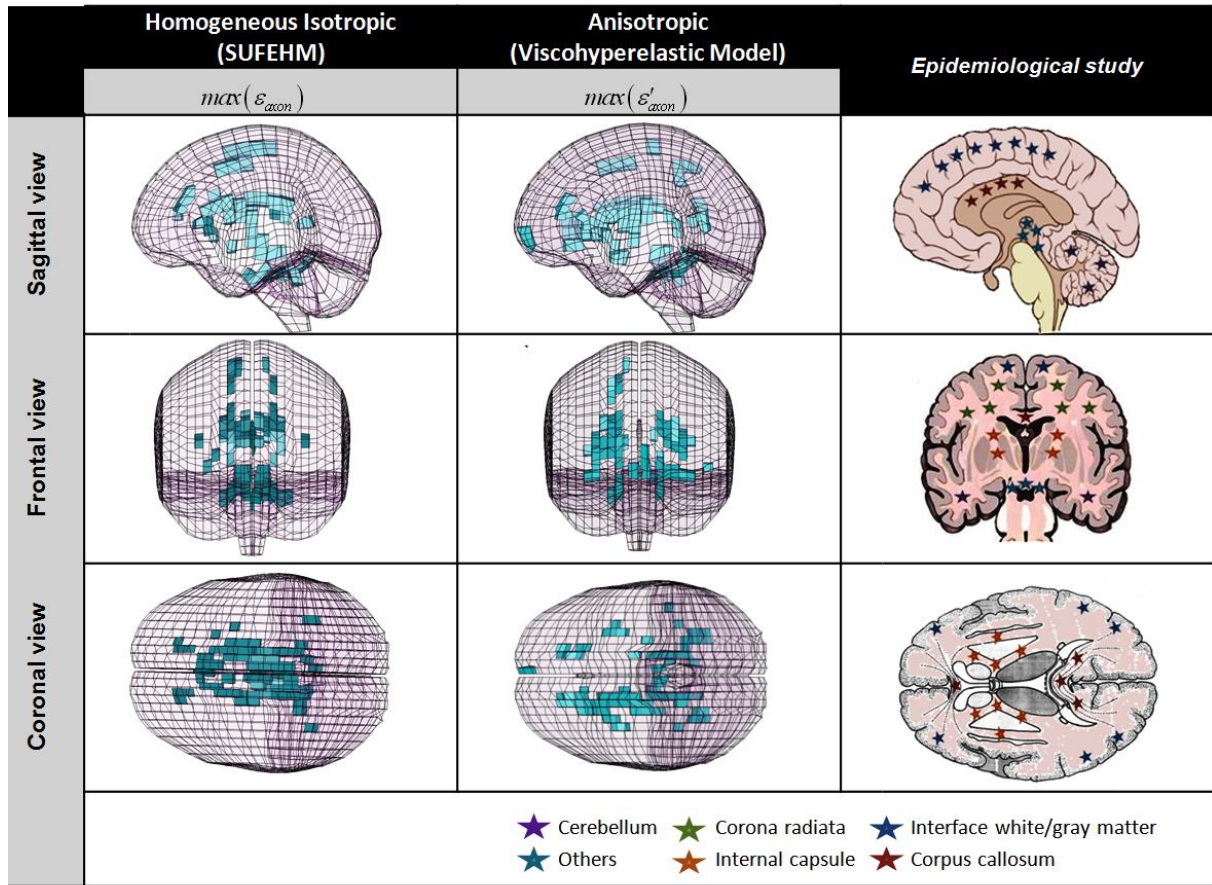


Figure 4 - 25. Location of the 100 elements with maximal axonal strain values for two simulations, between post-processing inclusion and inclusion of anisotropy in brain mechanical law. Comparison is done with the most common locations of DAI.

4.3.1 Conclusion

Although our new anisotropic model has not yet been validated, the previous part tends to confirm the pertinence of post-processing approach developed in Chapter 2 as well as the new associated parameters (axonal strains). According to these results, the two developed approaches seem relevant to the location of DAI:

- With the method of post-processing proposed in chapter 2;
- With the anisotropic brain model developed in this chapter.

Future developments for this work could first concern validation of the new anisotropic visco-hyperelastic model on cadavers impact replications, such as those proposed by Hardy et al. (2001), Yoganandan et al. (1994), Nahum et al. (1977) or Trosseille et al. (1992). In a second step, it would be necessary to reconstruct with this model a great number of accidents to validate axonal elongation ε_{axon} as a pertinent criterion for DAI prediction and location and to propose tolerance limits for this value.

4.4 Conclusion

Application of a new law has been proposed to develop a new anisotropic visco-hyperelastic brain FEM. Following conclusions have been done:

- While the behavior defined for the brain glia remains homogeneous, including different anisotropy degree for each element can take into account mechanical heterogeneity due to the distribution of axonal fibers in the brain;
- Stress and strain parameters (σ_{VM} , ϵ_I et ϵ_{VM}) usually used as DAI criteria are located in low anisotropy parts of the brain ;
- In contrast, the axonal elongation resulting from this law can account for areas with high DAI risk. The similarity of the results of axonal elongation by the anisotropic model with those obtained by the method developed in Chapter 2 on isotropic brain confirms the relevance of post-processing method proposed.

The application to the reconstruction of accidents has highlighted significant influence of structural anisotropy due to the presence of axons, on the mechanical behavior of brain tissue and the formation of DAI, despite the change of scale from the different modalities.

5 Conclusion

In this chapter, most finite element models of the human brain used to simulate accidents were compared by numerical simulation of classical rheological tests. The objective is to compare these models to identify key properties required for numerical modeling of the human brain. Based on the findings of this study, an anisotropic visco-hyperelastic model brain tissue was identified and then implemented in a finite element model of the human brain. The properties of this new anisotropic visco-hyperelastic model were then observed on the reconstruction of a motorcycle accident.

The first conclusions of this chapter show the properties of different brain models from literature. While the stiffness of these models is very sensitive to loading rate, the measurement of intracranial pressure is independent of the model and linked to the conditions of loading only. The propagation of shear waves has been characterized for loads similar to the accident conditions. However, the main finding of this study was to observe that the most rigid models better reflect in vivo properties of human brain tissue.

From these observations and conclusions of previous chapters, the constitutive law developed and implemented in the geometry of the SUFEHM has following properties:

- Consideration of the anisotropy as a stiffening of the brain tissue by the presence of fibers in a preferred direction. This feature leads to different properties of brain tissue in tension and compression;
- Inclusion of non linearities as a strong stiffening of brain tissue at large strain.

The study of this new law has shown that this model is able to be used on a wide range of loading speeds, covering in particular those used in traffic accident. The application of this new model on simulated accident showed that insertion of the fiber density distribution in the constitutive law can include heterogeneity in the brain, without change in the behavior law of the homogeneous brain matrix. The axonal elongation, similar to post-processing proposed in Chapter 2, makes it possible not only to strengthen this tool but also to show that our model anisotropic visco-hyperelastic was likely to assess areas with the highest axonal elongation and the highest DAI risk.

Following this study, we have a new and original anisotropic visco-hyperelastic human brain model, which include brain matrix as well as axons fibers in its mechanical law.

Conclusions and future developments

This PhD thesis contributes to impact Biomechanics for a better understanding of Traumatic Brain Injuries (TBI). This work aims at optimizing human brain mechanical modeling by integrating *in vivo* information obtained by recent medical imaging techniques.

Phenomena and factors linked with the main brain injuries are highlighted by studying human brain anatomy as well as physiological consequences of TBI. Explanation and comparison for experimental results between *in vitro* and *in vivo* protocols were proposed from bibliographic study on brain tissue mechanical properties. In spite of the huge disparities of experimental results in the literature, it was concluded that *in vivo* protocols, using MRE, are the most able to describe deep brain matter in physiological conditions. It can be observed that, due to *in vivo* vascularization, brain tissue stiffness under physiological conditions is in accordance with the highest values proposed by *in vitro* protocols.

Since 1970', Finite Element human brain models have been developed as predicting tools for brain injury understanding in case of head trauma. Models of brain tissue that takes microstructures into account or are used in numerical simulations have been presented.

However, a significant number of simplifying assumptions are used by most of the brain Finite Element Models (FEM) related in the literature:

- Linearity of the constitutive law for brain tissue, even at high strain level;
- Brain tissue mechanical parameters identified from *in vitro* experimental data;
- Isotropy of brain material;
- Homogeneity of brain material.

Consequently, first step consisted of developing a new post-processing tool that can be applied on accident simulations performed under LS-DYNA® software with the isotropic SUFEHM. The development of this post-processing tool has been done in two steps: first the inclusion of axons distribution from Diffusion Tensor Imaging (DTI) to the brain FEM and, secondly, the calculation of the deformation sustained by axons during head trauma simulation.

In addition to classical mechanical parameters (pressure, stresses and “classical” strains), calculation of strain sustained by axons during impact has been proposed. Diffusion images provided from 12 healthy patients were used. A three dimensional map of diffusion data at FEM scale was developed. At least, one principal diffusion direction (correlated with a “mean” orientation of the axons) and one anisotropy degree (relative to axons density) were allocated to each brain element of the Strasbourg University Finite Element Head Model (SUFEHM).

A new mechanical parameter was calculated as strain projection along principal diffusion direction. This new parameter, named *axonal strain* (ε_{axon}) takes not only anisotropy direction but also fractional anisotropy of the element into account. This strain has been evaluated in post-processing of two motorcyclist accident simulations for prediction and location of Diffuse Axonal Injuries (DAI).

Application of this post-processing for anisotropy inclusion in two accident cases lead to conclude that structural anisotropy, due to axons fibers distribution, is directly source of mechanical anisotropy and also play an important role in DAI appearance. By including a fiber density peculiar to each of the elements, heterogeneity has been induced in axonal strain calculation. This new tool has the advantage of predicting high DAI risk area without modifying brain FEM.

Second part of this work concerns brain heterogeneity. Almost all the existing brain FEM, like SUFEHM, has homogeneous mechanical laws with parameters identified from *in vitro* experimental protocols. However huge disparities can be observed in terms of brain mechanical properties. The aim of this part was to evaluate the influence of brain mechanical parameters on the FEM response in case of impact simulation. Therefore, a heterogeneous law was for the first time applied to brain FEM model by including a three dimensional heterogeneous map obtained by *in vivo* Magnetic Resonance Elastography (MRE). SUFEHM geometry was used to develop an *in vivo* MRE-based heterogeneous viscoelastic linear model of the brain. One elastic and one viscous parameters were implemented in each element. Heterogeneity was obtained by the definition of a viscoelastic model peculiar to each of the elements. In order to attest influence of stiffness as well as of heterogeneity of brain material, four brain FEM models have been successively developed:

- A stiff homogeneous brain FEM (SUFEHM in its actual version);
- A soft heterogeneous brain FEM (corresponding to the MRE 3D map);
- A soft homogeneous brain FEM;
- A stiff homogeneous brain FEM (obtained by rigidifying the MRE 3D map).

Results obtained by simulating two motorcyclist accidents showed that maxima and distribution of intracranial pressure are independent of brain FEM, irrespective of heterogeneity and stiffness. It can be concluded that heterogeneity has influence on accident simulation results only with highly stiff brain material (shear modulus of at least 10kPa).

Post-processing developed in chapter 2 was applied to these heterogeneous simulations in order to couple anisotropy and heterogeneity information. The best correlation between

highest axonal strain and most common DAI locations was observed for the stiffest brain models. Otherwise, while heterogeneity influence response for the stiffest brain models only, it does not influence distribution of the parameters that are commonly used as DAI criteria. Consequently, an anisotropic heterogeneous brain FEM with high stiffness seems to be a realistic solution for head trauma simulation.

Last part of this work is dedicated to the comparison of brain FEM actually used for accident simulation (SUFEHM, KTH, Dublin, WSU, SIMon 2003, SIMon 2008, Turin). Therefore, finite elements simulations of classical rheological tests were performed in shear, tensile and compression. It has been observed that model stiffness is highly sensitive to loading speed. However, pressure was observed to be independent of the brain FEM, depending only on loading. The main conclusion of this study was that the stiffest brain FEM best reproduces *in vivo* mechanical properties of brain tissue during simulations at high strains and high strain rates.

Based on observations and conclusions of the previous chapters, a new original dedicated law for brain tissue was developed and implemented into the SUFEHM geometry under LS-DYNA® software. This new anisotropic visco-hyperelastic law, based in the same time on *in vitro* and *in vivo* results, can be used in a wide speed range and takes the following properties into account:

- Anisotropy due to axon fibers orientation and distribution, which causes increase in brain tissue stiffness. This contributes to makes mechanical properties of the matter different in tensile and in compression;
- The inclusion of non linearities, which causes increase in stiffness at high strain levels;
- Differentiation of axon fibers and brain matrix mechanical behavior.

This new anisotropic visco-hyperelastic model has been used for accident simulation. It has been shown that inclusion of fiber density into the law results in brain heterogeneity, without modifying brain matrix. Axonal elongations calculated from this model in accident simulation give an estimate of brain areas that are most likely to sustain DAI.

At least, we have developed an anisotropic visco-hyperelastic model of brain matter that takes into account time brain matrix and axons fibers at the same time.

This work can be enhanced in a lot of ways. It would be necessary to apply the post-processing method developed in chapter 2 to a high number of accident reconstructions in order to validate “axonal strain” as a relevant criterion for prediction, locations and also proposing tolerance limits for DAI. Moreover, well documented accidents simulations

including medical imaging diagnosis would make it possible to improve relevance of this criterion and to identify precisely DAI locations.

Concerning the heterogeneous model based on MRE map, it would be interesting to include a three dimensional map based on more subjects. Concerning brain modeling, it could be interesting to implement heterogeneity in the viscoelastic component of the new law.

Also remeshing of the brain FEM including ventricles would permit to include anisotropy more precisely in the brain.

References

- Adams, J.H., Doyle, D., Ford, I., Gennarelli, T.A., Graham, D.I. and McLellan, D.R. (1989). *Diffuse axonal injury in head injury: definitions, diagnosis and grading*. Histopathology, 15, pp.49-59.
- Al-Bsharat, A., Hardy, W., Yang, K., Kahlil, T., Tashman, S., and King, A. (1999). *Brain/skull relative displacement magnitude due to blunt head impact: new experimental data and model*. Proc. 43th Stapp Car Crash Conf., Society of Automotive Engineers, pp. 321-332.
- Aldrich, E.F., Eisenberg, H.M., Saydjari, C., Luerksen, T.G., Foulkes, M.A., Jane, J.A., Marshall, L.F., Marmarou, A., and Youn, H.F. (1992). *Diffuse Brain Swelling in severely head-injured children*. J.Neurosurgery, 76, pp.450-454
- Alexander, D.C., Pierpaoli, C., Basser, P.J., and Gee, J.C. (2001). *Spatial transformation of diffusion tensor magnetic resonance images*. IEEE T. Med. Imaging, Vol.20, pp.1131-1139.
- Allsop, D.L., Perl, T.R. and Warner, C.Y. (1991). *Force/deflection and fracture characteristics of the temporoparietal region of the human head*. SAE paper 912907.
- Anderson, R. (2000). A study of the biomechanics of axonal injury. PhD Thesis, University of Adelaide, Australia.
- Anderson, R.W.G., Brown, C.J., Blumbergs, P.C., Scott, G., Finnie, J.W., Jones, N.R. and McLean, A.J. (1999). *Mechanisms of axonal injury: an experimental and numerical study of a sheep model of head impact*. Proceedings of IRCOBI Conference, Sitges (Spain), pp.107-120.
- Arbogast, K.B. and Margulies, S.S. (1997). *Regional differences in mechanical properties of the porcine central nervous system*. Proc. Of the 41st Stapp Car Crash Conf., SAE 973336, pp.293-300.
- Arbogast, K.B. and Margulies, S.S. (1998). *Material characterization of the brainstem from oscillatory shear tests*. Journal of Biomechanics 31, pp.801-807.
- Arbogast, K.B. and Meaney, D.F. (1995). *Biomechanical characterization of the constitutive relationship of the brainstem*. Proc. Of the Society of Automotive Engineers, pp.153-159.
- Arfanakis, K., Haughton, V.M., Carew, J.D., Rogers, B.P., Dempsey, R.J., and Meyerand, M.E. (2002). *Diffusion tensor MR imaging in diffuse axonal injury*. AJNR Am. J. Neuroradiol. 23, pp.794-802.
- Ashby, M.F., Jones, D.R.H. *Matériaux 1. Propriétés et applications*, éd. Dunod (2008, 3rd edition)
- Atay, S.M., Kroenke, C.D. and Sabet, A. (2008). *Measurement of the dynamic shear modulus of mouse brain tissue in vivo by magnetic resonance elastography*. J. Biomech. Eng Volume 130, Issue 2, 021013.
- Bain, A. C., Billiar, K. L., Shreiber, D. I., McIntosh, T. K., and Meaney, D. F. (1996) *In Vivo Mechanical Thresholds for Traumatic Axonal Damage*. AGARD Specialists Meeting, Mescalero, NM.
- Bain, A.C., and Meaney, D.F. (2000). *Tissue-level thresholds for axonal damage in an experimental model of central nervous system white matter injury*, J. Biomech. Eng. 122, pp.615-622.
- Bandak, F.A., Van Der Vorst, M.J., Stuhmiller, L.M., Mlakar, P.F., Chilton, W.E., and Stuhmiller J.H. (1994). *An imaging based computational and experimental study of skull fracture: finite element model development*. Proc. Of the Head Injury Symposium, Washington DC.

- Basser, P.J., Mattiello, J., and Le Bihan, D. (1994). *Estimation of the effective self-diffusion tensor from the NMR spin echo*. J. Magn. Reson. B 103, pp.247-254.
- Belingardi, G., Chiandussi, G. and Gaviglio, I. (2005). *Development and validation of a new finite element model of human head*. Proc. Of the 19th ESV conference, Washington.
- Bilston, L.E., Liu, Z. and Phan-Thien, N. (1997). *Linear viscoelastic properties of bovine brain tissue in shear*. Biorheology 34, pp.377-385.
- Bilston, L.E., Liu, Z. and Phan-Thien, N. (2001). *Large strain behaviour of brain tissue in shear: some new experimental data and differential constitutive model*. Biorheology 38(4), pp.335-345.
- Bossy, J., Bastide, G., Guérin, J., Lasjaunias, P., Lefebvre, D., Prat, D., Roland, J., Salama, J., Müller, F., O'Rahilly, R., Rodesch, G. and Sambuc, P. (1990). *Anatomie clinique – neuro-anatomie*, Springer-Verlag France, Paris.
- Bradshaw, G.A. and Finlay, B.L. (2005). *Natural symmetry*, Nature, 435, 149.
- Brands, D.W.A. (2002). *Predicting brain mechanics during closed head impact - Numerical and constitutive aspects*. Ph.D. Dissertation Thesis, University of Eindhoven, Eindhoven, The Netherlands.
- Brands, D.W.A., Bovendeerd, P.H. and Peters, G.W.M. (1999). *Comparison of the dynamic behaviour of brain tissue and two model materials*. Proc. Of the 43rd Stapp Car Crash Conf., pp.313-320.
- Brands, D.W.A., Bovendeerd, P.H. and Peters, G.W.M. (2000). *The large shear strain dynamic behaviour of in-vitro porcine brain tissue and a silicone gel model material*. Proc. Of the 44th Stapp Car Crash Conf., pp.249-260.
- Brodmann, K. (1909). *Vergleichende Lokalisationslehre der Grosshirnhinde*. Barth, Leipzig.
- Chafi, M.S., Karami, G. and Ziejewski (2010). *Biomedical Assessment of brain dynamic responses due to blast pressure waves*. Annals of Biomedical Engineering, Vol.38, pp.490-504.
- Chatelin, S., Vappou, J., Breton, E., Goetz, C., Choquet, P., Willinger, R. and Constantinesco, A. (2008). *Visco-Elastic Properties of Ex-Vivo and In-Vivo Brain Tissue by Low Field MR-Elastography*, Proceedings of the 7th International Conference on the Ultrasonic Measurement and Imaging of Tissue Elasticity, Lake Travis, Austin, Texas, USA, p.30.
- Cheng, S., Clarke, E.C. and Bilston, L.E. (2008). *Rheological properties of the tissues of the central nervous system: a review*. Medical Engineering & Physics 30, pp.1318–1337.
- Chinn, B.P., Doyle, D., Otte, D., and Schuller, E. (1999). *Motorcyclists head injuries: mechanisms identified from accident reconstruction and helmet damage replication*. Proceedings of IRCOB Conference, pp.53–72.
- Christ, A.F., Franze, K., Gautier, H., Moshayedi, P., Fawcett, J., Franklin, R.J.M., Karadottir, R.T. and Guck, J. (2010). *Mechanical difference between white and gray matter in the rat cerebellum measured by scanning force microscopy*. Journal of Biomechanics.
- Claessens, M., Sauren, F. and Wisman, J. (1997). *Modelling of the human head under impact conditions: a parametric study*. Proc. Of the STAPP Car Crash Conference, paper 973338, pp.315-329.

- Cloots, R.J.H., van Dommelen, J.A.W., Kleiven, S. and Geers, M.G.D. (2010). *Traumatic Brain Injury at multiple length scales: relating Diffuse Axonal Injury to discrete axonal impairment*, IRCOBI Conference, Hanover (Germany), pp.119-130.
- Cosnard, G., Derosier, C. and Bonsignour, A. (1991). *Les traumatismes crânio-encéphaliques, Vignaud-Cosnard IRM crânio-encéphalique*. Vigot éditeur, Paris, pp.410-424..
- Darvish, K.K. and Crandall, J.R. (2001). *Nonlinear viscoelastic effects in oscillatory shear deformation of brain tissue*. Medical Engineering & Physics 23, pp.633-645.
- Deck, C. (2004). *Modélisation par éléments finis des lésions crânio-encéphaliques. Application à l'optimisation du casque vis-à-vis de critères biomécaniques*. PhD Thesis, University of Strasbourg, France.
- Deck, C., and Willinger, R. (2008). *Head injury prediction tool for predictive systems optimization*. 7th European LS-DYNA Conference.
- Deck, C., and Willinger, R. (2008). *Improved head injury criteria based on head FE model*. International Journal of Crashworthiness, Vol.13, No6, pp.667-678.
- DiMasi, F., Marcus, J., and Eppinger, R. (1991). *3D anatomic brain model for relating cortical strains to automobile crash loading*. Proc. Of the International Technical Conference on Experimental Safety Vehicles, NHTSA, Vol.2, pp.916-923.
- Dodgson, M.C.H. (1962). *Colloidal structure of brain*. Biorheology 1, pp.21-3.
- Donnelly, B.R. and Medige, J. (1997). *Shear properties of human brain tissue*. Journal of Biomechanical Engineering, 119, pp.423-432.
- Donnelly, B.R. (1998). *Brain tissue material properties: A comparison of results*. Biomechanical Research: Experimental and Computational. Proceedings of the 26th International Workshop, 6, pp.47-57.
- Elkin, B.S., Ilankovan, A. and Morrison III, B (2010). *High rate, regional mechanical properties of the porcine brain: cross-comparison with two methods of indentation*. IRCOBI Conference, Hanover, Germany.
- El-Shimi, A.F. (1977). *In vivo skin friction measurements*. J. Soc.Cosmet. Chem. 2-8, pp.37-51.
- Estes, M.S. and McElhaney, J.H. (1970). *Response of brain tissue to compressive loading*. Proc. Of the 4th ASME Biomechanics Conf., 70-BHF-13.
- Fallenstein, G.T. and Hulse, V.D. (1969). *Dynamic mechanical properties of human brain tissue*. Journal of Biomechanics 2, pp.217-226.
- Faul, M., Xu, L., Wald, M.M., and Coronado, V.G. (2010). *Traumatic Brain Injury in the United States: emergency department visits, hospitalizations and deaths 2002-2006*. Atlanta (GA): Centers for Disease Control and Prevention, National Center for Injury Prevention and Control.
- Faul, M., Wald, M.M., Rutland-Brown, W., Sullivent, E.E. and Sattin R.W. (2007). *Using a cost-benefit analysis to estimate outcomes of a clinical treatment guideline: testing the brain trauma foundation guidelines for the treatment of severe Traumatic Brain Injury*. J. Trauma, 63, pp. 1271-1278.

- Finkelstein, E., Corso, P., and Miller, T. (2006). *The incidence and economic burden of injuries in the United States*. New York (NY): Oxford University Press.
- Franceschini, G., Bigoni, D., Regitnig, P. and Holzapfel, G. A. (2006). *Brain tissue deforms similarly to filled elastomers and follows consolidation theory*. J. Mech. Phys. Solids 54, pp.2592-2620.
- Gadd, C.W. (1966). *Use of a weighted- impulse criterion for estimating injury hazard*. Proc. 10th Stapp Car Crash Conf., pp. 164-174.
- Galford, J. E. and McElhaney, J.H. (1970). *A viscoelastic study of scalp, brain and dura*. Journal of Biomechanics 3, pp.211-221.
- Gefen, A., N. Gefen, Q. Zhu, R. Raghupathi, and Margulies, S. S. (2003). *Age-dependent changes in material properties of the brain and braincase of the rat*. J. Neurotrauma. 20, pp.1163–1177.
- Gennarelli, T.A. (1997). *The pathology of traumatic brain injury*. Neuroscientist 3, pp.73-81.
- Gennarelli, T.A. and Graham, D.I. (1998). *Neuropathology of the head injuries*. Seminars in clinical neuropsychiatry (3), pp.160-175.
- Gennarelli, T.A., Thibault, L.E., Adams, H., Graham, D.I., Thompson, C.J., and Marcincin, R.P. (1982). *Diffuse Axonal Injury and traumatic coma in the primate*. American Neurological Association 0364-5134/82/120564-11, pp.564-574.
- Gentry, L.R., Godersky, J.C., and Thompson, B. (1988). *MR Imaging of head trauma: review of the distribution and radiopathologic features of traumatic lesions*. AJR 150, pp. 663-672.
- Gentry, L.R., Godersky, J.C., Thompson, B., and Dunn, V.D. (1988). *Prospective comparative study of intermediate-field MR and CT in the evaluation of closed head trauma*. AJR 150, pp.673-682.
- Ghajar, J. (2000). *Traumatic brain injury*. The Lancet, vol. 356.
- Good, C. and Thannhauser, S. (2010). *Comparison of linear, rotational and finite element threshold of brain injury for impacts at multiple locations to the head*. Proc. Of the 20th Canadian Multidisciplinary Road Safety Conference, Niagara Falls, Ontario.
- Graham, D.I., and Genarelli, T.A. (1997). *Trauma – blunt head injury*. Graham DI, Lantos PL (eds) Greenfield's neuropathology. Arnold, London Sidney Auckland 1, pp.197–262.
- Green M, Bilston L and Sinkus R. (2006). *High resolution 3D Brain MR-Elastography*. Proc. Intl. Soc. Mag. Reson. Med. 14.
- Green M, Bilston L and Sinkus R. (2008). *In vivo brain viscoelastic properties measured by magnetic resonance elastography*. NMR Biomed 2008;21, pp.755–64.
- Greenleaf, J.F., Fatemi, M. and Insana, M. (2003). *Selected methods for imaging elastic properties of biological tissues*. Annual review of Biomedical Engineering, 5, pp.57-78.
- Hamhaber, U., Grieshaber, F.A., Nagel, J.H. and Klose, U. (2003). *Comparison of quantitative shear wave mr-elastography with mechanical compression tests*. Magnetic Resonance in Medicine, 49(1), pp.71-77.
- Hamhaber, U., Sack, I., Papazoglou, S., Rump, J., Klatt, D. and Braun, J. (2007). *Three-dimensional analysis of shear wave propagation observed by in vivo magnetic resonance elastography of the*

- brain*. Acta Biomater; 3(1), pp.127–37.
- Hardy, W., Foster, C., Mason, M., Yang, K., King, A. and Tashman, S. (2001). *Investigation of head injury mechanisms using neutral density technology and high speed biplanar x-ray*. Stapp Car Crash Journal, Vol. 45, pp.337-368.
- Hardy, W.N., Foster, C.D., Mason, M.J., Yang, K.H., King, A.I., and Tashman, S. (2001). *Investigation of head injury mechanisms using neutral density technology and high-speed biplanar X-ray*. Stapp Car Crash Journal, pp.375.
- Herrmann, L.R., and Peterson, F.E. (1968). *A numerical procedure for viscoelastic stress analysis*. Proceedings of the 7th Meeting of ICRPG Mechanical Behavior Working Group, Orlando.
- Horgan, T.J. (2005). *A finite element model of the human head for use in the study of pedestrian accidents*. PhD Thesis, University of Dublin, Ireland.
- Horsfield, M.A. (1999). *Mapping eddy current induced fields for the correction of diffusion-weighted echo planar images*. Magn Reson Imaging 17, pp.1335–1345.
- Hosey, R.R., and Liu, Y.K. (1980). *A homoemorphic finite element model of impact head and neck injury*. I.C.P. of Finite Elements in Biomechanics, Vol.2, pp.379-401.
- Hrapko, M., van Dommelen, J.A., Peters, G.W. and Wismans, J.S. (2006). *The mechanical behaviour of brain tissue: large strain response and constitutive modeling*. Biorheology, 43(5), pp.623–36.
- Hrapko, M., van Dommelen, J.A.W., Peters, G.W.M. and Wismans, J.S.H.M. (2008). *The Influence of Test Conditions on Characterization of the Mechanical Properties of Brain Tissue*. Journal of Biomechanical Engineering 130(3): 031003-10.
- Hrapko, M., van Dommelen, J.A.W., Peters, G.W.M. and Wismans, J.S.H.M. (2010). *On the consequences of non linear constitutive modelling of brain tissue for injury prediction with numerical head models*. International Journal of Crashworthiness, Vol.14, No.3, pp.245-257.
- Kang, H.S., Willinger, R., Diaw, B.M., and Chinn, B. (1997). *Validation of a 3D human head model and replication of head impact in motorcycle accident by finite element modeling*. Proc. 41th Stapp Car Crash Conf., Society of Automotive Engineers, Lake Buena Vista, USA, pp. 329-338.
- Kastler, B., Vetter, D., Patay, Z. and Germain, P. (2004). *Comprendre l'IRM – manuel d'auto-apprentissage (4^{ème} édition)*, Masson.
- Kelley, B.J., Farkas, O., Lifshitz, J. and Povlishock, J.T. (2006). *Traumatic axonal injury in the perisomatic domain triggers ultrarapid secondary axotomy and Wallerian degeneration*, Exp. Neurol. 198, pp.350–360.
- Kelley, B.J., Farkas, O., Lifshitz, J., and Povlishock, J.T. (2006). *Traumatic Axonal Injury in the perisomatic domain triggers ultrarapid secondary axotomie and wallerian degeneration*. Experimental Neurology, 198, pp.350-360.
- King, A., Yang, K., Zhang, L., and Hardy, W. (2003). *Is head injury caused by linear or angular acceleration?* IRCOB Conference, pp.1-12.
- Klatt, D., Asbach, P., Rump, J., Papazoglou, S., Somasundaram, R., Modrow, J., Braun, J. and Sack, I. (2006). *In vivo determination of hepatic stiffness using steady-state free precession*

- magnetic resonance elastography*. Invest. Radiol. 41(12), pp.841–848.
- Kleiven, S. (2007). *Predictors for traumatic brain injuries evaluated through accident reconstruction*. Proc. 51th Stapp Car Crash Conf., Society of Automotive Engineers paper 2007-22-0003, pp. 81-114.
- Kleiven, S. and Hardy, W.N. (2002). *Correlation of an FE model of the human head with experiments on localized motion of the brain-consequences for injury prediction*. Stapp Car Crash Journal, Vol.46, pp.123-144.
- Koenman, J.B. (1966). *Viscoelastic properties of brain tissue*. Unpublished M.S. Thesis, Case Institute of Technology.
- Kraus, M.F., Susmaras, T., Caughlin, B.P., Walker, C.J., Sweeney, J.A., and Little, D. (2007). *White matter integrity and cognition in chronic traumatic brain injury: a diffusion tensor imaging study*. Brain 130, pp.2508-2519.
- Kruse, S.A., Rose, G.H., Glaser, K.J., Manduca, A., Felmlee, J.P., Jack, Jr. C.R., and Ehman, R. (2007). *Magnetic Resonance Elastography of the brain*. NeuroImage 39, pp.231-237.
- Kruse, S.A., Rose, G.H., Glaser, K.J., Manduca, A., Felmlee, J.P., Jack, C.R.Jr., and Ehman, R.L. (2008). *Magnetic resonance elastography of the brain*. Neuroimage 39, pp.231–237.
- LeBihan, D., Mangin, J.-F., Poupon, C., Clark, C.A., Pappata, S., Molko, N., and Chabriet, H. (2001). *Diffusion Tensor Imaging: concepts and applications*. Journal of Magnetic Resonance Imaging 13, pp.534-546.
- Lewa, C.J. (1991). *Magnetic resonance imaging in the presence of mechanical waves*. Spectrosc Lett 24, pp.55–67.
- Lewa, C.J. and de Certaines, J.D. (1994). *Body temperature mapping by magnetic resonance imaging*. Spect Lett 27, pp.1369-1419.
- Lin, S-C., Shieh, S-J. and Grimm, M.J. (1997). *Ultrasonic measurements of brain tissue properties*. Proc. Of the Symposium of the Centers for Disease Control and Prevention, pp.27-31.
- Mai, J., K., Paxinos, G. and Voss, T. (2007). *Atlas of the human brain*, (3rd edition), Academic Press Elsevier.
- Manduca, A., Lake, D.F. and Ehman, R.L. (2003). *Improved inversion of mr elastography images by spatio-temporal directional filtering*. Proceedings of SPIE – The International Society for Optical Engineering, Vol 5032, I, pp.445-452.
- Manduca, A., Oliphant, T.E., Dresner, M.A., Mahowald, J.L., Kruse, S.A., Amromin, E., Felmlee, J.P., Greenleaf, J.F. and Ehman, R.L. (2001). *Magnetic Resonance Elastography: Non invasive mapping of tissue elasticity*. Medical Image Analysis, 5(4), pp.237-254.
- Marchesseau, S., Heimann, T., Chatelin, S., Willinger, R., Delingette, H. (2010). *Fast porous visco-hyperelastic soft tissue model for surgery simulation: application to liver surgery*
- Marchesseau, S., Heimann, T., Chatelin, S., Willinger, R., Delingette, H. (2010). *Multiplicative Jacobian energy decomposition method for fast porous visco-hyperelastic soft tissue model*. Proceedings of the Medical Image Computing and Computer Assisted Intervention (MICCAI)

Conference, 2010, Beijing, China.

- Marjoux, D., Baumgartner, D., Deck, C., and Willinger, R. (2007). *Head injury prediction capability of the HIC, HIP, SIMon and ULP criteria*. *Accid. Anal. Prev.* 40, pp.1135-1148.
- Marshall, L.F., Gautille, T., Klauber, M.R., Eisenberg, H.M., Jane, J.A., Luerssen, T.G., Marmarou, A. and Foulkes, M.A. (1991). *The outcome of severe closed head injury*. *Journal of Neurosurgery* 75, pp.528-536.
- Maurya, M.V., Bairaria, B.A.K.S., Adya, B.C.M. and Rajesh, C.Y.S. (2006). *Diffuse Axonal Injury*, *MJAFI*, 62, pp.277-279.
- McCracken, P.J., Manduca, A., Felmlee, J.P., and Ehman, R.L. (2005). *Mechanical transient-based magnetic resonance elastography*. *Magn. Reson. Med.* 53, pp.628–639.
- McElhaney, J.H., Melvin, J.W., Roberts, V.L. and Portnoy, H.D. (1973). *Dynamic characteristics of the tissues of the head*. R.M. Kenedi (Editor), *Perspectives in Biomedical Engineering*. MacMillan Press, London, pp.215-222.
- McElhaney, J.H., Roberts, V.L. and Hilyard, J.F. (1976). *Handbook of Human Tolerance*. *Japan Automobile Research Institut.*
- McElhaney, J.H., Stalnaker, R.L. and Estes, M.S. (1969). *Dynamic mechanical properties of scalp and brain*. *Proc. Of the 6th Annual Rocky Mountain Bioengineering Symposium*.
- Mendis, K. (1992). *Finite element modelling of the brain to establish diffuse axonal injury criteria*. PhD Dissert, Ohio State University.
- Metz, H. and Weber, D. (1982). *Interpretations of impact responses of a 3-year-old child dummy relative to child injury potential*. *Proc. Of the 9th Int. Conf. on Experimental Safety Vehicles*.
- Meythaler, J.M., Peduzzi, J.D., Eleftheriou, E., and Novack, T.A. (2001). *Current concepts: diffuse axonal injury-asociated traumatic brain injury*. *Arch. Phys. Med. Rehabil.* 82, pp.1461-1471.
- Miller, K. (1999). *Constitutive model of brain tissue suitable for finite element analysis of surgical procedures*. *Journal of Biomechanics* 32, pp.531-537.
- Miller, K. and Chinzei, K. (1997). *Constitutive modelling of brain tissue: experiment and theory*. *Journal of Biomechanics* 30(11/12), pp.1115-1121.
- Miller, K. and Chinzei, K. (2002). *Mechanical properties of brain tissue in tension*. *Journal of Biomechanics* 35(4), pp.483-490.
- Miller, K., Chinzei, K., Orssengo, G. and Bednarz, P. (2000). *Mechanical properties of brain tissue in-vivo: experiment and computer simulation*. *Journal of Biomechanics* 33, pp.1369-1376.
- Mori, S., Oishi, K., Jiang, H., Jiang, L., Li, X., Akhter, K., Hua, K., Faria, A.V., Mahmood, A., Woods, R., Toga, A.W., Pike, G.B., Neto, P.R., Evans, A., Zhang, J., Huang, H., Miller, M.I., van Zijl, P., and Mazziotta, J. (2008). *Stereotaxic white matter atlas based on diffusion tensor imaging in an ICBM template*. *NeuroImage* 40, pp.570-582.
- Morrison, III B., Cater, H.L., Wang, C. C.-B., Thomas, F.C., Hung, C.T., Ateshian, G.A., and Sundstrom, L.E. (2003). *A tissue level tolerance criterion for living brain developed with an in vitro model of traumatic mechanical loading*. *Stapp Car Crash Journal*, Vol.47, pp.93-105.

- Muthupillai, R., Lomas, D., Rossman, P., Greenleaf, J.F., Manduca, A., and Ehman, R.L. (1995). *Magnetic resonance elastography by direct visualization of propagating acoustic strain waves*. Science 269, pp.1854–1857.
- Nahum, A., Smith, R. and Ward, C. (1977). Intracranial pressure dynamics during head impact. Stapp Car Crash Journal, Vol. 21, pp.336-339.
- Newman, J., Barr, C., Beusenbergh, M., Fournier, E., Shewchenko, N., Welbourne, E., and Withnall, C. (2000). *A new biomechanical assessment of mild traumatic brain injury - Part 2- Results and conclusions*. Proceedings of the IRCOBI Conference, pp.223-234.
- Ng, H.K., Mahaliyana, R.D., and Poon, W.S. (1994). *The pathological spectrum of Diffuse Axonal Injury in blunt head trauma: assessment with axon and myelin strains*. Clinical Neurology and Neurosurgery 96, pp.24-31.
- Nicolle, S., Lounis, M. and Willinger, R. (2004). *Shear properties of brain tissue over a frequency range relevant for automotive impact situations: new experimental results*. Stapp Car Crash J 2004; 48, pp.239–258.
- Nicolle, S., Lounis, M., Willinger and R., Palierne, J.-F. (2005). *Shear linear behavior of brain tissue over a large frequency range*. Biorheology 42, pp.209–223.
- Nikou, C., Heitz, F., Nehlig, A., Namer, I.J. and Armspach, J.-P. (2003). *A robust statistics-based global energy function for the alignment of serially acquired autoradiographic sections*. Journal of Neuroscience Methods 124, pp.93-102.
- Nyquist, G.W., cavanaugh, J.M., Goldberg, S.J. and King, A.I. (1986). *Facial impact tolerance and response*. Proc. Of the 30th STAPP Car Crash Conference, SAE paper 861896, pp.379-389.
- Ommaya, A.K. (1968). Mechanical properties of tissues of the nervous system. Journal of Biomechanics 1, pp.127-138.
- Oudry, J., Perichon, N., Chatelin, S., Allemann, P., Soler, L., Willinger, R. and Sandrin, L. (2009). *Validation of Ultrasound-based Transient Elastography by means of Dynamic mechanical Analysis: Application to In vivo/In vitro Porcine Liver*, Proceedings of the IEEE International Ultrasonics Symposium, 2009, Roma, Italy, p.206.
- Papadakis, N.G., Xing, D., Houston, G.C., Smith, J.M., Smith, M.I., James, M.F., Parson, A.A., Huang, C.L.-H., Hall, L.D. and Carpenter, T.A. (1999). *A study of rotationally invariant and symmetric indices of diffusion anisotropy*. Magn Reson Imaging, 17, pp.881–892.
- Papazoglou, S., Braun, J., Hamhaber, U. and Sack, I. (2005). Two-dimensional waveform analysis in MR Elastography of skeletal muscles. Physics in Medicine and Biology, 50(6), pp.1313.
- Perichon, N., Oudry, J., Chatelin, S., Sandrin, L., Allemann, P., Soler, L. and Willinger R. (2009). *In Vivo Liver Tissue Mechanical Properties By Transient Elastography: Comparison With Dynamic Mechanical Analysis*, International Research Council on Biomechanics of Injury, York, UK.
- Pervin, F. and Chen, W.W. (2009). *Dynamic mechanical response of bovine gray matter and white matter brain tissues under compression*. Journal of Biomechanics 42, pp.731-735.
- Pervin, F. and Chen, W.W. (2010). *Effect of inter-species, gender, and breeding on the mechanical behavior of brain tissue*. NeuroImage.

- Peters, G.W.M., Meulman, J.H. and Sauren, A.A.H.J. (1997). *The applicability of the time/temperature superposition principle to the brain tissue*. Biorheology 34(2), pp.127-138.
- Pettus, E.H., and Povlishock, J.T. (1996). *Characterization of a distinct set of intra-axonal ultrastructural changes associated with traumatically induced alteration in axolemmal permeability*. J. Neurotrauma 11, pp.507-522.
- Pierpaoli, C., and Basser, P.J. (1996). *Toward a quantitative assessment of diffusion anisotropy*. Magn. Reson. Med. 36, pp.893-906.
- Povlishock, J.T. and Pettus, E.H. (1996). *Traumatically induced axonal damage: evidence for enduring changes in axolemmal permeability with associated cytoskeletal change*. Acta Neurochir Suppl (Wien) 66, pp.81– 86.
- Prange, M.T. and Margulies, S.S. (2002). *Regional, directional, and age-dependent properties of the brain undergoing large deformation*. J Biomech Eng 2002;124(2), pp.244–252.
- Prange, M.T., Meaney, D.F. and Margulies, S.S. (2000). *Defining brain mechanical properties: effects of region, direction and species*. Proc. Of the 44th Stapp Car Crash Conf., 2000-01-SC15, pp.205-213.
- Prevost, T.P., Balakrishnan, A., Suresh, S. and Socrate S. (2010). *Constitutive response of brain tissue*. Acta Biomaterialia 1384.
- Rashid, B., Gilchrist, M.D. and Destrade, M. (2010). *Influence of test conditions on dynamic viscoelastic and hyperelastic properties of brain tissue*.
- Robert, S.W. (1959). Control charts tests based on geometric moving averages, Technometrics, 1, pp.239-250.
- Ruan, J.S., Kahlil, T., and King, A.I. (1991). *Human head dynamic response to side impact by finite element modeling*. Journal of Biomechanical Engineering, Vol.113, pp.276-283.
- Sack, I., Beierbach, B., Hamhaber, U., Klatt, D. and Braun, J. (2007). *Noninvasive measurement of brain viscoelasticity using magnetic resonance elastography*. NMR Biomed doi: 10.1002/nbm.1189.
- Sack, I., Beierbach, B., Wuerfel, J., Klatt, D., Hamhaber, U., Papazoglou, S., Martus, P. and Braun, J. (2009). *The impact of aging and gender on brain viscoelasticity*. Neurolmage 46, pp.652–657.
- Sack, I., McGowan, C.K., Samani, A., Luginbuhl, C., Oaken, W. and Plewes, D.B. (2004). *Observation of non linear shear wave propagation using magnetic resonance elastography*. Magnetic Resonance in Medicine 52, pp.842–850.
- Shafieian, M., Darvish, K.K. and Stone, J.R. (2009). *Changes to the viscoelastic properties of brain tissue after traumatic axonal injury*. Journal of Biomechanics 4, pp.2136-2142.
- Shuck, L.Z. and Advani, S.H. (1972). *Rheological response of human brain tissue in shear*. ASME Journal of Basic Engineering 94, pp.905-911.
- Shuck, L.Z., and Advani, S.H. (1972). *Rheological response of human brain tissue in shearing*. ASME Journal of Biomechanical Engineering, pp.905-911.
- Shuck, L.Z., Haynes, R.R. and Fogle, J.L. (1970). *Determination of viscoelastic properties of human*

- brain tissue*. ASME Paper n° 70-BHF-12.
- Shugar, T.A. (1977). *A finite element head injury model*. Report No DOT HS 289-3-550-TA, Vol.1.
- Sinkus, R., Tanter, M., Catheline, S., Lrenzen, J., Kuhl, C., Sondermann, E. and Fink, M. (2005). *Imaging anisotropic and viscous properties of breast tissue by Magnetic Resonance Elastography*. *Magnetic Resonance in Medicine* 53, pp.372–387.
- Smith, D.H., Meaney, D.F., and Shull, W.H. (2003). *Diffuse axonal injury in head trauma*. *J. Head Trauma Rehabil.* 18, pp.307-316.
- Standring, S. (2005). *Gray's Anatomy: The Anatomical Basis of Clinical Practice (39th edition)*, edition Elsevier Churchill Livingstone.
- Stejskal, E.O. and Tanner, J.E and (1965). *Spin diffusion measurements: spin-echoes in the presence of a time-dependent field gradient*. *J. Chem. Phys.* 42, pp.288-292.
- Tagliaferri, F., Compagnone, C., Korsic, M., Servadei, F. and Kraus, J.A.(2006) *A systematic review of brain injury epidemiology in Europe*. *Acta Neurochir*, 148, pp.166-172.
- Takhounts, E.G. (1998). *The experimental determination of constitutive equations of human and bovine brain tissue*. PhD Dissertation Thesis, University of Virginia.
- Takhounts, E.G., Crandall, J.R. and Darvish, K.K. (2003). *On the importance of brain tissue under large deformations*. *Proc. Of The Stapp Car Crash Conf.*, pp.79-92.
- Takhounts, E.G., Hasija, V., Ridella, S.A., Tannous, R.E., Campbell, J.Q., Malone, D., Danelson, K., Stitzel, J., Rowson, S., and Duma, S (2008). *Investigation of Traumatic Brain Injuries Using the Next Generation of Simulated Injury Monitor (SIMon) Finite Element Head Model*. *Stapp Car Crash Journal* 52, pp.1–32.
- Tamura, A., Nagayama, K., and Matsumoto, T. (2007). *Variation in nerve fiber strain in brain tissue subjected to uniaxiale stretch*. *Proc. 51th Stapp Car Crash Conf.*, Society of Automotive Engineers, pp. 139-154.
- Tazarourte, K., Bensalah, N., Rebillard, L. and Vigué, B. (2008). *Epidémiologie des traumatismes cranniés*. MAPAR, pp.141-149.
- Thibault, K.L. and Margulies, S.S. (1998). *Age-dependant material properties of the porcine brain cerebrum: effect on pediatric inertial head injury criteria*. *Journal of Biomechanics* 31, pp.1119-1126.
- Thibault, L.E. (2003). *Brain injury from the macro to the micro level and back again: what have we learned to date?* *Proceedings of IRCOBI Conference*, Eindhoven (Netherlands), pp.3-25.
- Thibault, L.E. and Gennarelli, T.A. (1985). *Biomechanics and craniocerebral trauma. Central Nervous System Trauma*. Status Report, National Institutes of Health, 24, pp.379-389.
- Thibault, L.E., and Gennarelli, T.A. (1990). *Brain injury: an analysis of neural and neurovascular trauma in the nonhuman primate*. 34th Annual Proceedings of the Association for the Advancement of Automotive Medicine, Des Plaines, IL, pp.337-351.
- Thines, L., Lemarchand, F. and Francke, J.-P. (2008). *Atlas interactif de neuroanatomie clinique*, Elsevier Masson.

- Trosseille, X., Tarrière, C., Lavaste, F., Guillon, F. and Domont, A. (1992). *Development of a FEM of the human head according to a specific test protocol*. Proc. Of the 36th STAPP Car Crash Conference, SAE 922527, pp.235-253.
- Uffmann, K., Maderwald, S., Ajaj, W., Galban, C.G., Mateiescu, S., Quick, H.H. and Ladd, M.E. (2004). *In vivo elasticity measurements of extremity skeletal muscle with MR elastography*. NMR Biomed. 2004;17, pp.181–190.
- Van Dommelen, J.A.W., van der Sande, T.P.J., Hrapko, M. and Peters, G.W.M. (2010). *Mechanical properties of brain tissue by indentation: interregional variation*. Journal of the mechanical behavior of biomedical materials (3), pp.158-166.
- Vappou, J. (2007). *Biomechanical Study of Brain Tissue: in vivo approach using Magnetic Resonance Elastography and modeling of non linear properties*. PhD Thesis, University of Strasbourg, France.
- Vappou, J., Breton, E., Choquet, P., Goetz, C., Willinger, R. and Constantinesco, A. (2007). *Magnetic resonance elastography compared with rotational rheometry for in vitro brain tissue viscoelasticity measurement*. Magma 20 (5–6), pp.273–278.
- Vappou, J., Breton, E., Choquet, P., Willinger, R. and Constantinesco, A. (2008). *Brain viscoelasticity measured by magnetic resonance elastography*. Proc. Of The IRCOBI Conf., pp.441-444.
- Vappou, J., Willinger, R., Breton, E., Choquet, P., Goetz and Constantinesco, A. (2006). *Dynamic viscoelastic shear properties of soft matter by magnetic resonance elastography using a low-field dedicated system*. J. Rheol. 50(4), pp.,531-541.
- Velardi, F., Fraternali, F. and Angelillo, M. (2006). *Anisotropic constitutive equations and experimental tensile behavior of brain tissue*. Biomech Model Mechanobiol 5(1), pp.53–61.
- Wang, H.C. and Wineman, A.S. (1972). *A mathematical model for the determination of viscoelastic behavior of brain in vivo*. Journal of Biomechanics, 5, pp.431-446.
- Ward, C.C., Chan, M., and Nahum, A.M. (1980). *Intracranial pressure: a brain injury criterion*. SAE.
- Weiss, J.A. and Gardiner, J.C. (2001). *Computational modeling of ligament mechanics*. Critical reviews in biomedical engineering, 29(4), pp.1-70.
- Wiegell, M. R., Tuch, D. S., Larsson, H. B.W., and Wedeen, V. J. (2003). *Automatic segmentation of thalamic nuclei from diffusion tensor magnetic resonance imaging*. Neuroimage, 19(2), pp.391-401.
- Willinger, R., Baumgartner, D., Chinn, B. and Neale, M. (2000). *Head tolerance limits derived from numerical replication of real world accidents*. Proceedings IRCOBI, Montpellier (France), pp.209-221.
- Willinger, R., Kang, H.S., and Diaw, B.M. (1999). *3D human head finite element model validation against two experimental impacts*. Annals of Biomed. Eng., vol.27 (3), pp.403-410.
- Willinger, R., Taleb, L., and Pradoura, P. (1995). *Head biomechanics from the finite element model to the physical model*. Proceedings IRCOBI, Brunnen, 1995.
- Xiao, C., Jho, J.Y. and Yee A.F. (1994). Correlation between the shear yielding behavior and secondary relaxations of bisphenol a polycarbonate and related copolymers. Macromolecule, 27,

pp.2761-2768.

Yoganandan, N., Pintar, F.A., Sances, A., Walsh, P.R., Ewing, C.L., Snyder, T. and Snyder, R.G. (1994). *Biomechanics of skull fracture*. Proc. Of the Head Injury Symposium, Washington D.C., pp.227-236.

Zhang, M. and Mak, A.F.T. (1999). *In vivo friction properties of human skin..* Prosthetics and orthotics International, 23, pp.135-141.

Zhang, L., Yang, K., Dwarampudi, R., Omori, K., Li, T., Chang, K., Hardy, W., Kahlil, T., and King, A. (2001). *Recent advances in brain injury research: a new human head model development and validation*. Stapp Car Crash Journal, vol.45.

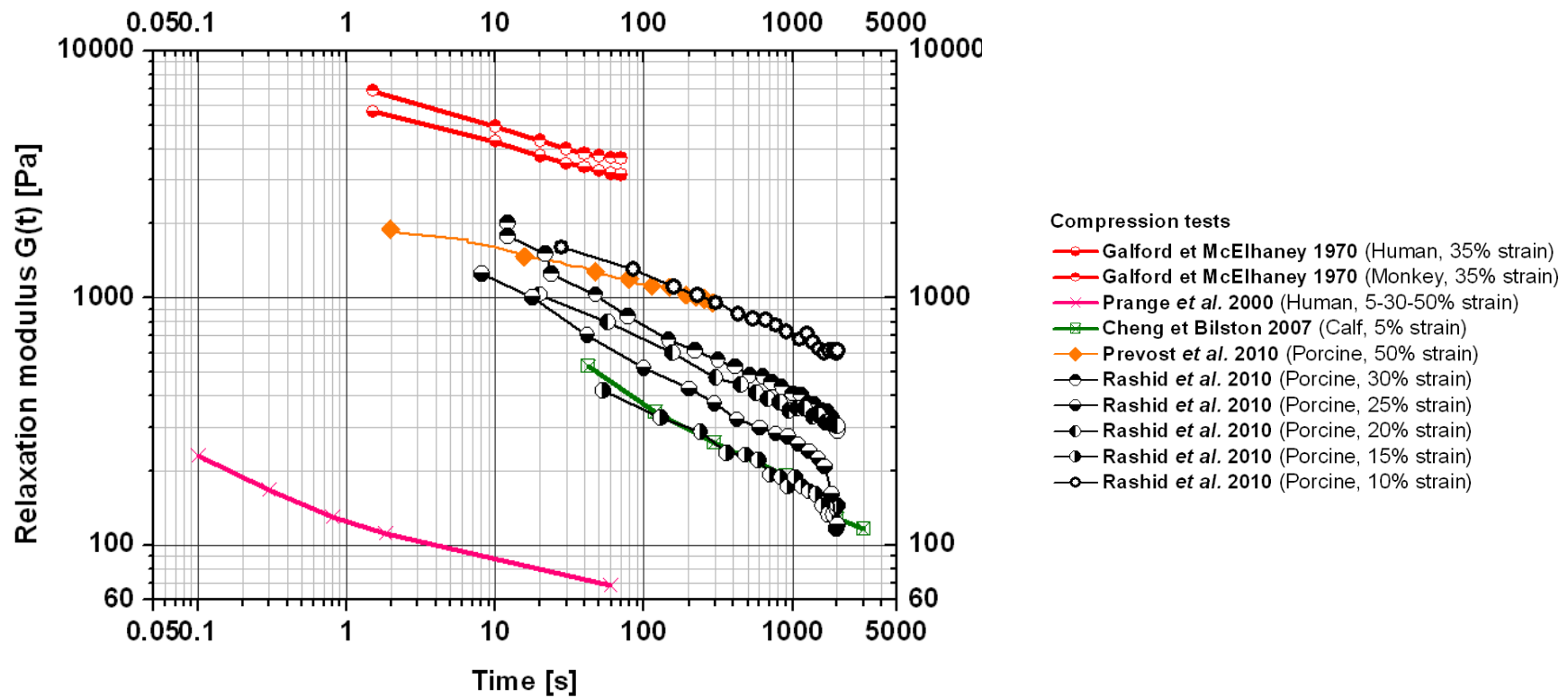
Zhou, C., Kahlil, T.B., and Dragovic, L.J. (1996). *Head injury assessment of a real world crash by finite element modeling*. Proc of the AGARD Conf.

Zhou, C., Khalil, T.B., and King, A.I. (1995). *A 3D human finite element head for impact injury analyses*. Symposium Proc. Of Prevention through Biomechanics, pp.137-148.

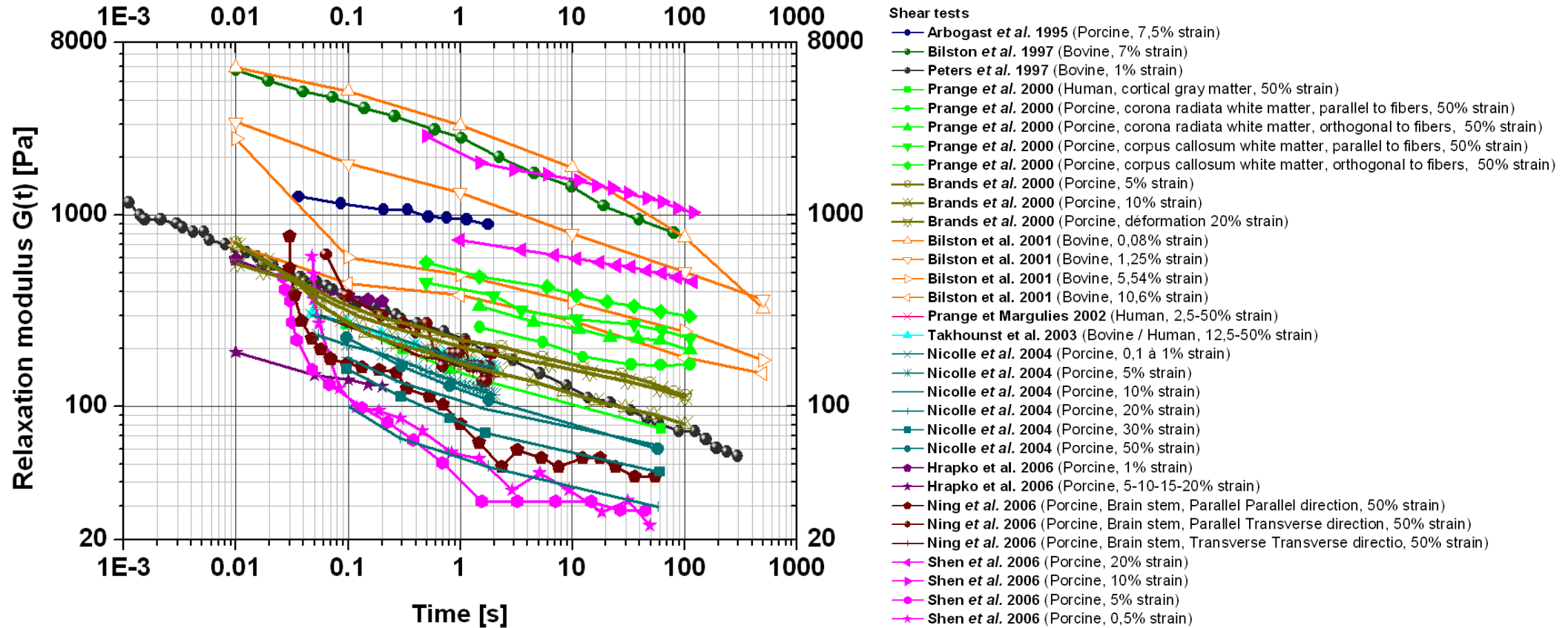
Appendix A

Bibliographical study

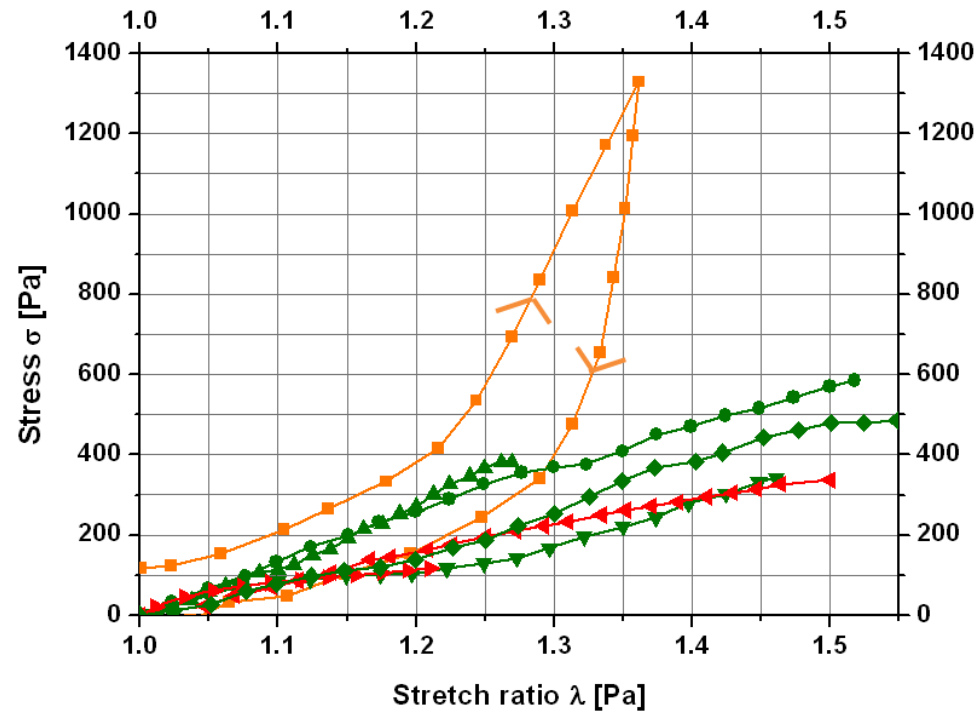




Appendix A. 1. Relaxation modulus from *in vitro* compression tests.



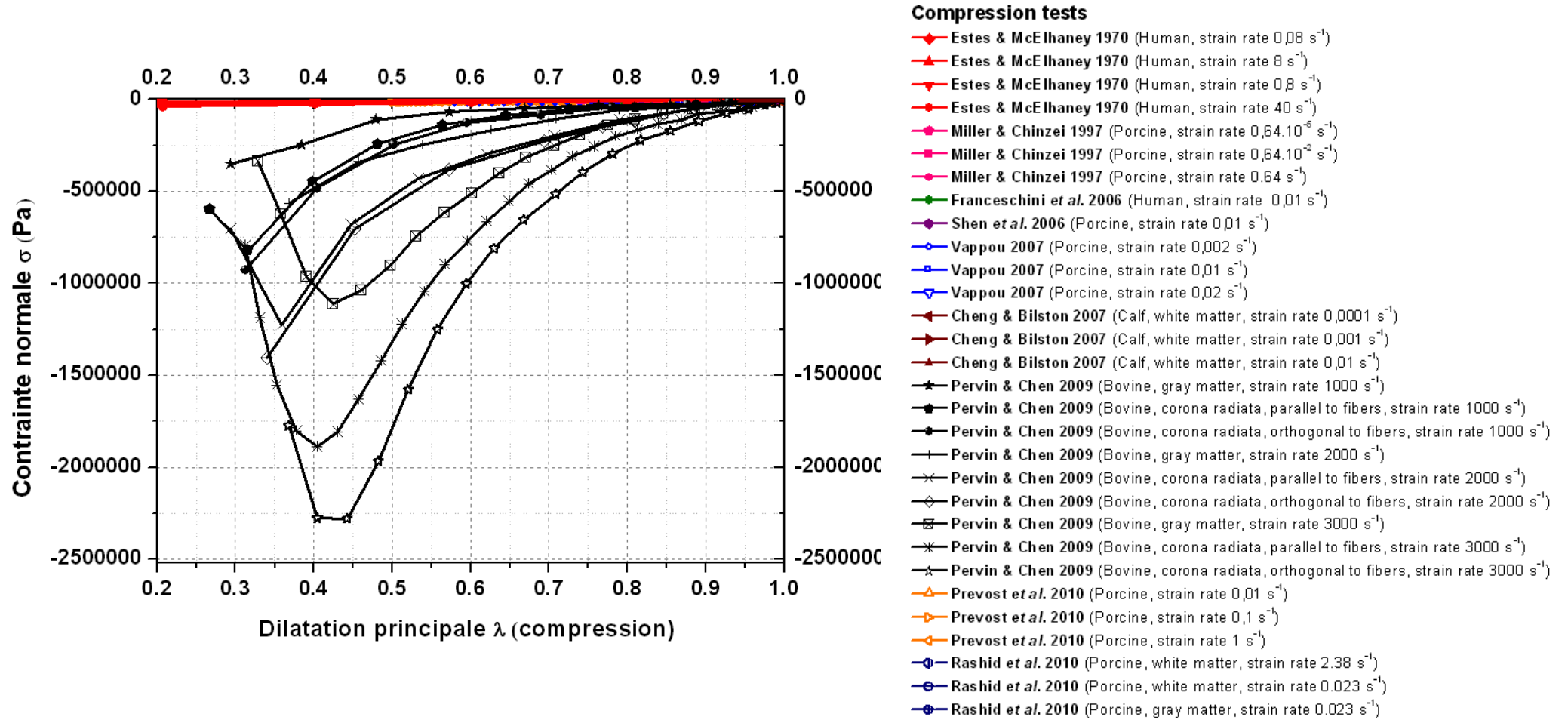
Appendix A. 2. Relaxation modulus from *in vitro* shear tests.



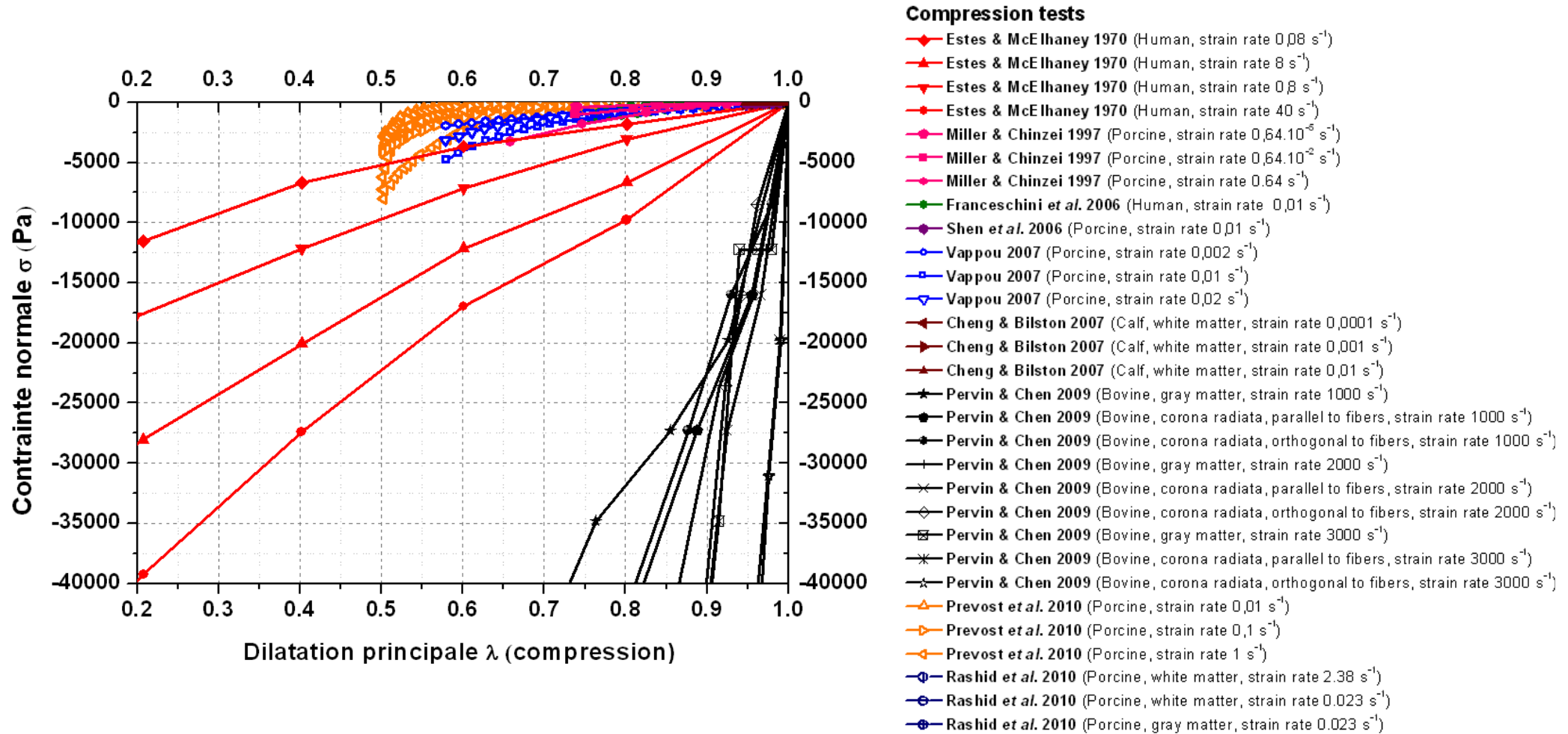
Tensile tests

- ◄ Miller *et al.* 2002 (Porcine, strain rate $0,64s^{-1}$)
- Miller *et al.* 2002 (Porcine, strain rate $0,64.10^{-2}s^{-1}$)
- ◆ Velardi *et al.* 2006 (Porcine, cortex, strain rate $0,01s^{-1}$)
- Velardi *et al.* 2006 (Porcine, corpus callosum, strain rate $0,01s^{-1}$)
- ▲ Velardi *et al.* 2006 (Porcine, corona radiata, parallel to fibers, strain rate $0,01s^{-1}$)
- ▼ Velardi *et al.* 2006 (Porcine, corona radiata, orthogonal to fibers, strain rate $0,01s^{-1}$)
- Franceschini *et al.* 2006 (Human, strain rate $0,01s^{-1}$)

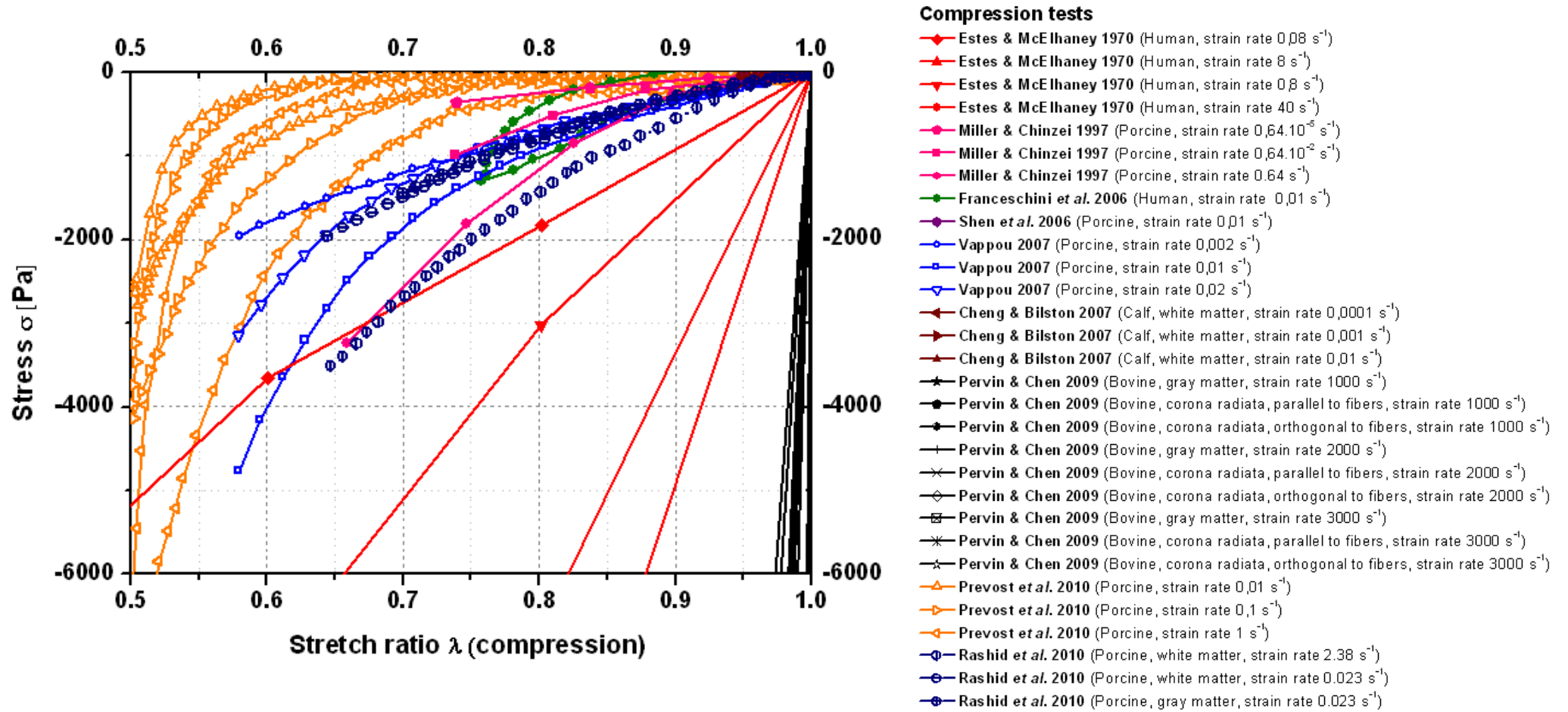
Appendix A. 3. Stress / stretch ratio curves from *in vitro* tensile tests.



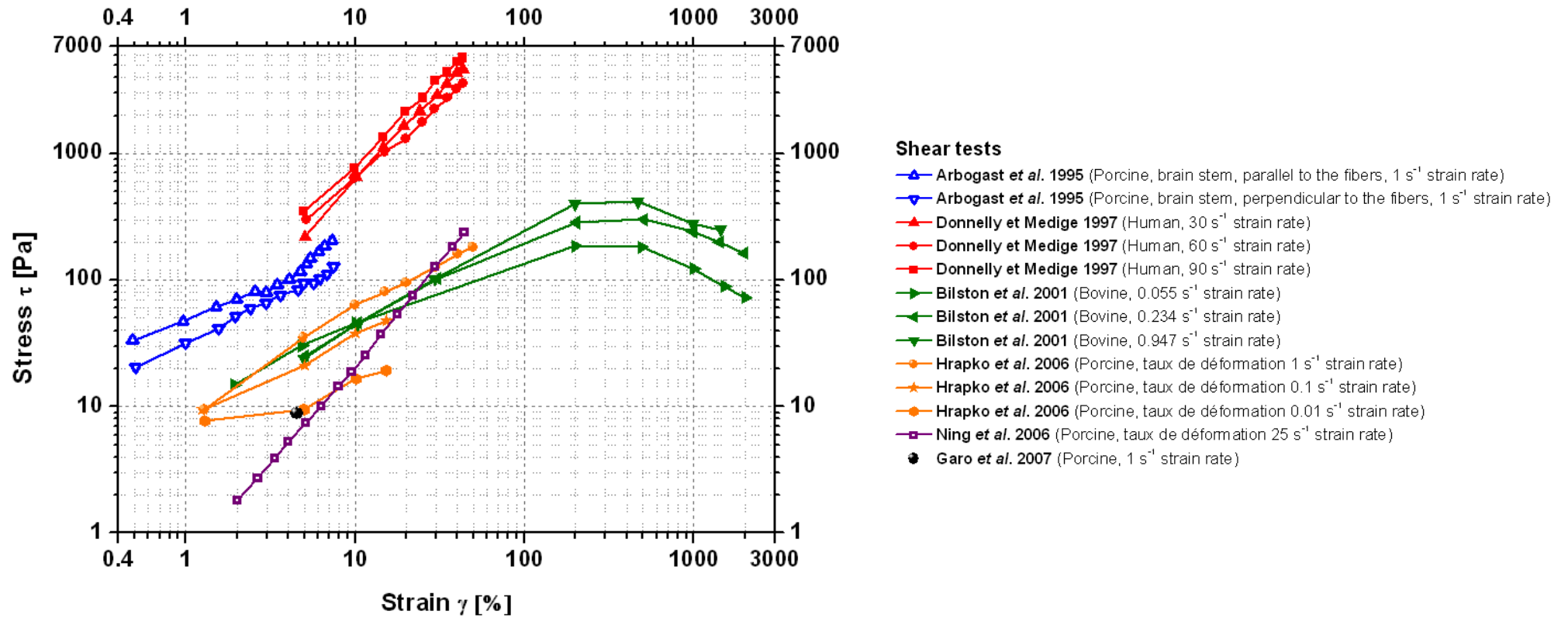
Appendix A. 4. Stress / stretch ratio curves from *in vitro* compression tests at constant strain rate (close to 1000 s^{-1}).



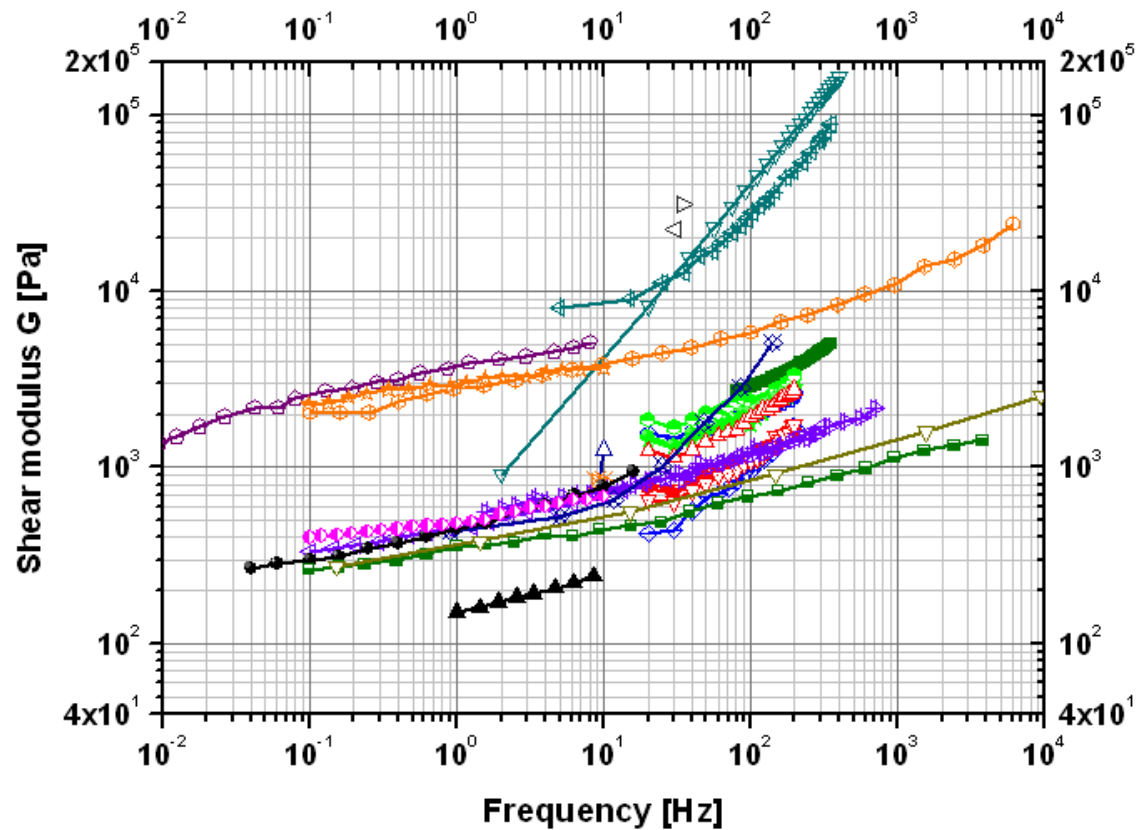
Appendix A. 5. Stress / stretch ratio curves from *in vitro* compression tests at constant strain rate (close to 10 s^{-1}).



Appendix A. 6. Stress / stretch ratio curves from *in vitro* compression tests at constant strain rate (close to 1 s^{-1}).



Appendix A. 7. Stress / strain curves from *in vitro* shear tests at constant strain rate.



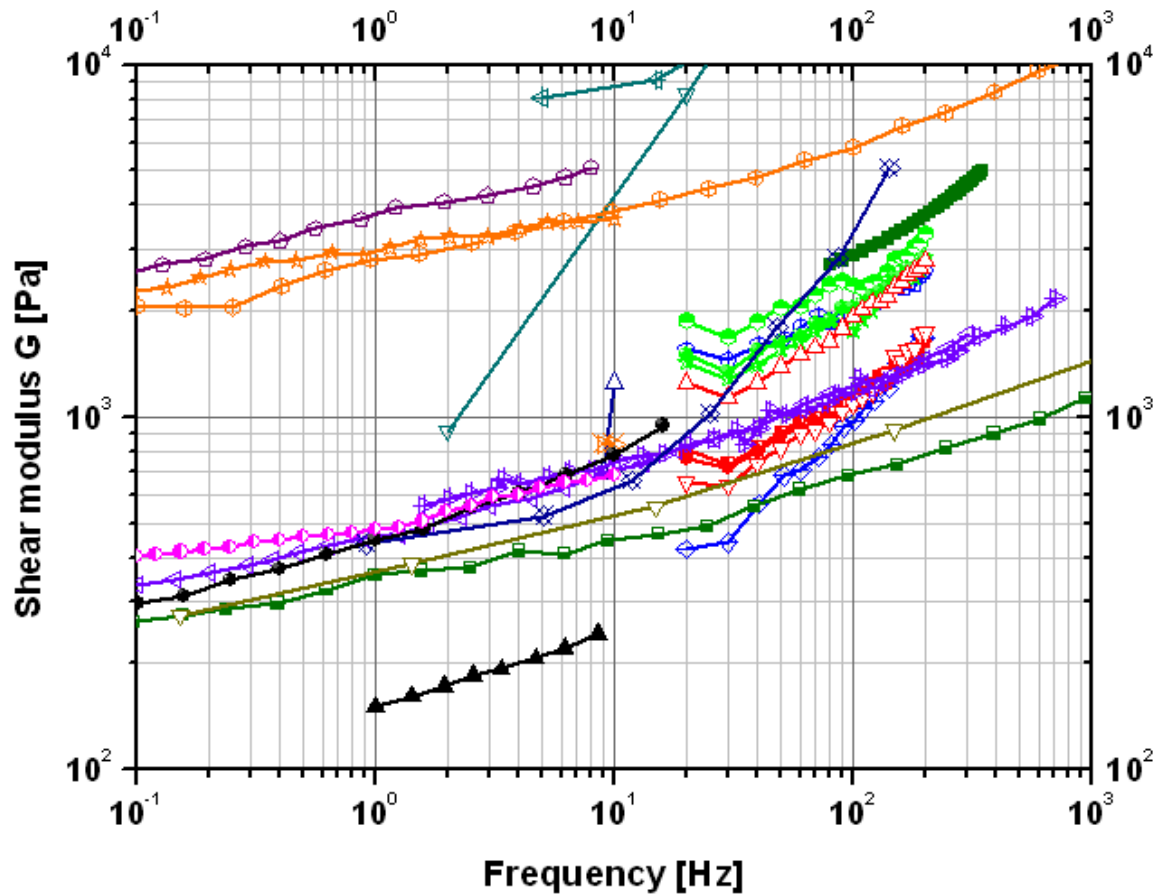
Compression in DMA

- Koeneman 1966 (Rabbit, Rat, Porcine, 25% strain)
- ◁ Galford et McElhaney 1970 (Monkey, 20% strain)
- ▷ Galford et McElhaney 1970 (Human, 20% strain)

Shear in DMA

- △ Fallenstein et Hulce 1969 (Human, 7 à 24,5% strain)
- ▽ Shuck et Advani 1970 (Human, 2,6% strain)
- ◊ Shuck et Advani 1972 (Human, 1,23% strain)
- ✕ McElhaney et al. 1973 (Human et Monkey)
- ▽ Peters et al. 1997 (Porcine, 1% strain)
- ◇ Arbogast et al. 1997 (Porcine, brain, 2,5% strain)
- ◇ Arbogast et al. 1997 (Porcine, brain stem, 2,5% strain)
- ◇ Arbogast et Margulies 1998 (Porcine, brain stem, PT direction, 2,5% strain)
- ◇ Arbogast et Margulies 1998 (Porcine, brain stem, TT direction, 2,5% strain)
- ◇ Arbogast et Margulies 1998 (Porcine, brain stem, PP direction, 2,5% strain)
- ◻ Thibault et Margulies 1998 (Young porcine, 2,5% strain)
- ◻ Thibault et Margulies 1998 (Young porcine, 5% strain)
- ◻ Thibault et Margulies 1998 (Old porcine, 2,5% strain)
- ◻ Thibault et Margulies 1998 (Old porcine, 5% strain)
- ▽ Brands et al. 1999 (Porcine, 1% strain)
- ▽ Brands et al. 2000 (Porcine, 1% strain)
- ✕ Darvish et Crandall 2001 (Bovine, 1% strain)
- ◻ Bilston et al. 2001 (Bovine, 0,1% strain)
- ◊ Nicolle et al. 2004 (Human, Porcine, 0,001% strain)
- ◊ Nicolle et al. 2004 (Human, Porcine, 0,1% strain)
- Hrapko et al. 2006 (Porcine, 1% strain)
- Shen et al. 2006 (Porcine, 1% strain)
- ◇ Vappou et al. 2007 (Porcine, 0,5% strain)
- ▲ Garo et al. 2007 (Porcine, 1% strain)

Appendix A. 8. Shear modulus for *in vitro* DMA tests between 0.01 and 10000Hz.



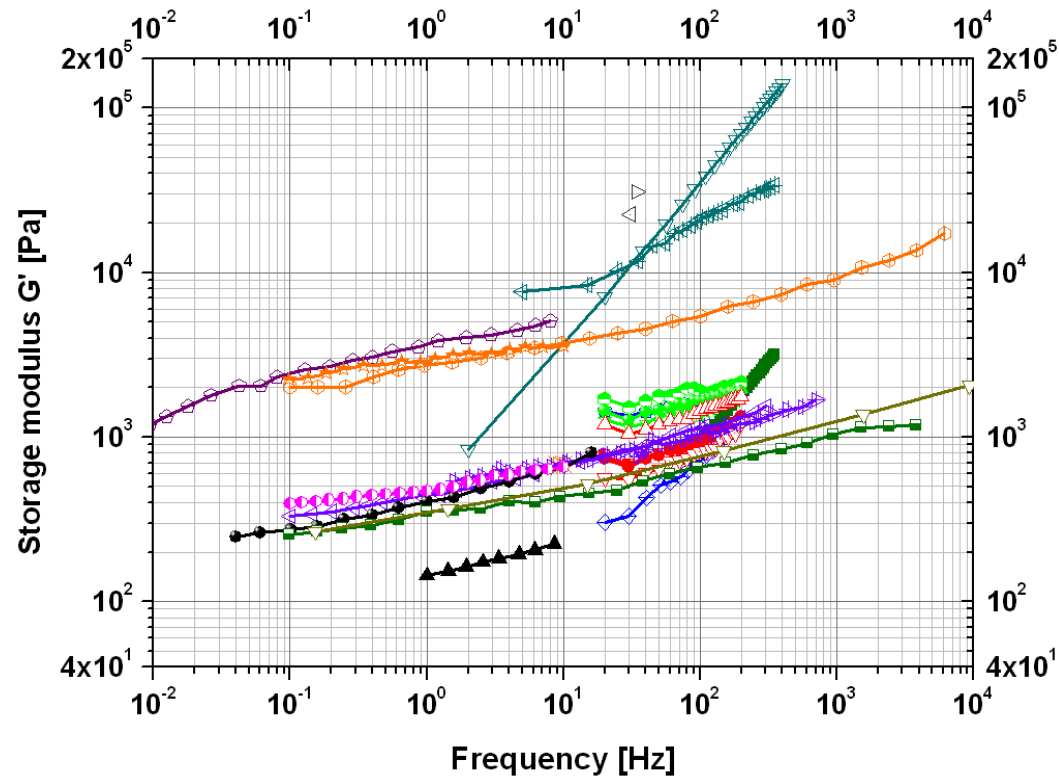
Compression in DMA

- Koeneman 1966 (Rabbit, Rat, Porcine, 25% strain)
- ◁ Galford et McElhaney 1970 (Monkey, 20% strain)
- ▷ Galford et McElhaney 1970 (Human, 20% strain)

Shear in DMA

- △ Fallenstein et Hulce 1969 (Human, 7 à 24,5% strain)
- ▽ Shuck et Advani 1970 (Human, 2,6% strain)
- ☆ Shuck et Advani 1972 (Human, 1,23% strain)
- ✱ McElhaney et al. 1973 (Human et Monkey)
- ◇ Peters et al. 1997 (Porcine, 1% strain)
- ◇ Arbogast et al. 1997 (Porcine, brain, 2,5% strain)
- ◇ Arbogast et al. 1997 (Porcine, brain stem, 2,5% strain)
- ◇ Arbogast et Margulies 1998 (Porcine, brain stem, PT direction, 2,5% strain)
- ◇ Arbogast et Margulies 1998 (Porcine, brain stem, TT direction, 2,5% strain)
- ◇ Arbogast et Margulies 1998 (Porcine, brain stem, PP direction, 2,5% strain)
- ◻ Thibault et Margulies 1998 (Young porcine, 2,5% strain)
- ◻ Thibault et Margulies 1998 (Young porcinee, 5% strain)
- ◻ Thibault et Margulies 1998 (Old porcine, 2,5% strain)
- ◻ Thibault et Margulies 1998 (Old porcine, 5% strain)
- ◇ Brands et al. 1999 (Porcine, 1% strain)
- ◇ Brands et al. 2000 (Porcine, 1% strain)
- ◇ Darvish et Crandall 2001 (Bovine, 1% strain)
- ◇ Bilston et al. 2001 (Bovine, 0,1% strain)
- ◇ Nicolle et al. 2004 (Human, Porcine, 0,001% strain)
- ◇ Nicolle et al. 2004 (Human, Porcine, 0,1% strain)
- Hrapko et al. 2006 (Porcine, 1% strain)
- Shen et al. 2006 (Porcine, 1% strain)
- ◇ Vappou et al. 2007 (Porcine, 0,5% strain)
- ▲ Garo et al. 2007 (Porcine, 1% strain)

Appendix A. 9. Shear modulus for *in vitro* DMA tests between 0.1 and 1000Hz.



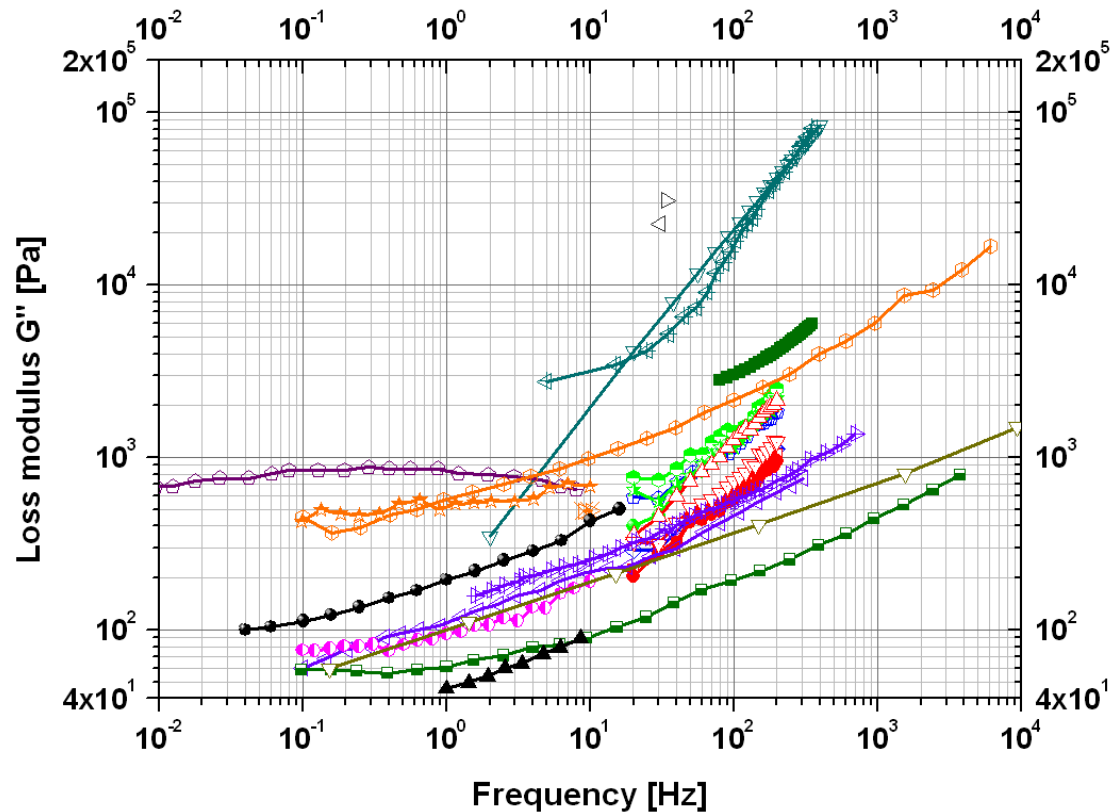
Compression in DMA

- Koeneman 1966 (Rabbit, Rat, Porcine, 25% strain)
- ◁ Galford et McElhaney 1970 (Monkey, 20% strain)
- ▷ Galford et McElhaney 1970 (Human, 20% strain)

Shear in DMA

- △ Fallenstein et Hulce 1969 (Human, 7 à 24,5% strain)
- ▽ Shuck et Advani 1970 (Human, 2,6% strain)
- ◆ Shuck et Advani 1972 (Human, 1,23% strain)
- ✕ McElhaney et al. 1973 (Human et Monkey)
- ◇ Peters et al. 1997 (Porcine, 1% strain)
- ◇ Arbogast et al. 1997 (Porcine, brain, 2,5% strain)
- ◇ Arbogast et al. 1997 (Porcine, brain stem, 2,5% strain)
- ◇ Arbogast et Margulies 1998 (Porcine, brain stem, PT direction, 2,5% strain)
- ◇ Arbogast et Margulies 1998 (Porcine, brain stem, TT direction, 2,5% strain)
- ◇ Arbogast et Margulies 1998 (Porcine, brain stem, PP direction, 2,5% strain)
- ◻ Thibault et Margulies 1998 (Young porcine, 2,5% strain)
- ◻ Thibault et Margulies 1998 (Young porcine, 5% strain)
- ◻ Thibault et Margulies 1998 (Old porcine, 2,5% strain)
- ◻ Thibault et Margulies 1998 (Old porcine, 5% strain)
- ◇ Brands et al. 1999 (Porcine, 1% strain)
- ◇ Brands et al. 2000 (Porcine, 1% strain)
- ◇ Darvish et Crandall 2001 (Bovine, 1% strain)
- ◇ Bilston et al. 2001 (Bovine, 0,1% strain)
- ◇ Nicolle et al. 2004 (Human, Porcine, 0,001% strain)
- ◇ Nicolle et al. 2004 (Human, Porcine, 0,1% strain)
- Hrapko et al. 2006 (Porcine, 1% strain)
- Shen et al. 2006 (Porcine, 1% strain)
- ◇ Vappou et al. 2007 (Porcine, 0,5% strain)
- ▲ Garo et al. 2007 (Porcine, 1% strain)

Appendix A. 10. Shear storage modulus for *in vitro* DMA tests between 0.01 and 10000Hz.



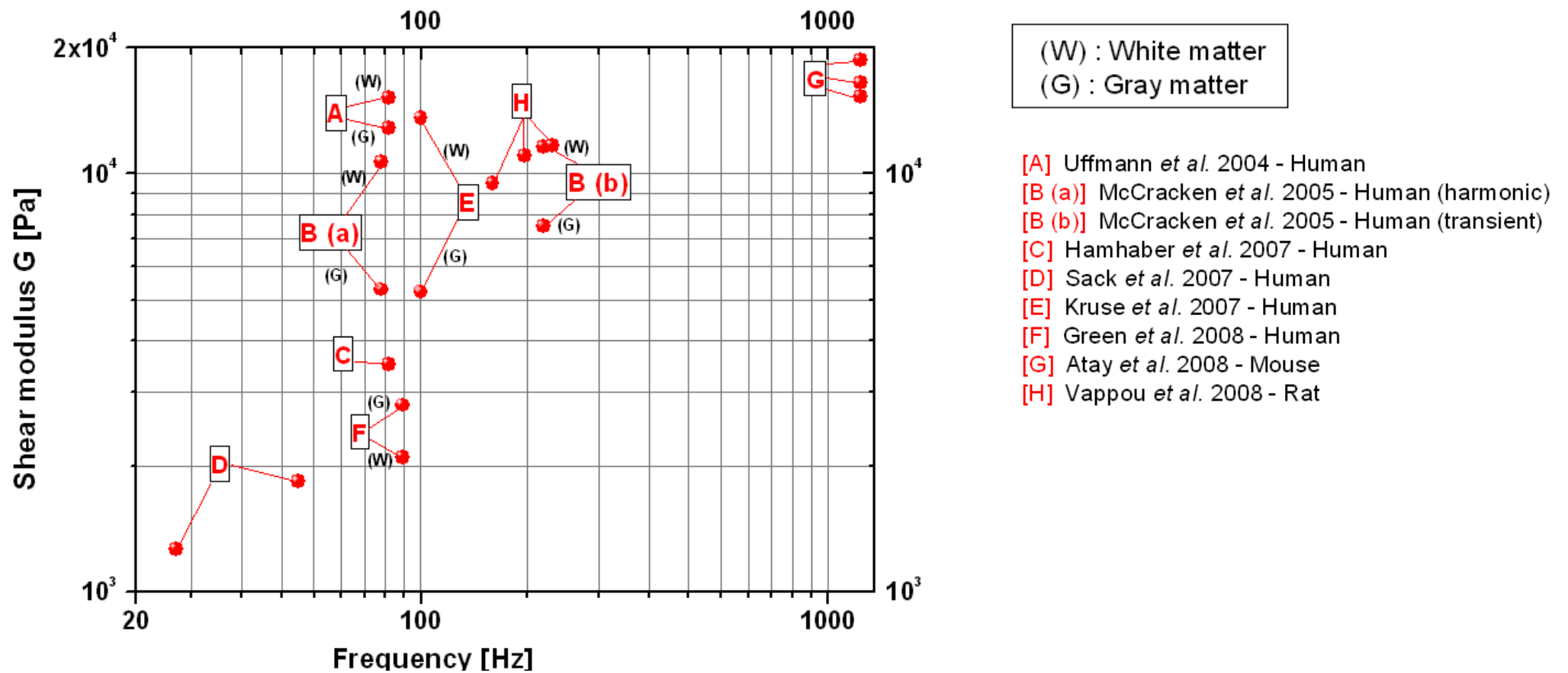
Compression in DMA

- Koeneman 1966 (Rabbit, Rat, Porcine, 25% strain)
- ◁ Galford et McElhaney 1970 (Monkey, 20% strain)
- ▷ Galford et McElhaney 1970 (Human, 20% strain)

Shear in DMA

- △ Fallenstein et Hulce 1969 (Human, 7 à 24,5% strain)
- ▽ Shuck et Advani 1970 (Human, 2,8% strain)
- ◊ Shuck et Advani 1972 (Human, 1,23% strain)
- ✕ McElhaney et al. 1973 (Human et Monkey)
- ▽ Peters et al. 1997 (Porcine, 1% strain)
- ◇ Arbogast et al. 1997 (Porcine, brain, 2,5% strain)
- ⊗ Arbogast et al. 1997 (Porcine, brain stem, 2,5% strain)
- ◇ Arbogast et Margulies 1998 (Porcine, brain stem, PT direction, 2,5% strain)
- ★ Arbogast et Margulies 1998 (Porcine, brain stem, TT direction, 2,5% strain)
- Arbogast et Margulies 1998 (Porcine, brain stem, PP direction, 2,5% strain)
- ◻ Thibault et Margulies 1998 (Young porcine, 2,5% strain)
- Thibault et Margulies 1998 (Young porcine, 5% strain)
- △ Thibault et Margulies 1998 (Old porcine, 2,5% strain)
- ▽ Thibault et Margulies 1998 (Old porcine, 5% strain)
- ▽ Brands et al. 1999 (Porcine, 1% strain)
- ▽ Brands et al. 2000 (Porcine, 1% strain)
- ⊗ Darvish et Crandall 2001 (Bovine, 1% strain)
- ◊ Bilston et al. 2001 (Bovine, 0,1% strain)
- ⊗ Nicolle et al. 2004 (Human, Porcine, 0,001% strain)
- ⊗ Nicolle et al. 2004 (Human, Porcine, 0,1% strain)
- Hrapko et al. 2006 (Porcine, 1% strain)
- Shen et al. 2006 (Porcine, 1% strain)
- ◇ Vappou et al. 2007 (Porcine, 0,5% strain)
- ▲ Garo et al. 2007 (Porcine, 1% strain)

Appendix A. 11. Shear loss modulus for *in vitro* DMA tests between 0.01 and 10000Hz.

Appendix A. 12. Shear modulus from *in vivo* MRE tests.

oAuthors	Subject	Frequency	G [kPa]	G' [kPa]	G' [kPa]
McCracken et al. 2005	Human				
	(WM)	80 Hz	10,7 ± 4,4	-	-
	(GM)	80 Hz	5,3 ± 1,3	-	-
	(WM)	200 Hz	11,6 ± 2,4	-	-
	(GM)	200 Hz	7,5 ± 1,6	-	-
Kruse et al. 2007	Human				
	(WM)	100 Hz	13,6 ± 1,3	-	-
	(GM)	100 Hz	5,2 ± 0,5	-	-
Uffmann et al. 2004	Human				
	(WM)	80 Hz	15,2 ± 1,4	-	-
	(GM)	80 Hz	12,9 ± 0,9	-	-
Hamhaber et al. 2007	Human	83,33 Hz	3,5	-	-
Sack et al. 2007	Human	25 Hz	1,27	1,17 ± 0,03	0,49 ± 0,06
		50 Hz	1,62	1,56 ± 0,07	0,43 ± 0,03
Vappou et al. 2008	Rat	150 Hz	9,5	6,33	4,8
		180 Hz	9,88	7,6	7,5
		210 Hz	11,7	8,45	8,15
Atay et al. 2008	Mouse	1200 Hz	16,8	-	-
Green et al. 2008	Human				
	(WM)	90 Hz	3,7	2,7 ± 0,1	2,5 ± 0,2
	(GM)	90 Hz	4,0	3,1 ± 0,1	2,5 ± 0,2

Table A - 1. Shear, storage and loss modulus from *in vivo* MRE tests.

Models	Authors	G_0 [kPa]	G_∞ [kPa]	β [s ⁻¹]	K [MPa]	ρ [kg.m ⁻³]	Experimental data
SUFEHM	Kang <i>et al.</i> 1997	49	16,2	145	1125	1040	Shuck et Advani 1972 (DMA in shear)
WSUBIM (White matter)	Zhang <i>et al.</i> 2001	12,5	2,5	80	2190	1060	Arbogast et Margulies 1998 (DMA in shear)
WSUBIM (Gray matter)		10	2	80	2190	1060	
SIMon	Thakhounts <i>et al.</i> 2003	10,34	5,2	100	560	1040	Arbogast <i>et al.</i> 1995 (Relaxation in shear)
Turin	Belingardi <i>et al.</i> 2005	49	16,7	145	5625	1140	Shuck et Advani 1972 (DMA in shear)
THUMS	Iwamoto <i>et al.</i> 2007	12,5	6,1	100	2,16	1000	Galford et McElhaney 1970 (Relaxation in compression)
SIMon	Thakhounts <i>et al.</i> 2008	1,66	0,928	16,9 5	558,47	1040	Takhounts <i>et al.</i> 2003 (Relaxation in shear)

Table A - 2. Mechanical properties of main brain FEM using viscoelastic linear law.